12-2018

Comparing the Therapeutic Efficacy of Human Amniotic Membrane and Adipose-Derived Mesenchymal Stem Cells in Mitigation of Osteoarthritis

Mackenzie Catherine Bowman
Clemson University, m.c.bowman@hotmail.com

COMPARING THE THERAPEUTIC EFFICACY OF HUMAN AMNIOTIC MEMBRANE AND ADIPOSE-DERIVED MESENCHYMAL STEM CELLS IN MITIGATION OF OSTEOARTHRITIS

A Thesis
Presented to
the Graduate School of
Clemson University

In Partial Fulfillment
of the Requirements for the Degree
Master of Science
Bioengineering

---

by
Mackenzie Catherine Bowman
December 2018

Accepted by:
Dr. Jeremy Mercuri, PhD, Committee Chair
Dr. Ken Webb, PhD
Dr. Brian Burnikel, MD

ABSTRACT

Osteoarthritis (OA) is a leading cause of disability and pain to patients worldwide, and is characterized by abnormal subchondral bone remodeling, such as sclerosis and osteophyte formation, synovial tissue inflammation, and the destruction of articular cartilage, with limited capability for intrinsic repair. Currently, only palliative options are available to help treat the debilitating effects of the disease as there are no therapies authorized to halt or prevent the progression of OA. Due to the destructive nature of OA and a lack of current treatment options, there is an urgent need to develop novel therapies to mitigate the progression of OA.

Stem cell-based regenerative strategies hold promising opportunities to provide enhanced therapeutic efficacy due to their increasingly investigated and reported ability to regulate inflammation *in vitro.* Our lab has previously shown, in an *in-vitro* explant co-culture study, that human perinatal amniotic membrane-derived stem cells (hAMSCs) demonstrated an enhanced chondro-protective effect compared human adipose-derived stem cells (hADSCs), which are commonly utilized in regenerative applications. To further our previous findings, the overall purpose of this research was to investigate and compare the therapeutic efficacy of these two stem cell sources in mitigation of OA *in vivo.* This was achieved by directly comparing hAMSCs to hADSCs via various histological and biochemical outcome measures as well as longitudinal fluorescent cell tracking ensuing direct intra-articular injection into a spontaneous OA model; the Dunkin Hartley Guinea Pig (DHGP).

Results indicate that the DHGP serves as a validated spontaneous OA model while histological trends demonstrated that use of stem cell treatments mitigated cartilage degradation in comparison to non-stem cell treated groups. However, it was observed that both stem cell sources did not provide a significant therapeutic effect *in vivo* as results revealed a limited residence time and lack of tissue engraftment of hAMSCs and hADSCs following injection. Altogether, these findings highlight the current limitations of stem cell-based therapy once indicated in a complex, pathological environment. Therefore, further investigations are warranted to evaluate the therapeutic capabilities of stem cells following transplantation in *in vivo* models of OA.

DEDICATION

The work herein is dedicated foremost to my parents, Veronica and Patrick Bowman, as well as my brother Sean. I thank them for their constant support throughout my academic endeavors and instilling the importance of following my dreams.

ACKNOWLEDGMENTS

I would like to acknowledge Dr. Jeremy Mercuri for his guidance and encouragement throughout my research and time in the Ortho-X lab. My research could not have been completed without his constant support and mentorship. I would also like to thank my committee members, Dr. Ken Webb and Dr. Brian Burnikel, for their assistance on the progression of this project. Additionally, I would like to recognize the Godley-Snell Research Center staff and their dedication and efforts in guiding me through this research. Lastly, I would like to thank the current members of the Ortho-X lab for their diligent involvements to this research and willingness to provide help. I would especially like to recognize Joshua Walters, thank you for your unwavering advice and constant laughs.

TABLE OF CONTENTS

LIST OF TABLES

LIST OF FIGURES

(LIST OF FIGURES CONTINUED)

(LIST OF FIGURES CONTINUED)

(LIST OF FIGURES CONTINUED)

(LIST OF FIGURES CONTINUED)

(LIST OF FIGURES CONTINUED)

(LIST OF FIGURES CONTINUED)

(LIST OF FIGURES CONTINUED)

CHAPTER ONE:

LITERATURE REVIEW

1.1 Introduction to Osteoarthritis

Osteoarthritis (OA) is a prominent arthritic joint disease that is both debilitating and progressive, leading to severe pain for patients. In comparison with other bone and arthritic pathologies, OA represents the primary condition, leading Rheumatoid Arthritis and Osteoporosis.[1] It is also estimated that more than 27 million Americans suffer from OA and has resulted in a total estimated cost of $128 billion dollars.[2,3] Long term studies have shown that knee OA, specifically, accounts for more than 80% of the disease's total affliction and has doubled in prevalence since the mid-20th century.[4] With an increasingly aged population and rising body mass index (BMI), this prevalence is expected to increase dramatically and rapidly over the next 20 years.[4]

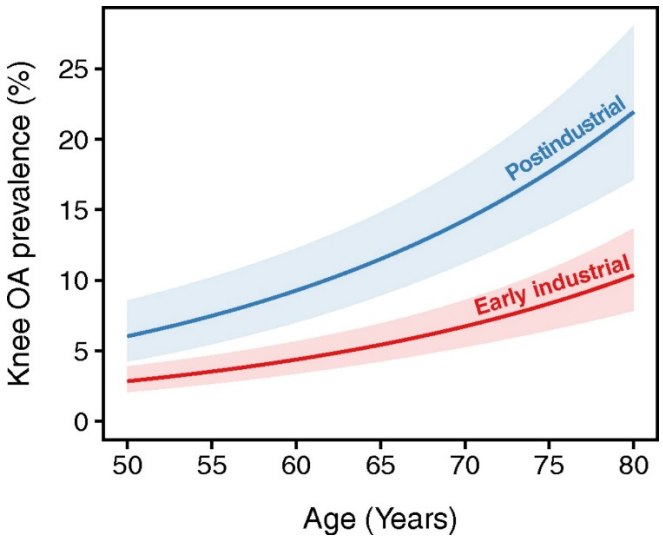

Figure 1: Graphical depiction of the increasing knee OA prevalence since the mid-20th century.[4]

OA is a multi-faceted disease characterized principally by cartilage degeneration, alterations in the subchondral bone, and inflammation of the synovium.[5] Additionally,

deterioration of surrounding menisci and ligaments, enlargement of the joint capsule, and changes in fat pads and muscles, influence the symptoms of OA.[6] The pathogenesis of OA can arise due to various causes including age. It is estimated that 34%-40% of the United States population over the age of 65 is affected.[7,8] Other risk factors include: obesity, prior joint trauma, genetic predisposition, overuse, and irregular joint shape.[6,9] Furthermore, it has become more apparent that inflammatory mechanisms and biochemical mediators, such as cytokine production, plays a central role in the imbalance of joint tissue homeostasis, leading to further damage.[10]

Currently, there is no cure for OA and patients afflicted by the disease are only offered palliative treatments options. Common treatments include self-care options such as exercise, diet, and physical therapy in prospect of lowering BMI and thus the mechanical load placed on the joint. Another primary non-invasive option employed is the use of oral medications, most commonly nonsteroidal anti-inflammatory drugs (NSAIDs) or acetaminophen.[11] However, with the use of these medications, there are risks of harmful systemic effects such as gastrointestinal or cardiovascular irregularities.[12] An additional non-surgical option includes viscosupplementation, in which intra-articular injection of hyaluronic acid (HA) is performed in order to assist in replacing loss of synovial fluid or to combat detrimental alterations in synovial fluid viscosity.[13] Although HA injections have shown to enhance function and alleviate pain, effectiveness depends on the composition and residual time in the joint, therefore, optimization of the procedure to improve efficacy is under investigation.[11,14,15,16]

As OA progresses, the entire joint structure is affected, resulting in further loss of function, pain, and malformation.[6] While managements that are more conservative may aid in relieving symptomatic pain, patients with increasing severity of OA may require further intervention. Surgical solutions includes the replacement of native tissue with either polymeric or metal implants via total joint replacement, overall helping to restore joint mobility to patients. However, there are many possible complications following arthroplasty, such as infection, inflammation, blood clot formation, implant loosening, and in some cases, continued pain.[17] As these associated issues frequently occur ensuing total joint replacement, it is usually necessary to perform a secondary revision surgery.[17,18] In 2003 alone, approximately 8% of the total knee replacements performed in the US needed a revision surgery.[17] In light of the shortcomings comprising current treatment options, it is necessary to develop a novel approach to repair and regenerate joint tissues.

Recent studies in the field of orthopaedic regenerative medicine have focused on the use of stem cell-based therapies to be used alone or in combination with either synthetic or natural scaffolds. Mesenchymal stem cells (MSCs), specifically, have gained attention as a therapeutic source as they possess the capacity to differentiate into numerous tissue cell types including chondrocytes, adipocytes, and osteocytes.[19,20,21] Clinically, this strategy would work to mitigate progression of OA or promote the repair of damaged joint tissues.

Evaluation of MSCs and their potential as a clinical therapy for OA will be furthered detailed in a later section.

In summary, OA is a debilitating disease that poses a large economic burden to patients. As treatment options only provide palliative care and with a growing demand for total joint replacements, there is a crucial need for further investigation into regenerative strategies to diminish the development of OA.

1.2 Knee Joint Physiology

1.2.1 Knee Joint Anatomy and Function

The knee joint represents an essential synovial hinge joint that facilitates the movement of the lower leg in association with the upper leg, while also supporting body weight. The knee joint, which contains two articulations, patellofemoral and tibiofemoral, is vital to everyday activities to allow walking, running, sitting, and standing, as the joint formed between the tibia and femur allow extension and flexation.[22]

Being the longest and strongest bone in the human body, the femur supports tremendous amounts of forces that act upon it. A smooth ball-and-socket joint forms at the proximal end of the femur with the hip to allow movement and rotation around its axis. Distally, the femur broadens above the knee to form curved and smooth medial and lateral condyles that convene with the medial and lateral plateaus of the tibia, ultimately forming the knee joint. The tibia is located medial to the fibula and endures most of the load

placed on the joint. On the upper extremity of the tibia, between the smooth, concave plateaus, forms the intercondylar region. This area offers points of attachments for the meniscus, anterior cruciate ligament (ACL), and posterior cruciate ligament (PCL). The ACL works to inhibit forward movement of the tibia and hyperextension of the knee, while the PCL, which lies behind the ACL, inhibits backward movement of the tibia, ultimately securing the knee along its anterior and posterior axis. Positioned amongst where the femur and tibia articulate is the meniscus. This thick portion of cartilage acts as a shock absorber to protect against the loads obtained from the knee, while also functioning to provide stabilization and lubrication. Connecting the lateral meniscus to the medial meniscus is the transverse ligament. The kneecap, or patella, represents the bone in front of the femur on the surface of the knee joint in order to provide protection. The patella is held in place by muscles and tendons such as the patellar ligament attaching to the tibia, and the quadriceps tendon attaching to the quadriceps muscle in front of the femur. Figure 2 below provides a visual representation of the total knee joint anatomy depicting corresponding components described.

Encasing the bones of the knee is a fibrous, connective joint capsule that offers supplementary strength by containing other sturdy ligaments, such as the medial collateral ligament (MCL) and the lateral collateral ligament (LCL), which work to support knee structure and appropriate orientation by averting lateral dislocation. Supplementary to the joint capsule, ligaments, tendons, and muscles that work to reinforce the knee, there are also numerous and imperative structures that aid in

defending the joint from friction and external forces. Bursae are fluid-filled sacs that encase the knee to moderate friction between adjoining structures such as tendons that move across the exterior of the joint and between the patella and femur.[23] Additionally, the infrapatellar fat pad which is located below the patella, is composed of adipose tissue to assist in suppressing forces encountered by the knee. Altogether, these structures help to reinforce the knee for optimal strength and stability for normal function.

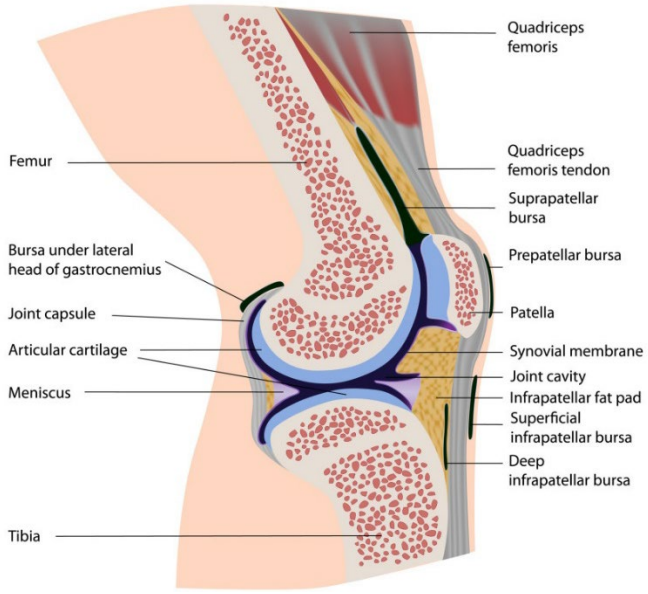

Figure 2: Image of total knee joint anatomy depicting corresponding components such as muscle, meniscus, synovial membrane, articular cartilage.[24]

1.2.2 Synovium

Lining the joint capsule is a thin synovial membrane (SM) that exudes synovial fluid (SF), providing lubrication to the knee in order to reduce friction and wear. Additionally, the SF participates in regulating the functional characteristics of the articular surface and chondrocyte activity, as the SM works as a semi-permeable membrane to allow component cross talk in and out of the joint space.[7] This cellular communication is vital

for conserving the normal physiologic state of articular cartilage by providing regulation of SF composition and cartilage nutrient exchange.[25,26] Furthermore, the surface layer of SF covering the articular surface creates a pressurized fluid film that tolerates significant load, ultimately providing protection for the opposing cartilage layers.[27]

The microscopic and histologic composition of normal synovial tissue comprises of fibrous, areolar, and adipose tissue in which one to two continuous layers of cells can be visualized at the synovial lining.[28] Additionally, capillaries and lymphatic vessels are present within the synovium.[28] The cellular components of normal synovium include fibroblast-like synovioctyes and macrophages in which residing macrophages arrive to the synovium via the vascularized network of vessels as circulating monocytes.[28] These macrophages are only minimally observed in normal synovial membrane, but significantly increase in cell number in osteoarthritic synovium. Similarly, synoviocytes are presented in one to two layers at the lining, however during OA pathogenesis, synovial membrane and villous hyperplasia is observed due to increase in cell layers.

Highlighting the principle SF molecules produced in the synovium via synoviocytes, Lubricin, Hyaluronic Acid (HA), and Surface-Active Phospholipids (SAPL) act to lessen friction and wear by adsorbing to the articular surface and supplying a boundary lubrication.[27-29] This extremely effective lubrication mode upholds exceptionally low friction coefficients (approximately $\mu = 0.0005–0.04$) in order to protect the articular joints.[30] The balance between the rate of loss, due to degradation and transport through

the semi-permeable membrane, and synthesis of SF molecules, dictates their concentration levels. It is therefore imperative to maintain the equilibrium of SF concentration as alterations will affect the boundary-lubricating ability, ultimately affecting articular cartilage integrity.[31] Inflammation of the synovial membrane is a hallmark of OA, and this pathological state will be furthered detailed in a later section.

1.2.3 Articular Cartilage

The articular cartilage lining the exterior of joints represents a specialized connective tissue that functions to provide a smooth and lubricated surface for articulation, while also diffusing loads to the underlying subchondral bone. The distinct biological and mechanical properties of articular cartilage are contingent upon the interactions between the extracellular matrix (ECM) and chondrocytes.[32] The compact ECM primarily comprises of water, collagen, and proteoglycans, along with other non-collagenous proteins and glycoproteins, while chondrocytes form the framework of the tissue matrix, ultimately forming distinct zones of non-calcified cartilage.[26]

To highlight the specific components of articular cartilage ECM, water is the most abundant constituent, supplying 80% of the total wet weight.[26,33] Across the articular surface, transport of water containing dissolved ions such as sodium, calcium, and potassium, help to distribute nutrients to the residing chondrocytes as well as supply another mode of lubrication.[26] Total water concentration decreases to approximately 65% in the deep zone as frictional resistance against the flow through the ECM is high,

ultimately producing a pressurization of water within the matrix, allowing the capability to endure significant loads.[26,34]

Comprising of approximately 60% of the cartilage dry weight, collagen fibrils form an extensive network to provide mechanical integrity.[26,35] There are multiple types of collagen present in the matrix including Type I, IV, V, VI, IX, and XI; however, Type II collagen is the predominant type. Representing 90% to 95% of the total matrix, Type II collagen intertwines with proteoglycan composites to ultimately provide structural support to stabilize the matrix.[26,36]

Accounting for 10% to 15% of the cartilage wet weight, proteoglycans are protein monomers in which negatively charged glycosaminoglycan (GAG) chains are covalently attached to the protein core.[26,37,38] The negative nature of GAG chains also attracts many positive sodium ions, inducing a large amount of water to rush into the matrix and create a swelling pressure, ultimately functioning to help the cartilage withstand compressive forces.[26,37,39] One well-characterized proteoglycan present in articular cartilage is aggrecan, being the largest in size and most abundant.[26,40,41,42] This protein monomer is distinguished by its capability to self-assemble and interact with hyaluronic acid to develop large proteoglycan aggregates.[42] This ultimately provides an imperative gel-like structure to provide resistance for load-bearing properties as well as chondrocyte-matrix interactions in the cartilage.[40,41,43] Other smaller proteoglycans existing in the ECM include fibromodulin, decorin, and biglycan, that work to interact with collagen fibrils in

the matrix.[26,40,42] The primary GAGs of the ECM include hyaluronic acid, chondroitin sulfate, heparin sulfate, and keratin sulfate, in which all contrast in molecular weight, configuration, and length.[26,39] These differences allow for various interactions with adjacent chains and permits the formation of proteoglycans in the matrix. Additional ECM components found within articular cartilage include noncollagenous proteins and glycoproteins in which their specific function is not fully understood; however, have shown to play a role in the organization and maintenance in the structure of the matrix.[26]

The resident cell type in articular cartilage is the chondrocyte, in which they play an exclusive role in the development, maintenance, and repair of the ECM.[26,44] Originating from mesenchymal stem cells (MSCs), chondrocytes occupy roughly 1%-5% of the total cartilage tissue and vary in size, shape, and number, depending on their functional location the cartilage.[44–46] In healthy tissue, chondrocytes are in a quiescent state; however, they have an intrinsic ability to respond to different stimuli, such as mechanical and biochemical stresses, as they contain receptors for components in the ECM.[25,26,47] Upon activation, the production of degradative enzymes, such as matrix metalloproteinases, and inflammatory mediators are stimulated to provoke a cycle of cartilage destruction, which will be further explored in a later section.[26,47,48] Furthermore, cartilage repair following damage is a prevalent issue, as articular cartilage does not contain the ability to self-heal.[26,48] This is due to the fact that chondrocytes have a constrained ability for replication and the tissue itself is non-vascularized, lacking blood vessels and nerves.[26,49,50]

To further highlight the structure of articular cartilage, Figure 3 below depicts healthy cartilage zones with chondrocyte organization and collagen fiber orientation. It can be visualized that below the articular surface, the thin superficial zone comprises primarily of type II and IX collagen fibers compacted tightly and aligned parallel, to form approximately 10-20% of the cartilage volume and acts to defend deeper layers from shear stresses.[26,44] Many chondrocytes occupy this layer and are flattened to help maintain the matrix and ultimately, this zone acts to oppose the compressive, shear, and tensile forces imposed by the joint.[6,25,26] Beneath the superficial zone, lies the middle zone to provide even more resistance to compressive forces. Spherical chondrocytes, proteoglycans, and thicker collagen fibers aligned obliquely to the surface, comprise this zone to make up approximately 40-60% of the total cartilage volume.[26] Under the middle zone and occupying approximately 30% of articular cartilage volume, the deep zone supplies the greatest resistance to compressive forces, containing the highest amount of proteoglycan content. Additionally, the collagen fibers are assembled perpendicular to the surface while the chondrocytes are arranged parallel to the collagen fibers in a column-like fashion.[26] Forming an interface at the deep zone, the tidemark separates the non-calcified cartilage from the calcified cartilage, while the cement line forms an anatomic bridge in which the calcified layer of cartilage attaches to the subchondral bone.[26,51]

Moreover, articular cartilage represents a unique and complex structure containing many ECM components necessary for tissue homeostasis. As observed in osteoarthritic

conditions, damage to the cartilage results in a destructive sequence of biochemical events in which there is no intrinsic ability to regenerate. It is therefore desirable to investigate strategies to restore damaged cartilage in order to restore its natural ability to withstand compressive loads.

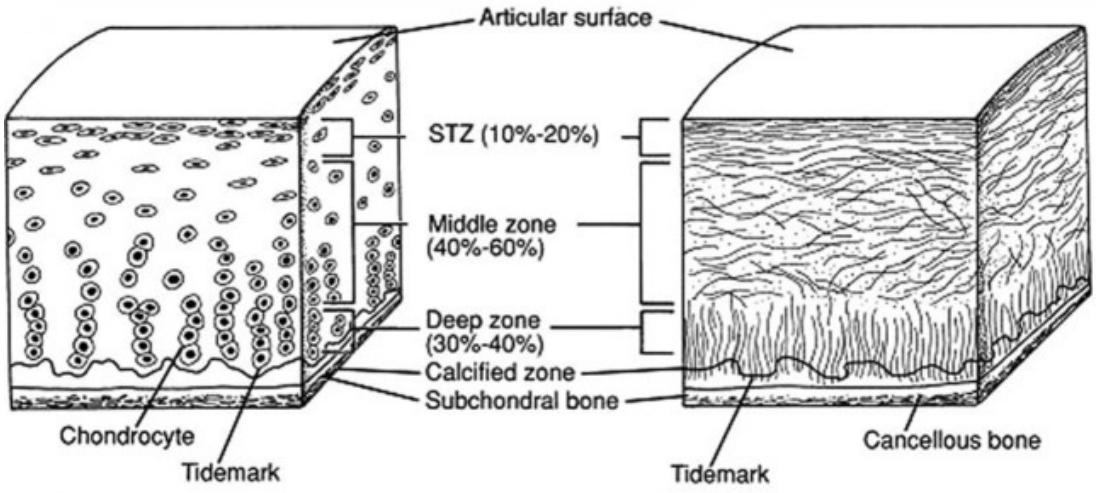

Figure 3: A cross-sectional image of healthy articular cartilage zones displaying chondrocyte organization and collagen fiber orientation.[26]

1.2.4 Subchondral Bone

Articular cartilage and subchondral bone are in close synthesis to form a functional unit called the osteochondral junction.[52] This intricate junction comprises of a tidemark to separate the deep layer of non-calcified cartilage with the calcified cartilage, and the cement line to separate the subchondral bone.[5,52] The subchondral bone is divided into two distinct compartments, the subchondral bone plate and subchondral trabecular bone.[5] The subchondral bone plate represents the cortical matrix lying directly below the calcified cartilage and serves to support the overlying articular cartilage by transmitting loads of the joint to the underlying trabecular bone.[53–55] Transitioning into a system of

cancellous bone, the subchondral trabecular bone acts as a dynamic structure, adjusting trabecular orientation, in order to adapt to mechanical forces acquired from the joint.[5,56] This ultimately provides important shock-absorbing properties in order to protect the articular cartilage.[5,56] Additionally, the subchondral trabecular bone is metabolically active as it is occupied with vascularized networks that provide a direct link between articular cartilage and subchondral bone in order to supply nutrients.[5,53] Overall, the biomechanical and biochemical cross-talk amongst the osteochondral junction, may play a role in the maintenance and degeneration of the joint.[52] Bone modifications associated with OA include sclerosis, development of osteophytes at the joint margin, formation of subchondral bone cysts, and due to abnormal bone remodeling, the subchondral bone is hypomineralized.[56] These pathological changes will be further highlighted in a later section.

1.3 Knee Joint Pathology

Knee OA is characterized as a chronic and slowly progressive disease that is commonly classified as a degenerative wear and tear disorder of the joint.[47,57] However, it is gaining acceptance that it is a condition that is also associated with biochemical and biomechanical alterations in the knee joint, eliciting pro-inflammatory mediators.[58–61] Pathologically, late-stage OA is distinguishable by inflammation of the synovium, destruction of articular cartilage, sclerosis of the subchondral bone, and osteophyte formation at the margins of the joint, overall affecting the entirety of the joint tissue.[47]

Moreover, OA can result in total joint failure and the components driving pathogenesis will be further outlined below.

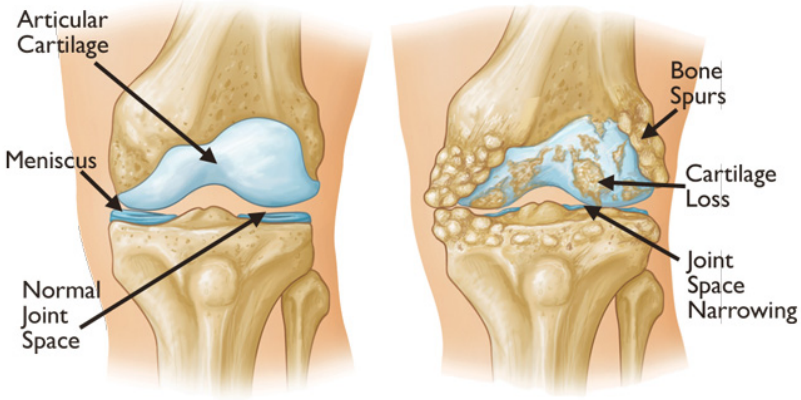

Figure 4: Image comparing a healthy knee joint versus an osteoarthritic knee joint, in which common pathological features such as cartilage loss, joint space narrowing, and osteophyte formation are depicted.[62]

1.3.1 Articular Cartilage Degradation and Synovitis

It is established that knee OA is a degenerative disease that results in damage to the joint tissues; however, ongoing investigations are examining the biochemical and molecular mechanisms that drive pathogenesis. It has been found that various associated pathways direct the irregular modifications of the joint tissues, in which a cycle of pro-inflammatory mediators elicit responses in the articular cartilage, subchondral bone, and synovium.[47,61]

Responsible for the smooth articulation of the joint and mechanical distribution of loads to the underlying subchondral bone, the articular cartilage structure and function is regulated by chondrocytes that maintain the extracellular matrix (ECM) and tissue homeostasis. In a healthy and normal physiologic condition, chondrocytes are in a resting

and quiescent state; however, due to their receptors for ECM components, they undergo phenotypic alterations and become activated in response to external stimuli and tissue damage.[6,44,63] It should be noted that the exact activation mechanism is not fully understood, although hypotheses indicate that age-related changes in ECM molecules and inflammatory stimulations may directly activate chondrocytes.[63,64] Activation of chondrocytes by mechanical and inflammatory stimuli occurs mainly through the NF-κB and MAPK pathways, which results in a loss of ECM homeostasis and is distinguished by cell proliferation, cluster formation, increased propagation of matrix-degrading enzymes, and upregulation of pro-inflammatory mediators.[6,63,65] The principle matrix-degrading components established in OA are aggrecanases and collagenases, comprising the matrix metalloproteinase (MMP) family, which are enzymes that cooperatively function to degrade components of the ECM.[6,64,66,67] It has been determined that matrix degradation in early OA stages may be due to MMP-3 and ADAMTS-5, which function to degrade aggrecan, the major proteoglycan of articular carrilage.[6] As OA progresses, it has been established that increased activity of MMP-1 and MPP-13 is provoked, in which these components are extremely proficient in degrading collagen, the essential and major ECM constituent, by cleaving the fibril structure.[6,66,68] More specifically, MMP-1 is implicated in the degradation of collagen types I, II, and III while MMP-3 is capable of damaging several extracellular molecules, comprising of collagen types II, III, IV, IX, and X, fibronectin, and various proteoglycans.[67] In addition, it has been shown that MMP-3 has the ability to upregulate the expression of other MMPs.[67] MMP-13 has a foremost ability to cleave collagen type II and therefore is commonly utilized as a

biomarker for the detection and study of osteoarthritis.[67] Due to the matrix-degrading components that are stimulated from activated chondrocytes, OA results in progressive cartilage degradation. This is characterized by fibrillation and destruction of the articular surface and loss of proteoglycan content, overall reducing the compressive stiffness and the lubricating nature of the tissue.[44] Furthermore, the joint space narrows and the articulating surface is no longer smooth which ultimately leads to additional pain to the patient as the bones begin to rub together.

While OA traditionally has been viewed as a disease of the articular cartilage with accompanying subchondral bone involvement, it is now recognized to be more complex as modern imaging modalities and increasing evidence suggests that synovitis and resulting pro-inflammatory mediators play a crucial role in the pathogenesis of OA.[61] In addition to activated chondrocytes, it has been established that resident synoviocytes from the synovium illicit pro-inflammatory mediators that progress the pathogenesis of OA. Inflammation of the synovium involves the infiltration of mononuclear cells, such as macrophages and lymphocytes, into the synovial membrane and production of various pro-inflammatory cytokines, including tumor necrosis factor-α (TNF-α) and interleukin 1β (IL-1β), chemokines, toll-like receptors (TLRs), and MMPs.[47,65] Osteoarthritic changes that are observed histologically in the synovial membrane contain characteristics indicative of an inflammatory response, such as synovial lining hyperplasia, villous hyperplasia, fibrosis, and infiltration of macrophages which can form clusters of multinucleated giant cells (MGCs) for enhanced phagocytosis.[7,61,69] Under normal

conditions, synovial fluid components such as lubricin and HA are not permeable through the synovial membrane due to their high molecular weight, while smaller molecules, such as growth factors, readily diffuse.[7] This permits the preservation of lubricating molecules within the joint, while blocking plasma proteins from entering and accumulating on the articular surface; however, when synovial inflammation and hyperplasia occur, the membrane permeability is changed. This alteration leads to decreased concentrations of lubricin and HA observed in synovial fluid.[7] Additionally, it has been observed that the presentation of synovitis varies with disease extent and associated structural changes in other joint tissues; however, it is established that the existence of synovitis in OA is coupled with increasing pain and joint dysfunction.[7,59] Recent investigations have offered insight into the various pathways and mechanisms motivating the progression of synovitis in OA and will be furthered detailed below.

In response to cellular stress and ECM damage that occurs in an osteoarthritic joint, immune system activation ensues via damage-associated molecular patterns (DAMPs).[7] This activation stimulates pattern recognition receptors known as toll-like receptors (TLRs) in response to tissue damage, and is a crucial impetus for NF-κB initiation and successive production of various pro-inflammatory mediators such as cytokines and chemokines.[6,7,10] This can be further visualized from the schematic depicted in Figure 5 below. It should be noted that the governing mechanisms implicated in TLR activation is not fully understood and their function in stimulating synovitis in OA is under investigation. The processes driving inflammation in OA are complex and there are

numerous pro-inflammatory cytokines that are measurable in the synovial fluid and joint tissues, therefore, the foremost mediators, IL-1β and TNF-α, will be discussed.

The cytokine IL-Iβ results in suppression of collagen and aggrecan synthesis, while promoting upregulating matrix-degrading components, ADAMST and MMPs.[7,9,44,65] Additionally, it has been found that chondrocytes exposed to IL-1β undergo apoptosis more readily and IL-1β initiates the production of reactive oxygen species (ROS) that causes destruction of the articular cartilage.[9,65] Along with synoviocytes, IL-1β may be synthesized by chondrocytes and macrophages, in which its activation causes a cyclic expression of other inflammatory mediators, causing a cascade of inflammation, and ultimately damages the joint tissues further.[6,9,44]

In addition to IL-1β, the cytokine TNF-α is evident in the synovial membrane of OA patients, and is a predominant mediator of inflammation.[7,9,60] TNF-α has the unique capability to bind to two membrane receptor superfamily isotypes, TNF-R1 and TNF-R2, both of which participate in signal transduction to activate various pathways, such as NF-κB, that stimulate an inflammatory response observed in the synovium.[9] Furthermore, TNF-α is associated with downstream cellular targets such as TNF receptor associated death domain protein (TRADD) and fas-associated protein with death domain (FADD), that further initiates cellular death.[9] In addition to synovial inflammatory effects, TNF-α inhibits chondrocyte synthesis of proteoglycan components and type II collagen, while also inducing chondrocyte apoptosis, affecting articular cartilage integrity.[9,70] Overall, the

effect of TNF-α concurs with the influences of IL-1β as both result in the initiation of similar components of signaling pathways to activate inflammatory responses, ultimately driving the pathogenesis of OA.[7]

In addition to the main cytokines that illicit inflammation in the joint, chemokines are small molecules that play a vital function in mediating recruitment of inflammatory cells. Chemokines mainly function by binding to G-protein coupled cell-surface receptors that activate signal transduction pathways.[10] Highlighting key chemokines observed in the mediation of OA pathogenesis, chemokine ligands 2, 5, 7, and 19 (CCL-2, -5, -7, -19) are associated with recruitment of inflammatory infiltrates, such as macrophages.[7,10] Additionally, synoviocytes express chemokine receptor 7 (CCR-7) which mediates the upregulation of vascular endothelial growth factor (VEGF) in response to CCL19, indicating angiogenesis.[7] It has also been found that CCL2 involvement with its receptor CCR2, increases MMP expression, inducing cartilage ECM loss.[10,71] In addition to synovial cell expression, evidence has shown that chondrocytes express CXC chemokine ligand 12 (CXCL-12) that also stimulates MMPs and other catabolic mediators, ultimately affecting tissue integrity.[10] Overall, the various chemokine families involved in the inflammatory response illustrates the complicated mechanisms that play a role in OA pathogenesis.

In conclusion, synovial lining hyperplasia, fibrosis, and infiltration of mononuclear cells are hallmarks of synovial inflammation in OA, which ultimately contributes to the

progression of cartilage loss as well as symptoms of the disease, including joint pain, swelling, and stiffness.[61] Moreover, the molecular cross-talk of pro-inflammatory mediators between cartilage and synovium could influence the impact of underlying OA development and pathogenesis in which cartilage damage in turn intensifies synovial inflammation and vice versa, creating a destructive cycle.[72]

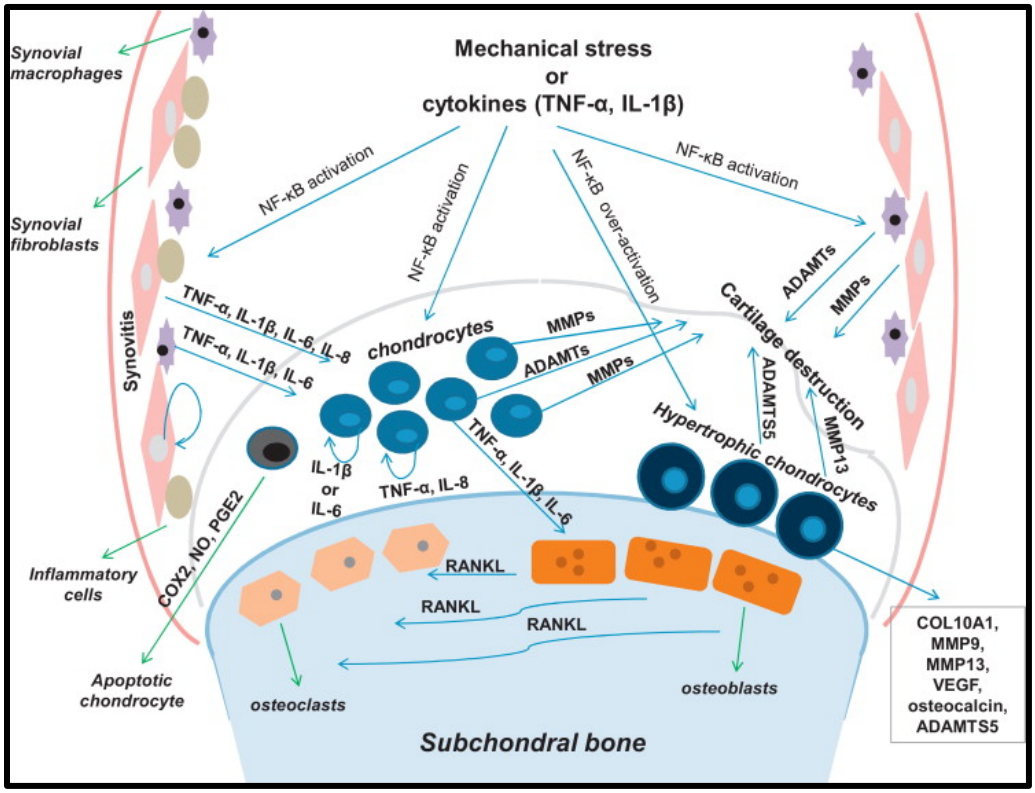

Figure 5: Schematic of the NF-κB signaling pathway initiated from mechanical stimuli and cytokines TNF-α and IL-1β, which further induces an up-regulation of pro-inflammatory mediators and degradation components.[73]

1.3.2 Subchondral Bone Sclerosis and Osteophyte Formation

The subchondral bone is a vascularized tissue that has vital shock-absorbing properties and is in close association with the articular cartilage via the osteochondral junction, in which a cross-talk between the two tissues plays a role in the maintenance of the joint.[5] As articular cartilage degradation occurs due to progressive OA pathogenesis, loads

experienced by the joint are changed and are transferred more readily to the subchondral bone. The repetitive and increased load placed on the subchondral bone results in abnormal remodeling and high bone turnover, which is initiated at sites of local bone damage.[5,47] This irregular bone remodeling results in thickening, which along with damage to the bone, leads to pain for patients and is a key hallmark of OA. Furthermore, as the subchondral bone is a dynamic stress-bearing structure that functions to distribute mechanical loads across the joint surface, hardened subchondral bone may result in increased loads being experienced by the remaining overlying cartilage, leading to additional cartilage damage.[5]

Although the biomechanical relationship between subchondral bone and articular cartilage is well established, the direct molecular interaction between the two tissues are still under investigation.[74] However, recent studies are establishing that as tissue homeostasis is disrupted due to effectors of OA, the metabolically active subchondral bone plays a role in the progression of the disease as channels via the tidemark are permitting the release and transport of pro-inflammatory cytokines to the cartilage.[74,75] This exchange of mediators is permitted due to the alteration of the calcified cartilage and subchondral bone plate permeability, ultimately allowing communication between subchondral bone and cartilage.[5]

It has been determined that increased remodeling and thickening of the subchondral bone is a determining factor of OA propagation in humans; however, various animal models

show varying results in subchondral bone and plate changes. In one specific study performed on canines, increased porosity and thinning of the subchondral cortical bone plate was observed along with increased bone volume fraction and trabecular thickness of the subchondral trabecular bone.[5,76] Contrastingly, other animals, such as rabbits, displayed a thickening of the plate with OA progression, as well as decreased bone volume fraction of the subchondral bone.[5,77] A recent study utilizing Micro-Computed Tomography on Dunkin Hartley Guinea Pigs observed decreased bone volume fraction and increased trabecular thickness of the subchondral bone along with an increase of cortical thickness with progressive OA.[78] The varying outcomes of subchondral bone and plate alterations in different animal models have resulted in convoluted inferences on its effect on progression of OA. Therefore, further investigations on the underlying mechanisms of subchondral bone remodeling is necessary *in vivo*. Moreover, it has been determined in humans that the subchondral bone plays a role in the pathogenesis of OA with convincing evidence that alteration of the bone results in further cartilage destruction. However, despite the changes observed in subchondral bone in association with OA, there is a deficiency in the clear understanding of the underlying biochemical and biomechanical mechanisms driving pathogenesis.

In addition to sclerosis, the abnormal remodeling of the subchondral bone results in osteophyte formation at the margins of the joint. Development of osteophytes are initiated as a repair mechanism by the joint in order to aid in stabilization.[44] The mechanism regulating osteophyte formation is currently unknown, but is hypothesized to

be due to irregular production of growth factors, such as bone morphogenetic protein two (BMP-2).[44] It has also been observed that osteophytes are the result of chondrogenic differentiation and subsequent endochondral ossification of recruited mesenchymal stem cells in the periosteum.[44,64] Overall, osteophyte formation leads to pain and decreased joint motility to patients.

1.3.3 Implications of OA Pathogenesis

It has been established that the inflammation of the synovium and alterations of the subchondral bone plays a role in the degradation of the articular cartilage. However, due to the lack of intrinsic repair of the articular cartilage, once the collagen and proteoglycan ECM is damaged, it cannot be naturally reversed. The pro-inflammatory interactions between tissues of the joint result in a vicious cycle of destruction and it is therefore it is crucial to investigate therapeutic interventions that can both reduce symptoms of OA and aid in mitigation of further damage to the joint.

1.4 Animal Models of Osteoarthritis

1.4.1 Introduction and Purpose for Utilization of Animal Models

In order to replicate the progression of degenerative damage, as observed in OA pathology, animal models aid in exhibiting symptoms of disease development in order to identify outcomes of novel treatment options.[79,80] Animal models of OA are regularly utilized in investigating the common alterations of the joint, such as cartilage

degeneration, in a controlled manner, in which the models are allocated as induced or spontaneous.[80,81,82]

Surgically induced models are commonly used in which alterations of the joint, including meniscal tears, ligament transections, and osteotomy, work to destabilize the joint and induce and replicate the onset of post-traumatic OA.[79,80] Biochemical alterations, such as intra-articular injection of noxious agents, such as iodoacetic acid which functions to kill chondrocytes, are useful for studying matrix degeneration; however, is limited as a model as it is not fully representative of either spontaneous or post-traumatic OA progression.[79–81] Spontaneous or naturally occurring OA models are observed in particular species, in which the occurrence of slowly progressing OA simulates the natural progression of human OA.[82] Transgenic models have also been developed via gene manipulation, especially in mice, to also mimic a slowly progressive model to more properly represent the human OA condition.[80,81,82]

Moreover, animal models deliver clinically significant methods of studying the pathology as well as the response of treatment options for OA. The specific types of methods and the considerations in selecting the appropriate animal model will be furthered detailed in the sections below.

1.4.2 Common OA Animal Models

OA models have been developed with utilization of both small and large animals. Smaller animals include rats, mice, rabbits, and guinea pigs, while larger animals comprise of horses, dogs, and goats, in which the choice of animal model depends on a variety of considerations. The common classes of *in vivo* OA models include naturally occurring or spontaneous models, comprising of genetically modified animals as well, and surgical and biochemical induction to provoke trauma to the joint.[79] Animals are chosen to correspond with the specific OA model selected depending on the investigation; however, the "best" animal model for the study of OA has not been determined, and each contains its own advantages and disadvantages.

Rabbits, sheep, dogs, mice, horses, and guinea pigs display naturally occurring OA, and give an optimal representation of progressive OA observed in humans. Additionally, the smaller animals of spontaneous OA become skeletally mature more rapidly compared to larger animals and display pathogenesis comparable to humans, ultimately promoting their use for investigating therapeutic strategies.[80–82] Mouse models employed have the particular advantage of having the ability to be genetically modified to have susceptibility for OA. Transgenic mice have been used extensively to study the molecular foundation of OA, as knockout mice lacking a specific pro-inflammatory marker could lead to understanding the development of OA from a biochemical perspective.[82]

Animal models used with surgical intervention are commonly used, as they ensure a more rapid study period while also providing highly reproducible results. However, this

invasive provocation may be too rapid to investigate early onset OA development and has shown to have no correlation to natural degenerative changes instigated by OA.[81,82] Therefore, utilization of this model is best suited for the study of post-traumatic OA alterations. The sheep or goat has been shown to be the ideal animal models for ACL transection, while the dog is most commonly used for a meniscectomies, due to their anatomical and mechanical similarities to humans.[82] Additionally, mice are frequently used as biochemical induced animal models. This method involves the injection of inflammatory or toxic composites, such as collagenase, directly into the knee joint and is commonly used to examine the efficacy of drug therapies due to these constituents.[79,82]

Overall, there are a variety of animal models that can be employed for the study of OA; however, there are important factors that must be taken into consideration when choosing the appropriate animal model, such as size, cost, and OA induction method, which will be furthered detailed below.

1.4.3 Considerations in Determining Applicable Animal Models for OA

Currently, each animal utilized for the study of knee OA has its own distinctive advantages and disadvantages, depending on the type of study and outcome measurements. It is therefore critical to identify the question under experimentation, in order to select a suitable animal model for investigation. Several key experimental elements to consider when selecting the appropriate animal includes: study length, ease of handling, cost, gender, induction method, anatomy, and biomechanics of the

animal.[79,80,82,83,84] Each consideration contains its own stipulations, for example, the length of time needed to fulfill the study depends on the skeletal maturation of each animal, in which smaller animals may be more desirable as well as their low cost; however, large animals are most advantageous in terms of biomechanical loading similarities to humans.[83] Table 1 indicates a general summary of the common small and large animals corresponding to their advantages and disadvantages as a model for OA experimentation.

Table 1: Common animal models for investigation of OA.

Animal	Advantages	Disadvantages	OA Model Type
Mouse	Low Cost Ease of handling/housing due to small size Early skeletal maturity (~10 weeks) [55]	Thin cartilage with non-distinctive zones of cartilage Joint load-bearing biomechanics dissimilar to human	Genetic manipulations Meniscal destabilization ACL transection Biochemical induction (Collagenase) [55] Spontaneous OA
Rat	Low Cost Ease of handling Early skeletal maturity (~3 months) [55]	Small knee joint Post-operative control challenging [59]	Meniscal destabilization ACL transection Spontaneous OA Biochemical induction (Iodoacetic Acid, Papain, Collagenase) [55]

Guinea Pig	Low Cost Ease of handling Early development of spontaneous OA (~3 months) Early skeletal maturity (~6 months) [55] Similar joint loading, anatomy, and histopathology to humans [59]	Inactive lifestyle [59]	Menisectomy ACL transection Osteotomy Patellectomy Spontaneous OA Biochemical induction (Iodoacetic Acid, Papain, Collagenase) [55]
Rabbit	Ease of handling	Does not develop spontaneous OA Lateral compartment of knee is loaded, unlike human knee Histological dissimilar to human	ACL transection Menisectomy Biochemical induction (Iodoacetic acid, Papain, Collagenase)
Dog	Feasible for arthroscopy and MRI Validated outcome measurements [59] Similar to human knee joint	Late development of skeletal maturity (~18 months) [55] Certain breeds are chondrodystrophic High cost Public inquiry	Groove model [60] ACL transection Menisectomy Biochemical induction (Iodoacetic acid, Papain, Quinolones) Spontaneous OA
Sheep	Large knee joint Feasible for arthroscopy and MRI	High cost Does not develop spontaneous OA Late skeletal maturity (~2 years) [55]	Partial and total menisectomy ACL transection
Horse	Large knee joint Feasible for arthroscopy and MRI	High cost Late skeletal maturity (~2 years) [55]	Carpal fracture Osteochondral fragment exercise Spontaneous OA

1.4.4 Dunkin Hartley Guinea Pig

Upon review of common animal models for OA investigation, the guinea pig presents an ideal model to evaluate spontaneous OA due to its unique set of advantages. The specific strain of guinea pig, the Dunkin Hartley Guinea Pig (DHGP), has been most commonly utilized and has shown to develop OA as early as three months of age, and therefore provides a feasible model for longitudinal studies.[57,85,86] The DHGP has similar anatomy to humans, in which the diarthrodial joint comprises the same physiological structures, such as the meniscus, ligaments, synovium, cartilage, and bones.[69] Additionally, DHGPs primarily load the medial compartment of the knee joint, while increased body weight and mechanical load increases the occurrence of the disease, similar to humans.[57,69,80,85,87] The biochemical and histological changes in DHGPs are similar to human OA as well, in which an established scoring system has been employed by the Osteoarthritis Research Society (OARSI).[69,88] Furthermore, DHGPs are subject to a variety of well-recognized OA risk factors that are shared with humans such as cartilage degeneration, changes in subchondral bone. Moreover, their low cost, ease of handling, development of spontaneous OA at an early age, while also providing various biomechanical similarities to humans, yields the DHGP an ideal animal model to evaluate treatment efficacy for mitigation of OA.

1.5 Use of Stem Cells for Therapeutic Treatment

1.5.1 Introduction to Stem Cell-Based Therapy

Although OA is considered a prevalent degenerative joint disease and a major cause of disability to patients globally, treatment options only work to alleviate the disorder.

Current medications do not restore the native structure or function of the joint tissues, such as damaged articular cartilage, and as a result, cell-based regenerative strategies have been developed as novel treatment options for OA. As a whole, cell-based treatment includes the method of introducing cells into tissues with the prospect to treat and mitigate degenerative disease.[58] This innovative therapeutic approach has the potential to alter treatments from conservative management options to establishing a cure. Ongoing investigation utilizing regenerative cell-based therapy includes the involvement of tissue engineering and biomaterials, in which this conjunction has gained attention in modern healthcare and is projected to grow exponentially as an established treatment constituent.[58] Overall, research in the field of stem cell-based therapy has been increasingly studied and has gained further attention due to promising results in various disorders such as neurodegenerative disease, osteoarthritis, retinal degenerative disease, and intervertebral disk disease, to highlight a few.[89–92] Ultimately, the goal for stem cell-based therapy is to utilize autologous or allogenic cells in order to replace diseased or absent cells and support regeneration of damaged tissue. Mesenchymal stem cells (MSCs) have shown to be an ideal source for cell-based therapy in various degenerative and inflammatory diseases due to their immunosuppressive and tissue repair capabilities.[92,93] MSCs and their accompanying properties will be further highlighted below.

1.5.2 Introduction to Mesenchymal Stem Cells

Mesenchymal stem cells (MSCs) are known as adult stem cells with the ability to self-renew and differentiate into a variety of specialized cell types in appropriate culture conditions. Mesodermal lineage-specific differentiation of MSCs can lead to the production of osteocytes, adipocytes, and chondrocytes, in which their potential to produce bone, adipose tissue, and cartilage, makes them an ideal candidate for regenerative stem cell-based therapy.[59,92,94]

Several investigations have concentrated on isolating MSCs from a variety of origins, in which the bone marrow is considered a primary source of adult stem cells, containing both hematopoietic stem cells (HSCs) and MSCs.[58] However, the existence of MSCs in other tissues and organs have been identified, such as skeletal muscle, adipose tissue, liver, lung, and other connective tissues.[58,95] Along with their ease of isolation and abundance, MSCs help to repair tissue via the secretion of growth and paracrine factors and immunomodulatory components such as cytokines.[58,92,96] It has been shown that after *in vivo* administration, MSCs have the ability to inhibit the release of pro-inflammatory cytokines and promote the repair of damaged tissue.[58] Furthermore, MSCs do not express major histocompatibility complex (MHC) class II on their cell surface, in which this absence allows allogenic transplantation of MSCs directly or via a tissue-specific scaffold to regenerate damaged tissues.[92,93]

Although the distinctive qualities of MSCs may be promising as an ideal source for stem cell-based therapy, such as their immunomodulatory properties and potential for multiple lineages, there are associated challenges with their use. Poor delivery of MSCs

to target tissues, migration of MSCs systemically, and spontaneous differentiation of transplanted MSCs, have given varied results in stem cell-based therapy investigations and it is therefore crucial to continue studying the utilization of MSCs as a regenerative source.[92,93]

1.5.3 Human Adipose Derived Stem Cells

To highlight a MSC utilized in stem cell-based investigations, human adipose-derived stem cells (hADSCs) have gained heightened attention due to many of their unique properties. Along with the capacity to differentiate into multiple lineages, they are easily expandable and highly available without ethical concerns, overall making them a compelling stem cell source for regenerative opportunities.[95,97]

Originating from human fat deposits, hADSCs can be isolated from adipose tissue obtained from minimally invasive techniques such as liposuction, capable of generating large amounts of aspirates.[97,98] Although the MSCs that are derived from adipose tissue are more heterogeneous, containing endothelial, fibroblast, and immune cell populations, adipose tissue comprises greater densities of MSCs than bone marrow, while also showing enhanced proliferation.[95,97–100] Along with their high yield, numerous studies have shown that hADSCs have the potential to differentiate into multiple cell types of mesodermal origin, such as adipocytes, osteoblasts, and chondrocytes, in which their transcriptional activation into these precise lineages are well known.[98,101,102] Additionally, hADSCs can be cultured and expanded without losing their multipotent characteristics

with long-term stability.[98] Although their potential has been shown *in vitro*, it is crucial to examine their properties *in vivo* in order to determine their efficacy for therapeutic applications to repair or regenerate tissues. In recent studies, hADSC injections *in vivo* have shown to have promising therapeutic effects for osteoarthritis by improving pain, function, and cartilage volume, however further investigation is necessary in order to obtain consistent results across ideal animal models, as well as to evaluate the therapeutic efficacy in the mitigation of osteoarthritis.[103,104]

1.5.4 Human Amniotic Derived Stem Cells

Deviating from adult mesenchymal stem cells, an alternative stem cell source that has been studied for regenerative applications are perinatal stem cells, which can be isolated from amnion and amniotic fluid, umbilical cord fluid, and placental tissue.[105] Notably, these cells are harvested from tissues that are normally considered medical waste and are discarded after child birth, ultimately providing no risk to the mother or the newborn and avoiding ethical concerns.[106] It is hypothesized that placental tissues contain cells that have preserved plasticity of early pre-gastrulation embryonic cells as they are derived from the initial phases of embryonic development, therefore, perinatal stem cells represent an intermediate cell type between pluripotent embryonic stem cells and multipotent adult mesenchymal stem cells, with the ability to differentiate into mesodermal lineages.[106,107] Additionally, it is suggested that perinatal stem cells may have immunomodulatory features, as the placenta is essential for supporting the biological communication between mother and fetus.[107] Recent *in vitro* studies targeted

the underlying immunomodulatory effects of human amniotic stem cells (hAMSCs) after allogenic and xenogenic transplantation, and found no provoked immune response.[100,108–110] Ultimately, immune-privileged properties would support the potential for allogenic transplantation in clinical applications. Additionally, in evaluation against hADSCs, hAMSCs demonstrated a higher differentiation ability toward cartilage and bone *in vitro*, while also containing more chondro-protective effects in an OA co-culture model, in order to mitigate cartilage damage.[111,112] Further evaluation of hAMSCs in an *in vivo* model is essential in order to determine the therapeutic efficacy towards the mitigation of osteoarthritis.

1.6 General Overview of Performed Studies

Overall, tissue engineering and regenerative medicine strategies integrate a combination of approaches that include either the isolated use of cells at the damaged tissue site or incorporation of a three-dimensional cell-seeded scaffold in order to provide functional and mechanical features of the native tissue. The studies performed herein involved direct injection of adult human adipose-derived stem cells (hADSCs) and perinatal human amniotic-derived stem cells (hAMSCs) into the knees of an ideal *in vivo* model. Various outcome measures were performed and analyzed in order to evaluate the effects of both stem cell treatments and compare the therapeutic efficacy to mitigate osteoarthritis.

CHAPTER TWO:

AIM 1

2.1 Introduction and Purpose

Osteoarthritis (OA) is the most common arthritic joint disease in the United States, in which 34%-40% of the United States population over the age of 65 is affected.[6,8] Knee OA, specifically, is characterized as a multifaceted disease in which the foremost pathologic changes include degeneration of the articular cartilage, subchondral bone remodeling, formation of osteophytes, and inflammation of the synovium.[6,8,63,113] The increased biomechanical stresses imposed on the joints as well as an upregulation and molecular cross-talk of pro-inflammatory mediators, such as TNF-α and IL-1β, causes a vicious cycle of destruction to the entire joint, ultimately leading to pain for the patient.[6,63,72] Despite the debilitating symptoms of the disease, there is currently no cure for OA, and patients are only offered palliative treatment options, such as medication, and in more severe cases, surgical alternatives such as total joint replacement. Additionally, the articular cartilage lining the bones of the joints, have limited intrinsic repair and self-healing capabilities due to its hypoxic nature.[26,50] Therefore, there is a crucial need to develop novel stem cell-based regenerative strategies to treat OA and assist in mitigation of disease pathogenesis. Various stem cell therapies have been utilized in different animal models of OA, and are usually intra-articularly injected into the knee joint. Investigations have found that stem cell therapies yielded superior outcomes in comparison to autologous transplantation of chondrocytes; however, to date, amniotic stem cells have yet to be tested *in vivo* as an OA therapeutic source.[114,115]

Previous *in vitro* explant co-culture studies have shown that human amniotic stem cells (hAMSCs) demonstrated a superior ability to effectively inhibit OA progression by demonstrating more chondro-protective characteristics compared to human adipose-derived mesenchymal stem cells (hADSCs).[111] To further these previous findings, the objective of this aim was to evaluate and compare the use of hAMSCs and hADSCs *in vivo*, in order to evaluate their efficacy in alleviation of OA progression. The studies performed herein include intra-articular injection of hADSCs and hAMSCs into the rear knee stifles of Dunkin Hartley Guinea Pigs (DHGPs), an animal model that develops spontaneous knee OA. Subsequent outcome measurements included the use of imaging modalities and biochemical, molecular, and histological assessments, in order to evaluate the effects of hADSCs and hAMSCs on the osteoarthritic joint.

The specific outcome measurements included the use of Micro-Computed Tomography (Micro-CT) to non-destructively obtain high resolution 3-dimensional (3-D) reconstructed images of the DHGP knees to assess morphologic changes of the subchondral bone. Biochemical analysis included Dimethymethylene Blue Assay (DMMB) in order to rapidly detect and evaluate glycosaminoglycan (GAG) concentration from the articular cartilage of the DHGP knees. Immunohistochemistry was utilized to detect macrophages in the synovium in order to evaluate the degree of synovial inflammation, as macrophages are the foremost components in the initiation and maintenance of the inflammatory process.[116] Histological assessment of the DHGP knee

included the use of Hematoxylin and Eosin, Toluidine Blue, and Safranin-O stains in order to semi-quantitatively grade the degree of alterations in the synovium and articular cartilage. Grading was accomplished via 2 blinded observers and guidance from the Osteoarthritis Research Society International (OARSI) scoring recommendations.[69] Additionally, a competitive Enzyme-Linked Immunosorbent Assay (ELISA), targeting Guinea Pig Immunoglobulin G (IgG), was performed on the DHGP blood in order to evaluate for potential immunogenic reaction from the injected human stem cells.

Evaluating the outcome measurements performed herein allows for a greater understanding and insight into the therapeutic mechanisms and potential clinical efficacy of these stem cells as a novel stem cell-based regenerative treatment for OA.

2.2 Materials and Methods

Human adipose-derived stem cells (hADSCs) were obtained from Invitrogen (R778810). Human amniotic-derived stem cells (hAMSCs) were harvested and isolated from human placentas following child birth from consenting patients (IRB Protocol: PRO31185—Greenville Heath System). All cell counts were performed with the TC20 Bio-Rad Automated Cell Counter with use of Trypan Blue purchased from Lonza (17-92E). Cell culture media for hAMSCs included Dulbecco's Modified Eagle's Medium (DMEM) purchased from Corning (10-D14-CM) with Fetal Bovine Serum (S1150H) purchased from Atlanta Biologicals and Antibiotic Antimycotic (300040CI) purchased from Corning. Cell culture media for hADSCs included MesenPro Basal Medium with growth

supplement (12747-010) purchased from Gibco. Trypsin was purchased from Corning (25053CI). Three month old Dunkin Hartley Guinea Pig (n=24) cohorts were obtained from Charles River Laboratories conferring to Clemson University's Institutional Animal Care and Use Committee (IACUC) approval (protocol number 2016-040). Sodium Hyaluronate was purchased from LifeCore Biomedical (HA700K-1) and sterile filtered with an Acrodisc 25mm Syringe Filter (4612) containing a 0.2µm filter membrane purchased from Pacc. Dimethyl-Methylene Blue (DMMB) Zinc powder (3410881), Chondroitin Sulfate (C4384), and Papain (P4762) was purchased from Sigma-Aldrich. Substances for DMMB Assay reagents included Dibasic Sodium Phosphate purchased from RMO Chemicals (SXO7201), L-Cysteine purchased from AMRESCO (J994), Ethylenediaminetetra Acetic Acid (EDTA) purchased from Fisher Scientific (BP118), Glycine purchased from Alfa Aesar (A13816), and Sodium Chloride purchased from VWR (7647-14-5). Formalin fixation of tissues was performed with 10% Phosphate Buffered Formalin purchased from Newcomer Supply (1090N). Bone decalcification was performed with Formic Acid purchased from Stat Lab (1414-1), in which Ammonium Hydroxide purchased from VWR (1336-21-6) and Ammonium Oxalate purchased from Poly Scientific (S2337-160Z) was used for confirmation of decalcification. Tissue Trek Automated Tissue Processor was used for all tissue processing. Leica RM 2155 Microtome was used for all tissue sectioning. Histological stains included Safranin-O (S8884) and Fast Green (F7258), both purchased from Sigma-Aldrich, Weigert's Hematoxylin Solution A and B (S216BA; S216BB) purchased from Poly Scientific, Glacial Acetic Acid (BP1185) purchased from Fisher Scientific, Toluidine Blue (E847)

purchased from VWR, and both Hematoxylin (7211) and Eosin-Y (71311) purchased from Thermo Fisher Scientific. All histological and cytological images were captured on a Zeiss Axiovert.A1 microscope in conjunction with Axiovision Software. Bruker 1176 Micro-Computed Tomography (Micro-CT) x-ray imaging system was used for all Micro-CT scans and image reconstructions. Enzyme-Linked Immunosorbent Assay (ELISA) was performed with the use of Guinea Pig IgG ELISA Kit purchased from LifeSpan Bio (LS-4435) according to the manufacturer's instructions. Immunohistochemistry (IHC) evaluation utilized a monoclonal Mouse Anti-Guinea Pig Macrophage primary antibody purchased from Bio-Rad (MCA518S). Secondary Anti-Mouse IgG antibody was purchased with Vecastain Elite ABC Kit from Vector Laboratories (PK-6100). Diaminobenzidine (DAB) Peroxidase Substrate Kit (SK-4100) and Avidin Biotin Blocking Kit (SP-2001) was also purchased from Vector Laboratories. Background Buster Blocking Agent was purchased from Innovex Biosciences (NB306). Citric Acid Monohydrate (A104-500), Sodium Azide (S2271-25), and Bovine Serum Albumin (BP9703-100) were purchased from Fisher Scientific. TritonX-100 was purchased form Alfa Aesar (A16046). 3% Hydrogen Peroxide was purchased from Publix. Dulbecco's Phosphate Buffered Saline (PBS) was purchased form Corning (55-031-PC).

2.2.1 Stem Cell Preparation and Injection

Twenty-four Dunkin Hartley Guinea Pigs (DHGPs) were allowed 14 days upon arrival to acclimatize to the Godley Snell Research Facility at Clemson University. Approximately $5x10^5$ hAMSCs or hADSCs (Passage 2) were re-suspended in 100µl of sterile medical

grade 0.5% sodium hyaluronic acid (HA). Direct intra-articular injection of hAMSCs+HA (n=8) and hADSCs+HA (n=8) treatments, as well as an HA-only vehicle control (n=8), were performed on the rear knee stifles of the DGHPs via a 28-gauge syringe needle and under ultrasound guidance. The needle was inserted posterior to the medial compartment of the patellar ligament, through the junction formed by the epicondyle of the femur and the tibial plateau. Additionally, all treatments were paired with a bilateral 100µL phosphate buffered saline (PBS) injection as a negative/degenerative control. Figure 6 below displays a schematic of the injection procedures and the corresponding groups. All DHGPs remained under anesthesia via isoflurane during all injections. Injections began at three months of age and were performed every two months until euthanasia was performed at nine months of age. All injection methods were approved via the Animal Care and Use Protocol and the Institutional Animal Care and Use Committee (IACUC) at Clemson University.

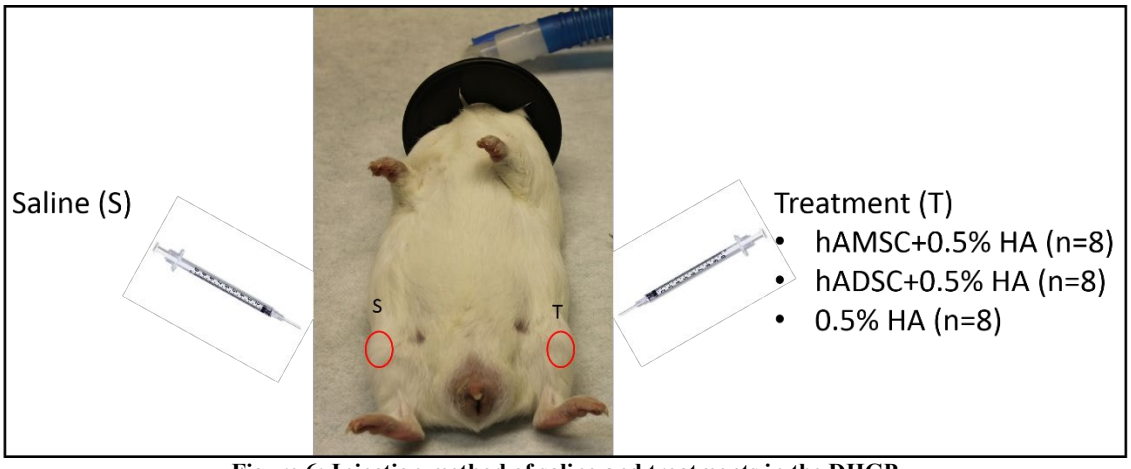

Figure 6: Injection method of saline and treatments in the DHGP.

2.2.2 Dunkin Hartley Guinea Pig Harvest

Ensuing euthanasia, knee joints were exposed and dissected as shown in Figure 7. Half of the paired knee joints (n=24) were immediately snap frozen in liquid nitrogen and stored at -80°C until ready for biochemical analysis, while the other half (n=24) were placed in 10% formalin for sample fixation. Figure 8 displays the experimental design schematic for the subsequent outcome measures performed.

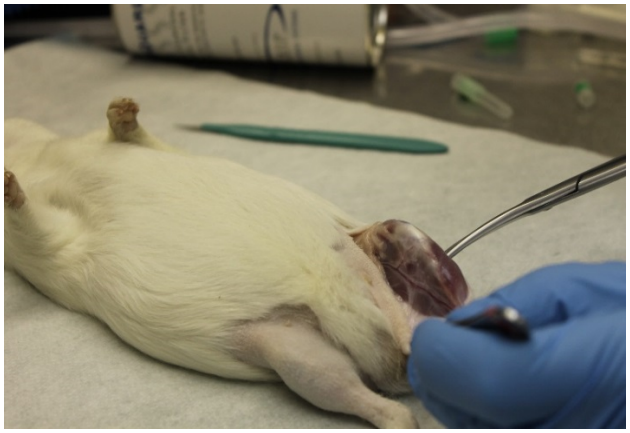

Figure 7: Harvest of DHGP knee.

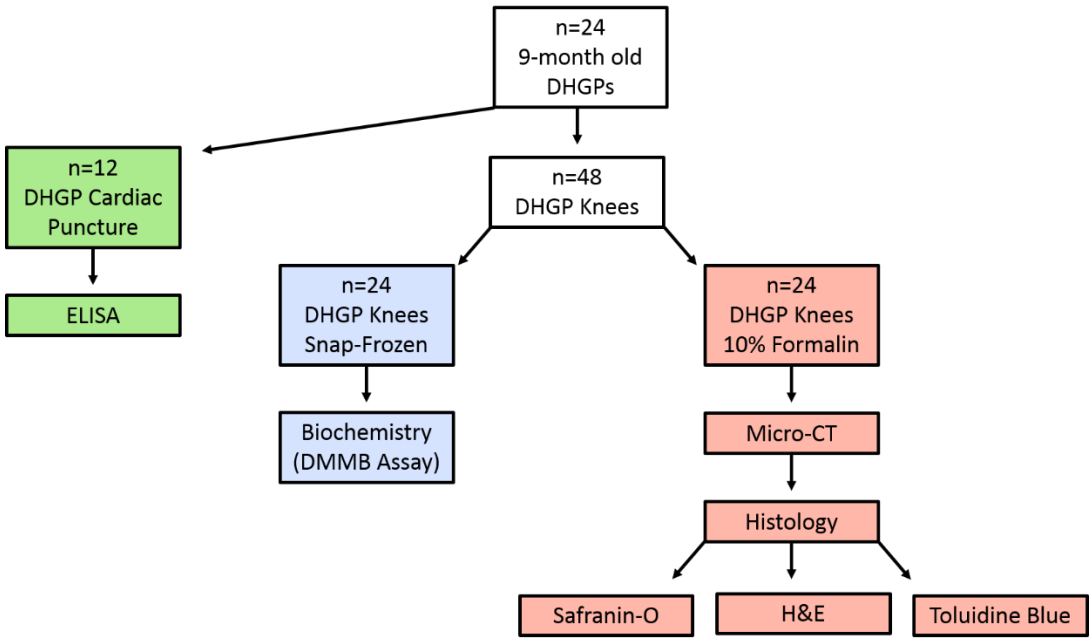

Figure 8: Experimental design schematic of outcome measures performed.

2.2.3 Dimethyl-Methylene Blue (DMMB) Assay

All snap-frozen knee samples (n=24) were taken out of -80°C and thawed at room temperature. Exposure of the cartilage surfaces of the femoral condyles and tibia plateaus was accomplished via dissection of the tissue and can be visualized in Figure 9 below. Once this was accomplished, the surfaces of the medial and lateral compartments of the femur and tibia were scrapped with a Meyer-Hoffer 1.5mm curette to obtain flakes of cartilage. Five to seven scrapes were performed in order to maintain consistent sample amount. Cartilage samples were placed in pre-weighed 1.5mL micro centrifuge tubes containing perforated caps and were then placed in -80°C for 24 hours. After freezing, samples were dehydrated immediately via lyophilization for 48 hours. Following, perforated tops of the tubes were substituted with original caps and were weighed in order to obtain dry weights of the cartilage samples. The samples were then placed in 250µL of papain (pH 6.5) at 65°C for 24 hours to allow for tissue digestion in which the samples were periodically vortexed to accelerate this process. Once the samples were completed digested they were diluted (50x) in PBE buffer in preparation for the DMMB Assay. Specified volumes of Chondrotin-6-Sulfate (CS) with PBE buffer was transferred to the wells of a 96-well plate in triplicate to generate a standard curve of known concentrations of glycosaminoglycan. Additionally, 50µL of diluted samples were pipetted into separate wells in triplicate. Once all wells were prepared with samples, 200µL of DMMB Reagent (pH 3.0) was transferred to each well. The plate was immediately read via a plate reader at an absorbance of 525nm. The linear standard curve (R^2 value>0.98) was generated by plotting the mean absorbance for each standard versus

corresponding CS concentrations. Triplicate readings of samples were then averaged, multiplied by the dilution factor, and were normalized to their respective sample dry weight in order to obtain GAG concentrations.

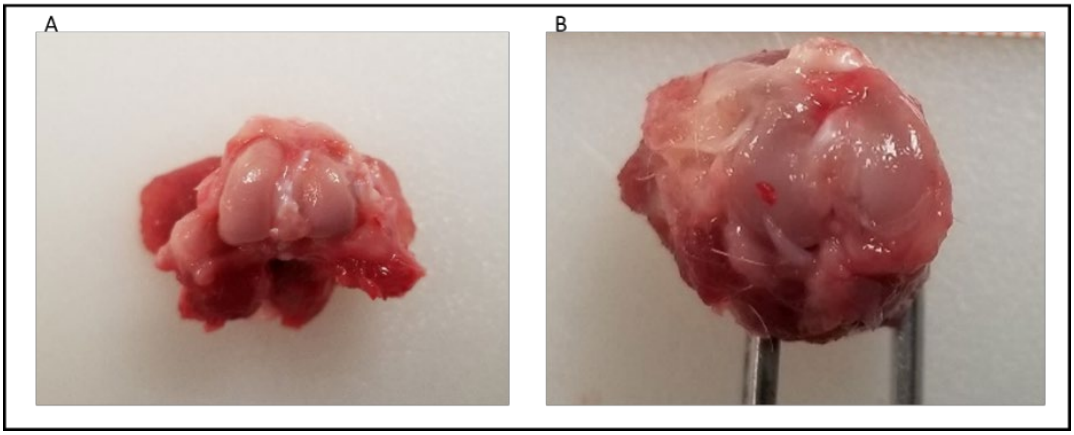

Figure 9: Dissected and exposed femoral condyle (A) and tibial plateau (B) surfaces of DHGP knee in preparation for cartilage scrapping for DMMB Assay.

2.2.4 Micro-Computed Tomography (Micro-CT)

All formalin fixed knee samples (n=24) were scanned via the Bruker 1176 Micro-CT imaging system using SkyScan Software. Once the x-ray was turned on and initialized, preliminary scout scans were performed in order to determine optimal filter and acquisition settings for the knee samples. Final filter settings included aluminum and copper with an x-ray setting of 80kV and 309µA. Final scan settings included: pixel size of 18µm, rotation step of 0.5, and frame average of 3. Once all scans were completed, NRecon Software was used in order to reconstruct the images in batch mode. Again, settings and parameters were optimized for the knee samples, in which post alignment was set at -1.5, beam hardening correction at 30%, smoothing level of 2, and ring artifact correction at 10. CS rotation was used in order to ensure proper alignment of the scanned

image. Once all samples were reconstructed, CTan Software was used to obtain 3D morphometric parameters from selected regions of interest (ROI). A 2.0 x 2.0 x 1.0mm rectangular box in the center of the plateaus was selected as the ROI for the subchondral trabecular bone of the tibia medial and lateral compartments.

Figure 10: Dissected DHGP knee joint placement in Micro-CT bedding in preparation for imaging.

2.2.5 Histology

Upon sample fixation, total decalcification of knee joints (n=24) was performed for 2 weeks in formic acid, with solution changes occurring every 3 days. Following complete decalcification, knee joints were processed for 36 hours and immediately embedded in paraffin. All knee samples were sectioned at 8µm and subsequently baked overnight in an oven at 55°C to ensure adherence to the histology slide. Following, all slides were deparaffinized and hydrated through a series of xylene, ethanol, and distilled water washes.

2.2.5.1 Safranin-O Staining

Once deparaffinized, slides underwent a 10-minute incubation in Weigert's Hematoxylin solution followed by a 10 minute wash step in tap water. Slides were then incubated in Fast Green solution for 5 minutes followed by an acetic acid rinse for 15 seconds. After, slides were placed in Safranin-O solution for 5 minutes and subsequently dehydrated and cleared in a series of ethanol and xylene rinses. Slides were cover slipped with mounting media and left to dry for 2 hours before microscopic imaging.

2.2.5.2 Toluidine Blue Staining

Once deparaffinized, slides underwent a 3-minute incubation in Toluidine Blue solution containing sodium chloride followed by a distilled water rinse. After, the slides were dehydrated and cleared in a series of ethanol and xylene rinses. Slides were cover slipped with mounting media and left to dry for 2 hours before microscopic imaging.

2.2.5.3 Hematoxylin and Eosin Staining

Once deparaffinized, slides underwent an 8-minute incubation in Hematoxylin solution followed by a tap water rinse. Slides were then dipped in Clarifier solution 5 times and was rinsed with tap water after. The slides were then placed in Bluing Reagent for 1 minute, again followed by a tap water rinse. Following, slides were placed in Eosin solution for 45 seconds and were then dehydrated and

cleared in a series of ethanol and xylene rinses. Slides were cover slipped with mounting media and left to dry for 2 hours before microscopic imaging.

2.2.5.4 Histological Grading

Semi-quantitative histological assessment of OA in DHGP knee joints stained with Toluidine Blue and Safranin-O was performed from a system recommended by the Osteoarthritis Research Society International (OARSI).[69] Images were assessed via a modified Mankin Grading Scale provided by OARSI shown in **Tables 2-4**. Two blinded observers scored the images and evaluations were then averaged to obtain final grading in which higher scores indicate increasing severity of OA. Hematoxylin and Eosin stained knee joints were evaluated for synovial hyperplasia via semi-quantitative cellularity analysis, in which representative synovium sections were counted for cell infiltration.

Table 2: Recommended semi-quantitative histologic DHGP knee joint scoring system for articular cartilage structure.[69]

Parameter	Grade	Description
Articular Cartilage Structure	0	Normal, smooth, uninterrupted surface
	1	Mild surface irregularities (undulations)
	2	Irregular surface, 1-3 superficial clefts (fissures)
	3	>3 fissures and/or loss of cartilage in the superficial zone
	4	1-3 fissures extending into the middle zone

	5	>3 fissures and/or loss of cartilage extending into the middle zone
	6	1-3 fissures extending into the deep zone
	7	>3 fissures extending into the deep zone and/or loss of cartilage to deep zone
	8	Fissures or loss of cartilage extending to the zone of calcified cartilage

Table 3: Recommended semi-quantitative histologic DHGP knee joint scoring system for proteoglycan content.[69]

Parameter	Grade	Description
Proteoglycan Content	0	Uniform throughout articular cartilage
	1	Decreased in superficial zone only and for <half the length of the condyle or plateau
	2	Decreased in superficial zone for half the length or greater of the condyle or plateau
	3	Decreased in superficial and middle zones <half the length of the condyle or plateau
	4	Decreased in superficial and middle zones half the length of the condyle or plateau
	5	Decreased in all 3 zones for <half the length of the condyle or plateau
	6	Decreased in all 3 zones for half the length of the condyle or plateau

Table 4: Semi-quantitative histologic DHGP knee joint scoring system for synovial membrane hyperplasia.[69]

Parameter	Grade	Description
Synovial Membrane Hyperplasia	0	Decrease in the number of lining cells
	1	Normal (1-2 layers of cells)
	2	Slight increase in number of layers (4-6)
	3	>6 layers of lining cells
	4	Increase in lining cells with inflammatory cells present

2.2.6 Enzyme-Linked Immunosorbent Assay (ELISA)

Cardiac puncture on 12 DHGPs was performed to obtain blood from the heart (approximately 8mL of blood obtained). Blood samples were placed in a serum separator tube that was immediately centrifuged at 3500rpm for 10 minutes to acquire serum. ELISA on serum samples was performed with a competitive Guinea Pig IgG ELISA kit and per manufacturer's instructions. A competitive ELISA indicates that the greater amount of antigen in the sample will produce a lower color development and Optical Density (OD) reading. Each well of the supplied microtiter plate was pre-coated with a target specific capture antibody and all reagents utilized (Wash Buffer, Horseradish Peroxidase (HRP)-conjugate, TMB substrate, and Stop Solution) were provided by the kit. Once all reagents were prepared, a standard curve was generated with stock solutions and sample diluents provided by the kit with known concentrations of target antigen. The standard curve dilution series was transferred to the wells of the microtiter plate in duplicate. Serum samples were then prepared and diluted (1:2,500), as per manufacturer's

recommendation for serum samples, in order to fall within the standard curve and transferred to the microtiter plate in duplicate. Once the standard curve and samples were plated, 50µL of HRP-conjugate was added to each well and the plate was incubated for 60 minutes at 37°C. The liquid was then removed and washed with 350µL of Wash Buffer 5 times with a multi-channel pipette. Following, 90µL of TMB Substrate was added to each well and the plate was incubated in the dark for 20 minutes at 37°C. After, 50µL of Stop Solution was added to each well in the same order and timing as the TMB Substrate solution. The OD of each well was determined via immediate use of a microplate reader at an absorbance of 450nm. The standard curve was generated by plotting the mean absorbance for each standard versus the corresponding antigen concentrations in which the data was linearized (R^2 value>0.98) by plotting the log of the standards and concentrations. Duplicate readings of samples were averaged and were multiplied by the dilution factor in order to obtain IgG concentrations.

2.2.7 Immunohistochemistry

Immunohistochemistry (IHC) on paraffin embedded Dunkin Hartley Guinea Pig (DHGP) spleen and knee sections was performed for detection of DHGP macrophages. Spleen samples (n=4) were processed for eight hours before embedment and were sectioned at 5µm, while knee samples (n=12) were processed for thirty-six hours before embedment and sectioned at 8µm. Upon sectioning, all samples were baked overnight in an oven at 55°C to ensure adherence to the histology slide. Both tissue types underwent the same IHC procedure in which upon deparaffinization and rehydration of slides, antigen

retrieval was performed via incubation of 10mM Citrate Buffer (Citric Acid Monohydrate) for 3 minutes in a pressure cooker. Permeabilization of samples was performed with a ten minute incubation in 0.1% TritonX-100 followed by subsequent non-specific, specific, and endogenous peroxidase blocking performed via incubation with Background Buster for thirty minutes, 0.3% Hydrogen Peroxide for five minutes, and Avidin-Biotin for fifteen minutes. Upon completion of blocking steps, incubation of a mouse monoclonal primary antibody towards Guinea Pig Macrophage, diluted 1:10 in 1% BSA and 0.01% Azide in PBS, was performed at room temperature for one hour. Subsequently, a thirty-minute incubation of a biotinylated secondary antibody and ABC complex, formulated according to manufacturer's instructions, was performed. Negative samples did not receive a primary antibody. Visualization of positive staining was performed via DAB Peroxidase Substrate incubation for two and a half minutes. After, nuclear counterstaining of samples was performed with diluted Hematoxylin in distilled water, followed by dehydration through ethanol dilutions. Permanent mounting medium was used to place cover slips over the slides. Additionally, it should be noted that thorough rinses and washes in PBS was performed between each step. Figure 11 below depicts a schematic of IHC steps performed.

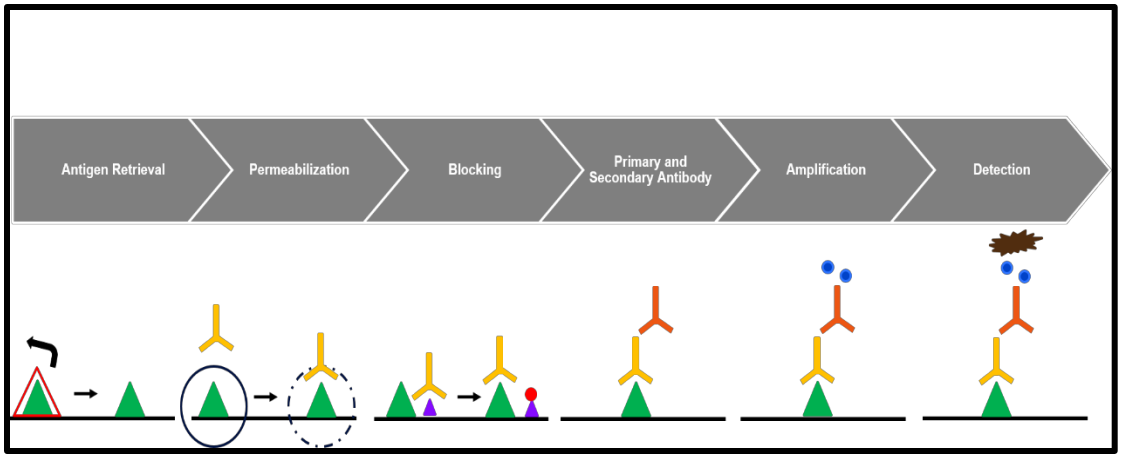

Figure 11: Schematic of IHC steps depicting antigen retrieval, permeabilization, blocking, primary and secondary antibody incubation, amplification, and detection.

2.2.8 Statistical Analysis

Statistical analysis was performed using GraphPad Prism7 software. Results are represented as mean ± standard error of the mean (SEM) and were statistically compared via paired t-test between treatments or analysis of variance (ANOVA) with a Tukey's post-hoc analysis. Significance was denoted as $p<0.05$ for all results.

2.3 Results

2.3.1 Glycosaminoglycan (GAG) Content Evaluation

Articular cartilage of 9-month old DHGP knee tibia plateaus and femoral condyles was evaluated for GAG content in order to assess for cartilage integrity. As seen in Figure 12, GAG content evaluated in the medial compartment of the femur revealed higher GAG concentration for hAMSC treatment compared to its respective saline control (35.8µg/mg versus 32.3µg/mg). Additionally, hADSC treatment demonstrated higher GAG concentration compared to its corresponding saline control (51.9µg/mg versus

34.7µg/mg). HA also revealed to have higher GAG concentration compared to its respective saline control (45.3µg/mg versus 33.5µg/mg). Comparing GAG concentration directly between hADSC and hAMSC treatments, hADSC results demonstrated higher GAG content (51.9µg/mg versus 35.8µg/mg), although results demonstrated no significant differences between all 9 month-old treatment groups. However, healthy 2 month-old DHGP knees assessed for GAG content displayed a statistically higher average GAG concentration (125.1µg/mg) compared to all 9 month-old groups, except for hADSC treatment.

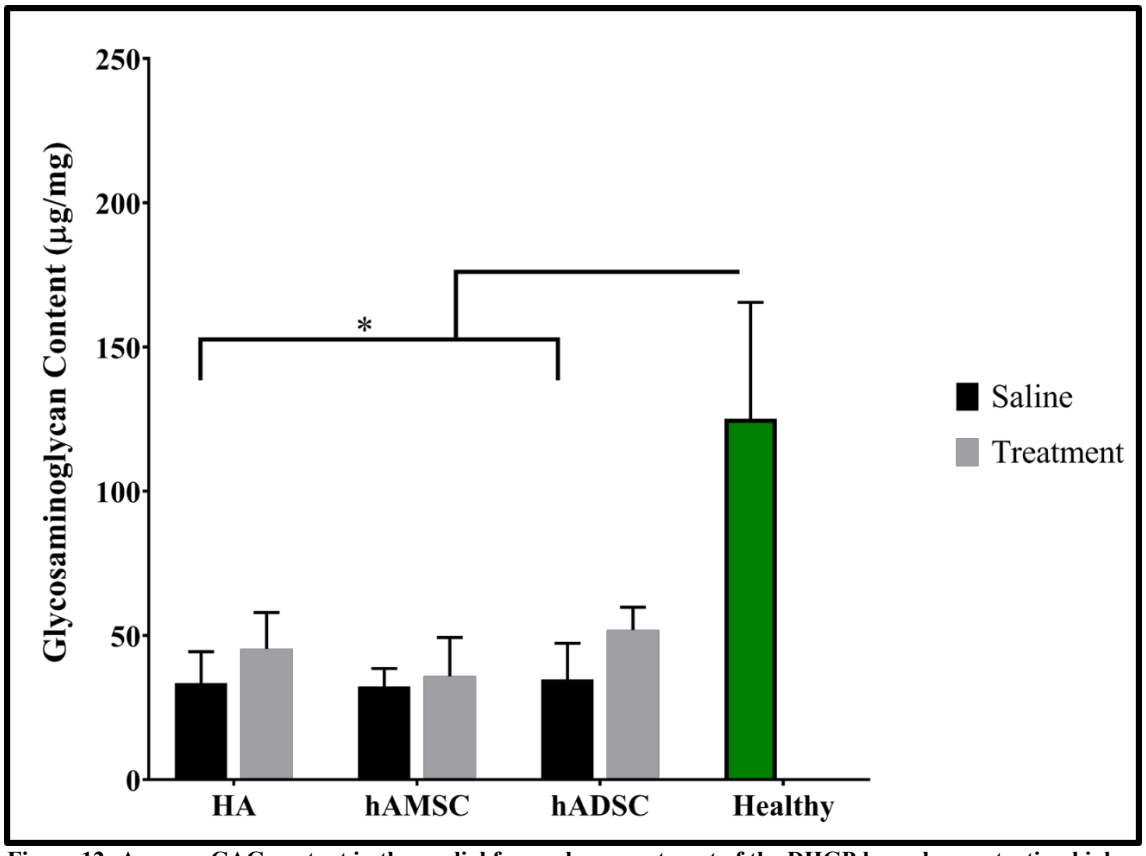

Figure 12: Average GAG content in the medial femoral compartment of the DHGP knee demonstrating higher concentrations of GAG for hADSC treatment compared to its corresponding saline control and hAMSC treatment, with overall statistically higher GAG content in the healthy 2 month-old knee compared to all 9 month-old groups.

Additionally, articular cartilage of the tibia in the medial compartment was assessed for GAG content. As seen in Figure 13, hAMSC treatment demonstrated less GAG concentration compared to its corresponding saline control (45.1µg/mg versus 58.8µg/mg). Conversely, hADSC treatment demonstrated higher overall GAG concentration compared to its respective saline control (73.3µg/mg versus 63.7µg/mg). Additionally, HA also revealed to have higher GAG concentration compared to its respective saline control (52.9µg/mg versus 37.5µg/mg). Comparing GAG concentration directly between hADSC and hAMSC treatments, hADSC results demonstrated higher GAG content (73.3µg/mg versus 45.1µg/mg); although results demonstrated no significant differences between all 9 month-old treatment groups. However, healthy 2 month-old DHGP knees assessed for GAG content displayed a statistically higher average GAG concentration (184.3µg/mg) compared to all 9 month-old groups as seen in Figure 13. Evaluation of GAG content of the lateral compartment of the knee can be found in Appendix Figures A.1-A.2.

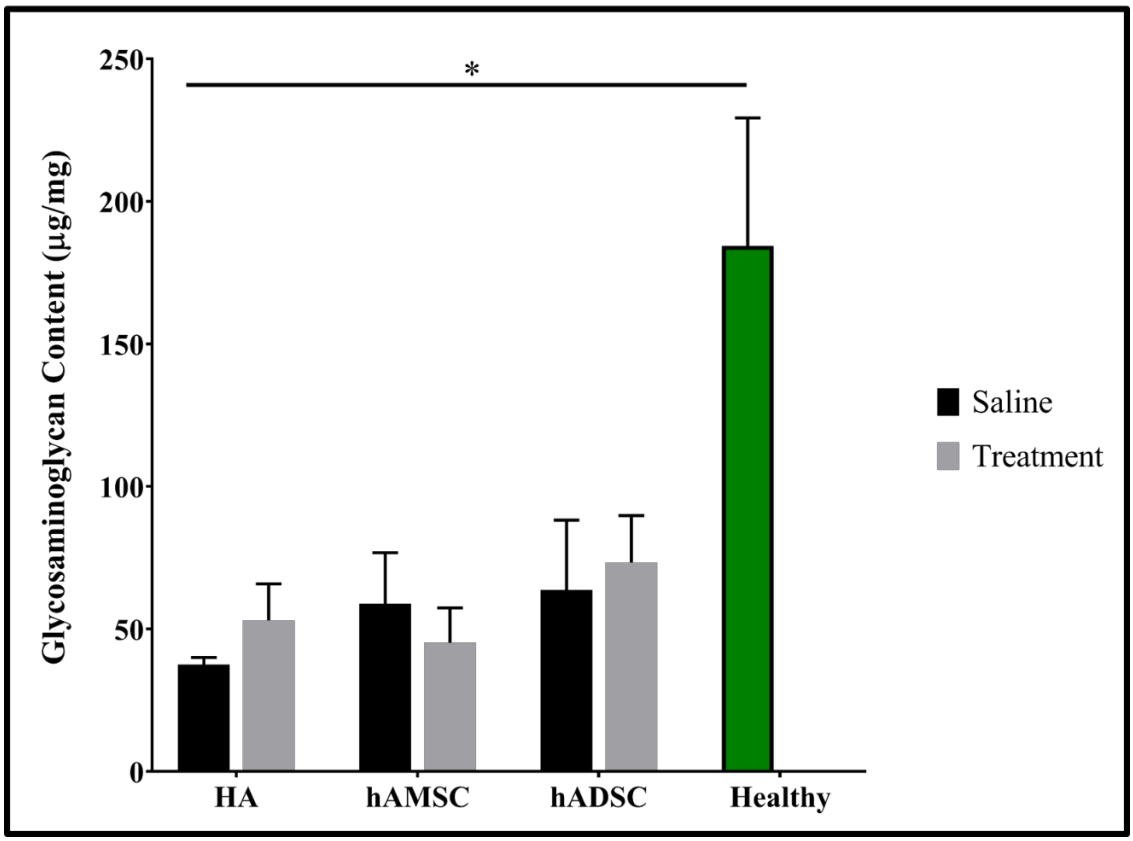

Figure 13: Average GAG content in the medial tibia compartment of the DHGP knee demonstrating higher concentrations of GAG for hADSC treatment compared to its corresponding saline control and hAMSC treatment, with overall statistically higher GAG content in the healthy 2 month-old knee compared to all 9 month-old groups.

2.3.2 Micro-Computed Tomography

2.3.2.1. Scanning and Reconstruction

Upon scanning of the knee joints via the Micro-CT, a 2-dimensional (2D) image was obtained as depicted in Figure 14.

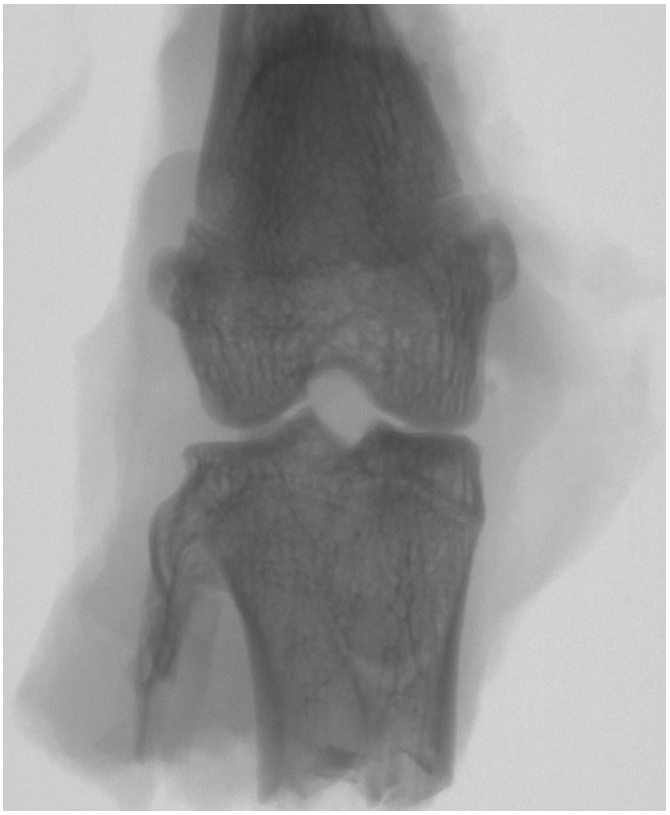

Figure 14: 2D scanned representative Micro-CT image of a DHGP knee using SkyScan Software.

Subsequently, transverse and coronal 3-dimensional (3D) images containing morphometric data was obtained via reconstruction of scanned images, as seen in Figure 15 and Figure 16.

Figure 15: Representative reconstructed DGHP knee depicted in the transverse plane via NRecon Software.

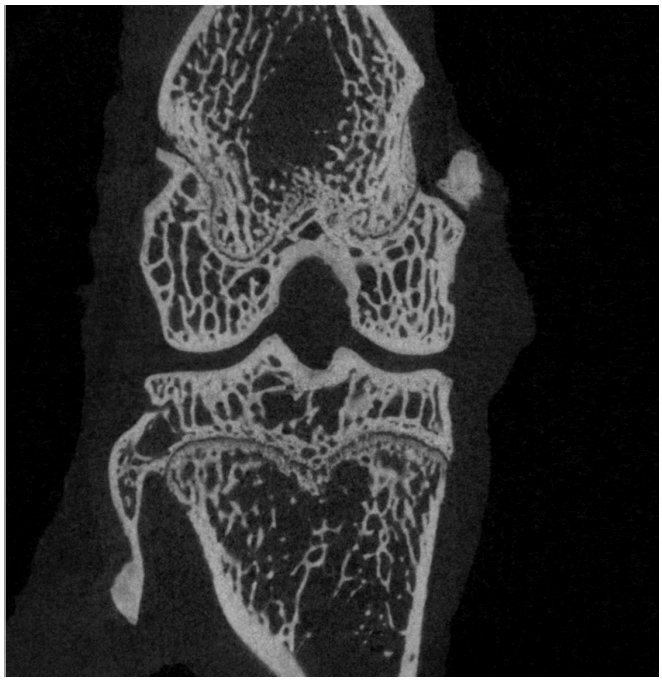

Figure 16: Representative reconstructed DHGP knee in the coronal plane containing 3D morphometric data.

Figure 17: Progression of representative DGHP scanned knee to full reconstructed 3D image containing morphometric data.

The coronal 3D reconstructed images clearly depict the medial and lateral compartments of the tibia plateaus in which anatomical features of the knee, such as the subchondral trabecular bone and subchondral bone plate can be visualized. Figure 18 depicts a representative image displaying the region of interest (ROI) chosen for the subchondral trabecular bone in the medial compartment of the tibia, in which the same ROI was chosen for the lateral compartment. Additionally, Figure 19 depicts a representative image showing the ROI chosen for the subchondral bone plate in the medial compartment of the tibia.

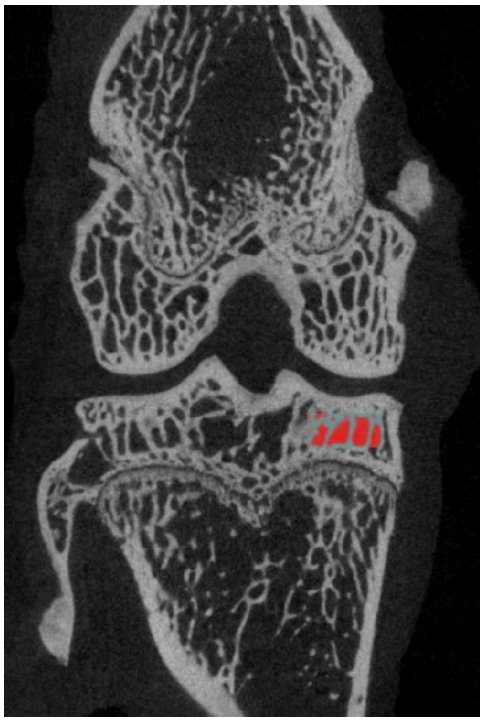

Figure 18: ROI of subchondral trabecular bone in the medial compartment of the tibia.

Figure 19: ROI of subchondral bone plate in the medial compartment of the tibia.

2.3.2.2 Subchondral Trabecular Bone Morphometric Parameters

Upon ROI selection, 3D morphometric parameters including subchondral trabecular bone volume density (BV/TV) and thickness (Tb.Th) were obtained for 9 month-old DHGP knees. Bone volume density measurements are displayed in Figure 20 in which hAMSC treatment exhibited slightly higher average BV/TV compared to its respective saline control (56.6% versus 52.9%). Additionally, it is observed that hADSC treatment also displayed slightly higher average BV/TV compared to its corresponding saline control (56.1% versus 47.3%). HA groups revealed to have a similar BV/TV value to its respective saline control (64.8% versus 65.1%). All paired groups displayed no statistical differences. Comparing BV/TV directly between hAMSC and hADSC treatment, both display similar measurements (56.6% versus 56.1%), overall indicating no statistical difference. Bone volume fraction for healthy 2 month-old DHGP knees were also obtained in which the measurements displayed lower average BV/TV (37.2%) compared to all 9 month-old groups.

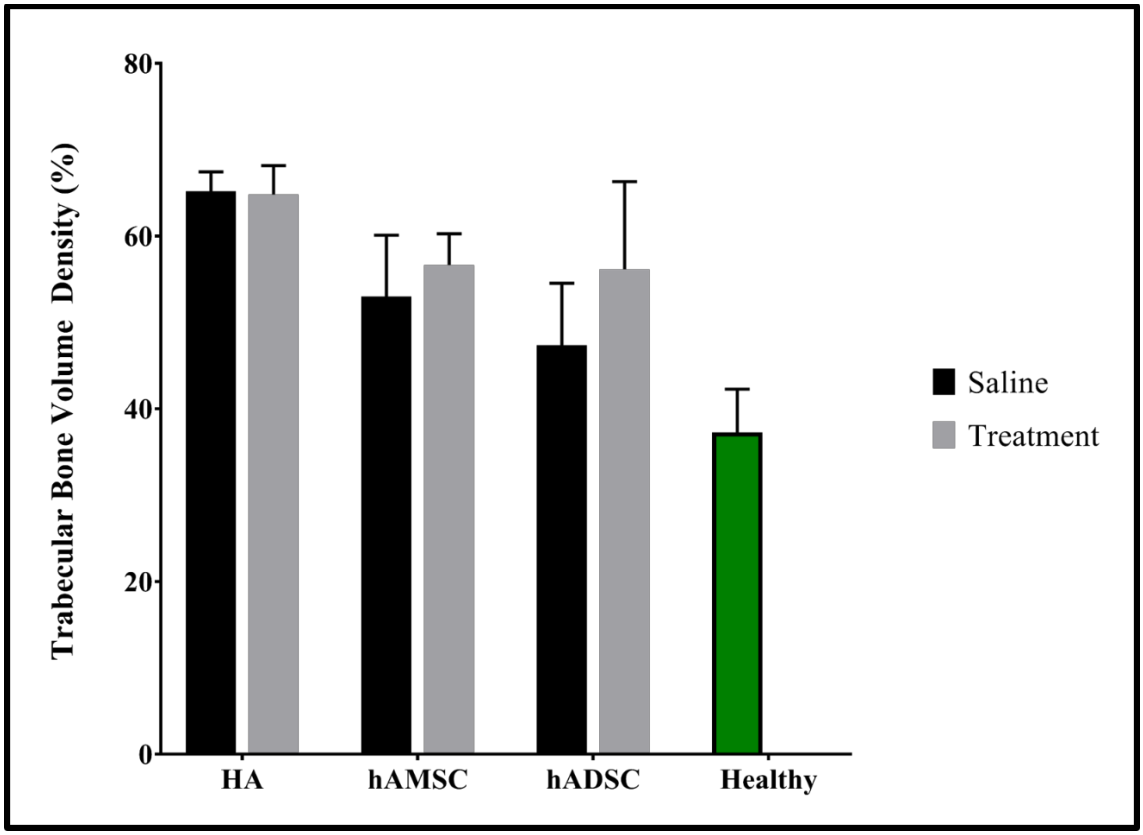

Figure 20: Average subchondral trabecular bone volume density (BV/TV) in the medial compartment of the tibia.

Subchondral trabecular bone thickness measurements are displayed in Figure 21 in which HA treatment shows similar average thickness values with its corresponding saline control (0.576mm versus 0.567mm). Similarly, hADSC treatment shows comparable average thickness values (0.528mm versus 0.530mm) with its paired saline control. The hAMSC treatment exhibited slightly lower average thickness compared to its respective saline control (0.533mm versus 0.574mm); however, all paired groups displayed no statistical differences. Comparing trabecular thickness directly between hAMSC and hADSC treatments, both display similar measurements (0.533mm versus 0.528mm), overall

indicating no statistical difference. Trabecular thickness for healthy 2 month-old DHGP knees were also obtained in which the measurements displayed lower average thickness (0.333mm) compared to all 9 month-old groups. Evaluation of subchondral trabecular bone morphometric parameters of the lateral compartment of the knee can be found in Appendix Figures A.3-A.4.

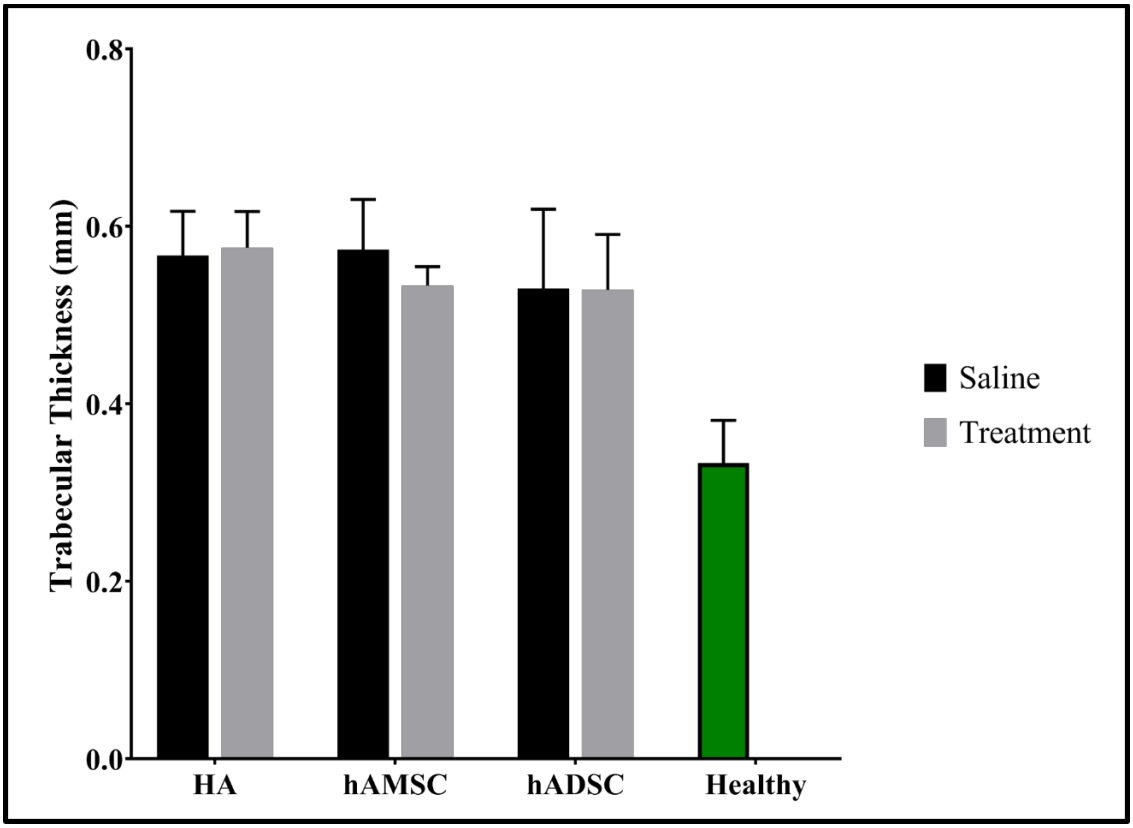

Figure 21: Average trabecular thickness in the medial compartment of the tibia.

2.3.2.3 Subchondral Bone Plate Morphometric Parameters

Ensuing ROI selection, subchondral bone plate thickness was measured for 9 month-old DHGP knees. Figure 22 displays subchondral bone plate thickness measurements in which all treatment groups exhibited higher average thickness

compared to their paired saline controls; however with no statistical difference. Comparing plate thickness directly between hAMSC and hADSC treatments, hADSCs exhibit a slightly higher average thickness measurement (0.395mm versus 0.384mm), although indicating no statistical difference. Additionally, thickness values for healthy 2 month-old DHGP knees were obtained in which the measurements displayed statistically lower average thickness compared to all 9 month-old treatment and control groups (0.308mm). Evaluation of subchondral trabecular bone plate morphometric parameters of the lateral compartment of the knee can be found in Appendix Figures A.5-A.7.

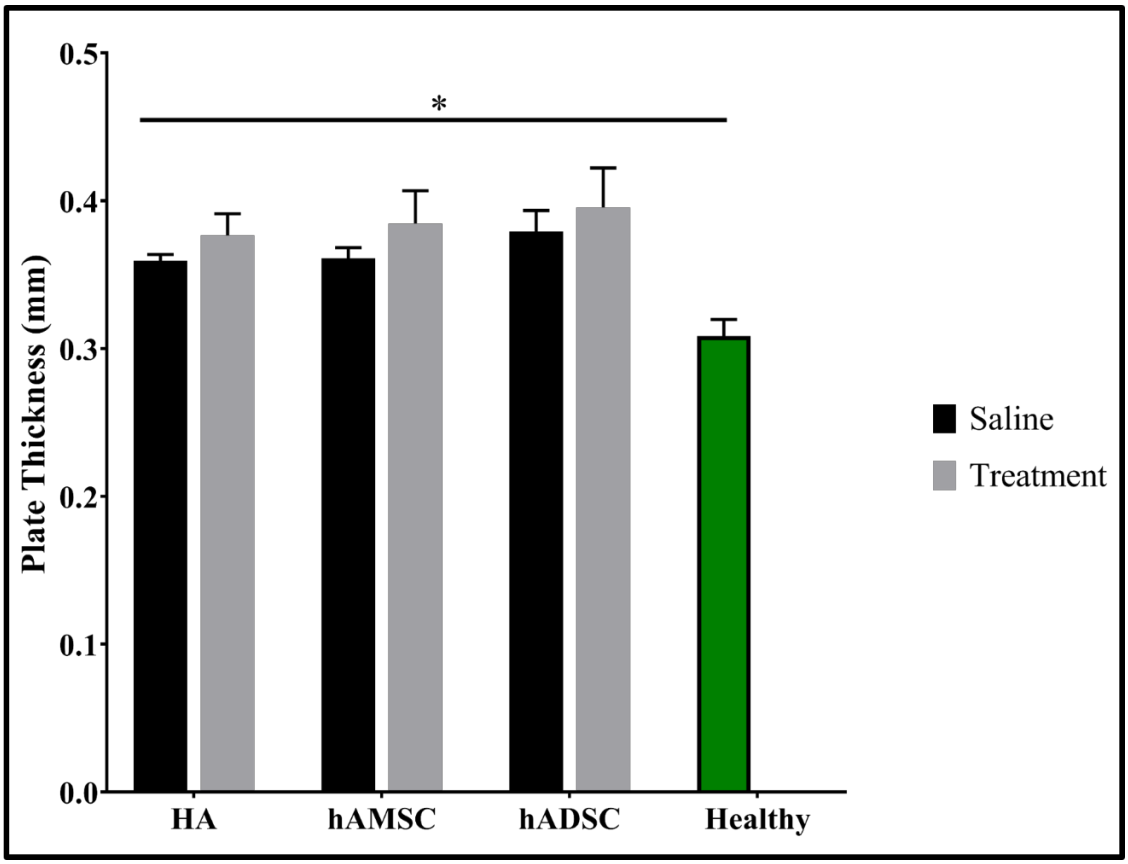

Figure 22: Average subchondral bone plate thickness in the medial compartment of the tibia.

2.3.2.5 Osteophyte Observations

Upon reconstruction of 9 month-old DHGP knees, osteophyte formation at the margins of the joint were observed as represented in Figure 23 and Figure 24**.**

Figure 23: Representative DHGP knee Micro-CT reconstructions in which the red arrows indicate osteophyte formation. Panel A represents a saline control knee while panel B represents an hAMSC treated knee.

Figure 24: Representative DHGP knee Micro-CT reconstructions in which the red arrows indicate osteophyte formation. Panel C represents a hADSC treated knee while panel D represents a HA treated knee.

Upon semi-quantitative blind evaluation of the DHGP knees in the medial compartment of the femur, the saline control contained the overall highest percentage of osteophytes (75%) compared to all treatment groups as seen in Figure 25. HA and hADSC treatments both displayed 37.5% osteophytes observed, while hAMSC treatment contained the lowest amount of osteophytes observed (25%); however, average values were not statistically different.

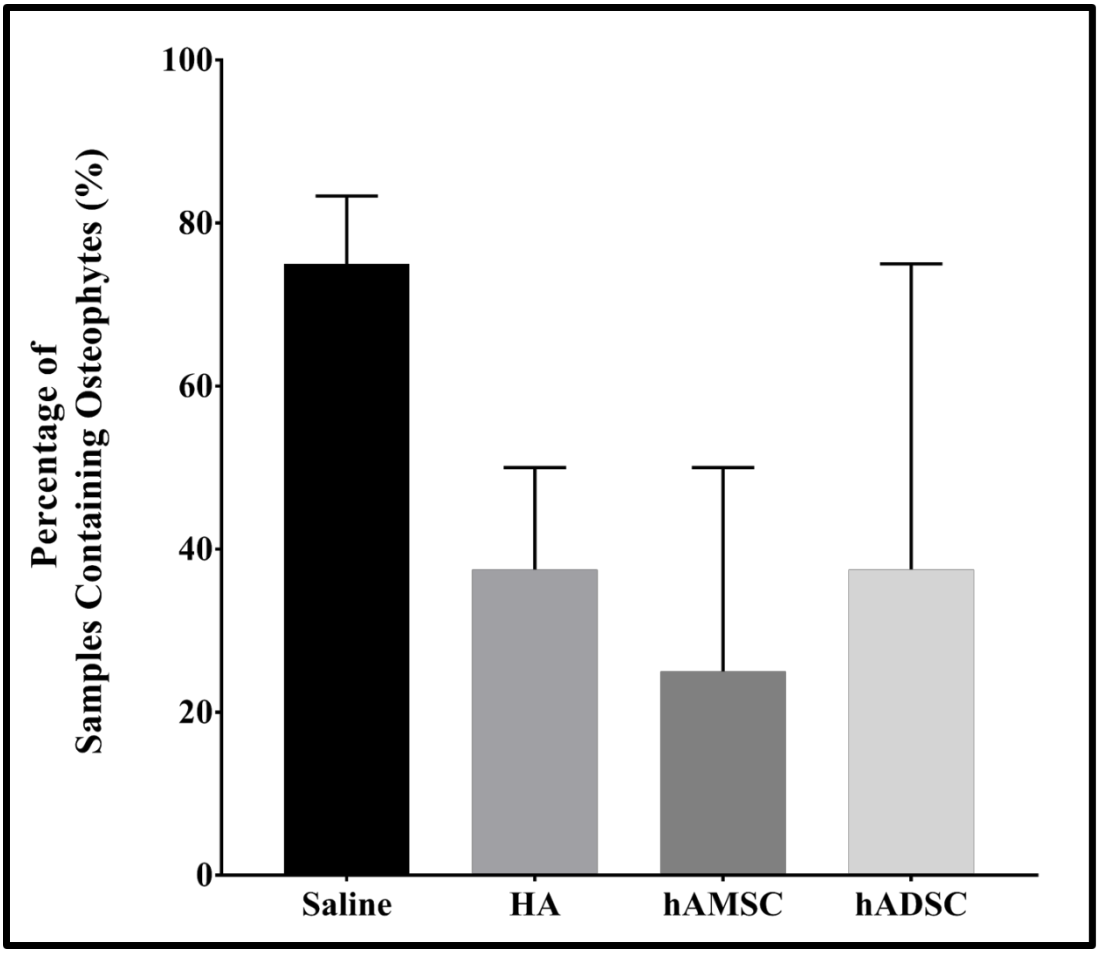

Figure 25: Percent of osteophytes observed in the medial compartment of the femur.

Additionally, semi-quantitative blind evaluation of the DHGP knees in the medial compartment of the tibia displayed that 87.5% of osteophytes were observed in the saline control, hAMSC treatment, and hADSC treatment, as seen in Figure 26. HA treatment contained the lowest amount of osteophytes observed (62.5%); however, average values were not statistically different.

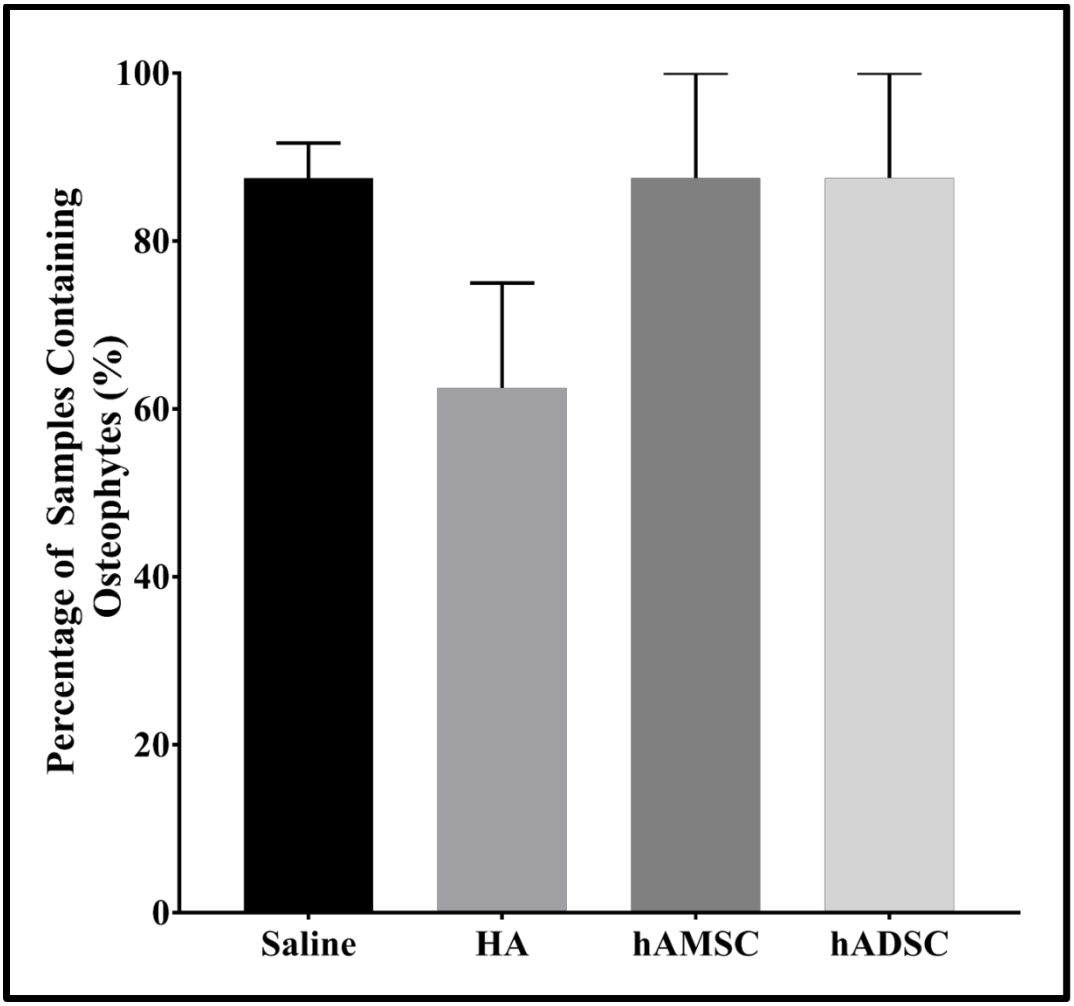

Figure 26: Percent of osteophytes observed in the medial compartment of the tibia.

2.3.3 Histological Evaluation

2.3.3.1 Articular Cartilage Surface Integrity

DHGP knee joints stained with Safranin-O was performed in order to semi-quantitatively evaluate articular cartilage surface integrity. Figure 27 displays a representative stained knee in which articular cartilage of the femoral condyles and tibia plateaus can be visualized as chondrocyte nuclei are stained red.

Figure 27: Representative DHGP knee stained with Safranin-O for articular cartilage evaluation.

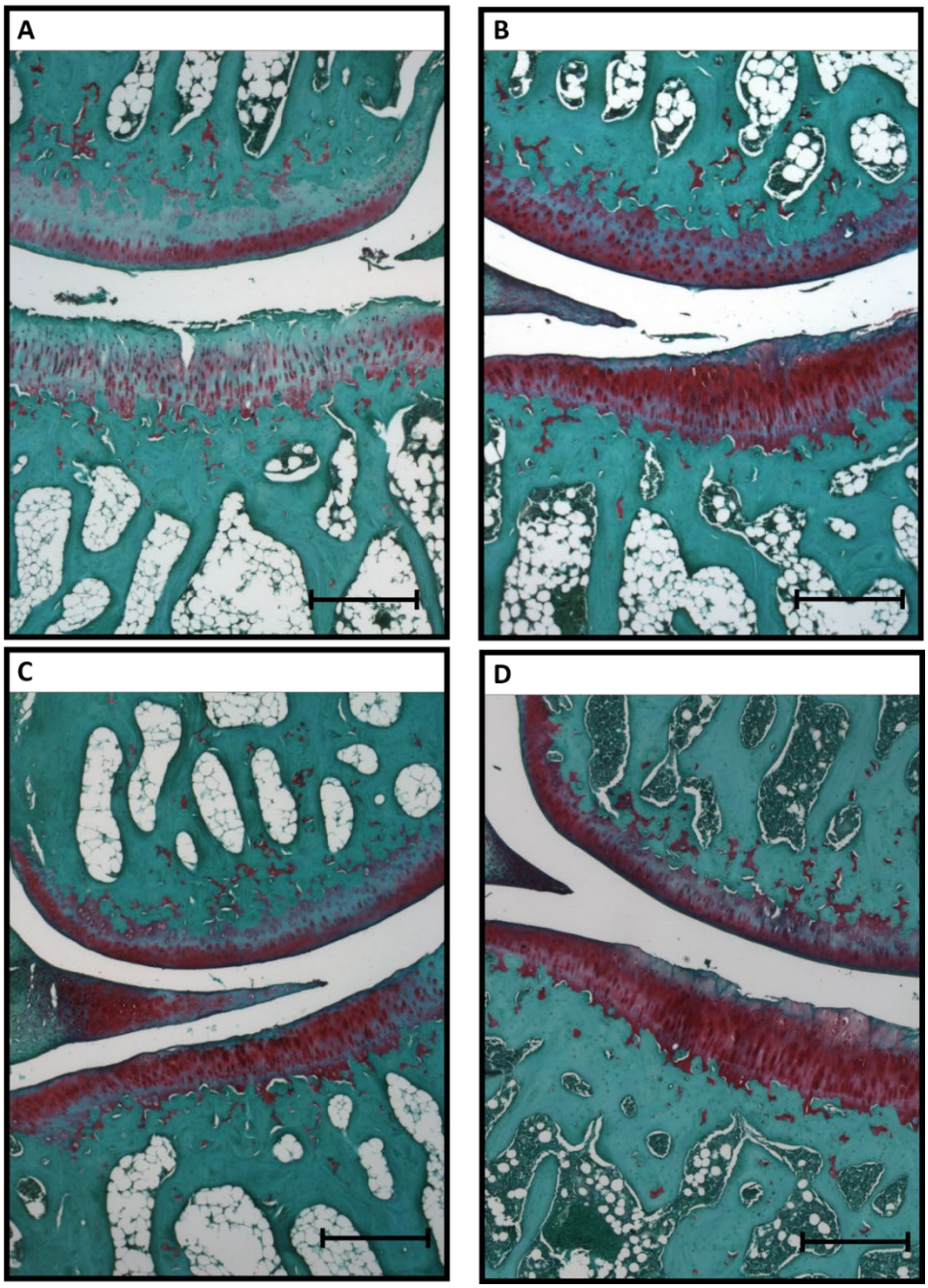

Figure 28: Representative Safranin-O stained DHGP knee joints (aged 9 months) depicting the articular cartilage of the femur and tibia to demonstrate varying severities of histological lesions scored by the recommended histological scoring as shown in Table 2. Panel A depicts a saline control knee, panel B is a HA treatment knee, panel C is a hADSC treatment knee, and panel D is a hAMSC treatment knee. All scale bars represent 500µm.

Representative Safranin-O stained knee joints semi-quantitatively evaluated and scored, via two blind observers, are displayed in Figure 28. The tibia plateau observed in panel A displays fibrillation and clefts that extend into the deep zone of the articular cartilage. Panel B and D display mild surface irregularities with superficial fissures, while panel C represents normal, smooth and uninterrupted articular surface. Semi-quantitative scoring of the articular cartilage surface of the tibia, illustrated in Figure 29, indicates that HA treatment revealed a higher average score compared to its paired saline control (4.71 versus 2.75). Conversely, hAMSC treatment displayed overall lower average histologic scores compared to its respective saline control (3.25 versus 5.25). Additionally, hADSC treatment displayed lower average histologic scores compared to its paired saline control (4.0 versus 5.5). Directly comparing hADSC treatment to hAMSC treatment, hAMSCs displayed an overall slightly lower score compared to hADSCs (3.25 versus 4.0). No statistical difference was observed between all groups.

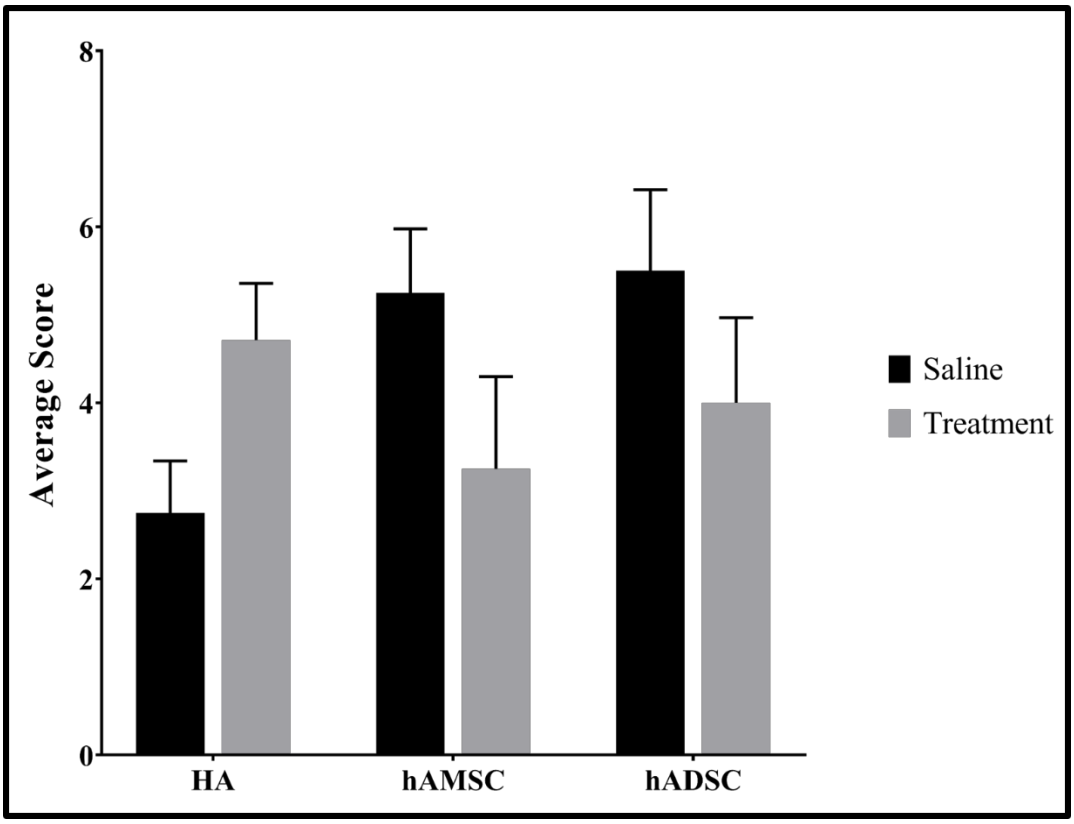

Figure 29: Average semi-quantitative articular surface scores of the DHGP tibia.

Semi-quantitative scoring of femoral articular cartilage illustrated in Figure 30, reveals that HA treatments exhibit a slightly lower average score compared to its respective saline control (1.0 versus 1.125). Similarly, hAMSC treatment displays a lower average score compared to its corresponding saline control (0.375 versus 0.875). Conversely, hADSC treatment displays a slightly higher average score compared to its paired saline control (1.0 versus 0.5) as well as the hAMSC treatment (1.0 versus 0.375); however, no statistical difference is observed between all groups. Additionally, it can be observed that the overall average scores for groups evaluated in the femur was lower than that observed in the tibia.

Qualitatively this can be observed in the representative images seen in Figure 28, where the femoral condyles display smooth and uninterrupted surfaces. All Safranin-O stained DHGP knees can be viewed in Appendix Figure A.8.

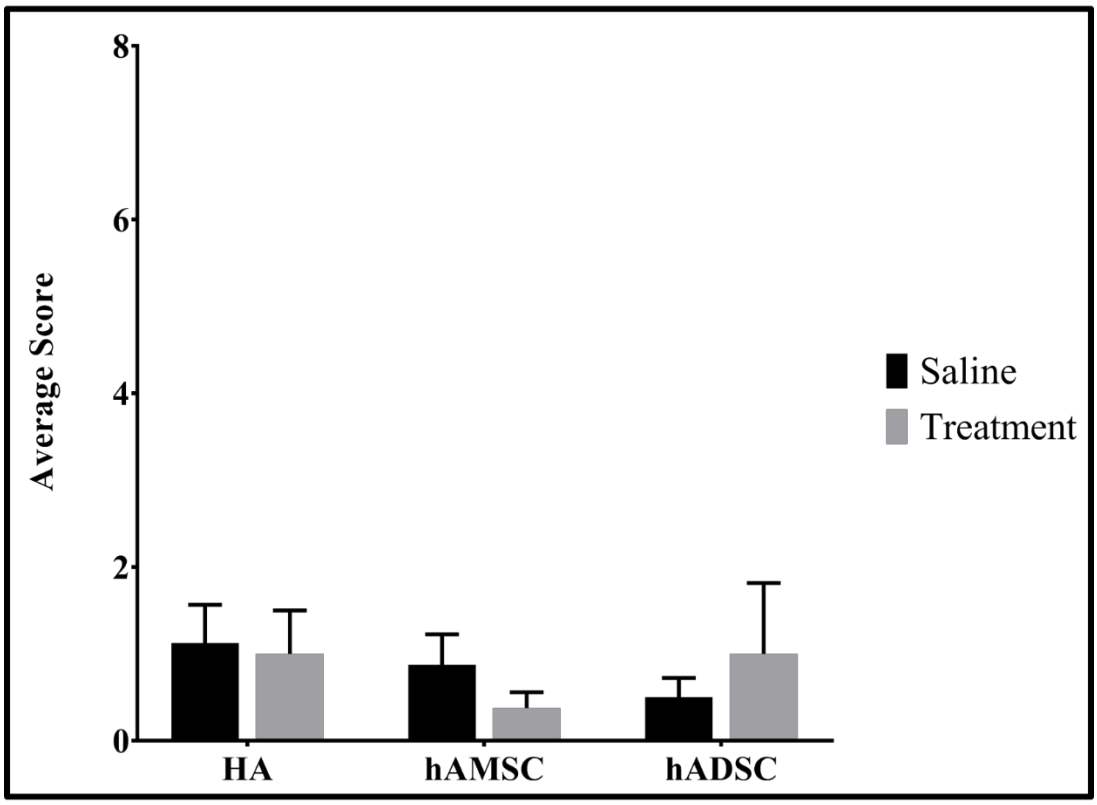

Figure 30: Average semi-quantitative articular surface scores of the DHGP femur.

2.3.3.2 Proteoglycan Content

DHGP knee joints stained with Toluidine Blue was performed in order to semi-quantitatively evaluate proteoglycan content of the articular cartilage. Figure 31 displays a representative stained knee in which articular cartilage matrix of the femoral condyles and tibia plateaus can be visualized as the cartilage is stained blue.

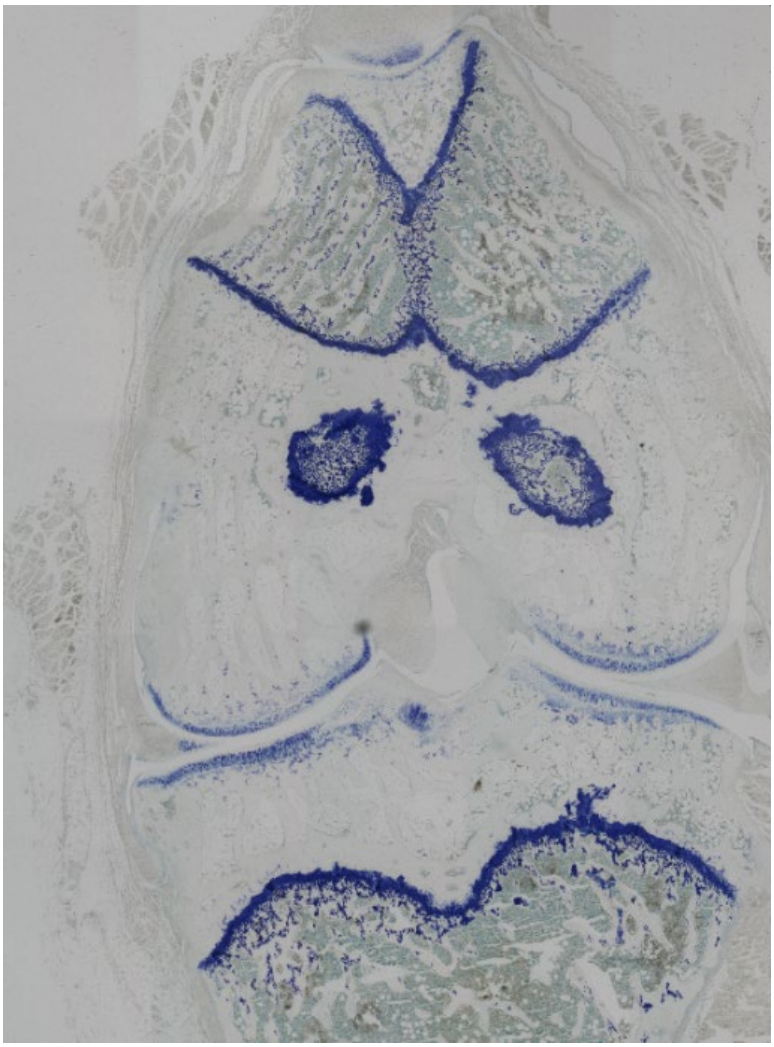

Figure 31: Representative DHGP knee stained with Toluidine Blue for proteoglycan content evaluation.

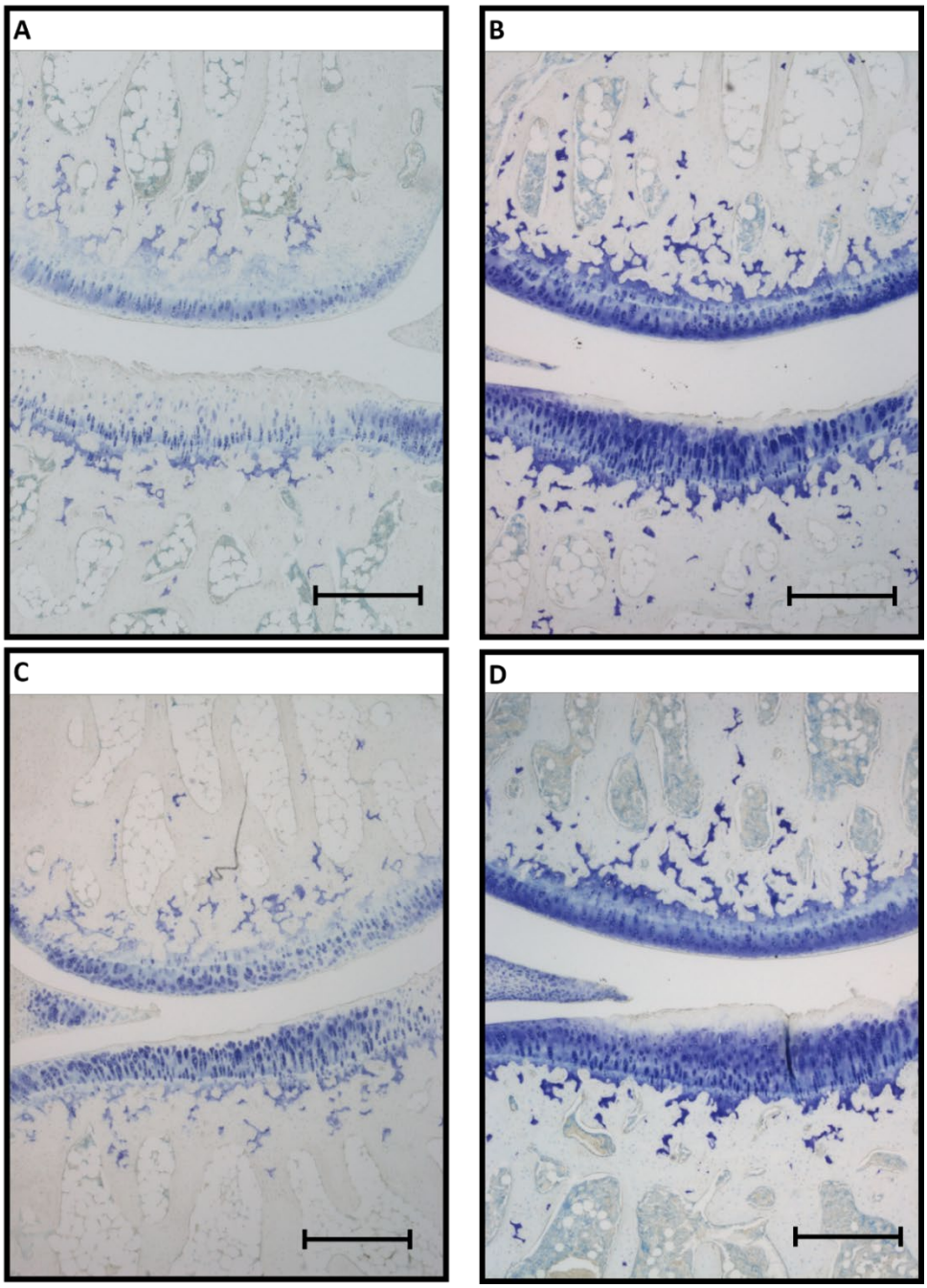

Figure 32: Representative Toluidine Blue stained DHGP knee joints (aged 9 months) depicting the proteoglycan of the articular cartilage to demonstrate varying severities of histological lesions scored by the recommended histological scoring scheme as shown in Table 3. Panel A depicts a saline control knee, panel B is a HA treatment knee, panel C is a hADSC treatment knee, and panel D is a hAMSC treatment knee. All scale bars represent 500µm.

Representative Toluidine Blue stained knee joints semi-quantitatively evaluated and scored, via two blind observers, are displayed in Figure 32. The tibia plateau observed in panel A displays decreased proteoglycan content in all 3 zones (superficial, middle, and deep) for greater than half the length of the plateau. Panels B and C display uniform proteoglycan staining throughout the articular surface with slight decrease in the superficial zone, while panel D displays decreased proteoglycan content in superficial and middle zones for half the length of the plateau. Figure 33 depicts the semi-quantitative scoring of proteoglycan content of the tibia in which HA treatment exhibits a lower average score compared to its respective saline control (2.75 versus 4.125). Additionally, hAMSC treatment displays a lower average score compared to its corresponding saline control (3.75 versus 4.75). Furthermore, hADSC treatment displays significantly lower average scores ($p=0.0173$) compared to its paired saline control (2.66 versus 5.0), while also illustrating lower average score in comparison to the hAMSC treatment (2.66 versus 3.75). Moreover, all treatment groups demonstrated lower scores compared to their paired saline control groups.

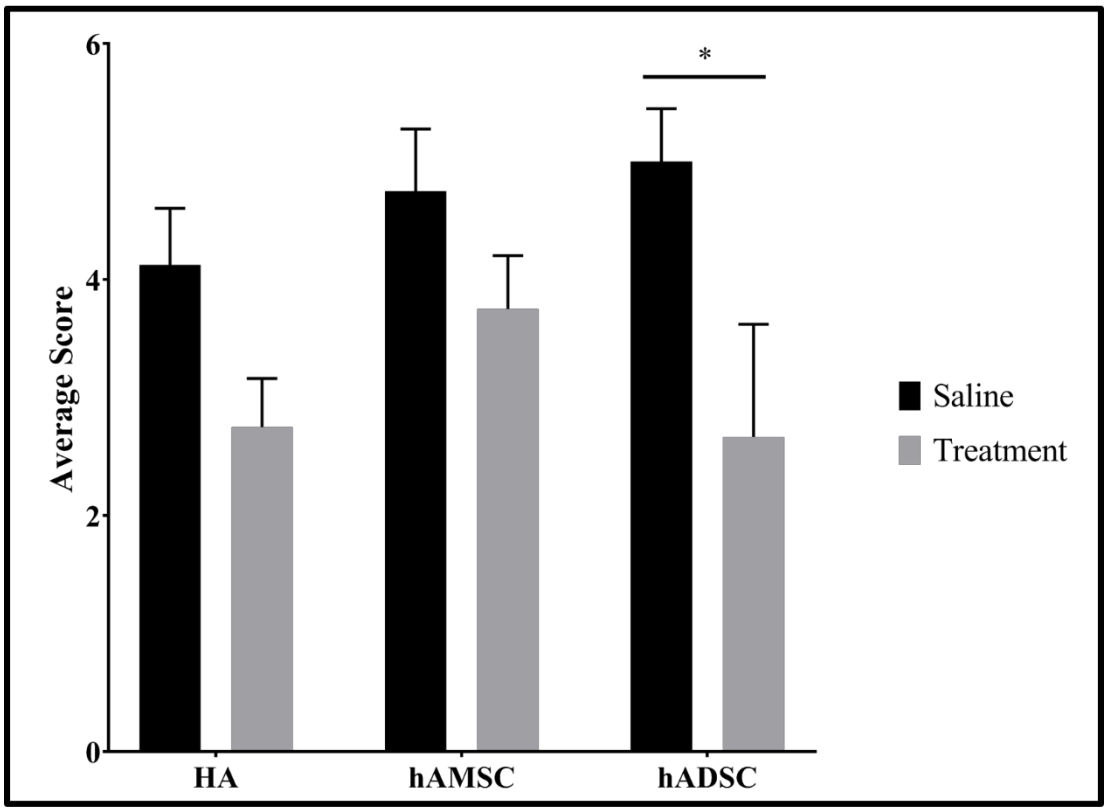

Figure 33: Average semi-quantitative proteoglycan content scores of the DHGP tibia. One star represents statistical significance ($p<0.05$).

Semi-quantitative scoring of proteoglycan content in the femur reveals that the HA treatment exhibits a lower average score compared to its respective saline control (1.75 versus 3.0), as depicted in Figure 34. Additionally, hAMSC treatment displays a lower average score compared to its respective saline controls (2.625 versus 3.75). Furthermore, hADSC treatment displays a slightly lower average score compared to its paired saline control (2.33 versus 2.5) as well as the hAMSC treatment (2.33 versus 2.625); however, no statistical difference was observed between all groups. All Toluidine Blue stained DHGP knees can be viewed in Appendix Figure A.9.

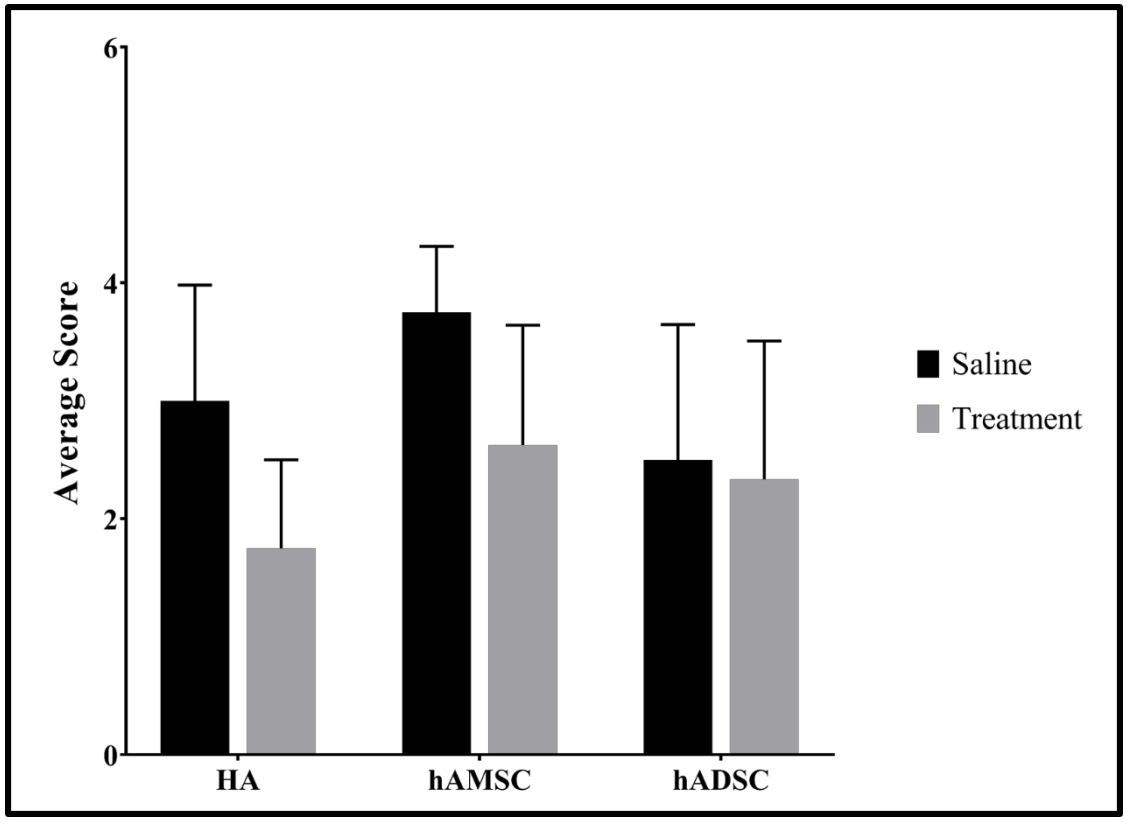

Figure 34: Average semi-quantitative proteoglycan content scores of the DHGP femur.

2.3.3.3 Synovial Hyperplasia

DHGP knee joints stained with Hematoxylin and Eosin (H&E) was performed in order to evaluate synovial membrane hyperplasia via semi-quantitative grading of membrane cellularity. Figure 35 displays a representative stained knee in which the synovium, characterized by the adipose, areolar, and fibrous soft tissue surrounding the knee joint, can be visualized.

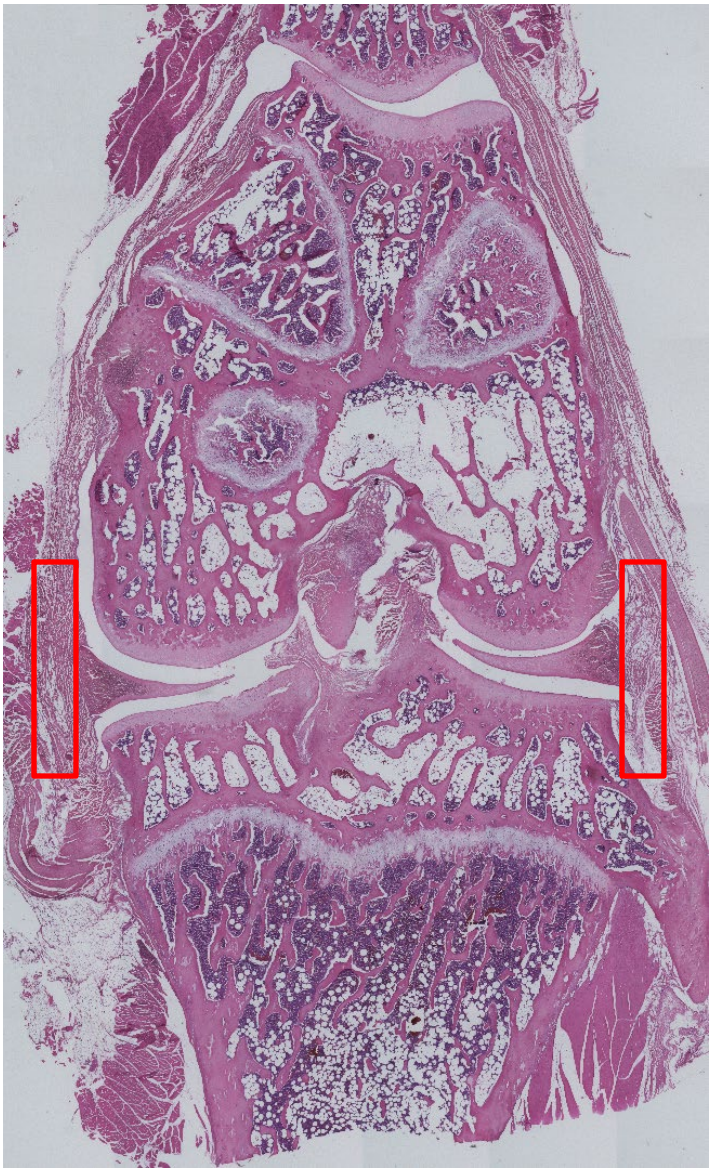

Figure 35: Representative DHGP knee stained with H&E for synovial membrane hyperplasia evaluation. The location of the synovial membrane is indicated by the red boxes.

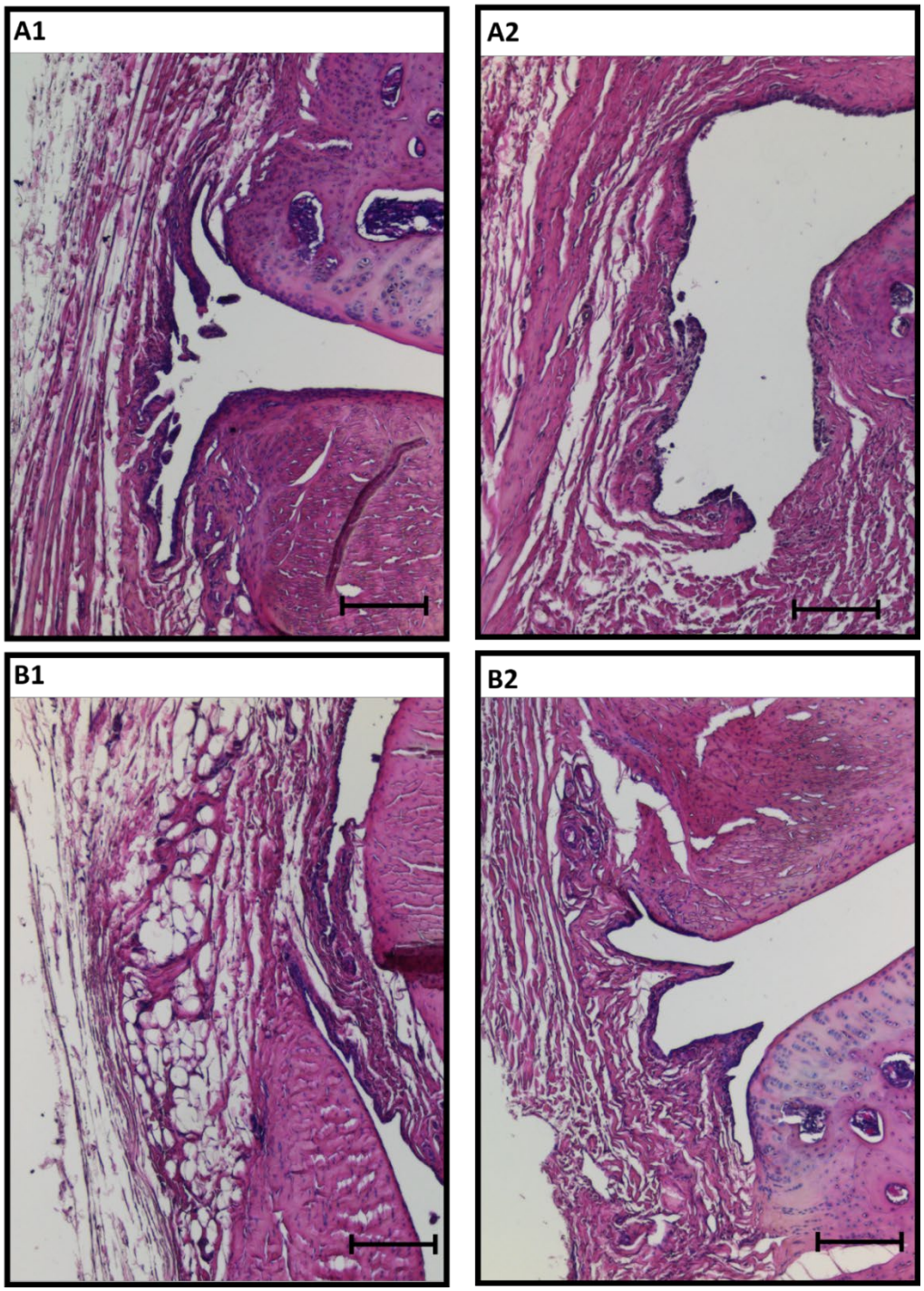

Figure 36: Representative H&E stained DHGP knee joints (aged 9 months) depicting the synovium to demonstrate varying severities of synovitis scored according to a histological scoring scheme as shown in Table 4. Panels A1 and A2 depict saline control knees while panels B1 and B2 represent HA treatment knees. All scale bars represent 200 µm.

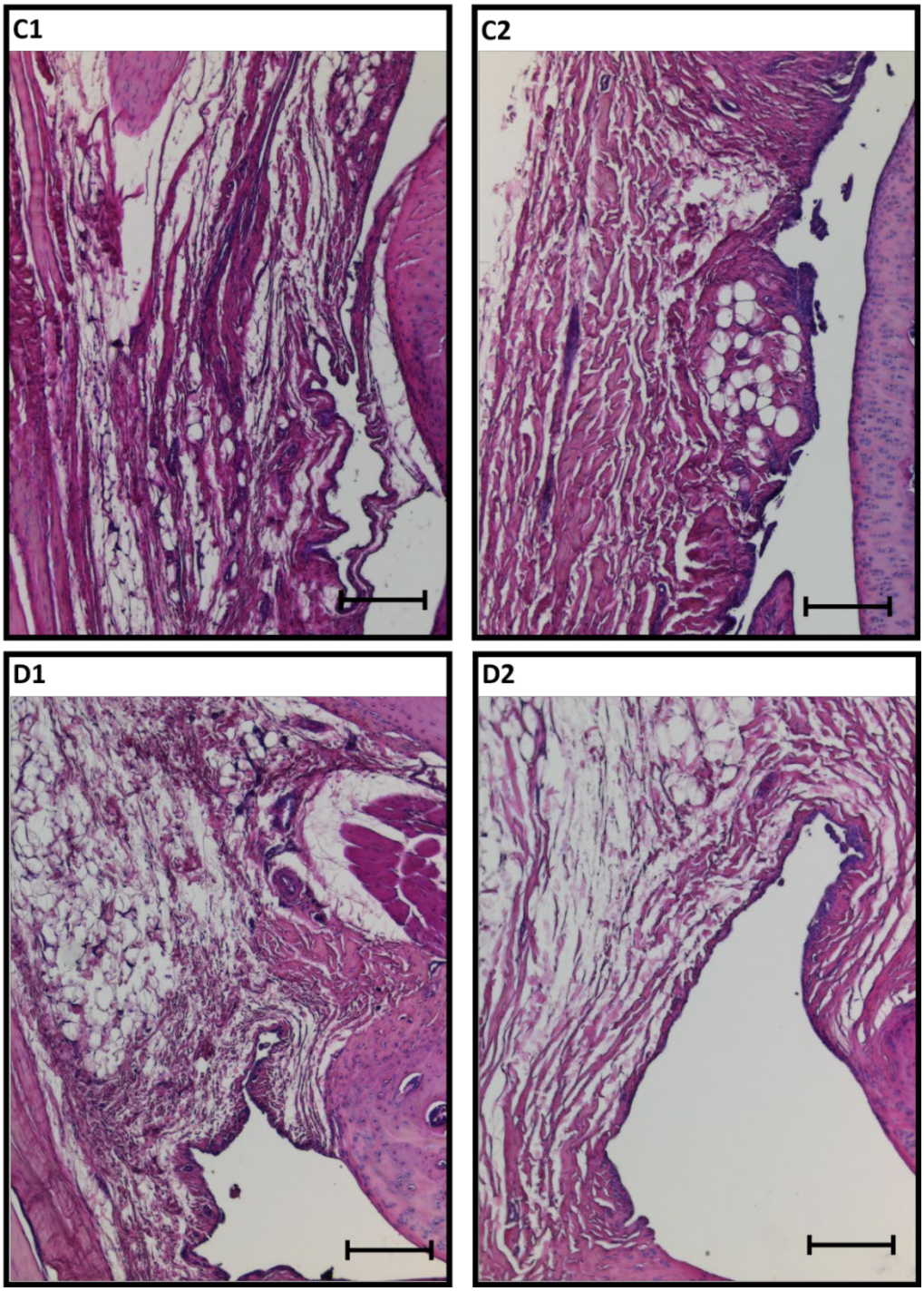

Figure 37: Representative H&E stained DHGP knee joints (aged 9 months) depicting the synovium to demonstrate varying severities of synovitis scored according to a histological scoring scheme as shown in Table 4. Panels C1 and C2 represent hADSC treatment knees while panels D1 and D2 display hAMSC treatment knees. All scale bars represent 200 µm.

Representative H&E stained knee joints semi-quantitatively evaluated and scored for cellularity, via two blind observers, are displayed in Figure 36Figure 37. Panels A1, A2, and C2 illustrate an increase in the number of cellular layers (4-6 layers) with marked villous hyperplasia at the membrane lining. Panels B1, B2, and C1 exhibit normal cellularity (1-2 layers) at the membrane lining, while Panels D1 and D2 display slight increase in cellularity as well as villous hyperplasia in some areas of the membrane lining. These observations can be further visualized from Figure 38 through Figure 45 which depict the same representative H&E stained knee joints seen in Figure 36 and Figure 37 but have been magnified (400x total magnification) in order to more accurately semi-quantitatively score synovium cellularity at the membrane lining.

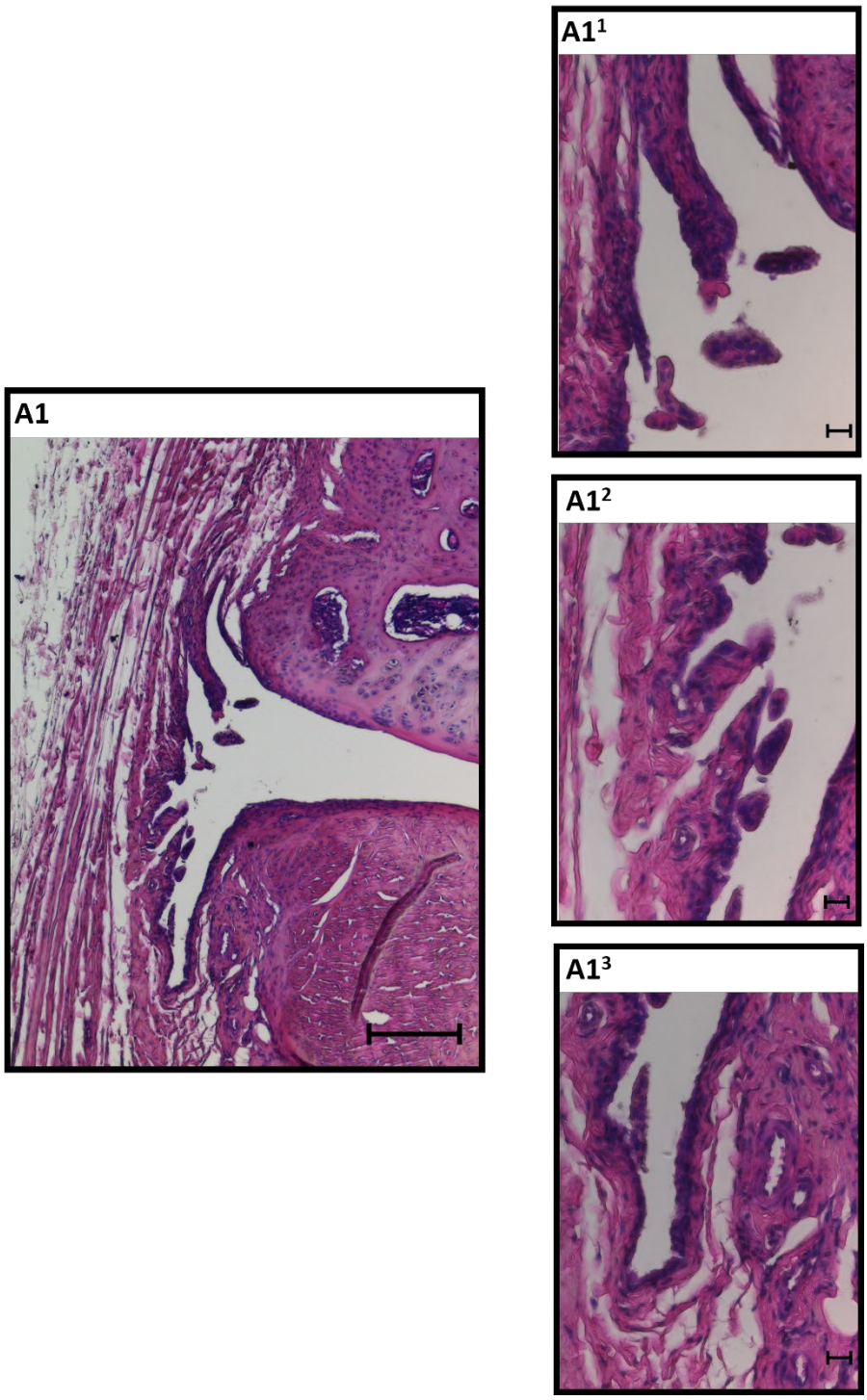

Figure 38: Representative H&E stained saline control DHGP synovium. Panel A1 represents a 100x total magnification image with scale bar depicting 200 µm, while panels A1[1], A1[2], and A1[3] represent 400x total magnification images with scale bar depicting 20 µm.

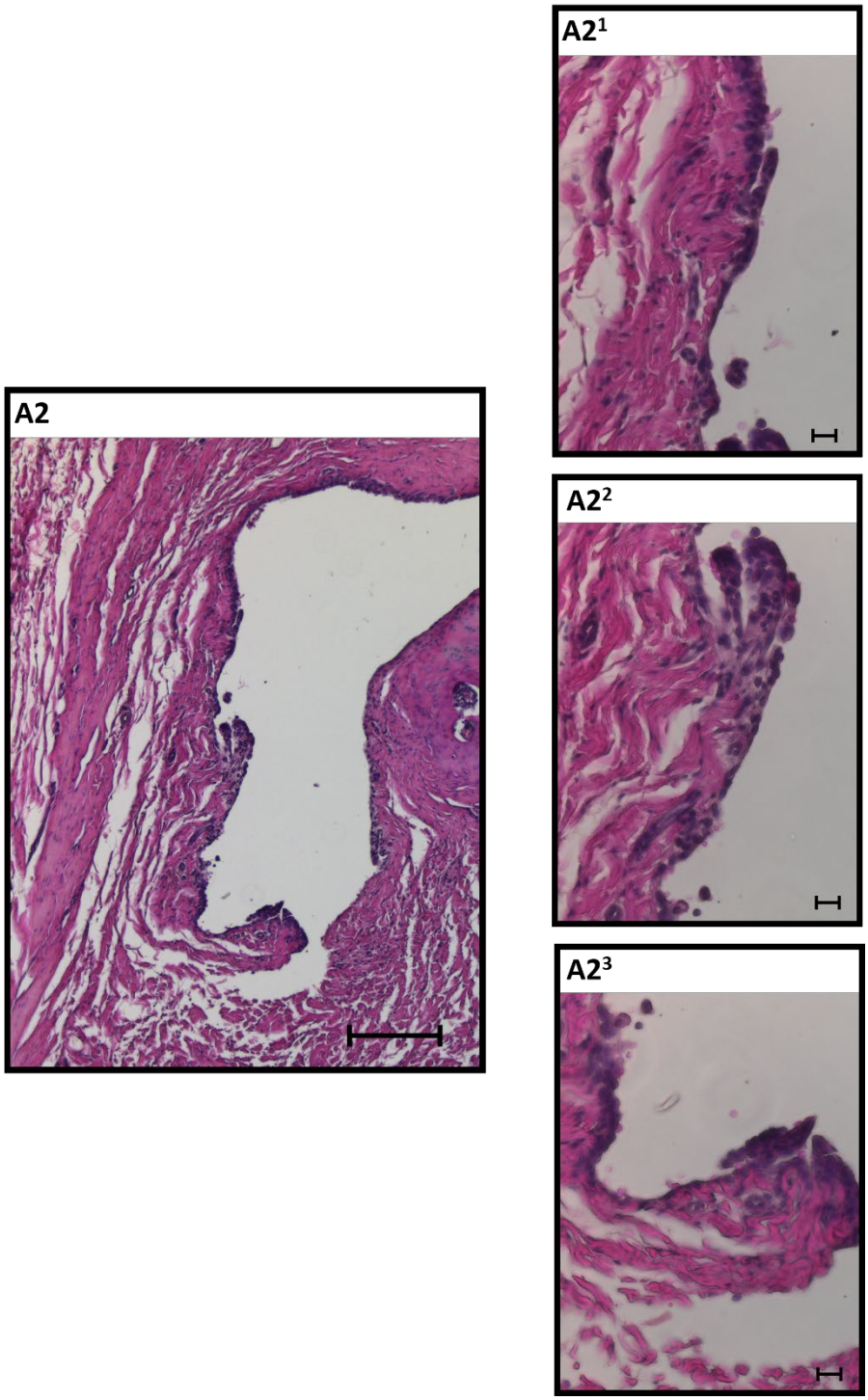

Figure 39: Representative H&E stained saline control DHGP synovium. Panel A1 represents a 100x total magnification image with scale bar depicting 200 µm, while panels A1[1], A1[2], and A1[3] represent 400x total magnification images with scale bar depicting 20 µm.

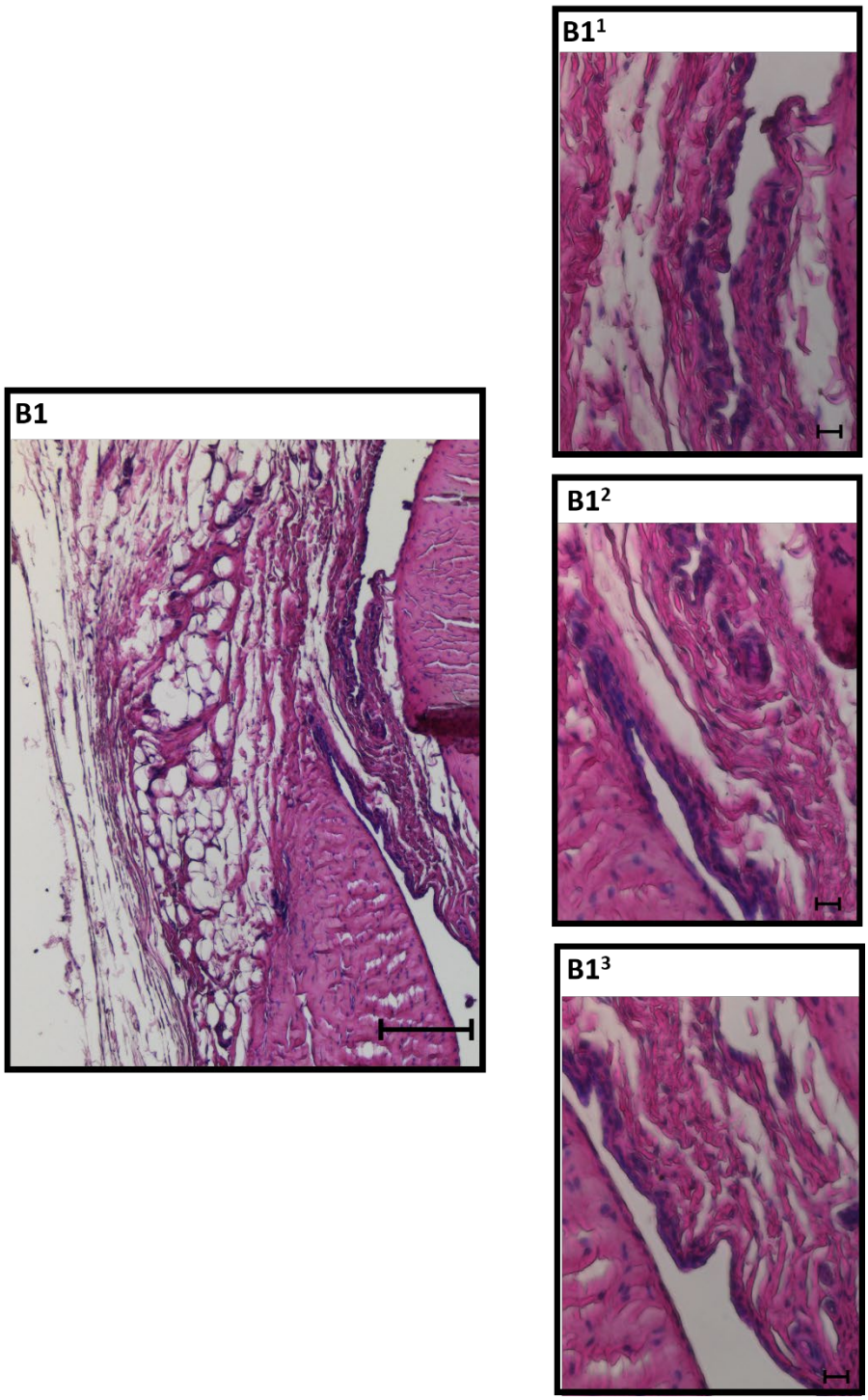

Figure 40: Representative H&E stained HA treatment DHGP synovium. Panel A1 represents a 100x total magnification image with scale bar depicting 200 µm, while panels A1[1], A1[2], and A1[3] represent 400x total magnification images with scale bar depicting 20 µm.

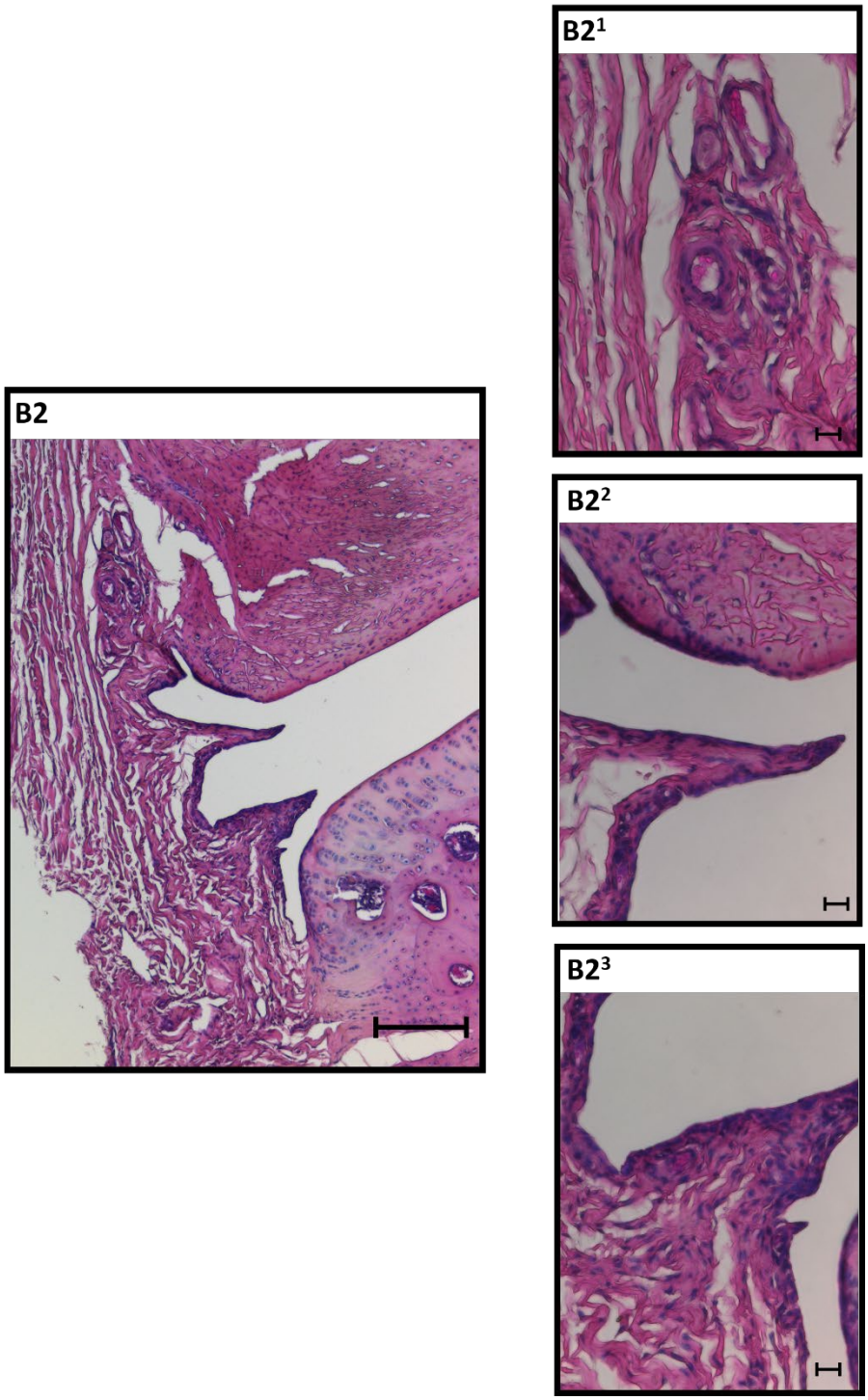

Figure 41: Representative H&E stained HA treatment DHGP synovium. Panel A1 represents a 100x total magnification image with scale bar depicting 200 µm, while panels A1[1], A1[2], and A1[3] represent 400x total magnification images with scale bar depicting 20 µm.

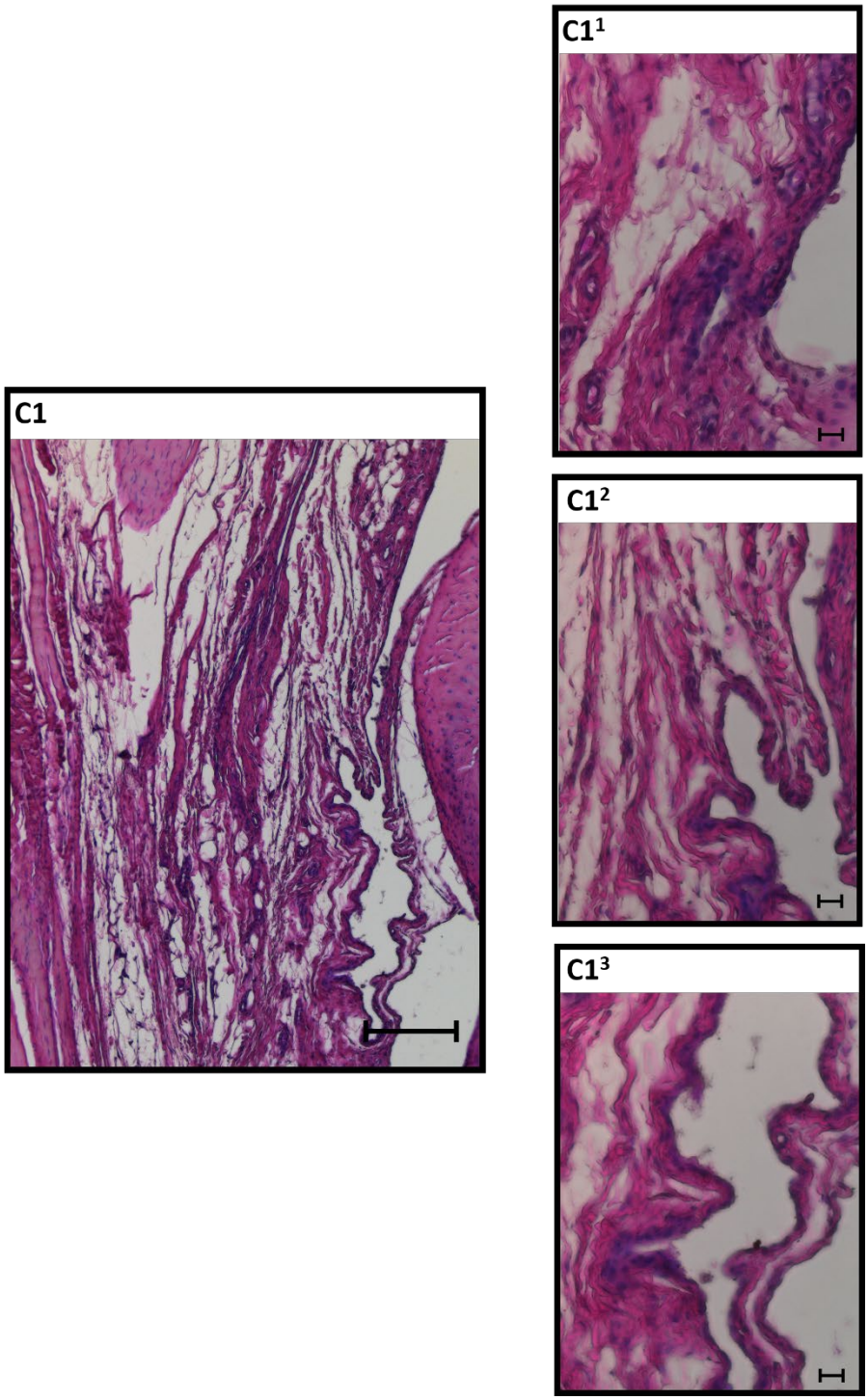

Figure 42: Representative H&E stained hADSC treatment DHGP synovium. Panel A1 represents a 100x total magnification image with scale bar depicting 200 µm, while panels A1[1], A1[2], and A1[3] represent 400x total magnification images with scale bar depicting 20 µm.

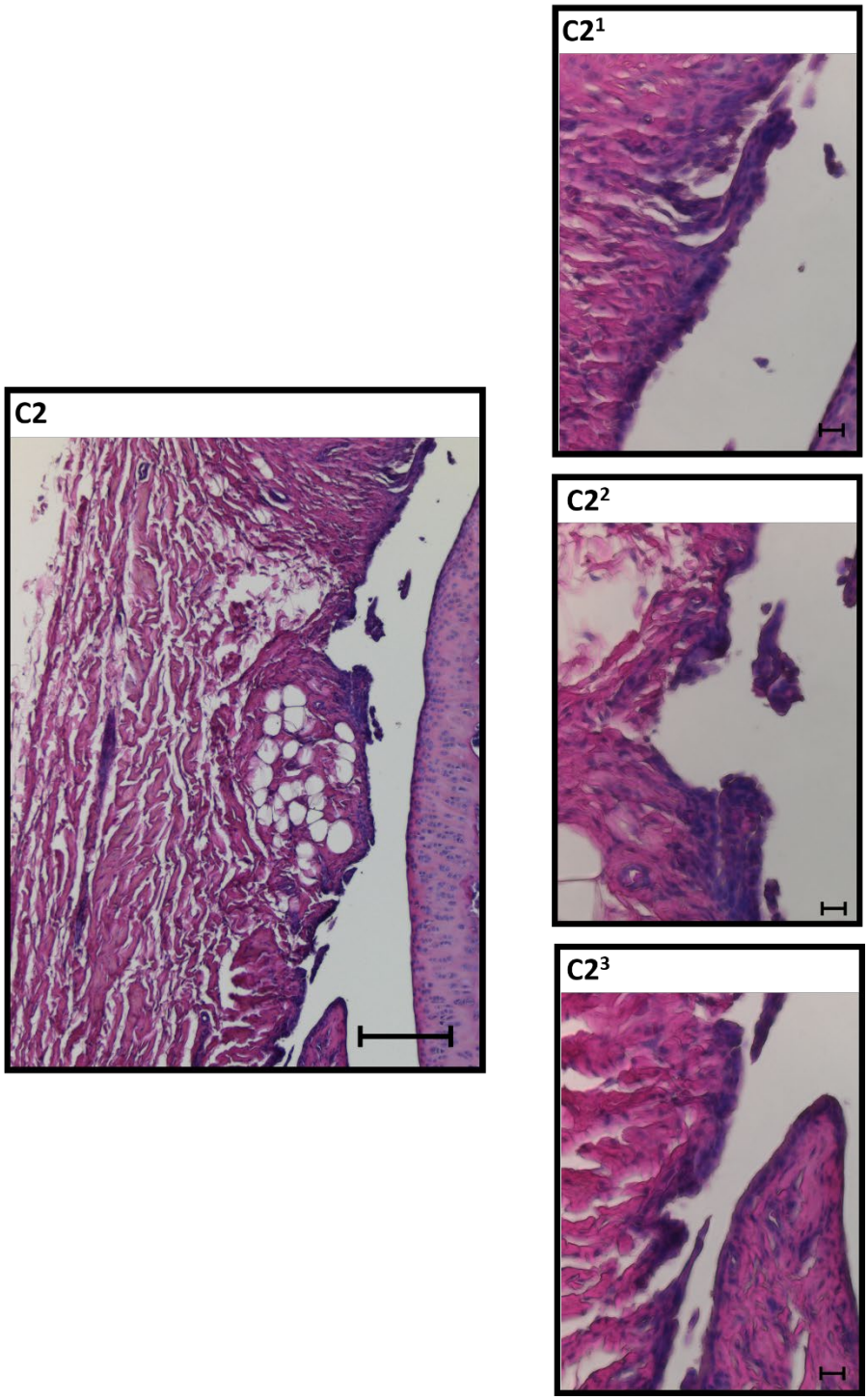

Figure 43: Representative H&E stained hADSC treatment DHGP synovium. Panel A1 represents a 100x total magnification image with scale bar depicting 200 µm, while panels A1[1], A1[2], and A1[3] represent 400x total magnification images with scale bar depicting 20 µm.

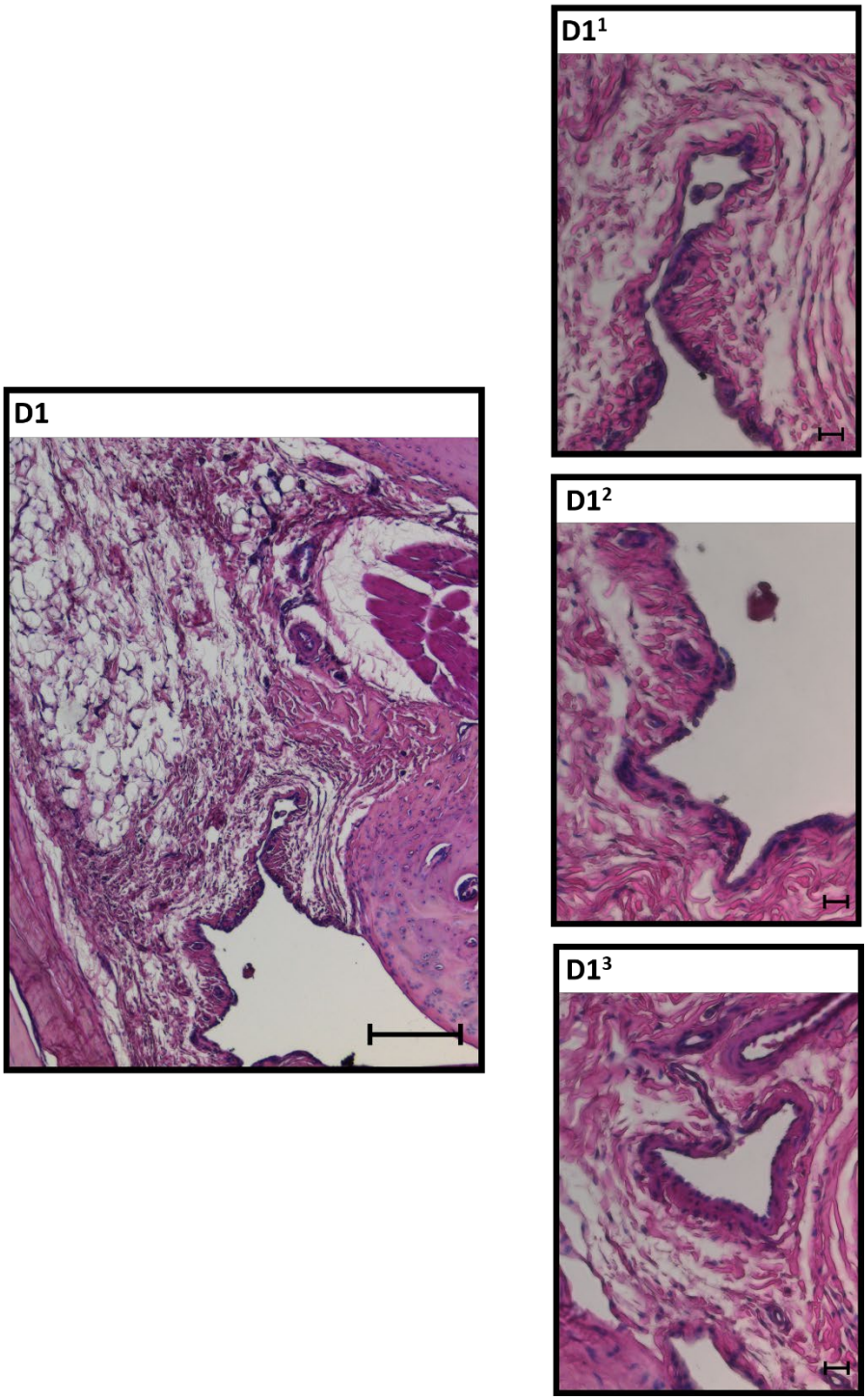

Figure 44: Representative H&E stained hAMSC treatment DHGP synovium. Panel A1 represents a 100x total magnification image with scale bar depicting 200 µm, while panels A1[1], A1[2], and A1[3] represent 400x total magnification images with scale bar depicting 20 µm.

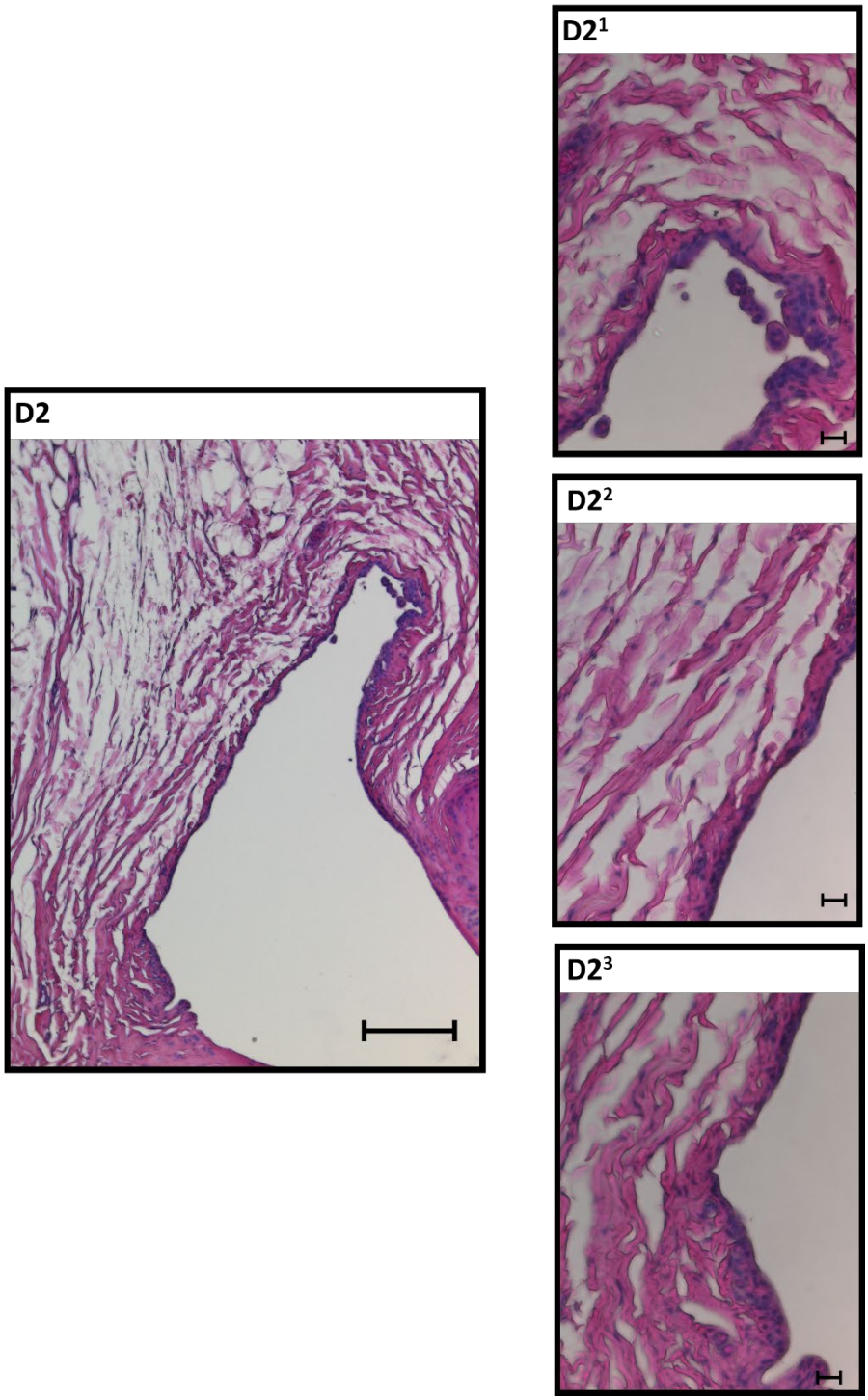

Figure 45: Representative H&E stained hAMSC treatment DHGP synovium. Panel A1 represents a 100x total magnification image with scale bar depicting 200 µm, while panels A1[1], A1[2], and A1[3] represent 400x total magnification images with scale bar depicting 20 µm.

Additionally, representative healthy 2-month old H&E stained knee joints semi-quantitatively evaluated and scored for cellularity are displayed in Figure 46. All panels illustrate a decreased and normal cellularity at membrane lining in comparison to the 9-month old knees. These observations can be further visualized from Figure 47 through Figure 49, which depict the same representative H&E stained knee joints seen in Figure 46 but have been magnified (400x total magnification) in order to more accurately semi-quantitatively score synovium cellularity at the membrane lining.

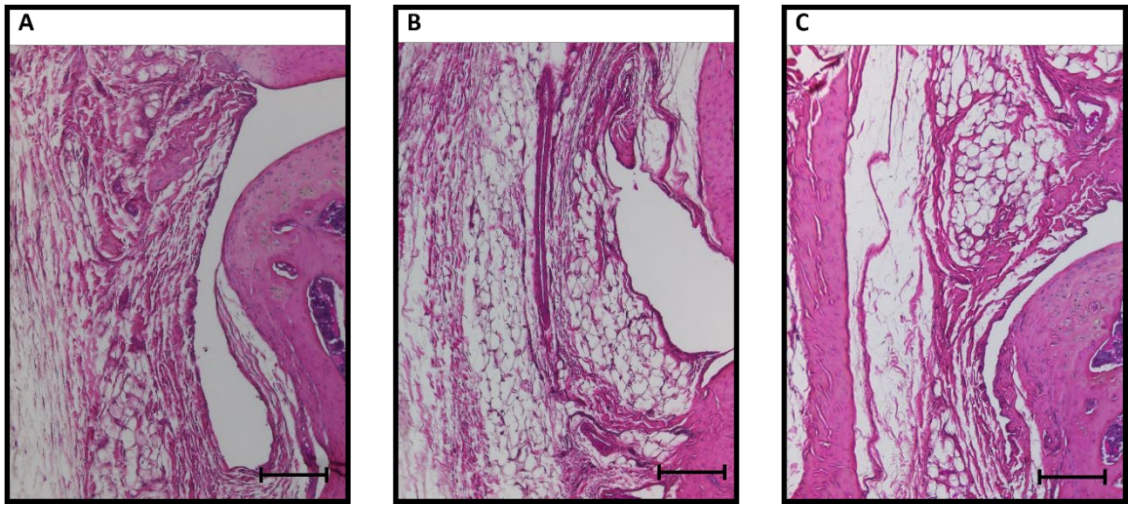

Figure 46: Representative healthy H&E stained DHGP knee joints (aged 2 months) depicting the synovium. Decreased and normal cellularity (1-2 layers) are observed. All scale bars represent 200 µm.

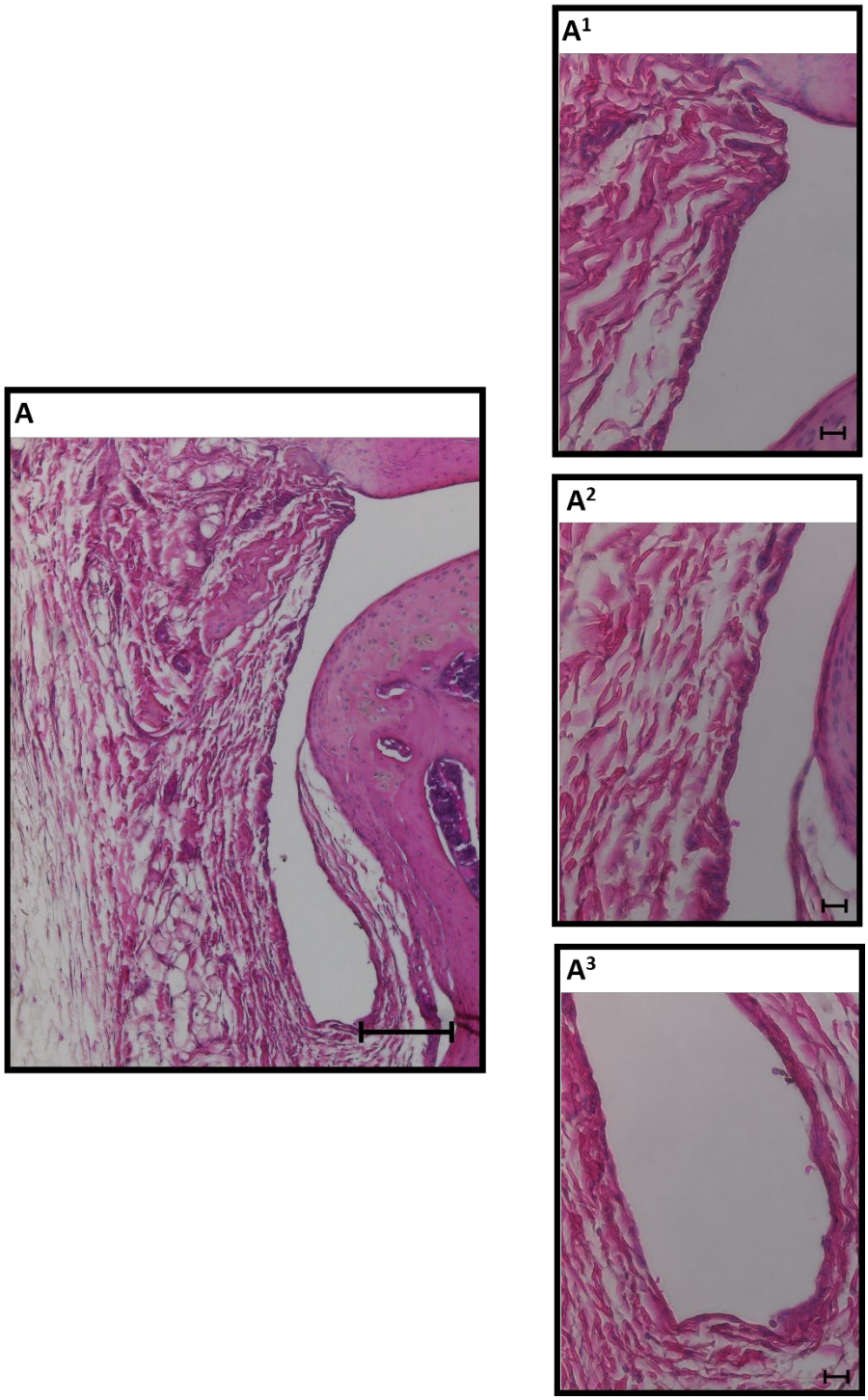

Figure 47: Representative healthy 2-month old H&E stained DHGP synovium. Panel A represents a 100x total magnification image with scale bar depicting 200 µm, while panels A^1, A^2, and A^3 represent 400x total magnification images with scale bar depicting 20 µm.

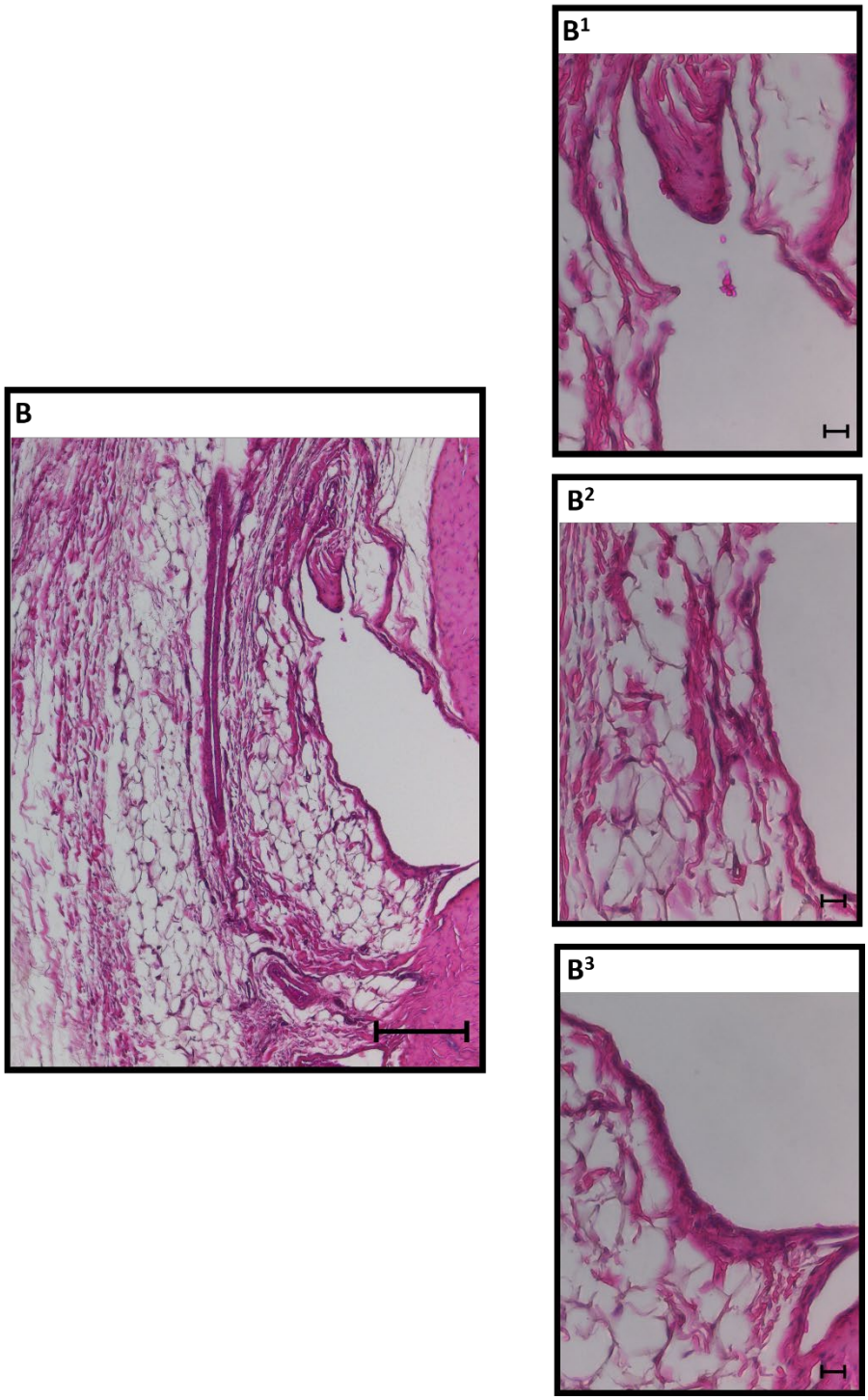

Figure 48: Representative healthy 2-month old H&E stained DHGP synovium. Panel B represents a 100x total magnification image with scale bar depicting 200 µm, while panels B^1, B^2, and B^3 represent 400x total magnification images with scale bar depicting 20 µm.

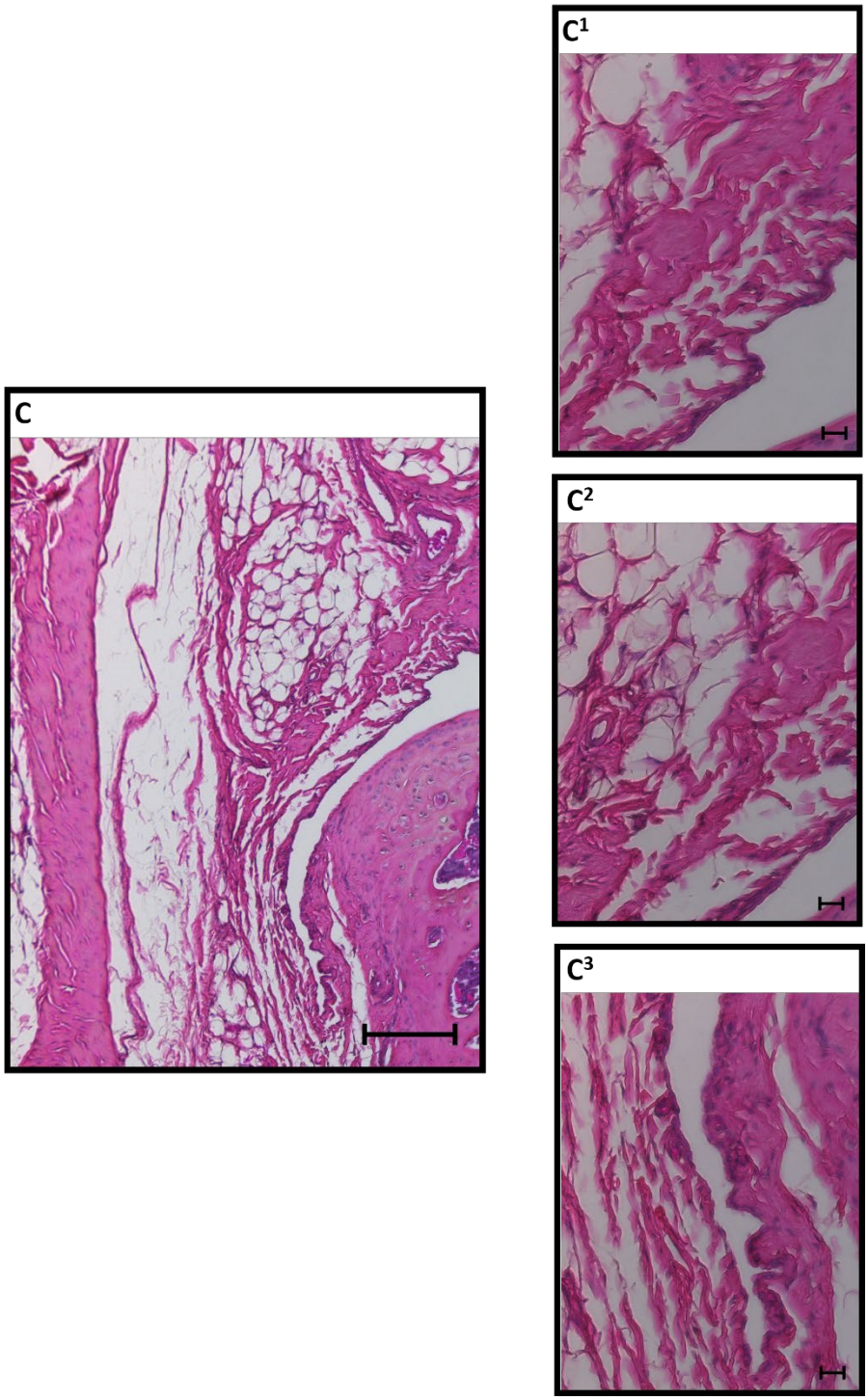

Figure 49: Representative healthy 2-month old H&E stained DHGP synovium. Panel C represents a 100x total magnification image with scale bar depicting 200 µm, while panels C^1, C^2, and C^3 represent 400x total magnification images with scale bar depicting 20 µm.

Semi-quantitative scores of the magnified images were averaged to obtain a total synovial hyperplasia grade for each 9-month old treatment and saline control, as well as the healthy 2-month old groups. It is observed from Figure 50 that the saline control contains the highest average histologic score (2.16) compared to all groups, while also exhibiting statistically higher average score than the healthy 2-month old group ($p=0.0004$). Comparing the hAMSC and hADSC treatments directly, hADSCs display a slightly higher average cellularity score compared to hAMSCs (1.91 versus 1.45), however with no statistical difference. Additionally, it is observed that hADSC treatments display a statistically higher average score compared to the healthy 2-month old group ($p=0.0068$). Furthermore, the healthy 2-month old synovium contained the lowest average score (0.888) compared to all knees, indicating normal cellularity layers at the membrane.

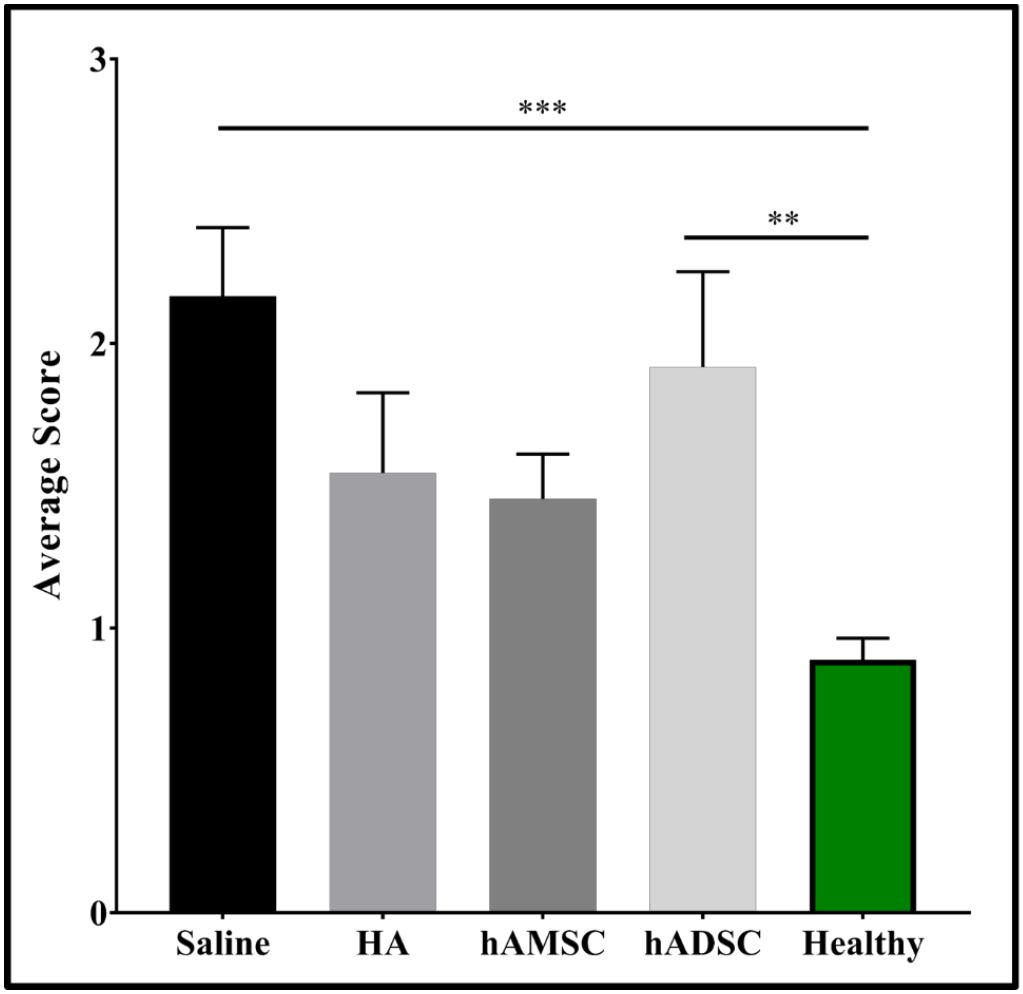

Figure 50: Average semi-quantitative cellularity scores of the DHGP synovium. Two stars represents statistical significance in which (p<0.01) and three stars represents (p<0.001).

2.3.4 Immunogenic Reaction Evaluation

In order to determine if the DHGPs had an adverse immune reaction to the transplantation of human cells, an ELISA was performed on DHGP serum to determine IgG concentration. As observed in Figure 51, DGHPs injected with the HA treatment contained the lowest levels of antigen concentration (4.85mg/mL), in which the hADSC treatment had slightly higher levels (6.14mg/mL) in comparison. The hAMSC treatment

demonstrated statistically higher (p=0.0244) concentrations compared to HA, ultimately displaying the highest level of antigen concentration (6.93mg/mL) across all groups.

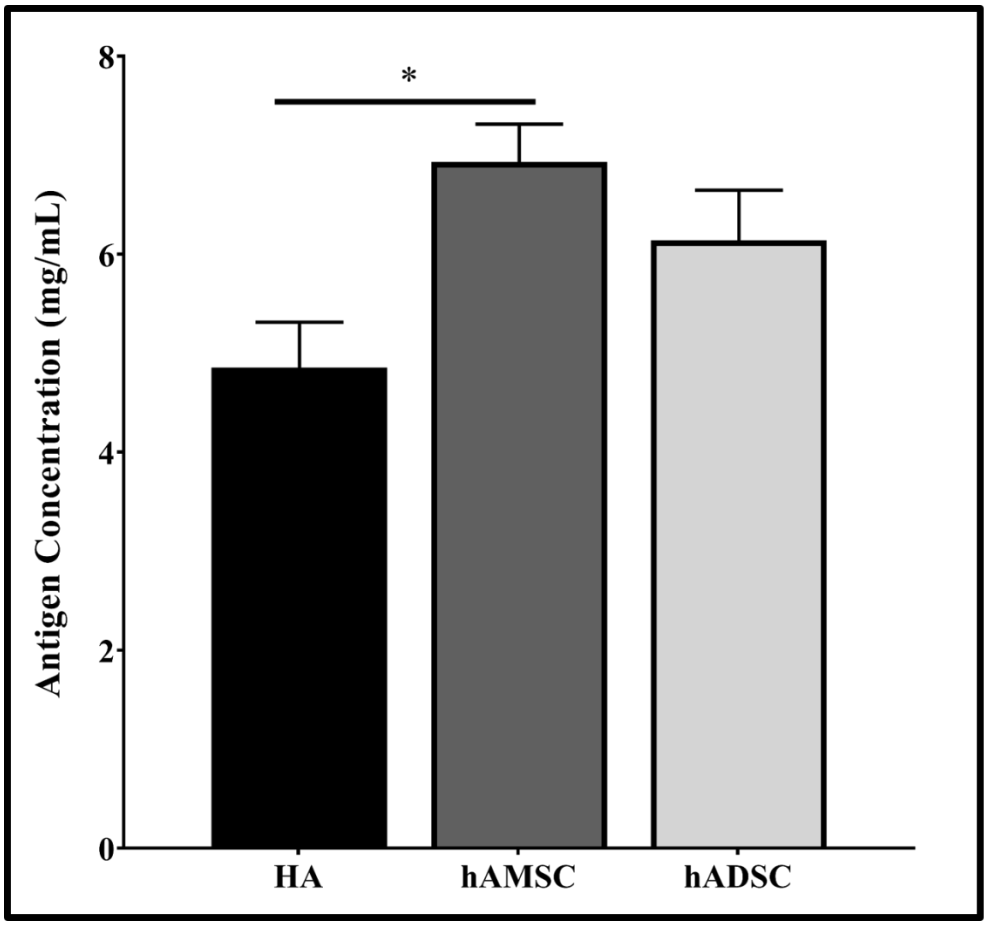

Figure 51: IgG antigen concentration analyzed from DHGP serum via ELISA. The star represents statistical significance (p<0.05).

2.4 Discussion

2.41. Glycosaminoglycan (GAG) Content Evaluation

In order to assess for articular cartilage matrix integrity, DMMB assay was performed in order to quantify GAG concentration from DHGP knee tibia plateaus and femoral condyles in the medial load-bearing region. Higher GAG concentration would demonstrate a more intact articular cartilage matrix as GAGs are covalently attached to

the protein core of proteoglycans, a major component of articular cartilage matrix. Evaluations were conducted on healthy 2-month old DHGP knees as well as 9-month old DHGP knees that were injected with hAMSCs, hADSCs, or HA-only treatments including the bilaterally injected saline control knees.

Results from the evaluation of the femoral condyles in the medial compartment demonstrated (Figure 12) that all treatment groups exhibited slightly higher GAG content in comparison to their paired saline controls, in which hADSC treatment exhibited the highest GAG concentration compared to all groups; however, no statistical differences were observed. This reveals that although the knees that were injected with treatment contained a less damaged articular cartilage matrix compared to knees that were not treated, it cannot be concluded that injected treatments provided a pro-regenerative effect on the articular cartilage matrix. Additionally, it cannot be concluded whether hAMSCs or hADSCs provide a more enhanced OA mitigation effect in comparison to one another. Therefore, a higher sample size is warranted for further investigations in which these trends may be further improved statistically. Alternatively, the healthy 2-month old knees demonstrated a statistically and almost four times higher GAG concentration in comparison to all 9-month old knees (except for the hADSC treated knee). This observation validates the DHGP as an appropriate spontaneous osteoarthritic model as the articular cartilage matrix severely loses GAG content with increasing age and thus increasing OA progression.

Similarly, results from the evaluation of the tibia plateaus in the medial compartment demonstrated (Figure 13) that all treatment groups, except for the hAMSC treatment, exhibited slightly higher GAG concentration in comparison to their corresponding saline controls in which hADSC treatment again exhibited the highest GAG concentration compared to all groups; however, no statistical differences were observed. This reveals that although the knees that were injected with HA and hADSC treatment contained a more intact articular cartilage matrix compared to knees that were not treated, it cannot be concluded that injected treatments provided a pro-regenerative influence on the articular cartilage matrix. Additionally, it cannot be concluded whether hAMSCs or hADSCs provide a more enhanced OA mitigation effect in comparison to one another. Again, a higher sample size is warranted for further investigations in which these trends may be further improved statistically. Alternatively, the healthy 2-month old knees demonstrated a statistically and over three times higher GAG concentration in comparison to all 9-month old knees. Again, this observation validates the DHGP as an appropriate spontaneous osteoarthritic model. Ultimately, the healthy 2-month old GAG content from both the femoral condyles and tibia plateaus serve as a baseline for further investigations into the incorporation of stem cell treatments for the regenerative potential of the articular cartilage.

2.4.2 Micro-CT 3D Morphometric Measurements and Osteophyte Formation

After all DHGP knees were successfully scanned and reconstructed, 3D morphometric measurements were obtained in the load-bearing region of the subchondral trabecular

bone for evaluation of bone volume density (BV/TV, %) and thickness (Tb.Th, mm), as well as the subchondral bone plate for evaluation of plate thickness (Th., mm) and porosity (%). Evaluations were conducted on healthy 2-month old DHGP knees as well as 9-month old DHGP knees that were injected with hAMSCs, hADSCs, or HA-only treatments including the bilaterally injected saline control knees. These measurements were chosen for analysis as they are the most commonly evaluated Micro-CT parameters for characterizing 3D bone structures, as well as they give the greatest insight into the morphologic changes occurring during OA pathogenesis, such as sclerosis. As described in section 1.2.4, the subchondral bone plate represents the cortical matrix lying directly below the calcified cartilage to support and protect it by transmitting loads of the joint to the underlying trabecular bone. The subchondral trabecular bone represents a cancellous and dynamic bone structure to adapt to mechanical forces acquired from the joint. Ultimately, the subchondral bone plate and trabecular bone work in conjunction as a shock-absorber to protect the overlying articular cartilage. With increasing OA pathogenesis, the articular cartilage matrix is damaged in which mechanical loads are then directly applied to the subchondral bone, ultimately leading to abnormal bone remodeling and subsequent thickening. This is also believed to be due to biomechanical adaptation to micro-damage as well as possible cyst formation in the subchondral bone.[5]

BV/TV represents the ratio of a given region of interest (ROI) total volume (TV) that is occupied by bone volume (BV), ultimately, indicating a bone volume to total bone volume ratio reported as a percentage value. Although there are varying results and

inferences on the subchondral bone morphologic changes, depending on the animal model utilized, as highlighted in section 1.3.2, it is intuitive to consider that with increasing OA severity, BV/TV values would increase, as more space is occupied by bone due to the ensuing thickening of the subchondral bone. This is further supported by Wang et al.'s investigation into subchondral bone changes in the DHGP via Micro-CT evaluation, in which it was found that as DHGPs aged, there was an increase in BV/TV.[117] In evaluating the subchondral trabecular bone volume density in the load-bearing medial compartment of the tibia (Figure 20**)**, it is observed that hAMSC and hADSC treatments exhibit slightly higher values compared to their corresponding saline controls, however with no statistical difference. Additionally, HA treatment exhibits almost equal values to its paired saline control, again with no statistical difference. These results demonstrate that it cannot be concluded that injected treatments provided a pro-regenerative effect in the joint in order for the underlying subchondral bone to undergo less bone remodeling and subsequent sclerosis, in comparison to controls. Additionally, it cannot be concluded whether hAMSCs or hADSCs provide a more enhanced OA mitigation effect in comparison to one another. Therefore, a higher sample size is warranted for further investigations. Although not statistically significant, the healthy 2-month old knees demonstrated a 1.5 times lower average BV/TV in comparison to all 9-month old DHGP control knees. Again, this validates the hypothesis that a progressive osteoarthritic condition would result in a higher BV/TV.

Trabecular thickness (Tb.Th) represents the average thickness (mm) of the trabeculae from a selected ROI. A key hallmark of OA is the thickening of the subchondral bone due to irregular bone remodeling, as described in section 1.3.2, in which a thicker subchondral trabecular thickness measurement would indicate a more osteoarthritic condition. In evaluating the subchondral trabecular bone thickness in the medial compartment of the tibia (Figure 21), it is observed that all treatment groups display a similar Tb.Th value in comparison to their paired saline controls, in which no statistical difference is present. Additionally, it is observed that hAMSC and hADSC treatment also contain almost equal Tb.Th values, indicating no statistical difference between them. These results demonstrate that it cannot be concluded that injected treatments provided a pro-regenerative effect in the joint in order for the underlying subchondral bone to undergo less bone remodeling and subsequent sclerosis, in comparison to controls. Additionally, it cannot be concluded whether hAMSCs or hADSCs provide a more enhanced OA mitigation effect in comparison to one another. Therefore, a higher sample size is warranted for further investigations. The healthy 2-month old DGHP knees evaluated for Tb.Th displayed a 1.6 times lower average trabecular thickness in comparison to 9-month old knees. Again, this validates the hypothesis that a progressive osteoarthritic condition would result in a higher Tb.Th.

Plate thickness (Th.) represents the average thickness of cortical bone from a selected ROI. It has been established that subchondral bone plate thickness increases in late-stage OA along with gradual non-calcified cartilage damage.[5] In evaluating the thickness of the

subchondral bone plate in the medial compartment of the tibia **(**Figure 22**)**, it is observed that all treatment groups display a similar thickness value in comparison to their paired saline controls, in which no statistical difference is present. Additionally, it is observed that hAMSC and hADSC treatments also contain almost equal thickness values, indicating no statistical difference between them. Similar to previous analyzed 3D morphometric parameters, these results indicate that it cannot be concluded that injected treatments provided mitigation of subchondral bone sclerosis. Alternatively, the healthy 2-month old DGHP knees evaluated for subchondral bone plate thickness displayed an overall lower average cortical thickness in comparison to 9-month old control knees. Again, this validates the hypothesis that a progressive osteoarthritic condition would result in increasing subchondral bone plate thickness.

Another consequence of irregular bone remodeling of the subchondral bone is the formation of osteophytes at the margins of the joint, which is commonly observed with progressive OA. Blinded observations of osteophyte formation in the medial compartment of the femur (Figure 25**)** indicate that the majority of osteophytes were present in the saline control DHGP knees compared to all treatment groups. Furthermore, hAMSC treated knees display a lower average percent of osteophytes compared to hADSC and HA treated knees; however, no statistical difference was indicated between all groups. Additionally, blinded observations of osteophyte formation in the medial compartment of the tibia (Figure 26) indicate that osteophytes were observed equally across all groups, except for the HA treated knees, which displayed slightly lower

average percent of osteophytes. From both femur and tibia results, it can be concluded that progressive OA does result in abnormal subchondral bone remodeling and subsequent osteophyte formation. Additionally, these results indicate that it cannot be concluded that injected treatments provided mitigation of subchondral bone osteophyte formation.

2.4.3 Histologically Evaluated Articular Cartilage Surface Integrity

Nine-month old DHGP knee joints were histologically stained with Safranin-O in order to semi-quantitatively evaluate for articular cartilage surface integrity. Scoring was performed based on OARSI recommended guidelines as outlined in **Table 2**. Normal and healthy articular cartilage is characterized as smooth with no surface abnormalities. With progressive OA pathology, deterioration of the cartilage surface is observed in which surface irregularities and fibrillations are visually distinct. These undulations range from mild surface irregularities to extending into the superficial, middle, and deep zones. Overall a higher score represents a more pathological condition.

Results from the evaluation of the articular cartilage of the tibia in the medial compartment demonstrated (Figure 29) that both hADSC and hAMSC treated knees contained an overall lower average score compared to their respective saline controls; however with no statistical difference. Additionally, on average, the saline un-treated knees depicted more than 3 fissures and loss of cartilage extending into the middle zone. This again validates that the DHGP spontaneously develops progressive OA with

increasing age and is an appropriate *in vivo* model. Furthermore, hADSCs and hAMSCs had comparable scores to each other, in which on average the treated knees displayed more than 3 fissures and loss of cartilage in the superficial and middle zones. This indicates that severe damage to the articular cartilage is present and therefore it cannot be concluded that injected treatments provided a pro-regenerative influence on the articular cartilage matrix. Although it cannot be concluded whether hAMSCs or hADSCs provide a more enhanced OA mitigation effect in comparison to one another, histological assessment is regarded as a "gold-standard" evaluation technique, and it is therefore promising to observe trends in which hADSC and hAMSC treatments are indicating overall lower histological scores in comparison to non-treated knees. Therefore, a higher sample size is warranted for further investigations in which these trends may be further improved statistically.

Results from the evaluation of the articular cartilage of the femur in the medial compartment demonstrated (Figure 30) that all groups had comparable low histologic scores, in which no statistical differences were observed. Additionally, all scores on average displayed only mild surface irregularities which further confirms that progressive OA pathogenesis occurs in the load-bearing region of the tibia, in which the femur is only marginally affected in comparison.[118] Furthermore, appropriate evaluation of treatments and their effects in mitigation of OA, should be conducted in the medial compartment of the tibia.

2.4.4 Histologically Evaluated Proteoglycan Content

In order to semi-quantitatively evaluate for proteoglycan content, 9-month old DHGP knee joints were histologically stained with Toluidine Blue in which scoring was performed based on OARSI recommended guidelines as outlined in **Table** 3. In healthy cartilage, proteoglycan content is intensely stained blue and visualized uniformly throughout the cartilage matrix; however, with increasing OA pathology, decreased staining is visualized. This decreased staining can range from mild reduction in the superficial zone to extreme loss of staining into the middle and deep zones. Overall a higher score represents a more pathological condition.

Results from the evaluation of proteoglycan content of the tibia in the medial compartment demonstrated (Figure 33) that all treatment groups displayed an average lower histologic score in comparison to their respective saline controls. Furthermore, hADSC treated knees, specifically, depicted an overall lower average score compared to all groups and a statistically lower score than its corresponding saline control. On average, the saline un-treated knees portrayed decreased proteoglycan content in all 3 zones for at least half of the length of the plateau. This again validates that the DHGP is an appropriate spontaneous OA model with observable and progressive pathogenesis with increasing age. Contrastingly, on average all treatment groups displayed decreased proteoglycan content in only the superficial zone of the plateau and not the middle and deep zones, indicating a potential mitigation of deterioration of the cartilage matrix. In comparing hADSC and hAMSC treatments directly, hADSCs depicted a slightly lower

average score, however with no statistical difference. Overall, a higher sample size is warranted for further investigations in which these trends may be further improved statistically.

Results from proteoglycan content assessment of the femur in the medial compartment demonstrated (Figure 34) that all treatment groups had lower histologic scores in comparison to respective saline controls; however, no statistical differences were observed. The hADSC and hAMSC treatment groups displayed comparable scores in which it cannot be concluded whether hAMSCs or hADSCs provide a more enhanced OA mitigation effect in comparison to one another. Overall, a higher sample size is warranted for further investigations in which these trends may be further improved statistically.

2.4.5 Histologically Evaluated Synovial Hyperplasia

Semi-quantitative evaluation of 9-month old and healthy 2-month old DHGP synovium was performed via Hematoxylin and Eosin staining to determine synovial inflammation. Normal synovium comprises of one to two layers of fibroblast-like synoviocytes and resident macrophages visualized at the synovial lining. With increasing OA pathogenesis, cell number significantly increases at the lining, depicting multiple layers, as well as increased macrophage and lymphocyte infiltration. Inflammation of the microvilli is also observed in which cell clusters form bud-like aggregates at the synovial lining. Scoring

was performed based on OARSI recommended guidelines as outlined in **Table 4**, in which overall a higher score represents a more pathological condition.

Results from the histological evaluation of synovial hyperplasia demonstrated (Figure 50) that the 9-month old saline control groups contained the overall highest average score in comparison to all 9-month old treatment groups. On average, saline groups displayed slight increase in number of cellular layers (4-6) and scores were statistically higher than average healthy 2-month old scores. Additionally, comparing the 9-month old hADSC and hAMSC treatment groups, hAMSCs displayed a slightly lower score, in which normal cell layers were observed on average; however, no statistical difference was assessed. Therefore, it cannot be concluded whether hAMSCs or hADSCs provide a more enhanced OA mitigation effect in comparison to one another. Ultimately, a higher sample size is warranted for further investigations in which these trends may be further improved statistically. Alternatively, the healthy 2-month old knees demonstrated a statistically and more than two times lower score in comparison to 9-month old knees saline control knees. This observation again validates the DHGP as an appropriate spontaneous osteoarthritic model as the healthy 2-month old DHGPs displayed normal cell layers at the synovial lining with no synovial hyperplasia observed compared to the 9-month old DHGPs. Further evaluations into potential macrophage infiltration is depicted in Appendix Figures A.10-A.12 in which IHC was performed on the synovium targeted for guinea pig macrophages. No macrophages were detected in the synovial membrane,

however samples were limited due to histological evaluation and further investigations are warranted with higher sample size.

2.4.6 Immunogenic Evaluation

As human stem cells were injected into the DHGPs, evaluation for a potential adverse immunogenic reaction was performed on the blood of the DHGPs via an ELISA targeted for IgG antigen concentration. IgG antibodies represent the most abundant type of antibody in circulating blood in humans, protecting against invading pathogens due to bacterial and viral infections.[119] IgG protection involves a variety of mechanisms including complement system activation and direct binding to pathogens for immobilization and opsonization of phagocytic immune cells, such as macrophages. Elevated levels of IgG antigen concentrations observed via ELISA would indicate an increased immunogenic reaction as this signifies increased binding to IgG antibodies. IgG antigen concentration observed in DGHP serum (Figure 51**)** indicates that the HA-injected DHGPs blood illustrated the lowest IgG concentration compared to injected human stem cells. This was expected as HA should not illicit an immune reaction, as it is already naturally present physiologically, as a synovial fluid and glycosaminoglycan constituent, and IgG levels detected would signify a normal circulating concentration. The hADSC-injected DGHPs revealed a slightly higher IgG antigen concentration in comparison to the HA-injected DHGPs, however with no statistical difference. This reveals that hADSCs did not impose an adverse immunogenic reaction to the DHGPs. The hAMSC-injected DHGPs revealed the highest IgG antigen concentration in

comparison to both HA and hADSC-injected DHGPs. This indicates that hAMSCs initiated a more immunogenic response compared to the hADSCs. This could potentially result in higher levels of circulating and migrating immune cells, such as macrophages. Lastly, it should be noted that qualitatively, all DHGPs did not display or indicate any form of infection or adverse reaction following injections. All DHGPs remained healthy throughout the six-month course of the study and injections.

2.4.7 Summary

In combination with biochemical, histological, and imaging modalities, it cannot be concluded that injected stem cell treatments provided either a pro-regenerative effect or mitigation of OA *in vivo.* Although histological evaluations of articular cartilage matrix indicated that injected hAMSC and hADSC treatments exhibited a more significant effect compared to other outcome measures, further investigations with higher sample size is warranted in order to more effectively observe statistical trends. The second objective of this study, as detailed below, aims to provide a deeper insight as to why the injected stem cell treatments were not as effective *in vivo* and how these injected treatments could potentially be improved for greater therapeutic efficacy.

CHAPTER THREE:

AIM 2

3.1 Introduction and Purpose

Stem cell-based regenerative medicine aims to target the underlying causes of disease to replace damaged/diseased cells and promote regeneration of tissues in the body given their established effector functions. Developments in novel treatment options utilizing stem cell therapy can provide therapeutic solutions for patients with debilitating diseases, especially to those with conditions that are beyond repair with current treatment options. Although research in stem-cell regenerative strategies is rapidly growing, there are still multiple challenges that are presented, such as cell retention, viability, distribution, and functional integration within the local environment into which they are administered. Therefore, further investigations into these challenges are necessary to provide for a more comprehensive understanding to improve targeted delivery and therapeutic efficacy of stem cells. Moreover, the objective of this aim was to evaluate and compare the migration and retention of human amniotic stem cells (hAMSCs) and human adipose stem cells (hADSCs) within the knee joint of the Dunkin Hartley Guinea Pig upon intra-articular injection. Gaining a further understanding of potential differences in site-specific retention could help explain potential differences in MSC therapeutic efficacy.

To longitudinally track injected stem cells *in vivo*, the IVIS Spectrum Imaging System was utilized in which epi-illumination, at specific excitation and emission wavelengths, allowed for visualization of fluorescently-labeled hAMSCs and hADSCs. Upon

completion of *in vivo* imaging, immunohistochemistry (IHC), targeting human mitochondria, was performed on the lungs and knees of the DHGPs to detect the potential presence of the stem cells. The lungs were chosen for evaluation as they are a primary targeted organ in which systemic migration of stem cells is commonly observed.[120–122] The knees were also assessed in order to observe if the stem cells were still residing in the joint.

Evaluating the *in vivo* tracking and of stem cells and subsequent outcome measures performed herein will provide an enhanced understanding into the bio-distribution and retention of two stem cell sources. This will ultimately offer insight into novel strategies to improve and enrich cell retention in the desired area of the body.

3.2 Methods and Materials

Human adipose-derived stem cells (hADSCs) were obtained from Invitrogen (R778810). Human amniotic-derived stem cells (hAMSCs) were harvested and isolated from human placentas from consenting patients immediately following child birth (Greenville Heath System). All cell counts were performed with the TC20 Bio-Rad Automated Cell Counter with use of Trypan Blue purchased from Lonza (17-92E). Cell culture media for hAMSCs included Dulbecco's Modified Eagle's Medium (DMEM) purchased from Corning (10-D14-CM) with Fetal Bovine Serum (S1150H) purchased from Atlanta Biologicals and Antibiotic Antimycotic (300040CI) purchased from Corning. Cell culture media for hADSCs included MesenPro Basal Medium with growth supplement (12747-

010) purchased from Gibco. Trypsin was purchased from Corning (25053CI). Two month old Dunkin Hartley Guinea Pig cohorts were obtained from Charles River Laboratories conferring to Clemson University's Institutional Animal Care and Use Committee (IACUC) amendment approval (protocol number 2016-040). Sodium Hyaluronate was purchased from LifeCore Biomedical (HA700K-1) and Xenolight DiR Fluorescent Dye was purchased from Perkin Elmer (125964) in which both were sterile filtered with an Acrodisc 25mm Syringe Filter (4612) containing a 0.2µm filter membrane purchased from Pacc. Dulbecco's Phosphate Buffered Saline (PBS) was purchased form Corning (55-031-PC). All fluorescent imaging was performed with Perkin Elmer's IVIS Spectrum Imaging System. Formalin fixation of tissues was performed with 10% Phosphate Buffered Formalin purchased from Newcomer Supply (1090N). Bone decalcification was performed with Formic Acid purchased from Stat Lab (1414-1), in which Ammonium Hydroxide purchased from VWR (1336-21-6) and Ammonium Oxalate purchased from Poly Scientific (S2337-160Z) was used for confirmation of decalcification. Tissue Trek Automated Tissue Processor was used for all tissue processing. Leica RM 2155 Microtome was used for all tissue sectioning. Immunohistochemistry (IHC) evaluation utilized a Mouse Anti-Human Mitochondria primary antibody purchased from Abcam (ab79479). Secondary Anti-Mouse IgG antibody was purchased with Vecastain Elite ABC Kit from Vector Laboratories (PK-6100). DAB Peroxidase Substrate Kit (SK-4100) and Avidin Biotin Blocking Kit (SP-2001) was also purchased from Vector Laboratories. Background Buster Blocking Agent was purchased from Innovex Biosciences (NB306). Citric Acid Monohydrate (A104-

500), Sodium Azide (S2271-25), Bovine Serum Albumin (BP9703-100), and Hematoxylin (7211) were purchased from Fisher Scientific. TritonX-100 was purchased form Alfa Aesar (A16046). 3% Hydrogen Peroxide was purchased from Publix. All histological images were captured on a Zeiss Axiovert.A1 microscope in conjunction with Axiovision Software.

3.2.1 Stem Cell Fluorescent Tagging

Three T-175 flasks containing hADSCs (Passage 2) were washed twice with 10mL sterile PBS. After, 4mL of Trypsin was then added and the flask was incubated for 3 minutes at 37°C in order to detach cells from the flasks. Cells were viewed under the microscope to ensure rounded and floating cells. Following, 8mL of sterile cell culture media was added in order to inhibit the Trypsin, and the suspended cells were placed into a 15mL conical tube. The tubes were then centrifuged for 5 minutes at 1000xG, the supernatant was removed, and the cells were re-suspended in 2mL of fresh cell culture media. Cells were then counted with an automated cell counter to determine cell number ($3.10x10^6$ cells/mL) and viability (97%). The conical tubes containing the cells were then centrifuged again for 5 minutes at 1000xG in which they were then re-suspended in 2mL of sterile 10µM XenoLight DiR fluorescent dye. The cells were incubated with the dye for 20 minutes in 37°C and were re-suspended every 5 minutes. After, the tagged cells were washed twice and re-suspended with 5mL of PBS. Tagged cells were counted via an automated cell counter in order to determine cell number ($2.39x10^6$ cells/mL) and viability (95%). This same procedure was repeated for hAMSCs (Passage 1) in which

before fluorescent tagging, cell number was at $3.12x10^6$ cells/mL with viability of 97%. After tagging the cells with the XenoLight DiR fluorescent dye, cell number was at $1.90x10^6$ cells/mL with viability at 91%.

XenoLight DiR is a lipophilic dye that works to tag to the cytoplasmic membrane of stem cells for non-invasive *in vivo* imaging, resulting in precise and stable cell staining with negligible dye transfer between cells. XenoLight DiR fluorescent dye was chosen for its compatible and recommended use with the IVIS Spectrum Imaging System by Perkin Elmer, as well as containing a near infrared (NIR) fluorescence which makes it ideal for *in vivo* imaging due to significantly reduced auto fluorescence from the animal. Upon fluorescent tagging of hADSCs and hAMSCs, it was observed that both cell lines retained high cell number and viability, indicating the dye was not damaging to the cells.

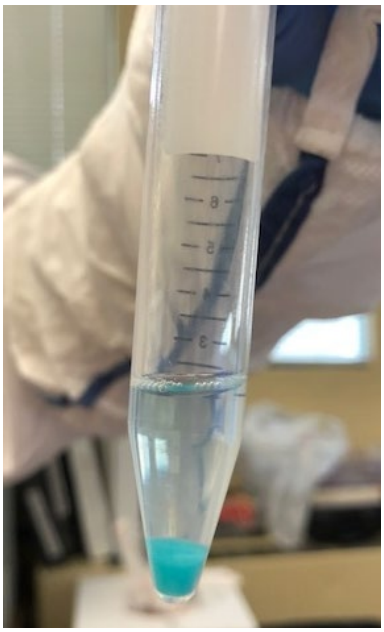

Figure 52: XenoLight DiR fluorescently labeled hADSC pellet.

3.2.2 IVIS Spectrum Fluorescent Thresholding

Once both hADSCs and hAMSCs were tagged with the XenoLight DiR Fluorescent dye, serial dilutions of the cells were made to determine optimal imaging settings and *in vitro* threshold for the IVIS Spectrum Imaging System. Dilutions of 10^6, $5x10^5$, 10^5, 10^4, and 0 cells were suspended in a 100µL sterile 0.5% hyaluronic acid (HA) and PBS solution in 1.5mL Eppendorf tubes. Once the IVIS was initialized, the tubes containing the tagged cells were immediately imaged via epi-fluorescence in which the ideal imaging settings included: an exposure time of 1.00 seconds, medium binning, an F/Stop of 1, an excitation filter of 710nm, and an emission filter at ICG. These settings were used for all *in vivo* imaging of the DHGPs.

3.2.3 Tagged Stem Cell Injections

Fluorescent tagging of hADSCs (Passage 2) and hAMSCs (Passage 2) with XenoLight DiR dye followed the same procedure described in 3.2.1. Cell number of hADSCs after fluorescent tagging was $1.86x10^6$ cells/mL at 97% viability, while hAMSC cell number after tagging was $2.87x10^5$ cells/mL at 96% viability.

Approximately 480,000 tagged hADSCs and hAMSCs were suspended in separate tubes of 100µL sterile 0.5% hyaluronic acid (HA). Immediate intra-articular injection of tagged stem cells into the left knee stifles of two month old DHGPs was performed via an insulin syringe needle in which three DHGPs received hADSCs while three other DGHPs

received hAMSCs. Right knee stifles of all DHGPs received a 100µL injection of HA as a control. Figure 53 below displays a schematic of the injection methods performed. Before injections were performed, all knees were shaved in order to reduce autofluorescence. Additionally, all injection methods were approved from an Animal Care and Use Protocol (2016-040) by Clemson University in conjunction with an approved Amendment by IACUC.

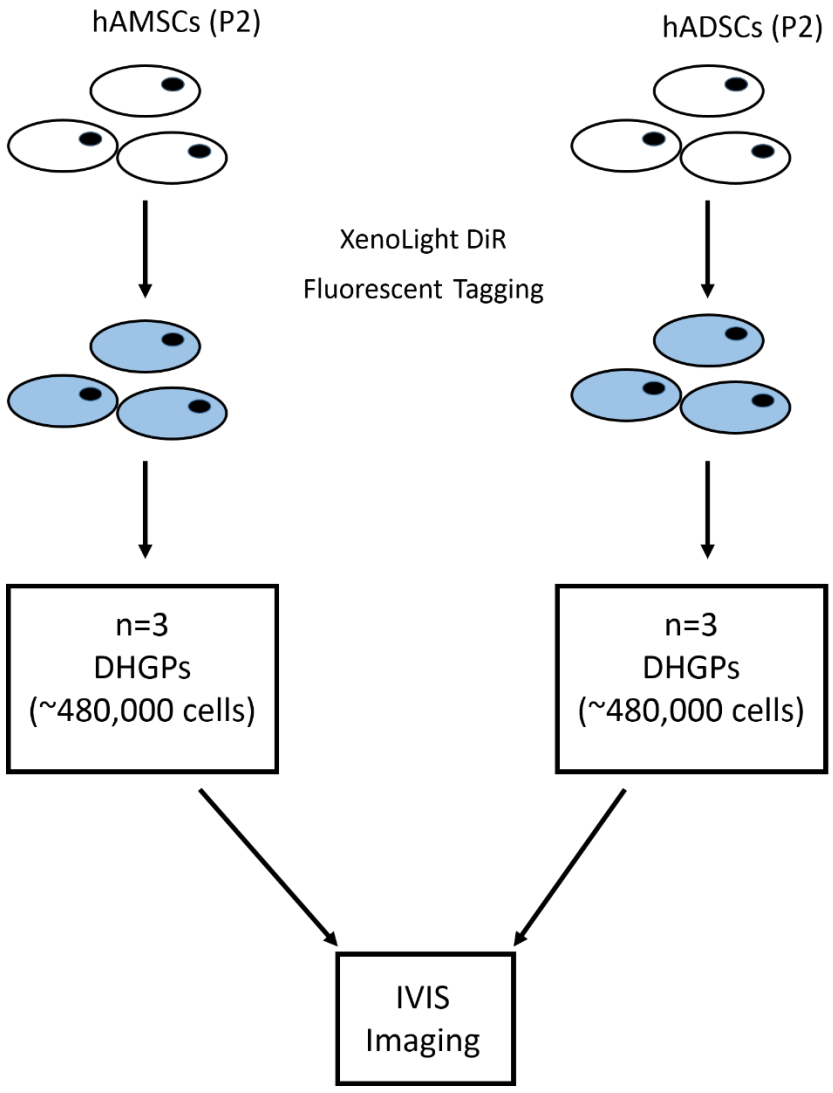

Figure 53: Experimental design schematic of tagged stem cell injections performed.

3.2.4 IVIS Spectrum Imaging

Upon injection of tagged hADSCs and hAMSCs, all guinea pigs were immediately imaged (Day 0) with the IVIS Spectrum Imaging System, in which all remained under anesthesia via isoflurane during imaging. Optimal IVIS filter settings were adjusted as described in section 3.2.2. DHGPs were then imaged on Day 3, 6, 10, 13, 16, and 21. Radiant efficiency scales per image depicts the fractional ratio of emitted photons per incident excitation photon. A region of interest (ROI) was drawn around the fluorescent area via the IVIS Spectrum Software in order to obtain average radiant efficiency for each image.

3.2.5 Dunkin Hartley Guinea Pig Harvest

Following IVIS Spectrum imaging on Day 21, DHGPs were immediately euthanized. Knee joints were exposed and dissected in which all treatment knees (n=6) were placed in formalin for sample fixation in preparation for immunohistochemistry (IHC). Half of the control knees (n=3) were immediately snap frozen in liquid nitrogen and stored at -80°C until ready for biochemical analysis, while the other half (n=3) were placed in 10% formalin for Micro-CT evaluation. Additionally, the lungs (n=6) and spleen (n=6) were harvested and placed in formalin for sample fixation in preparation for IHC.

Following fixation, treatment knee samples were decalcified for 2 weeks in formic acid, with solution changes occurring every 3 days. Following complete decalcification, knee

joints were processed for 36 hours and immediately embedded in paraffin. All knee samples were sectioned at 8µm and subsequently baked overnight in an oven at 55°C to ensure adherence to the histology slide. Ensuing fixation of the lungs, they were processed for 8 hours prior to paraffin embedment, sectioned at 5µm, and subsequently baked overnight in an oven at 55°C. Additional processing of spleen samples in preparation for IHC was described in section 2.2.7.

3.2.6 Immunohistochemistry (IHC)

Immunohistochemistry (IHC) on paraffin embedded Dunkin Hartley Guinea Pig (DHGP) lungs (n=6) and knee sections (n=6), as well as human cartilage (n=4), was performed for detection of human mitochondria. Human cartilage (positive control) and DHGP lung samples were sectioned at 5µm, while knee samples were sectioned at 8µm, and baked overnight in an oven at 55°C. All tissue types underwent the same IHC procedure described in section 2.2.7; however, a Mouse Anti-Human Mitochondria primary antibody, diluted 1:100 in 1% BSA and 0.01% Azide in PBS, was utilized. Again, negative samples did not receive a primary antibody.

3.2.7 Micro-Computed Tomography (Micro-CT)

Micro-CT imaging of healthy two-month old DHGP knee samples (n=3) was performed according to the procedure described in section 2.2.4.

3.2.8 Dimethyl-Methylene Blue (DMMB) Assay

DMMB assay on healthy two-month old DHGP knee samples (n=3) was performed according to the procedure described in section 2.2.3.

3.3 Results

3.3.1 Stem Cell Fluorescent Tagging and IVIS In Vitro Thresholding

Cell viability was determined before and after tagging the hAMSCs and hADSCs with the XenoLight DiR fluorescent dye. As depicted in Figure 54, cell viability did not statistically decrease after tagging the cells with the dye. Before tagging, hAMSCs displayed a cell viability of 97% and after tagging displayed a 93.5% cell viability. Additionally, before tagging hADSCs, cell viability was 97.5%, while cell viability after tagging 96%.

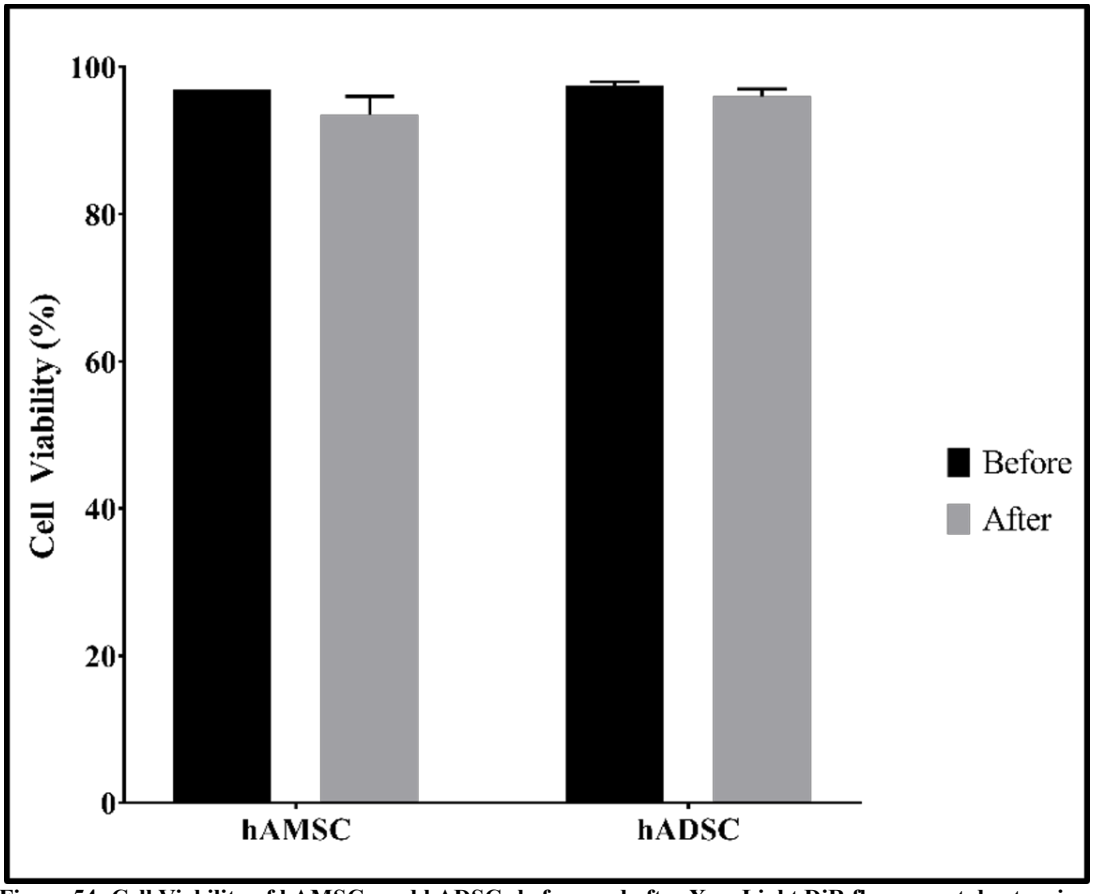

Figure 54: Cell Viability of hAMSCs and hADSCs before and after XenoLight DiR fluorescent dye tagging.

IVIS Spectrum filter thresholding was performed *in vitro* for both fluorescently tagged hAMSCs and hADSCs before injection and *in vivo* imaging of the DHGPs. Serial dilutions of the cells were made in order to obtain correct filter settings and gain a radiant efficiency threshold, in which it is observed in Figure 55 that at 10^4 cells, hAMSCs are no longer detected. This is consistent with the tagged hADSCs, in which Figure 56 depicts that at 10^4 cells, hADSCs are no longer detected. In both thresholds, it can be visualized that the PBS/HA suspension (containing no cells) does not display radiant efficiency detection, while the 10^6 cell suspension contains the highest level of radiant efficiency detection, qualitatively visualized via the radiant efficiency scale.

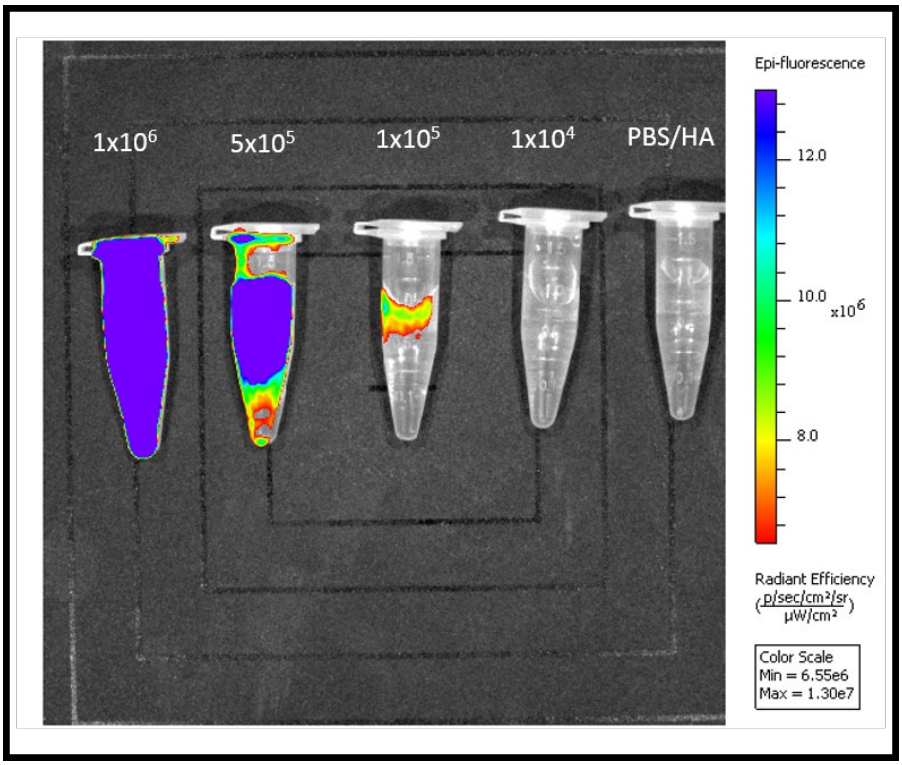

Figure 55: Representative IVIS Spectrum filter thresholding of hAMSC serial dilutions of 10^6, $5x10^5$, 10^5, 10^4, and 0 cells.

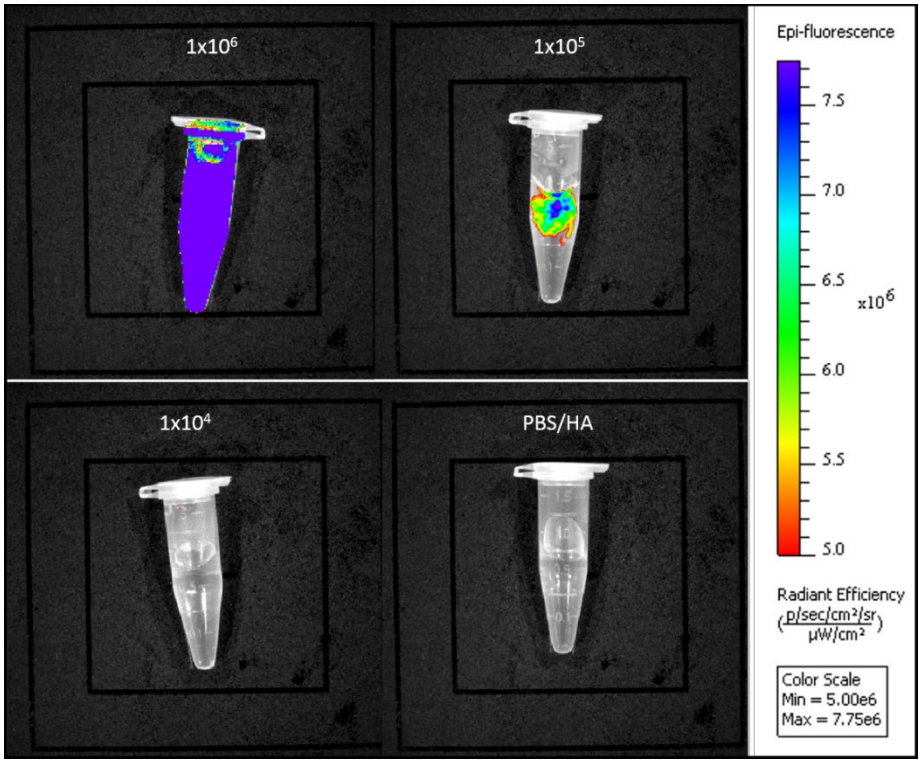

Figure 56: Representative IVIS Spectrum filter thresholding of hADSC serial dilutions of 10^6, 10^5, 10^4, and 0 cells.

3.3.2 Longitudinal Imaging of Fluorescently Tagged Stem Cells

Figure 57 and Figure 58 depict the longitudinal imaging of the DHGPs injected with tagged hAMSCs (~480,000 cells). Panel A represents Day 0, in which imaging was immediately performed following injection. Panel B represents Day 3, panel C represents Day 6, panel D represents Day 10, panel E represents Day 13, and panel F represents Day 16. Qualitatively, a steady and consistent decrease in radiant efficiency over time can be visualized, in which by Day 16, there is no fluorescent detection. This trend is observed in both representative DHGPs injected with hAMSCs.

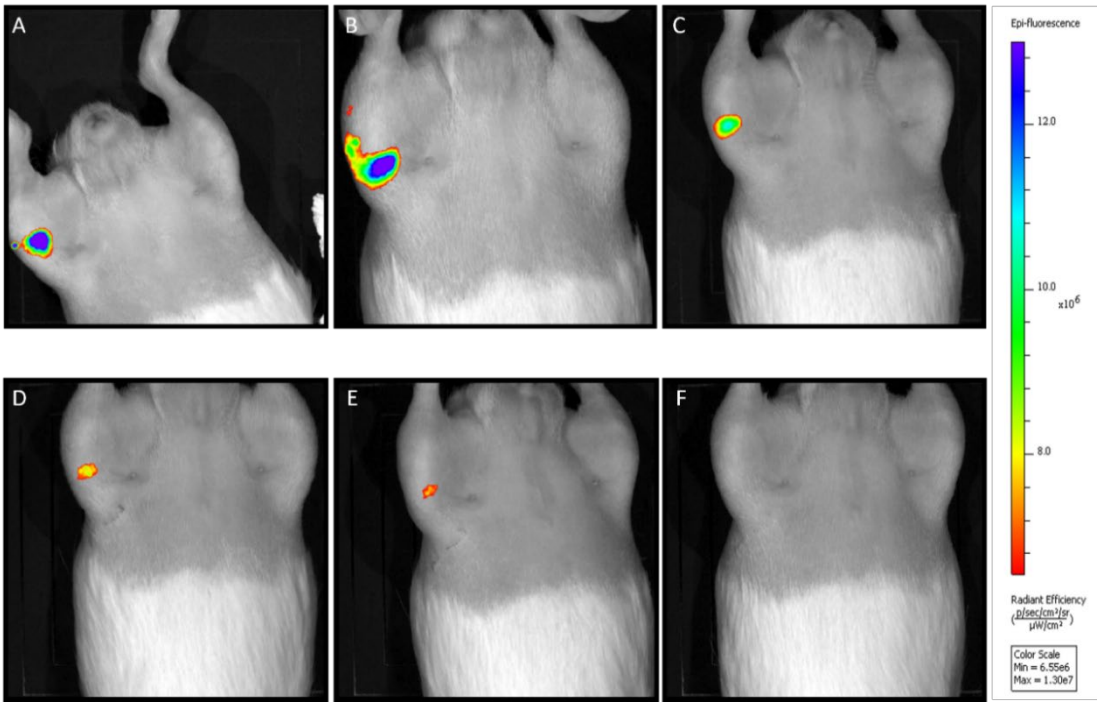

Figure 57: Longitudinal IVIS Spectrum imaging of a DHGP (animal 1) injected with tagged hAMSCs.

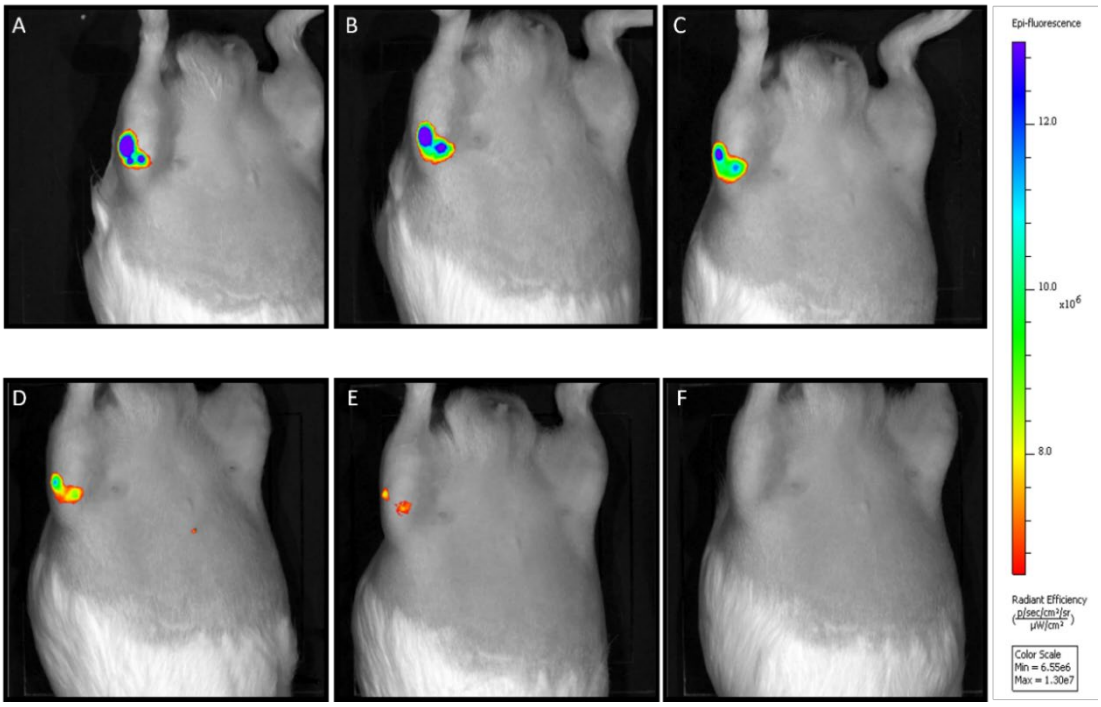

Figure 58: Longitudinal IVIS Spectrum imaging of a DHGP (animal 5) injected with tagged hAMSCs.

Figure 59 displays longitudinal imaging of the DHGPs tagged with hAMSCs in order to qualitatively visualize the decreased progression of fluorescence over time. Rows A and B differentiate between two different DHGP animals.

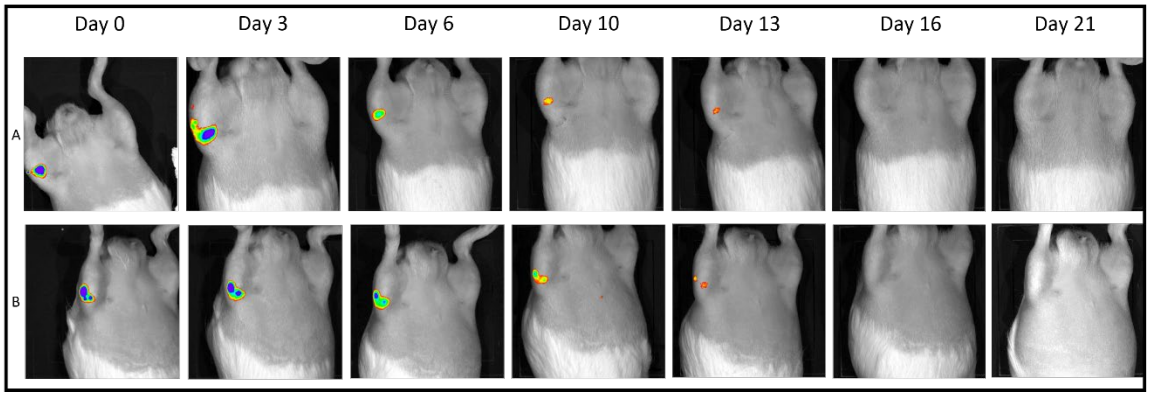

Figure 59: Longitudinal IVIS Spectrum imaging of two DHGP (row A is animal 1 and row B is animal 5) injected with tagged hAMSCs.

Figure 60 and Figure 61 depict the longitudinal imaging of the DHGPs upon injection of tagged hADSCs (~480,000 cells). Panel A represents Day 0, in which imaging was immediately performed following injection. Panel B represents Day 3, panel C represents Day 6, panel D represents Day 10, panel E represents Day 13, panel F represents Day 16, and panel G represents Day 21. Similar to the hAMSC injected DHGPs, a steady and consistent decrease in radiant efficiency over time can be visualized qualitatively. However, conversely to the hAMSC injected DHGPs, by Day 16 there is still fluorescent detection. This trend is observed in both representative DHGPs injected with hADSCs, in which by day 21 there is no fluorescent detection in the knee joint. It should be noted that the panels D, E, and G in Figure 60 and the panels D, F, and G in Figure 61, contain auto-fluorescence present in the stomach of the DGHP and is not considered fluorescence from the cells.

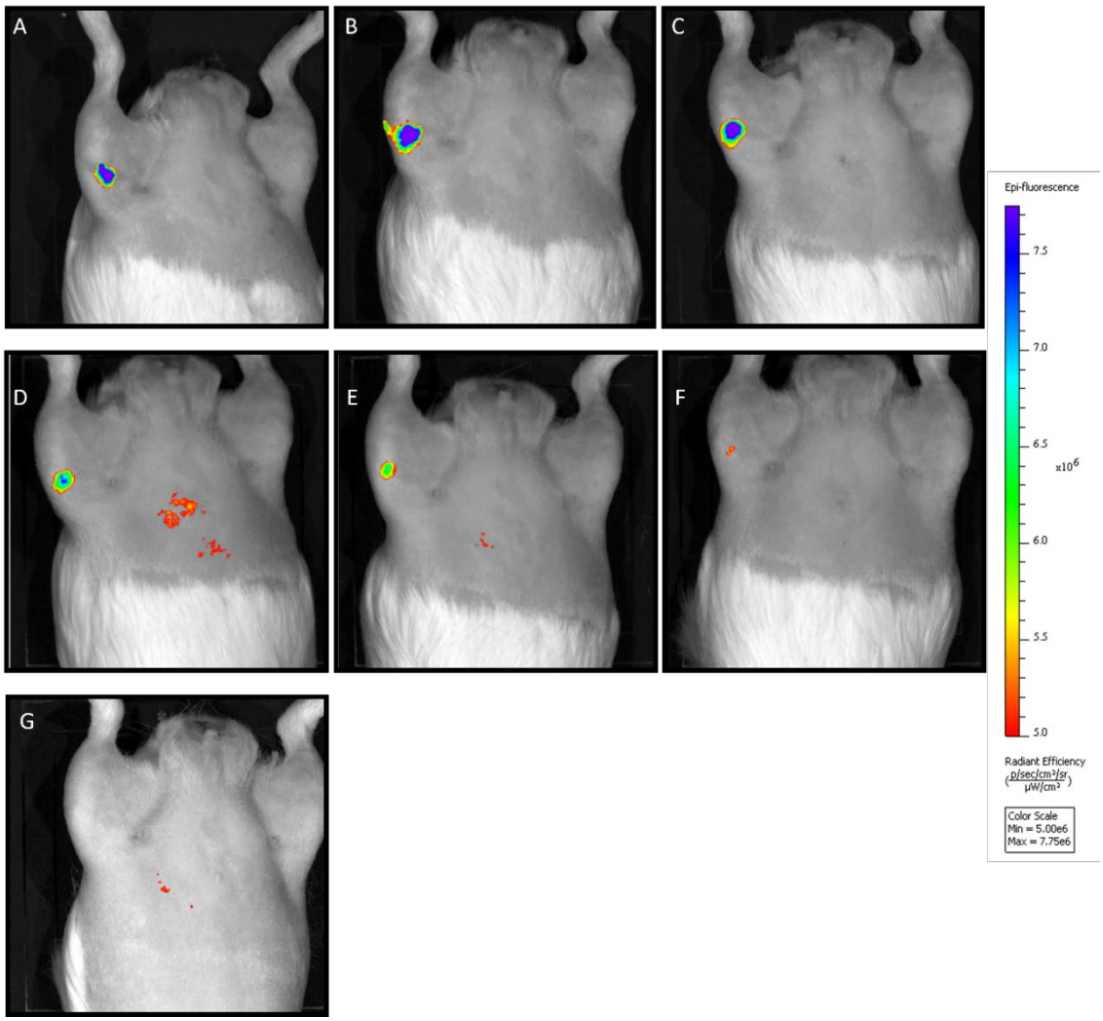

Figure 60: Longitudinal IVIS Spectrum imaging of a DHGP (animal 2) injected with tagged hADSCs.

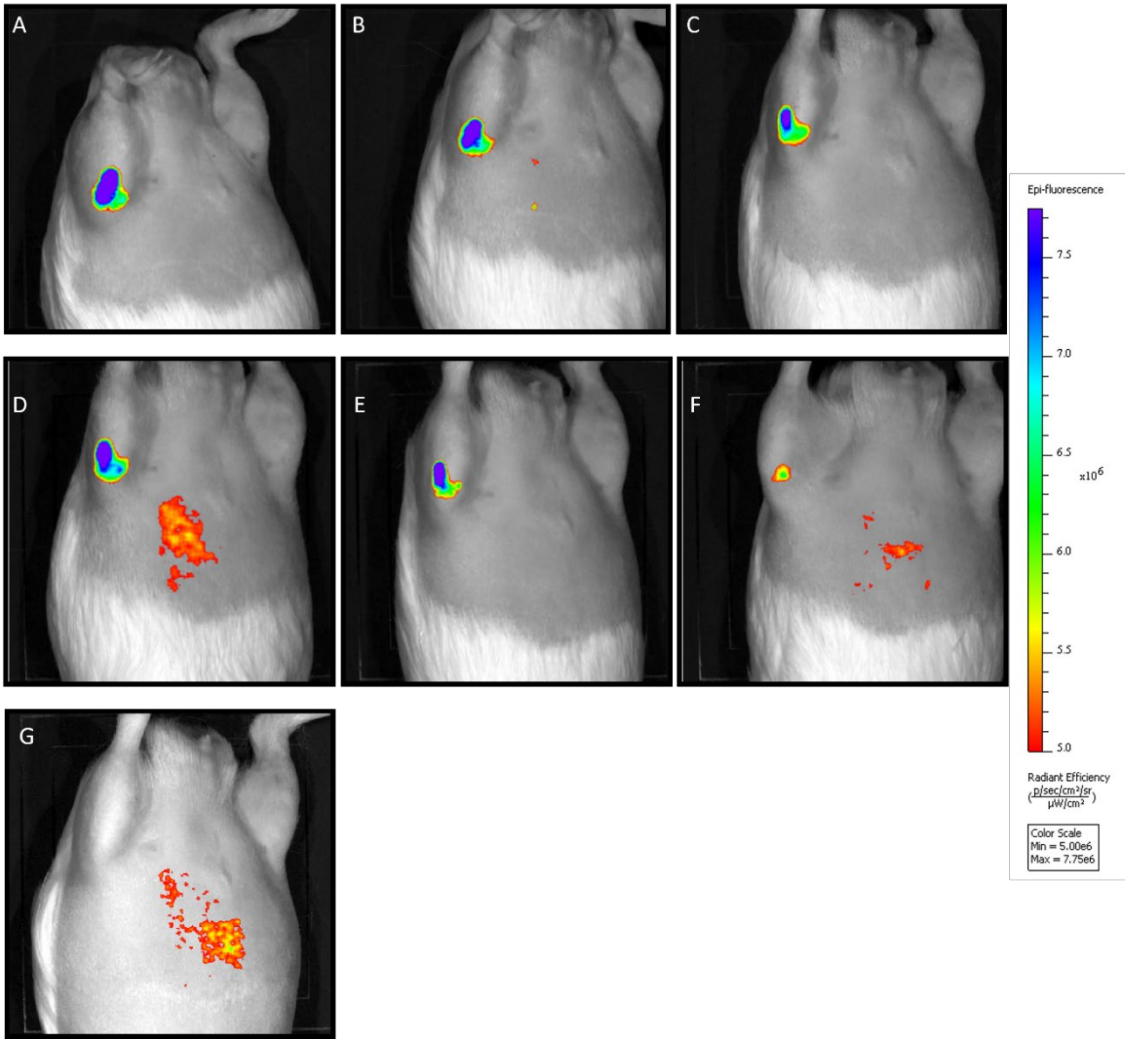

Figure 61: Longitudinal IVIS Spectrum imaging of a DHGP (animal 6) injected with tagged hADSCs.

Figure 62 displays longitudinal imaging of the DHGPs tagged with hADSCs in order to qualitatively visualize the decreased progression of fluorescence over time. Rows A and B differentiate between two different DHGP animals.

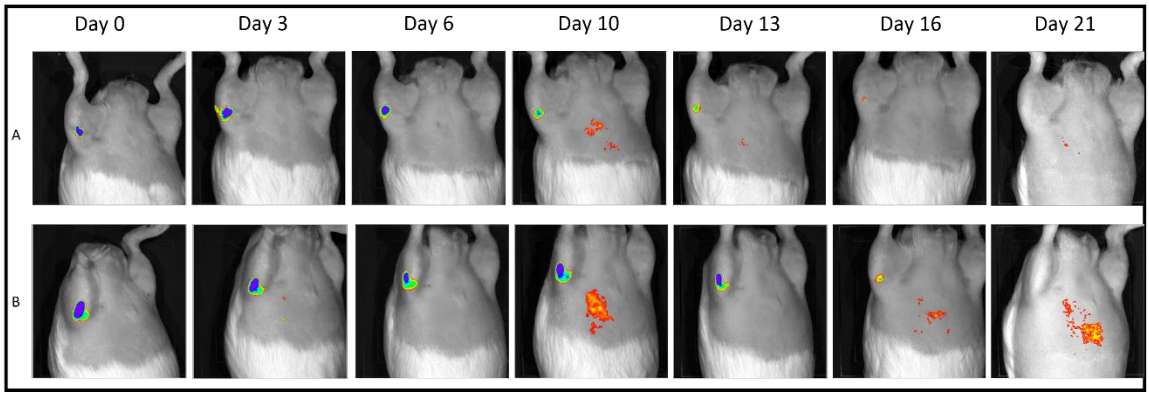

Figure 62: Longitudinal IVIS Spectrum imaging of two DHGP (row A is animal 2 and row B is animal 4) injected with tagged hADSCs.

Following imaging, a region of interest (ROI) was automatically drawn around the detected fluorescence via the IVIS Imaging Spectrum Software in order to obtain average radiant efficiency values. Figure 63 depicts a representative image of a DHGP injected with hAMSCs on Day 0 with an ROI drawn around the area of fluorescence as indicated by the blue line.

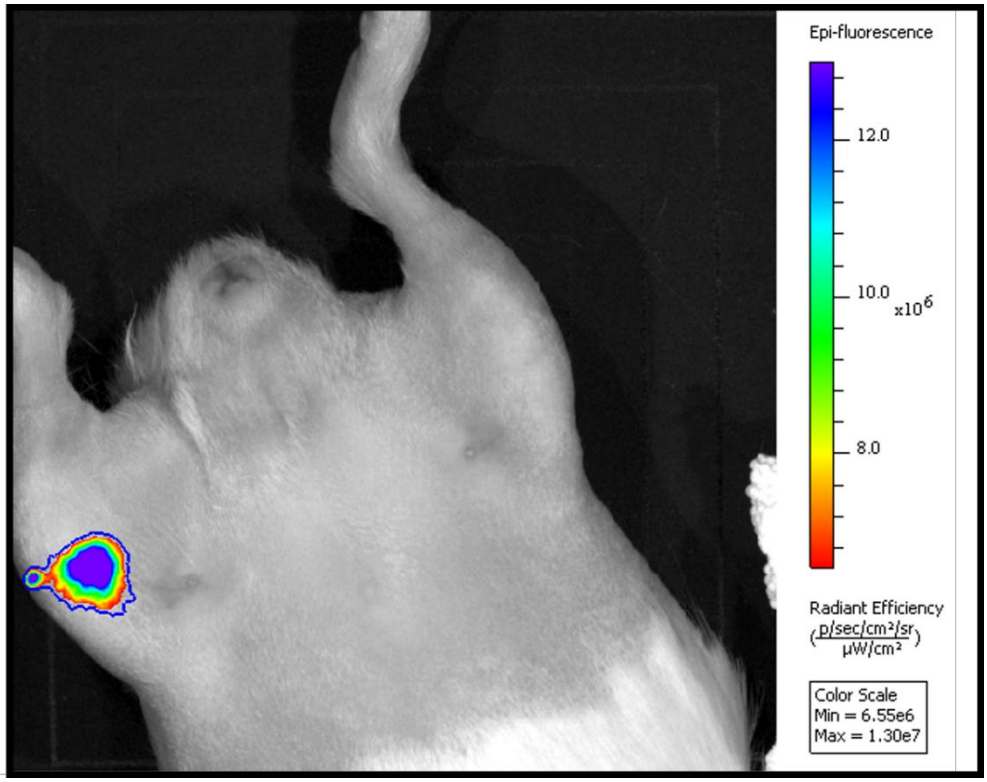

Figure 63: Representative image of an ROI automatically drawn around the detected fluorescence via the IVIS Spectrum Imaging Software.

After ROIs were drawn around all detected fluorescent areas for each imaging time point, average radiant efficiency values were obtained in order to assess resident time of hAMSCs and hADSCs quantitatively. Values were then normalized to Day 0 average radiant efficiency, in which average radiant efficiency ratios were obtained as depicted in Figure 64. It is observed that hAMSCs were no longer detected by Day 16, while hADSCs were still detected at this time point, indicating they resided at least three days longer in the knee joint. Additionally, following the trend of hADSCs fluorescence, it can be estimated that by Day 19, hADSCs would have a similar radiant efficiency to hAMSCs at Day 13, hypothetically indicating they could reside in the knee joint

approximately 6 days longer than hAMSCs. Ultimately, hADSCs were not detected by Day 21.

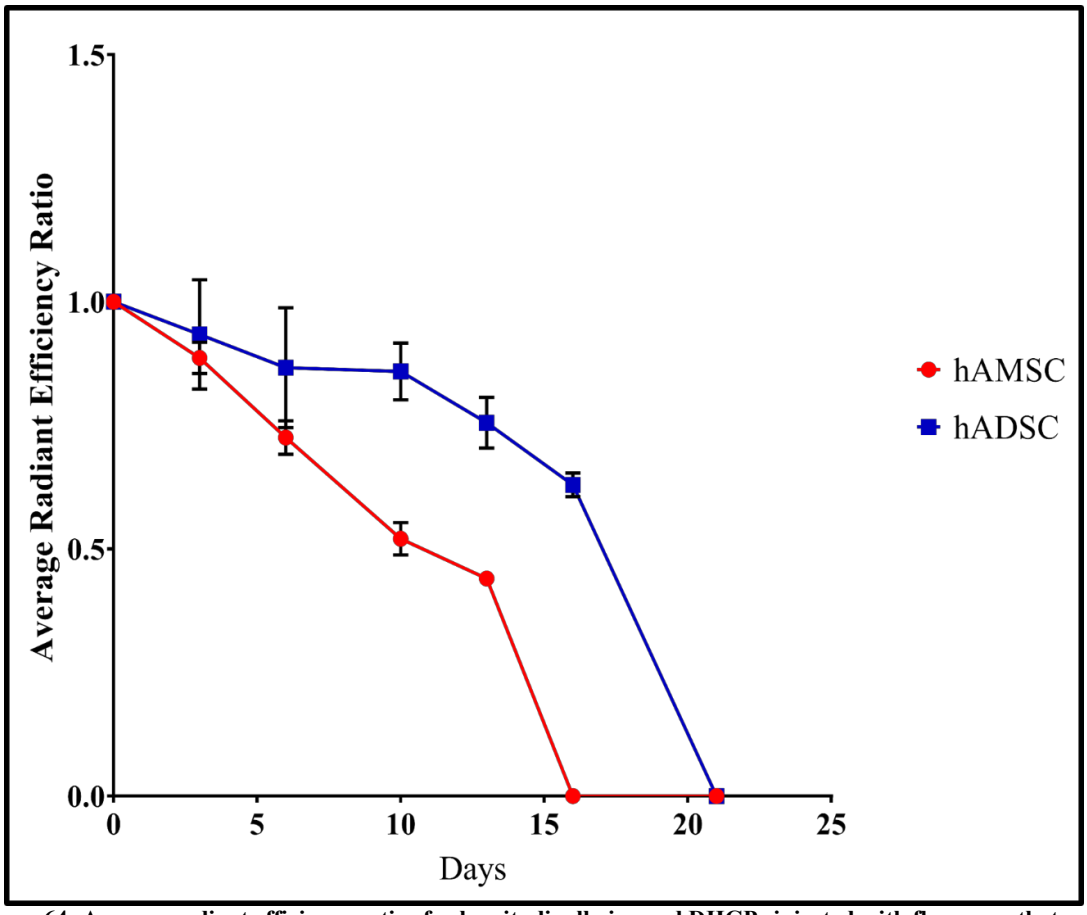

Figure 64: Average radiant efficiency ratios for longitudinally imaged DHGPs injected with fluorescently tagged hAMSCs and hADSCs.

3.3.3 Stem Cell Migration

Following fluorescent imaging, DHGP lungs were harvested in order to detect for possible migration of hAMSCs and hADSCs to distant organs via IHC targeted to detect human mitochondria. Human native cartilage was used as a positive control for the Mouse Anti-Human Mitochondria primary antibody, as displayed in Figure 65. Panel A represents the negative control, in which no brown staining is detected in the

chondrocytes. Conversely, the positive control, depicted in panel B, has evident brown staining in the chondrocytes, indicating human mitochondria was detected.

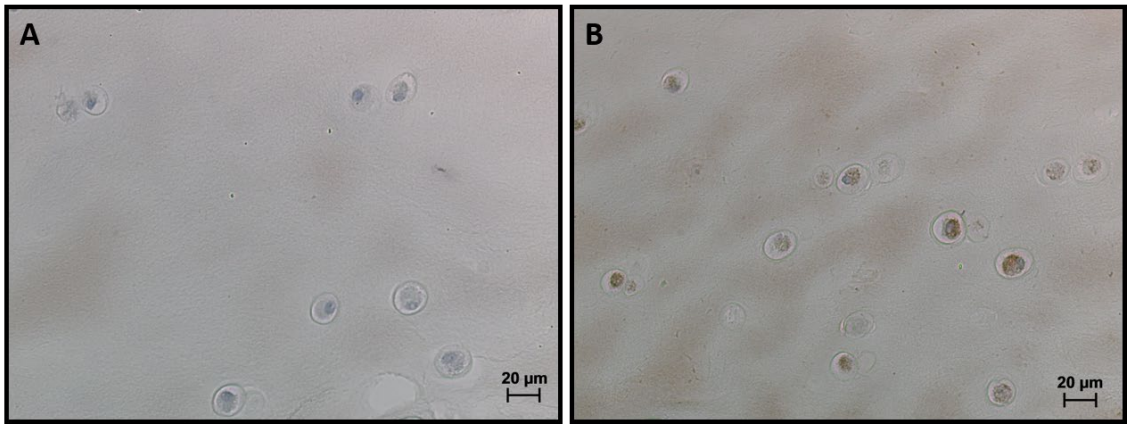

Figure 65: Human cartilage as a positive control for detection of human mitochondria via IHC. Panel A represents the negative control, while panel B represents the positive control containing Mouse Anti-Human Mitochondria primary antibody, in which positive staining is evident in the chondrocytes.

Figure 66 displays IHC stained lung samples from the DHGPs injected with tagged hAMSCs. Panels A and C represent the negative control for each hAMSC-injected DHGP (animals 1 and 5), while panels B and D represent the positive control. For both animals, it is observed that the negative controls do not contain any brown staining therefore no detection of human mitochondria. Conversely, for both animals, the positive control lung samples do contain brown staining in the lungs, therefore signifying detection of human mitochondria in the lungs.

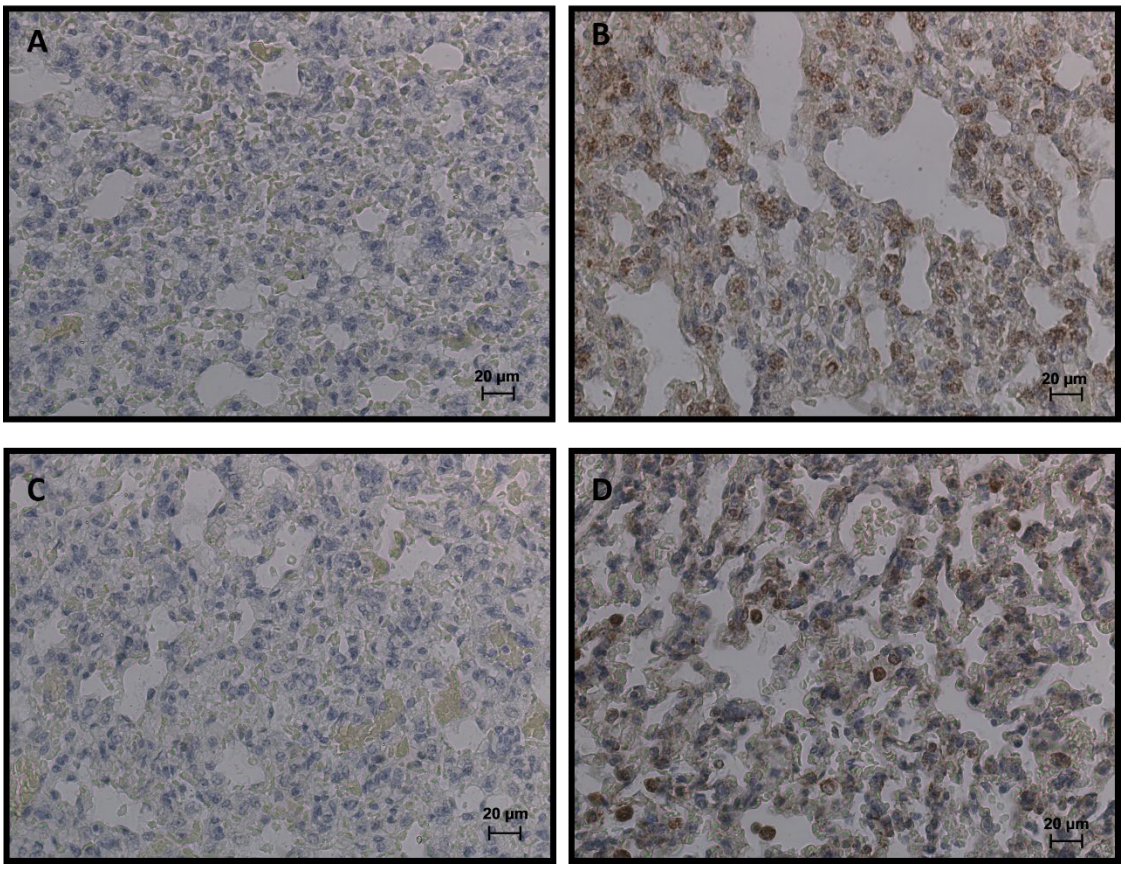

Figure 66: Representative lung samples of DHGPs injected with tagged hAMSCs that were targeted for detection of human mitochondria. Panel A represents the negative control of one DHGP (animal 1), while panel B represents the positive control. Similarly, panel C represents the negative control of another DHGP (animal 5), while panel D represents the positive control. Both DHGPs exhibit human mitochondria detection in the lungs.

Figure 67 displays IHC stained lung samples from the DHGPs injected with tagged hADSCs. Panels A and C represent the negative control for each hADSC-injected DHGP (animals 2 and 6), while panels B and D represent the positive control. For both animals, it is observed that the negative controls do not contain any brown staining therefore no detection of human mitochondria. Similarly, for both animals, the positive control lung samples do not contain brown staining, therefore signifying no detection of human mitochondria in the lungs.

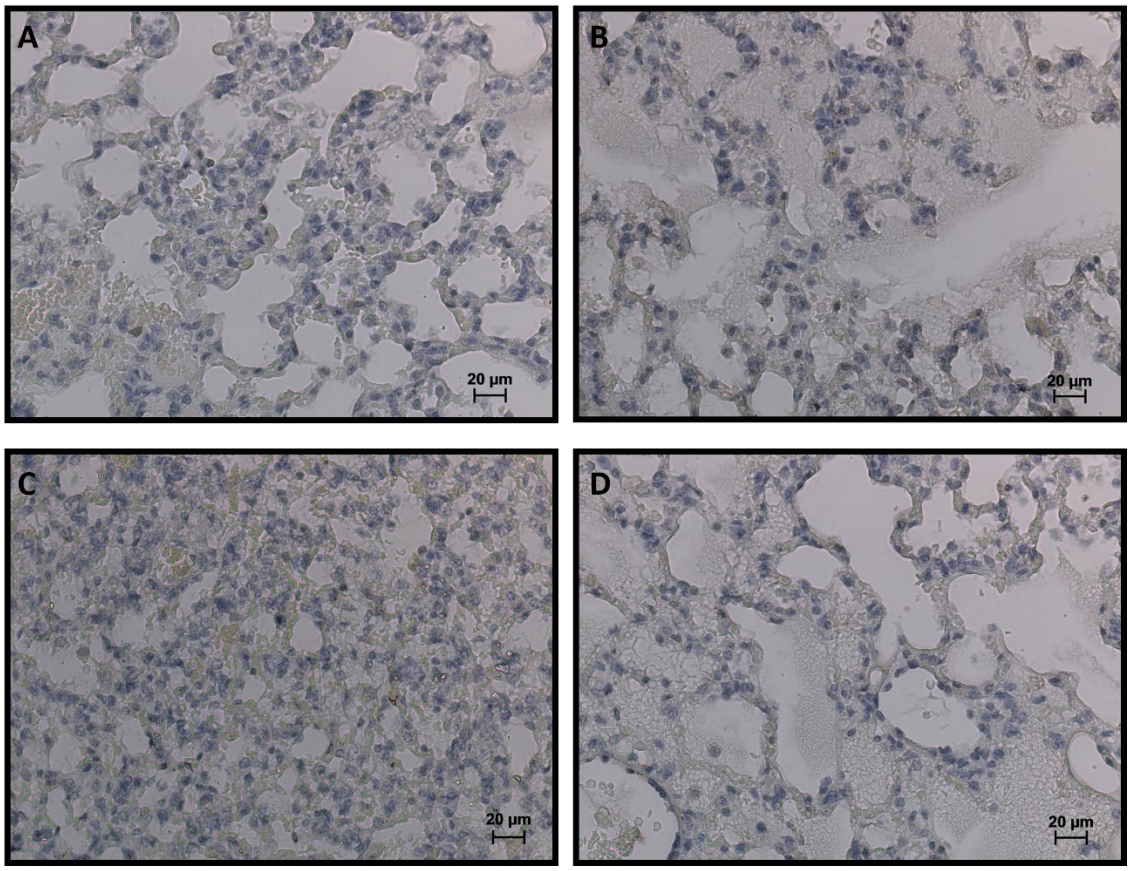

Figure 67: Representative lung samples of DHGPs injected with tagged hADSCs that were targeted for detection of human mitochondria. Panel A represents the negative control of one DHGP (animal 2), while panel B represents the positive control. Similarly, panel C represents the negative control of another DHGP (animal 6), while panel D represents the positive control. Both DHGPs do not exhibit human mitochondria detection in the lungs.

Knees of the DHGPs injected with tagged hAMSCs and hADSCs were harvested in order to detect for any remaining cells residing in the knee joint via detection of human mitochondria. Figure 68 through Figure 71 display representative areas of the IHC stained knee joint of the DHGPs injected with tagged hAMSCs, including the synovium, ACL, and articular cartilage of the tibia and femur. From Figure 68, panels A and B represent the negative and positive samples of the synovium, while panels C and D represent the negative and positive samples of the ACL. It is observed that the negative

controls for both sample types do not exhibit brown staining. Similarly, the positive controls for both sample types do not contain brown staining, therefore indicating no detection of human mitochondria in the synovium and ACL. From Figure 69, the negative and positive samples of the tibial articular cartilage are represented by panels E and F, while panels G and H represent the negative and positive femoral articular cartilage samples. It is observed that the negative controls for both sample types do not exhibit brown staining. Similarly, the positive controls for both sample types do not contain brown staining, therefore indicating no detection of human mitochondria in the articular cartilage of the tibia and femur. Figure 70 and Figure 71 represents the other DHGP injected with tagged hAMSCs, in which the panels denote the same sample type. Similar results are exhibited, in which human mitochondria is not detected in the synovium, ACL, or articular cartilage of the tibia and femur.

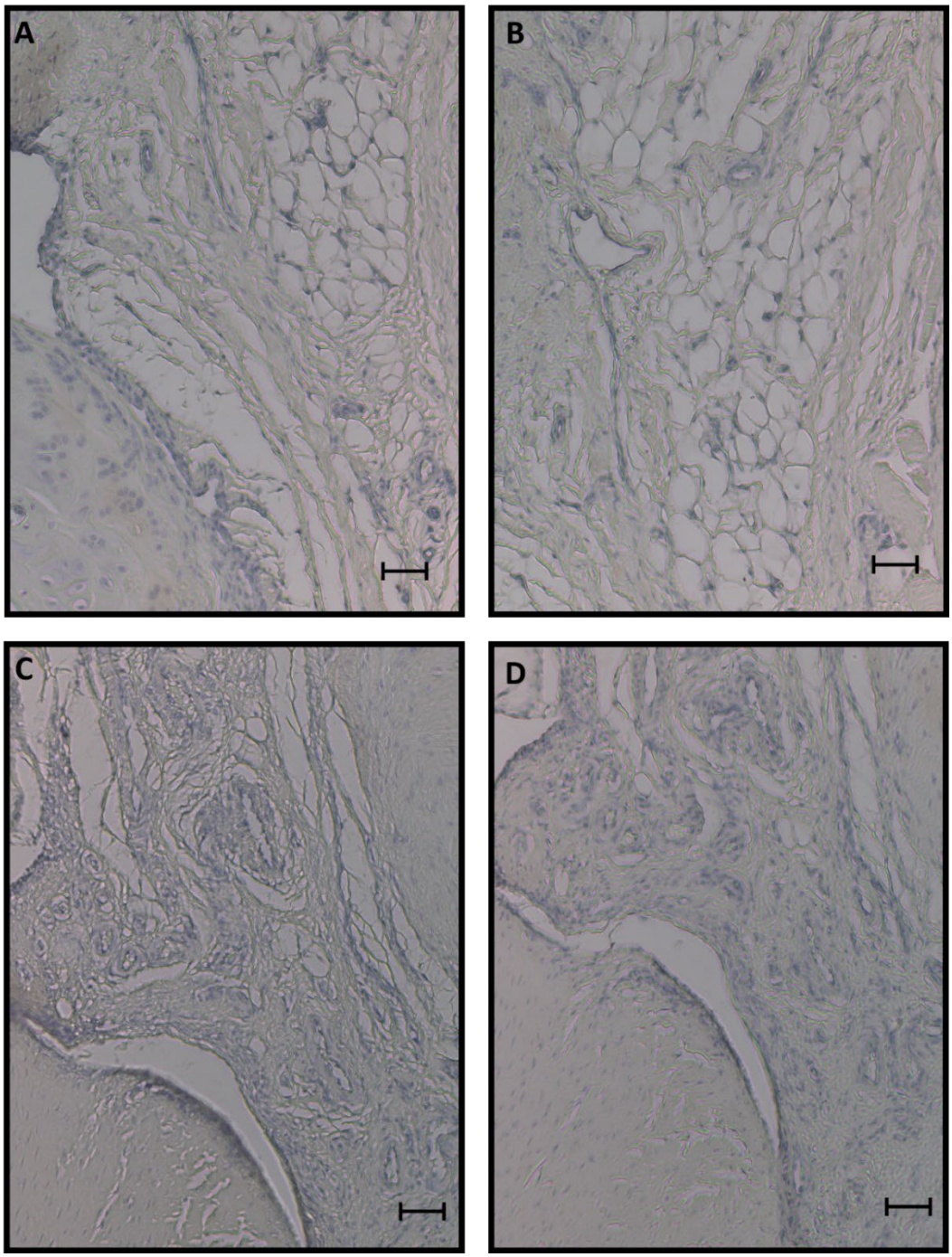

Figure 68: Representative images of IHC stained synovium and ACL from a DHGP (animal 1) injected with tagged hAMSCs for detection of human mitochondria. Panel A signifies the negative control of the synovium, while panel B represents the positive. Panel C represents the negative control for the ACL, while panel D denotes the positive. All scale bars represent 50 µm.

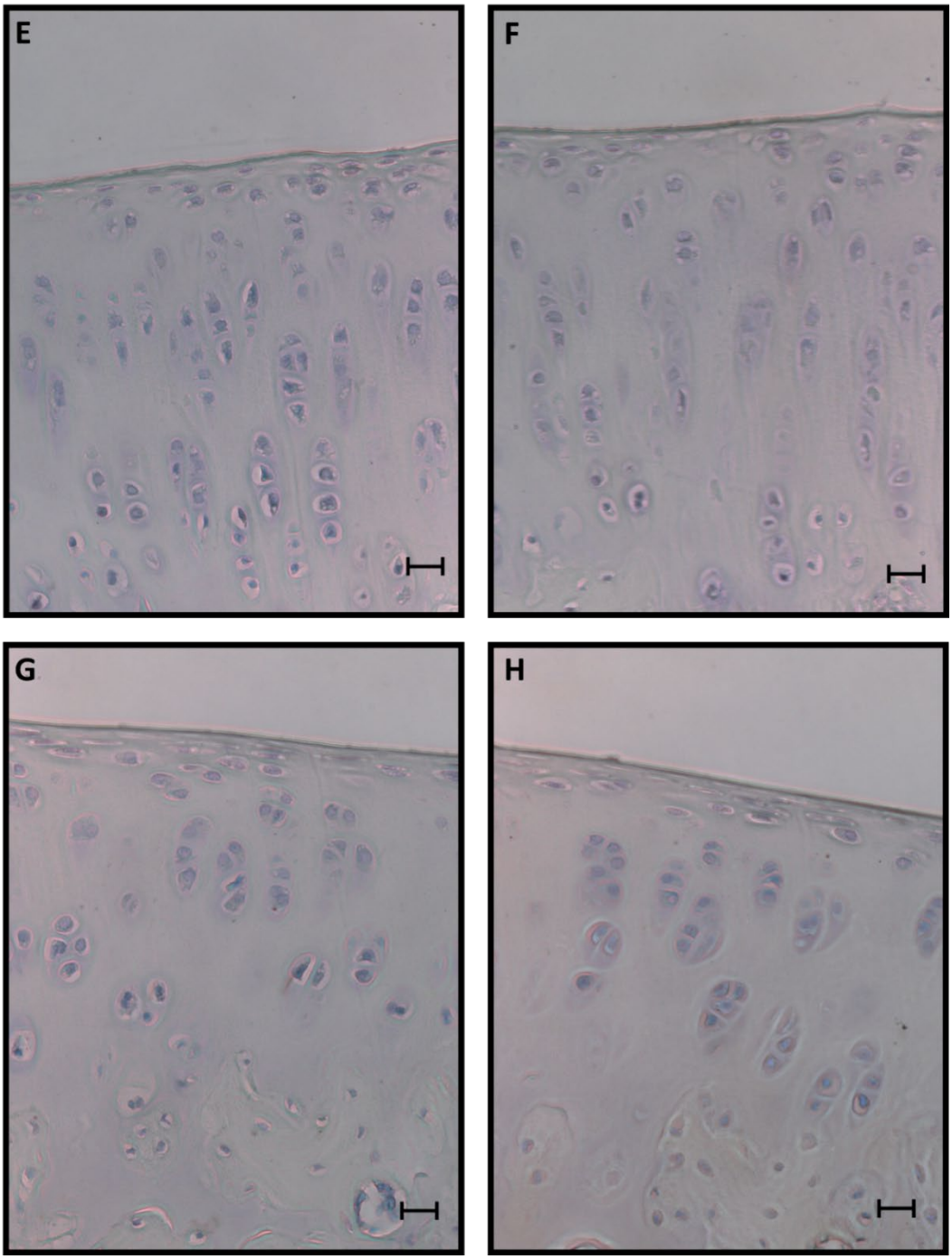

Figure 69: Representative images of IHC stained tibia and femur articular cartilage from a DHGP (animal 1) injected with tagged hAMSCs for detection of human mitochondria. Panel A signifies the negative control of the synovium, while panel B represents the positive. Panel C represents the negative control for the ACL, while panel D denotes the positive. All scale bars represent 20 μm.

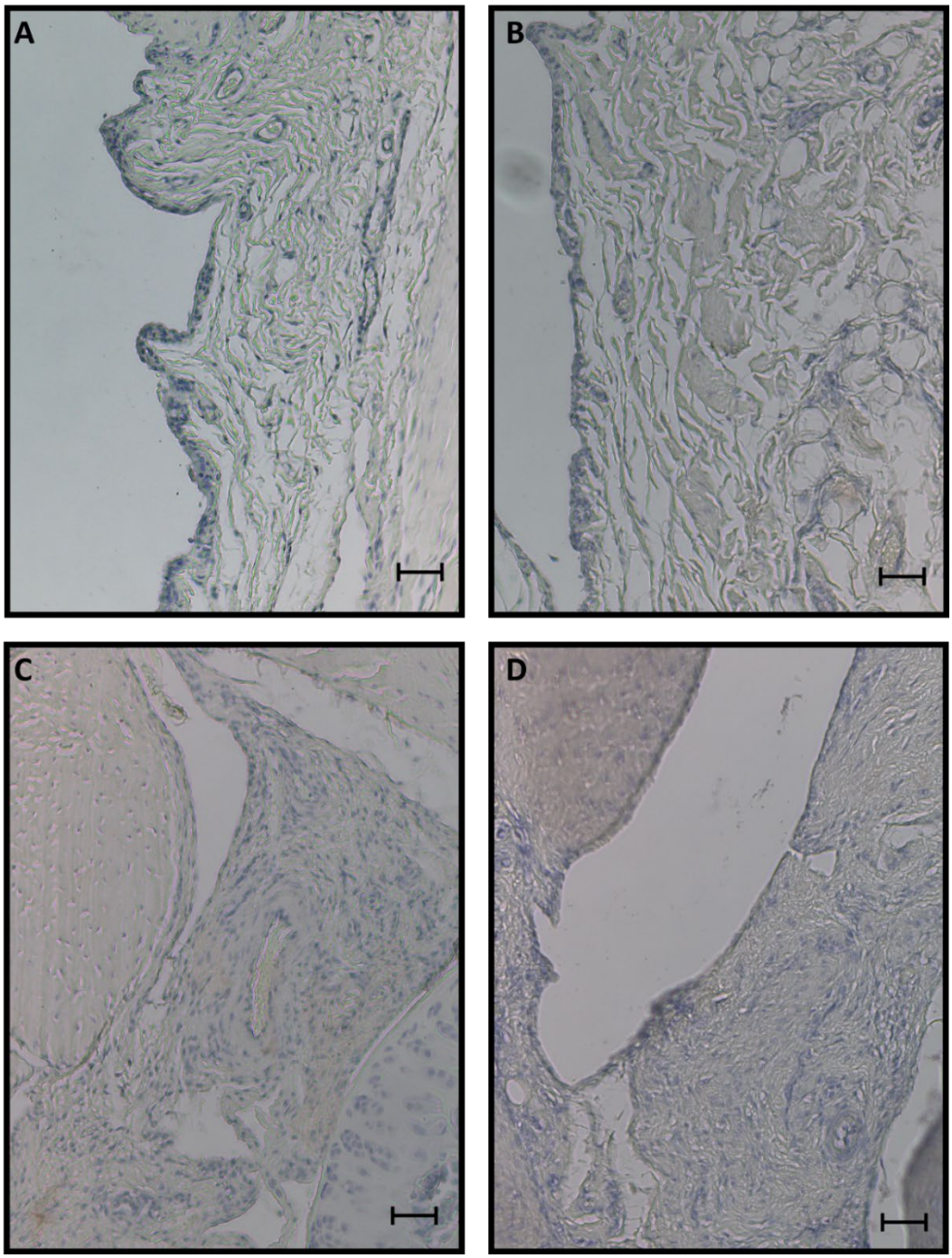

Figure 70: Representative images of IHC stained synovium and ACL from a DHGP (animal 5) injected with tagged hAMSCs for detection of human mitochondria. Panel A signifies the negative control of the synovium, while panel B represents the positive. Panel C represents the negative control for the ACL, while panel D denotes the positive. All scale bars represent 50 µm.

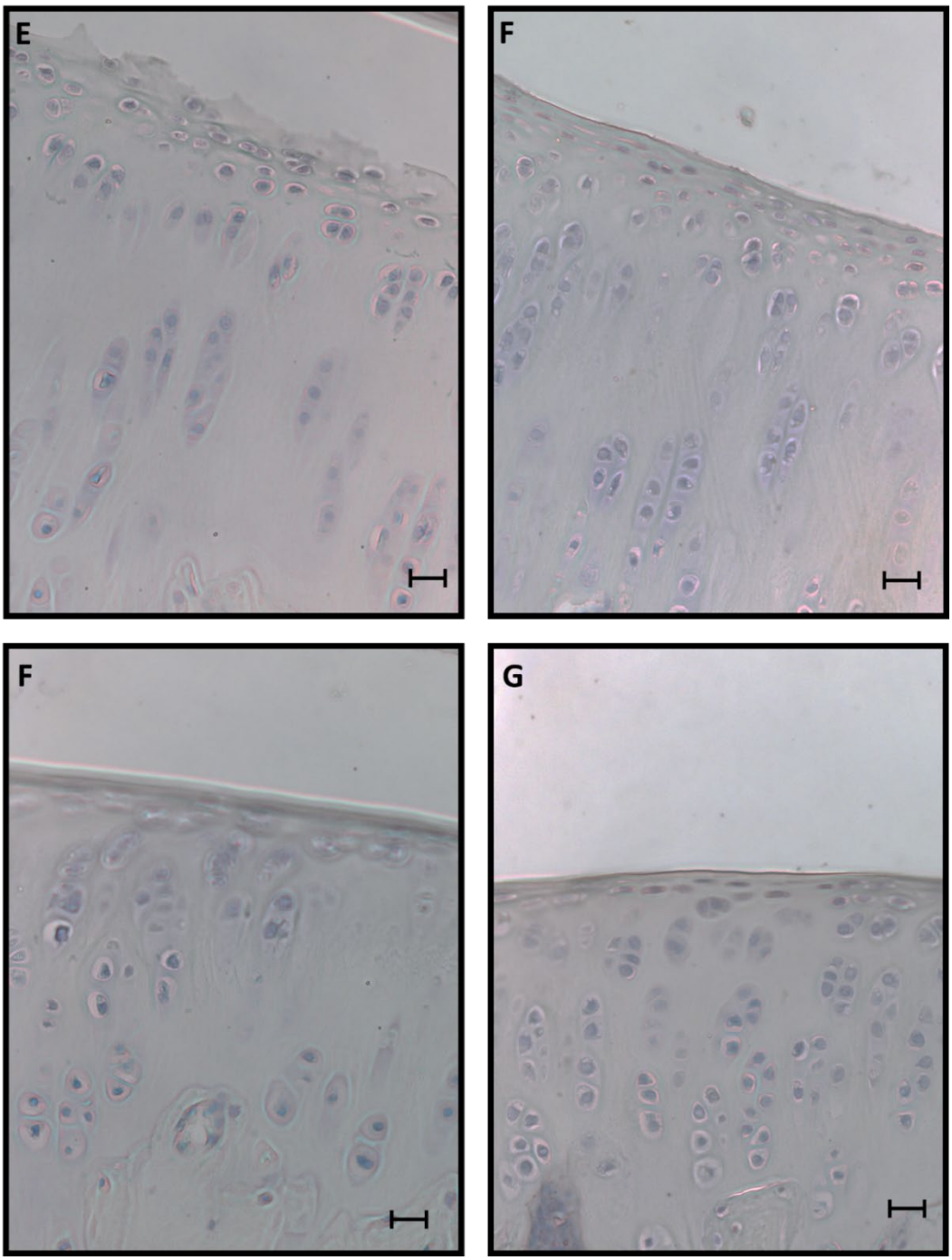

Figure 71: Representative images of IHC stained tibia and femur articular cartilage from a DHGP (animal 5) injected with tagged hAMSCs for detection of human mitochondria. Panel A signifies the negative control of the synovium, while panel B represents the positive. Panel C represents the negative control for the ACL, while panel D denotes the positive. All scale bars represent 20 μm.

Figure 72 through Figure 75 display representative areas of the IHC stained knee joint of the DHGPs injected with tagged hADSCs, including the synovium, ACL, and articular cartilage of the tibia and femur. From Figure 72, panels A and B represent the negative and positive samples of the synovium, while panels C and D represent the negative and positive samples of the ACL. Similar results to the DHGPs injected with tagged hAMSCs are indicated, in which it is observed that the negative controls for both sample types do not exhibit brown staining. Similarly, the positive controls for both sample types do not contain brown staining, therefore indicating no detection of human mitochondria in the synovium and ACL. From Figure 73, the negative and positive samples of the tibial articular cartilage are represented by panels E and F, while panels G and H represent the negative and positive femoral articular cartilage samples. Again, similar results to the DHGPs injected with tagged hAMSCs are observed, in which the negative controls for both sample types do not exhibit brown staining. Similarly, the positive controls for both sample types do not contain brown staining, therefore indicating no detection of human mitochondria in the articular cartilage of the tibia and femur. Figure 74 and Figure 75 represents the other DHGP injected with tagged hADSCs, in which the panels denote the same sample type. Similar results are exhibited, in which human mitochondria is not detected in the synovium, ACL, or articular cartilage of the tibia and femur. Ultimately, no human mitochondria were detected in the entire knee joint of the DHGPs injected with tagged hAMSCs as well as those injected with tagged hADSCs.

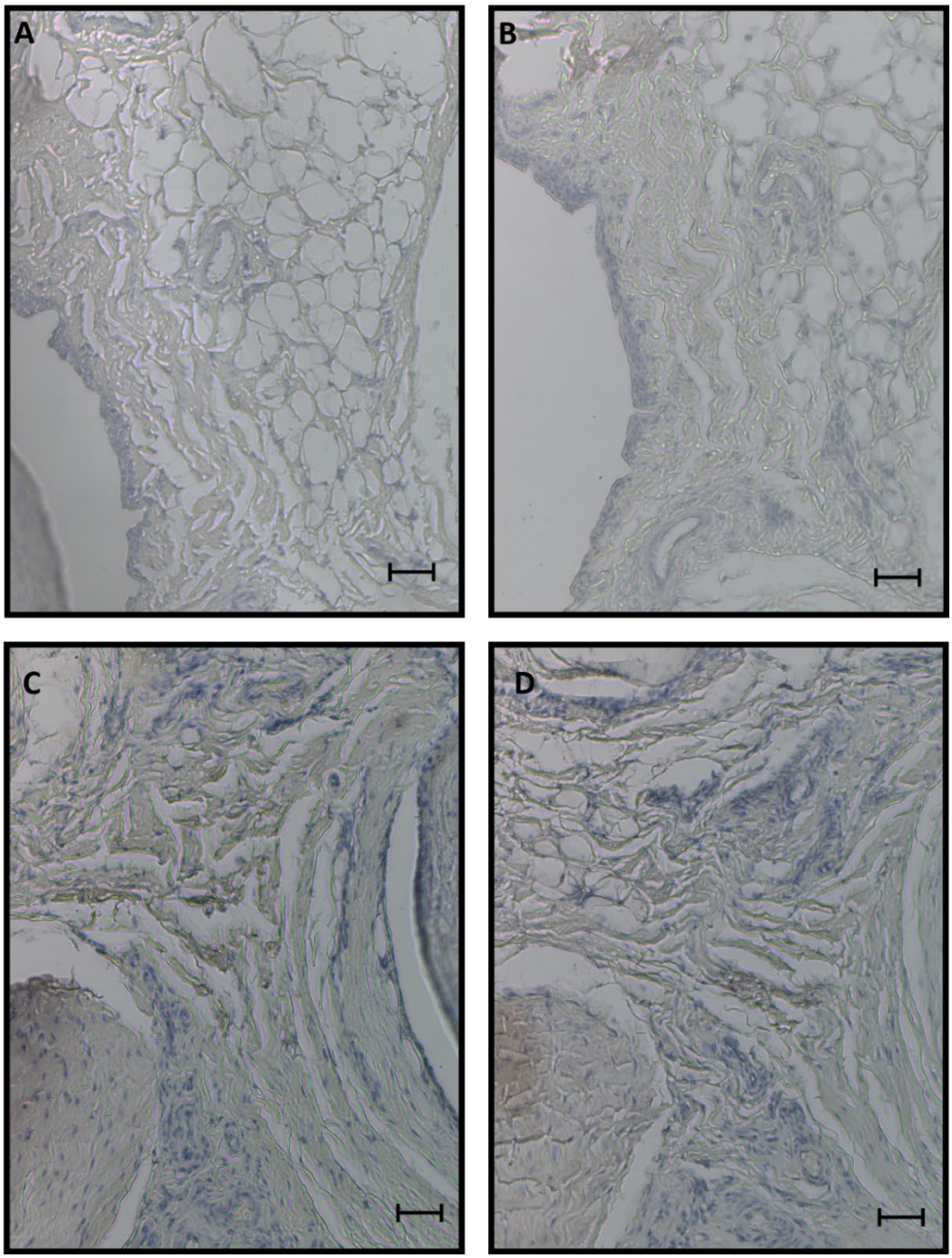

Figure 72: Representative images of IHC stained synovium and ACL from a DHGP (animal 2) injected with tagged hADSCs for detection of human mitochondria. Panel A signifies the negative control of the synovium, while panel B represents the positive. Panel C represents the negative control for the ACL, while panel D denotes the positive. All scale bars represent 50 µm.

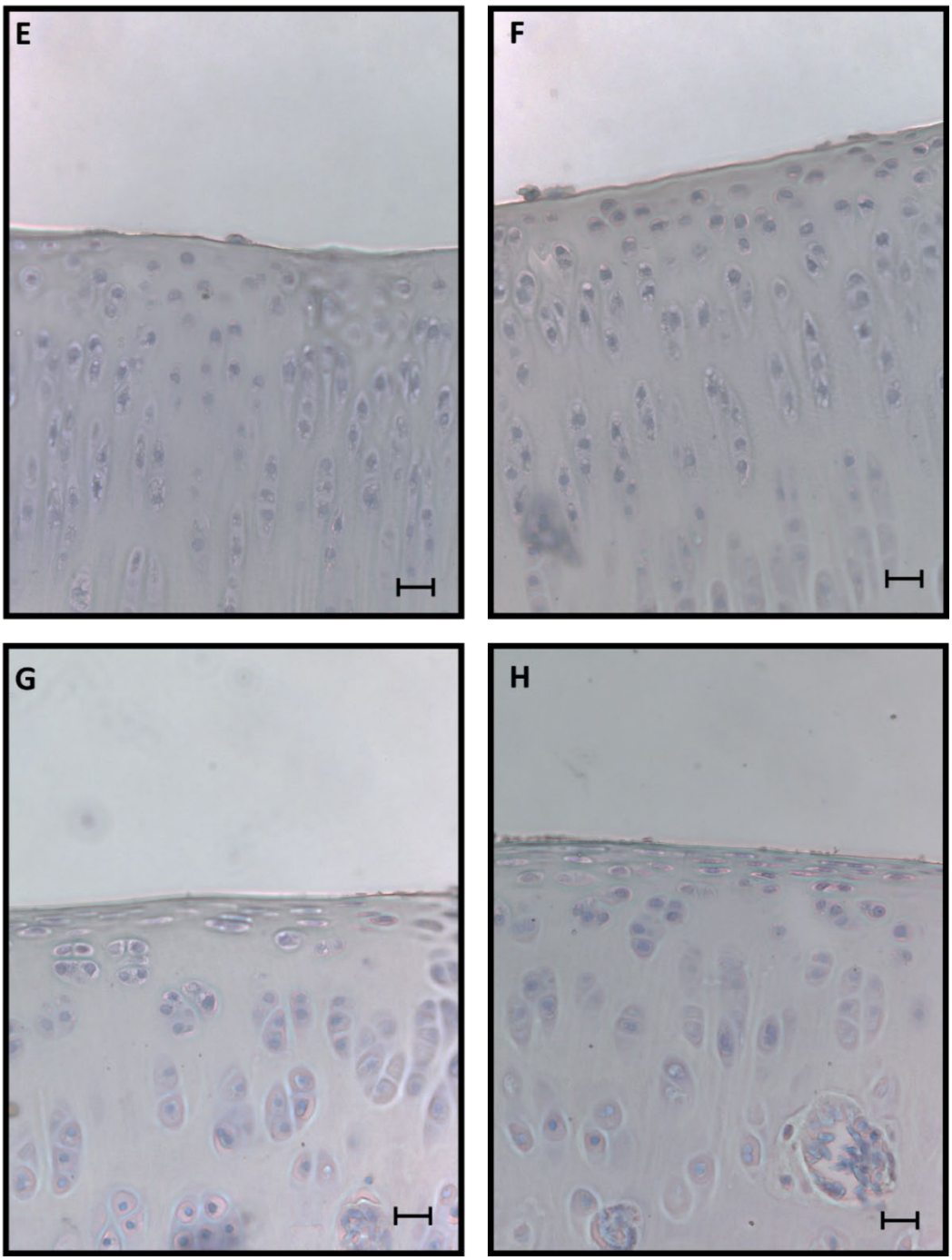

Figure 73: Representative images of IHC stained tibia and femur articular cartilage from a DHGP (animal 2) injected with tagged hADSCs for detection of human mitochondria. Panel A signifies the negative control of the synovium, while panel B represents the positive. Panel C represents the negative control for the ACL, while panel D denotes the positive. All scale bars represent 20 µm.

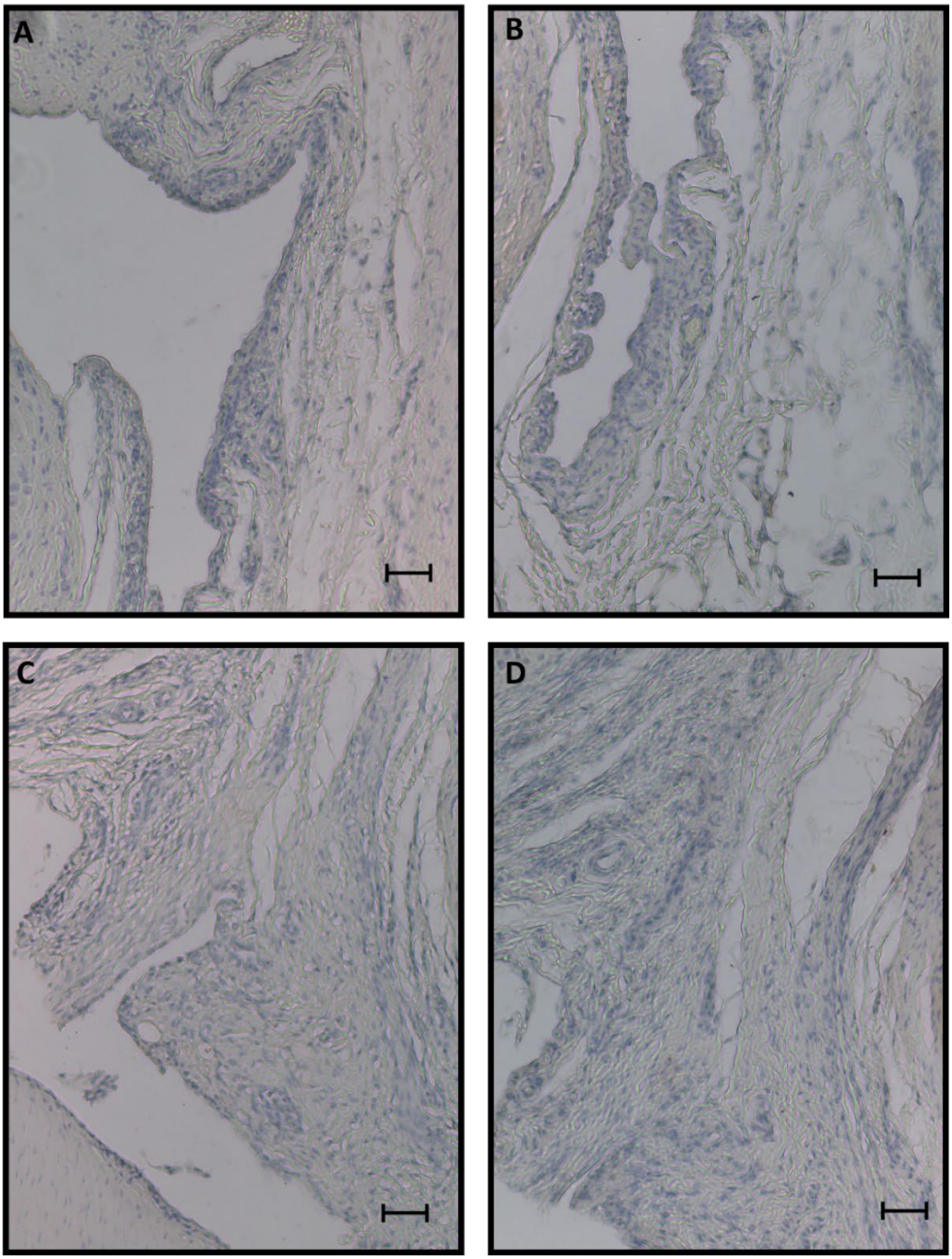

Figure 74: Representative images of IHC stained synovium and ACL from a DHGP (animal 6) injected with tagged hADSCs for detection of human mitochondria. Panel A signifies the negative control of the synovium, while panel B represents the positive. Panel C represents the negative control for the ACL, while panel D denotes the positive. All scale bars represent 50 µm.

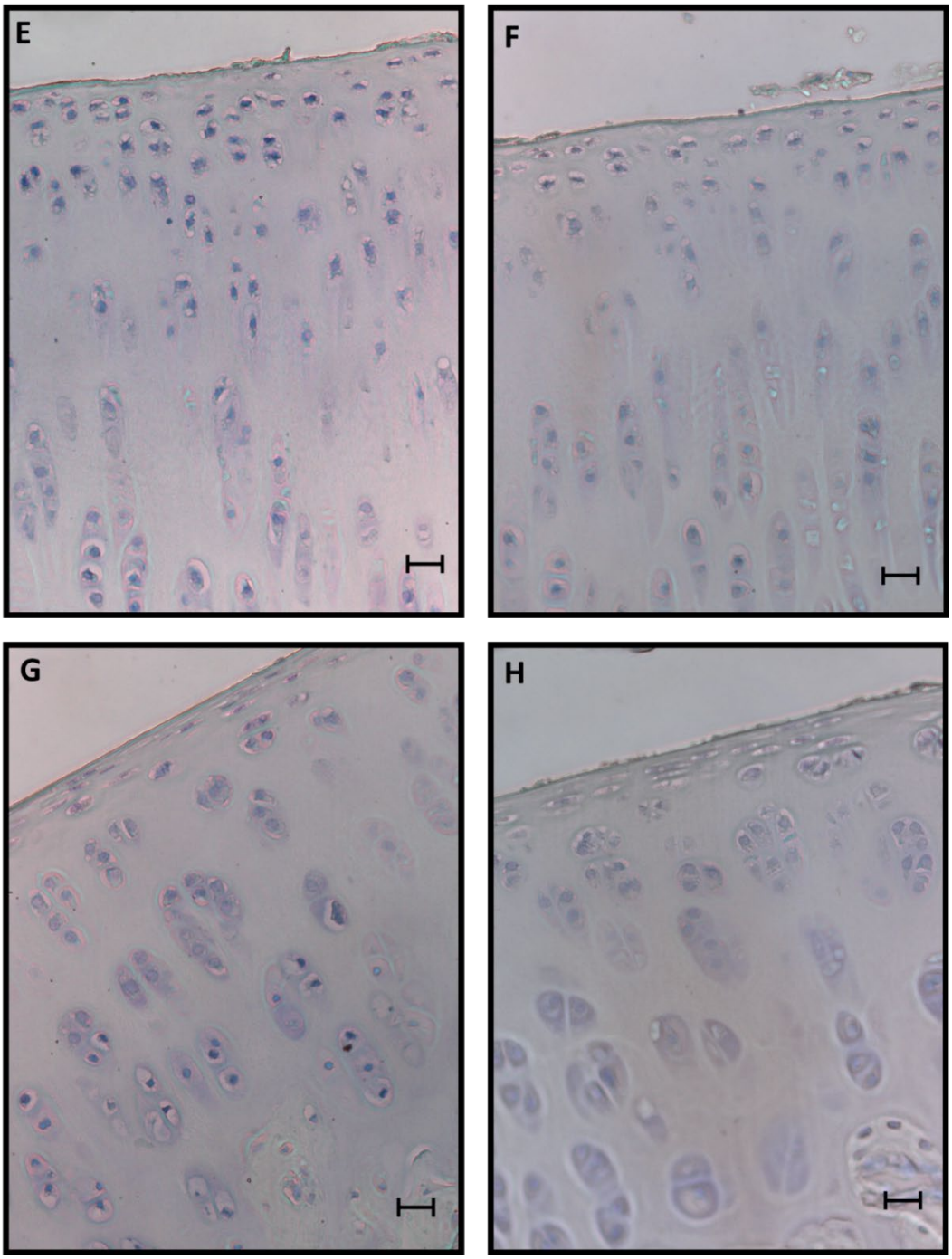

Figure 75: Representative images of IHC stained tibia and femur articular cartilage from a DHGP (animal 6) injected with tagged hADSCs for detection of human mitochondria. Panel A signifies the negative control of the synovium, while panel B represents the positive. Panel C represents the negative control for the ACL, while panel D denotes the positive. All scale bars represent 20 μm.

3.4 Discussion

3.4.1. Stem Cell Fluorescent Tagging and IVIS In Vitro Thresholding

As indicated in section 3.2.1, XenoLight DiR fluorescent dye (Perkin Elmer, USA) was chosen to tag the injected stem cells due to its compatible use with the IVIS Spectrum Imaging System (Perkin Elmer, USA). Its high wavelength property makes it an optimal fluorophore to limit autofluorescence, which was especially vital in imaging a white animal that produces naturally high wavelengths. It was not predicted that stem cell viability would be negatively affected upon fluorescent tagging of stem cells with XenoLight DiR. This was further validated (Figure 54**)** in which hAMSCs and hADSCs did not exhibit loss of cell viability after being fluorescently tagged with XenoLight DiR fluorescent dye, indicating this was still a suitable and appropriate dye for labeling the hAMSCs and hADSCs.

Before *in vivo* imaging of DHGPs, *in vitro* thresholding of fluorescently tagged hAMSCs and hADSCs was performed in order to obtain the correct IVIS Spectrum Imaging filters as well as a fluorescent tolerance. Serial dilutions of both fluorescently tagged stem cells were made and imaged (Figure 55 and Figure 56**)**, in which an optimal filter setting were enacted. Results indicate that for both hAMSCs and hADSCs, at 10^4 cells, fluorescence is no longer detected, indicating that cell number falling below this threshold will not be identified by the IVIS Spectrum Imaging system. Additionally, it can be visualized that the PBS/HA suspension that contains no cells, has no detectable fluorescence, which was predicted. This also indicates that no autofluorescence is impacting the fluorescent

detection of the other dilutions. Lastly, it is observed that for both hAMSCs and hADSCs, 10^6 cells depicts the highest level of detectable fluorescence, which was again predicted. Qualitatively, the fluorescently tagged cell dilutions can be viewed to progressively decrease in radiant efficiency as less cells are present. It should be noted that the cells are displayed in the middle of the Eppendorf tubes, as indicated by the maximum level of fluorescence observed, due to the fact that they are re-suspended in a solution containing 0.5% HA. The viscous nature of HA caused the cells to no longer descend to the bottom of the tube, and resulted in congregation in the middle of the tube upon re-suspension. Moreover, the serial dilutions were successful in obtaining appropriate IVIS Spectrum Imaging filters and fluorescent thresholds for both stem cell sources.

3.4.2. Longitudinal Imaging of Fluorescently Tagged Stem Cells

Upon injection of tagged hAMSCs and hADSCs into the knee joint, DHGPs were immediately imaged via the IVIS Spectrum Imaging system in order to evaluate and compare residence times of hAMSCs and hADSCs *in vivo*. Longitudinal imaging occurred on Days 3, 6, 10, 13, 16, and 21. It is qualitatively observed that with increasing time, fluorescence steadily decreases for both hAMSC and hADSC treated DHGPs, in which this was predicted. Additionally, it is observed that by Day 16, there is no radiant efficiency detected for the hAMSC injected DHGPs, while hADSCs are still exhibiting fluorescence (Figure 57 through Figure 62**)**. The hADSCs are no longer detected in the DHGP by Day 21, in which this trend can be observed for both treatment groups **(**Figure

57 through Figure 62**).** Ultimately, hADSCs appear to reside longer in the knee joint, for at least 3 days, in comparison to hAMSCs. To quantitatively evaluate the residence time of hAMSCs and hADSCs within the knee joint, a region of interest was chosen around the detected fluorescence area via the IVIS Spectrum Imaging Software to obtain average radiant efficiency values for each imaging time point. It should be noted that radiant efficiency scales for hAMSCs and hADSCs are different from each other in order to account for difference in cell surface area and size. In order to account for this difference, average radiant efficiency values were normalized to Day 0 average radiant efficiency values. From the normalized radiant efficiency graph (Figure 64**)**, it is observed that fluorescence steadily decreases over time and ultimately hADSCs have a longer residence time in the knee joint in comparison to hAMSCs. There is not an imaging time point in between Days 16 and 21, but if the average radiant efficiency trend line were to continue for the hADSCs, it can be observed that by Day 19 there would be a potentially similar average radiant efficiency observed as the hAMSCs on day 13. This indicates that hypothetically hADSCs could reside 6 days longer in the knee joint in comparison to hAMSCs.

Moreover, it was observed that by Day 16 hAMSCs were no longer detected and by Day 21, hADSCs were no longer detected. Overall, this short residence time of stem cells in the target tissue is consistent with current investigations and various applications, in which recent studies suggest that stem cells may not have a long lifespan after administration or have poor engraftment into the target site.[120,123,124]

It is currently unclear as to what mechanisms restrict stem cell survival and engraftment after transplantation *in vivo*; however, the rapid disappearance of the hAMSCs and hADSCs could explain the lack of therapeutic efficacy in mitigation of OA following intra-articular injection into the DHGP knee joint. The lower injected hAMSC and hADSC density (~500,000 cells) could also have an impact on their limited residence time within the joint. One study showed that a higher cell density ($7x10^6$ cells) of intra-articularly injected MSCs in the DHGP knee joint resided up to 5 weeks post-transplantation.[125] Additionally, while mesenchymal stem cells (MSCs) have the unique ability to differentiate into various cell types and potentially secrete anti-inflammatory factors, as described in section 1.5.2, it is currently unknown whether these mechanisms are effective and if MSCs persist locally after administration.[124] In order to increase the therapeutic effectiveness of stem cells *in vivo* following injection, potential suggestions are described in Chapter 4.

3.4.3 Stem Cell Migration

To determine whether the stem cells indeed died within the knee joint over time or if they systemically migrated to distant organs, stem cell migration was assessed via immunohistochemistry (IHC) targeted to detect human mitochondria. To determine if the Anti-Human Mitochondria primary antibody was effective, a native human cartilage sample was used as the positive control in which chondrocytes present within the cartilage would stain positively for human mitochondria. This was validated (Figure 65**)**

as positive brown staining occurred in the positive sample, while no staining was observed in the negative sample.

The lungs of the DHGPs were harvested in order to detect for human mitochondria present. Identifying human mitochondria in the lungs would indicate that the stem cells did migrate to the organ. The lungs were chosen as the optimal organ to assess as it has been determined that this is the primary and initial migratory organ that stem cells travel to systemically. This is especially detected after intravenous administration, and although the hAMSCs and hADSCs were intra-articularly injected, this same migratory mechanism could be observed.[124,126,127] Results showed no positive staining in the lungs of the DHGPs that were injected with hADSCs (Figure 67**).** From this, it can be concluded that hADSCs did not migrate to distant organs and therefore presumably died over time within the knee joint. Conversely, results of the hAMSC injected DHGPs indicated clear and intense positive staining in the lungs for both groups, indicating that hAMSCs did in fact migrate to the lungs. This is a very interesting result, as there are currently no investigations on the migration outcomes of hAMSCs upon intra-articular administration *in vivo.* Although direct injection benefits from precise and targeted delivery to a specific site, investigations show that regardless of the route of delivery, only 1-5% of cells engraft within the target site.[120] The current mechanisms by which stem cells migrate to the lungs from distant areas of the body are unknown; however, a mechanical mechanism for cell trapping in the lung is postulated.[120] Additionally it is unclear if capillaries need to employ certain characteristics to entice and retain MSCs.

Furthermore, future studies investigating the mechanisms regulating systemic migration are warranted.

Ultimately, it is hypothesized that the hAMSCs injected into the knees migrated to the lungs via the capillary network present in the synovium surrounding the knee joint. As the synovium is a vascularized tissue, it is possible that hAMSCs were able to migrate through blood vessels and systemically travel to the lungs from the knee joint. The mechanisms by which the hAMSCs were able to systemically migrate to the lungs, and not the hADSCs, is currently unclear. It may potentially be due to their perinatal characteristics in which they have a broader range of differentiation potential compared to hADSCs, which may remain in the knee joint due to its restrained capability to differentiate into the mesoderm lineage and recognize a more natural environment in the knee joint. Additionally, it is uncertain if stem cells that are trapped in the lungs following migration are still viable and contain effector functions.[120] Therefore, future investigations into the bio-distribution mechanisms of hAMSCs are warranted, as will be described more in Chapter 4.

The knee joints of the DHGPs were also evaluated for potential detection of human mitochondria in order to determine if any remaining stem cells resided in the joint. The anterior cruciate ligament (ACL), synovium, and the articular cartilage of the tibia and femur were evaluated in order to account for any stem cell distribution in the joint itself. Both hAMSCs and hADSCs were not seen in the any of the knee joint tissues (Figure 68

through Figure 75**)**, in which these results further validate that the hADSCs did indeed die in the knee joint. Additionally, it can be concluded that hAMSCs traveled systemically to the lungs or some may have died in the knee joint as well. Moreover, from IVIS longitudinal imaging and IHC evaluation, it can be validated that by Day 16, hAMSCs are no longer present in the knee joint, while by Day 21, hADSCs are no longer present in the knee joint. Although it was observed that hADSCs did reside longer in the knee joint and eventually died, hAMSCs were detected on Day 21 in the lungs. This shows that hAMSCs did not die quicker than hADSCs, but rather they migrated out of the knee joint earlier and therefore were no longer detected by the IVIS Imaging System. It is unclear when exactly and how quickly hAMSCs begin to migrate, and therefore future studies are warranted to investigate this.

3.4.4 Summary

In combination with IVIS longitudinal imaging and IHC evaluation, it was determined that hADSCs resided longer in the knee joint in comparison to hAMSCs and died in within the knee joint by day 21, showing no systemic migration to distant organs. Conversely, hAMSCs were no longer detected in the knee joint by Day 16 and were found to migrate to the lungs, in which they were detected at Day 21. Moreover, although hAMSC engraftment capabilities in the target tissue site are lacking in comparison to hADSCs, they are still detectable longer than hADSCs in the body. Therefore, it can hypothesized that if techniques to ensure the engraftment of the hAMSCs in the knee joint could be improved, they could potentially survive longer in the joint than the

hADSCs and provide a more therapeutic effect. Ultimately, the results from Aim 2 helped to justify why the hADSCs and hAMSCs were not as therapeutically effective in mitigating OA, as seen in Aim 1, due to their short life-span within the knee joint and potential loss of effector functions. Future suggestions are warranted, as described below in Chapter 4, in order to increase the therapeutic efficacy of these stem cell sources and to improve their residence time and engraftment in the knee joint.

CHAPTER FOUR

CONCLUSIONS AND FUTURE SUGGESTIONS

In conclusion, it cannot be determined if hAMSCs had a superior pro-regenerative effect in comparison to hADSCs *in vivo*. As described in Aim 1, outcome measures exhibited very similar results and no statistical significance between the two stem cell sources in mitigation of osteoarthritis from articular cartilage, subchondral bone, and synovium analyses. Additionally, it cannot be concluded that either stem cell source had a pro-regenerative effect *in vivo* as results also indicated similar results to the HA-only treated groups. Aim 2 aided in explaining potentially why these stem cells did not display an enhanced therapeutic effect, in which it was observed that both stem cell sources were no longer residing in the knee joint after 3 weeks, either due to cell death or migration. This deficiency in residence time substantiates the lack of therapeutic efficacy from hAMSCs and hADSCs, as they are no longer able to elicit their effector functions in the knee joint. Overall, further investigations with higher sample size is warranted in order to more effectively observe statistical trends, and suggestions for future studies will be described below. Lastly, it can also be concluded that the DHGP served as an effective spontaneous OA model, which was validated from results described in Aim 1.

Although a lack of regenerative effects were observed from stem cell injections *in vivo*, the studies performed herein provide great insight into future directions and studies to improve the therapeutic efficacy of injected hAMSCs and hADSCs in mitigation of OA.

Further investigations are warranted and suggestions for these studies are described below.

5.1 Enhance Residence Time and Integration of Stem Cells at the Target Tissue Site

There are various challenges presented in developing novel stem cell-based therapies, which commonly include cell retention or survival and functional integration of the cells at the target site. Further investigations into these components are necessary to provide for a more comprehensive understanding to improve targeted delivery and therapeutic efficacy of stem cells. In order to increase residence time and survival of stem cells upon transplantation, increasing the number of injections could be potentially beneficial in order to sustain a uniform number of cells within the joint over a prolonged period of time. It was observed that with ~500,000 cells injected, they were no longer residing in the joint by 3 weeks. Therefore, if the same number of cells are injected, then at a 3 week time point, another injection should be performed. Another suggested option would be to initially inject a higher cell density in order to increase residence time within the joint.

In order to improve the engraftment and integration of stem cells at the tissue specific site, phenotypic modification of cells before injection could be performed in order to give the cells a "boost" into a specific and desired lineage. Being cultured and injected alone may prove challenging for the stem cells to differentiate into the desired lineage just by being present in the tissue environment itself. Therefore, current investigations are focusing on the direct control of stem cell differentiation *in vitro* for various

applications.[128–130] Potential suggested strategies for this study would be to co-culture and inject stem cells in combination with chondrocytes. It has been found that maintaining stability of chondrocyte phenotype and regulating chondrogenic differentiation of stem cells over time ensuing transplantation is a large challenge to stem cell-based strategies for OA, in which cells tend to transition into a fibrocartilage phenotype.[131,132] Having chondrocytes present in the milieu may allow the stem cells to undergo desired chondrocyte phenotypic alterations with an enhanced differentiation potential, therefore eliciting a better regenerative and anti-inflammatory effect. Another suggestion could be to culture the stem cells in differentiation media immediately prior to injection. Allowing the stem cells to be cultured in chondrogenic media could again give them a heightened ability to differentiate into desired chondrocytes and therefore engraft more efficiently into the knee joint to stimulate their anti-inflammatory effector functions. Moreover, these strategies may help to lessen the probability of spontaneous differentiation of stem cells into undesired lineages. Overall, increasing the functional integration and of the stem cells within the joint would allow for less systemic migration to distant organs, as observed with hAMSCs, and increased therapeutic efficacy for mitigation of OA.

5.2 Improve Injection Method

Cell therapy success profoundly relies on the effective delivery of viable and functional cells to a specific site, where cells can yield a desired therapeutic effect. Intra-articular injection is a desired method for transplantation of stem cells as it allows for targeted delivery of cells to the desired and targeted tissue. One of the disadvantages to this

method is the subsequent and damaging mechanical properties it provokes to the cells via shear forces.[133,134] Investigations have found that direct injection of stem cells via syringe-based techniques increase the linear velocity of the cells as they pass through the needle and can negatively affect cell viability due to the disturbance of the cell membrane.[133] It has been found that with current clinical injections that utilize saline as the cell carrier, up to 40% of cells did not survive the injection procedure.[134] There are currently various strategies proposed to protect the cells from mechanical forces, such as cell encapsulation within micro-carrier hydrogels.[134,135] An additional protective strategy suggested is to surround the cells in alginate beads, in which it is hypothesized that forming a protective covering around the cells would limit the mechanical forces and therefore increase cell viability upon direct injection.[133,136] Moreover, investigations into the use of hydrogel-based carriers for the direct intra-articular injection of hAMSCs and hADSCs within the knee joint is suggested in order to improve cell viability upon transplantation.

5.3 Cell Surface Engineering and Signaling Pathway Inhibition

A novel approach to regenerative cell-based therapy includes the investigation into cell surface engineering in which the cell membrane is customized to moderate cellular interactions and functions. Research into this field holds great potential as adaptations to the cell surface can lead to control over stem cell fate as well as modulating specific ligand-receptor binding to ultimately affect downstream effector functions.[137–139] The cell surface comprises of various proteins, glycans, and lipids that play critical roles in cell

adhesion, cell-cell communication and recognition, as well as signal transduction which ultimately governs the fate of the cell.[140] Currently, there are several methods aimed to modify the cell surface, such as chemical, enzymatic, and physical approaches, in which these strategies have been employed for various transplantation and targeted cell delivery applications in order to manipulate intracellular signaling and cell fate.[137] Herein, a suggested future investigation into modulating the cell surface for an enhanced affinity in the target tissue site and inhibition of the nuclear factor-kappa B (NF-κB) pathway will be described.

One of the main challenges in advancing the therapeutic efficacy of stem cell-based therapy is how to not only guide the cells into the specific target tissue site but also to ensure they remain in the area.[141] As cell retention is a major limitation, improving the preservation of cells at the target tissue is currently being investigated for OA applications. Lim et al. developed an approach to modifying the mesenchymal stem cell (MSCs) surface in conjunction with a homing peptide and recombinant protein to aid in migration of cells to the target site.[142] The group's results indicated that inclusion of the targeted ligand on the cell surfaces assisted the migration of the cells toward their molecular target. Future studies into enhancing the retention and affinity of stem cells in the knee joint is warranted.

In addition to cellular interactions, the cell surface plays a role in signal transduction in which the signal being transmitted intracellularly can elicit distinct biochemical responses. One of the driving pathways of OA is the initiation of the NF-κB pathway in which upon activation, expression of genes that stimulate mediators that contribute to the destruction of the joint occurs.[73] Damage-associated molecular patterns (DAMPs) and fragments induced by mechanical stress serve as ligands that binds to toll-like receptors (TLRs) expressed on chondrocyte surfaces. This ultimately induces the activation NF-κB cascade of pro-inflammatory mediators such as cytokines, chemokines, and degradation components which serve to disrupt the matrix and induce a progressive cycle of destruction hallmarked in OA pathogenesis. Strategies directed to restrict NF-κB signaling and ultimately limit the activation of pro-inflammatory mechanisms may offer possible OA treatment options. The inhibition of the NF-κB pathway via the incorporation of pharmacologic agents, chemical components, and various receptor agonists have been explored in which glycosaine hydrochloride and thalidomide has been observed to block the IL-1β and TNF-α mediated activation of NF-κB.[73,143,144] Additionally IL-1 receptor antagonist (IL-1Ra) and TNF-R has been shown to down-regulate NF-κB activity.[145] Various methods and investigations to inhibit the signaling activation of NF-κB is warranted in order to inhibit the production of various degrading products of OA.

Moreover, the cell surface is an essential characteristic of cell function in which modulating the cell membrane provides opportunities to regulate the biochemical and

cellular mechanisms in cell-based therapies including OA clinical applications. Therefore, future studies exploring cell surface engineering for improvement of cell retention and inhibition of NF-κB signaling pathway is suggested.

5.4 Summary

Moreover, the use of stem cells for regenerative therapy has shown promise as an optimal therapeutic source to mitigate OA progression *in vitro*; however, the findings herein highlight the current limitations of stem cell-based therapy once transplanted *in vivo* and introduced in to the complex physiologic environment. Therefore, further investigations are warranted improve the regenerative capabilities of stem cells *in vivo* in order to provide a clinically significant therapeutic effect.

APPENDIX

ADDITIONAL DATA AND FIGURES

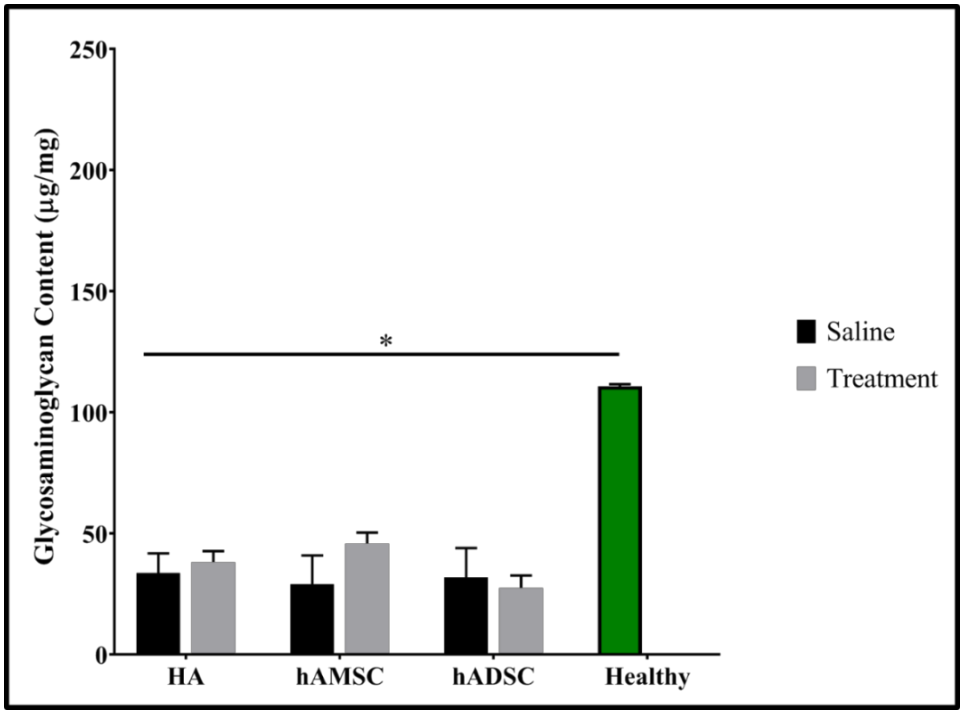

Figure A.1: Average GAG content in the lateral femoral compartment of the DHGP knee demonstrating statistically higher average concentrations of GAG for healthy 2-month old DHGP knees compared to all 9 month-old groups.

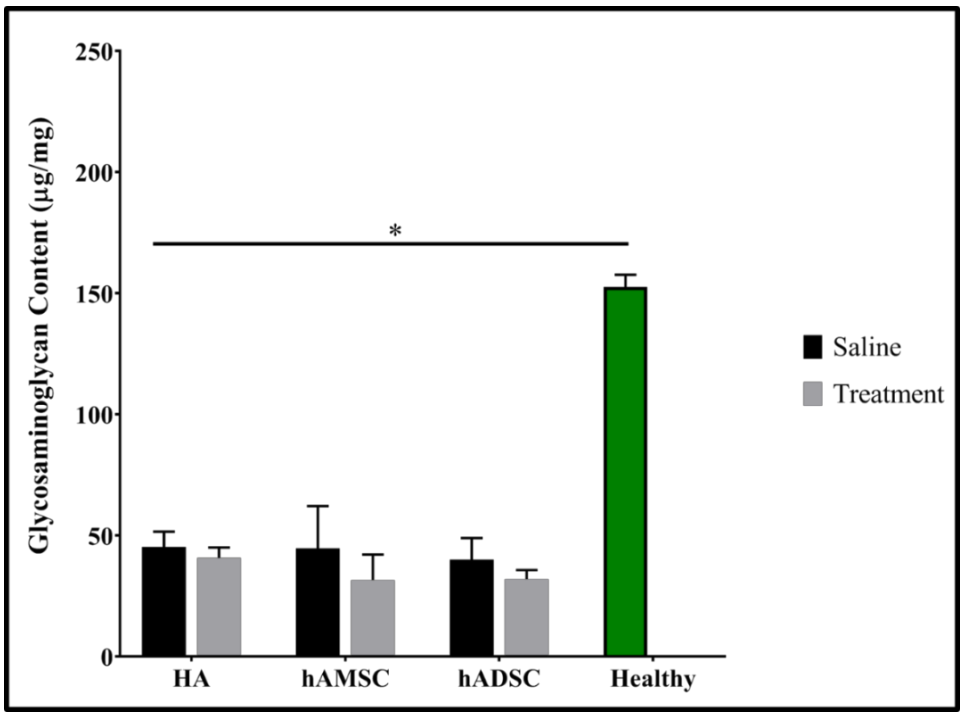

Figure A.2: Average GAG content in the lateral tibia compartment of the DHGP knee demonstrating statistically higher average concentrations of GAG for healthy 2-month old DHGP knees compared to all 9 month-old groups.

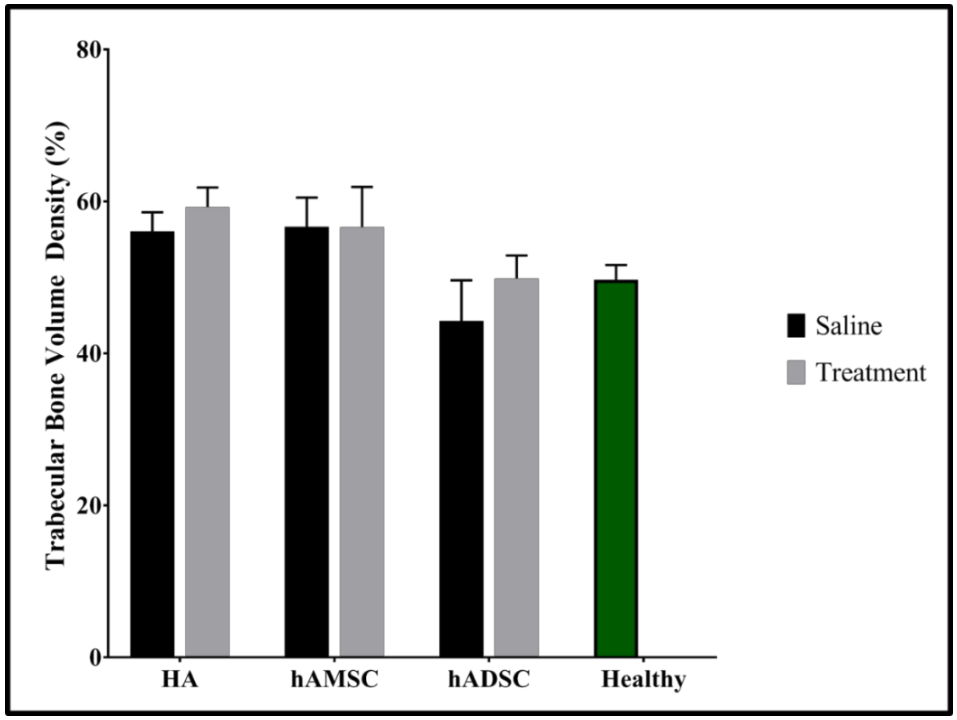

Figure A.3: Average subchondral trabecular bone volume density (BV/TV) in the lateral compartment of the tibia.

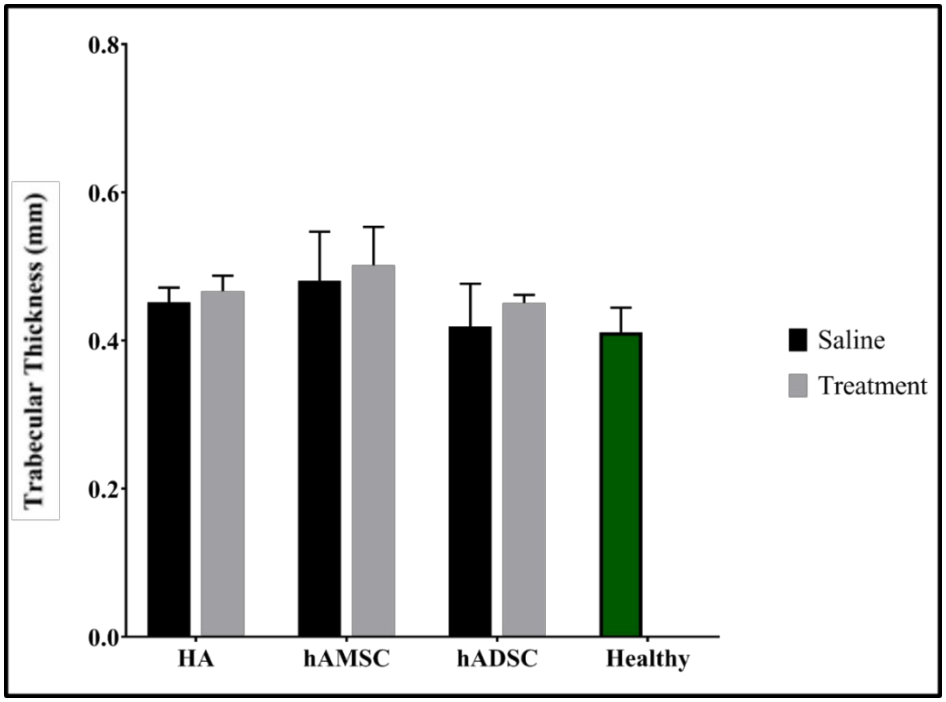

Figure A.4: Average trabecular thickness in the medial compartment of the tibia.

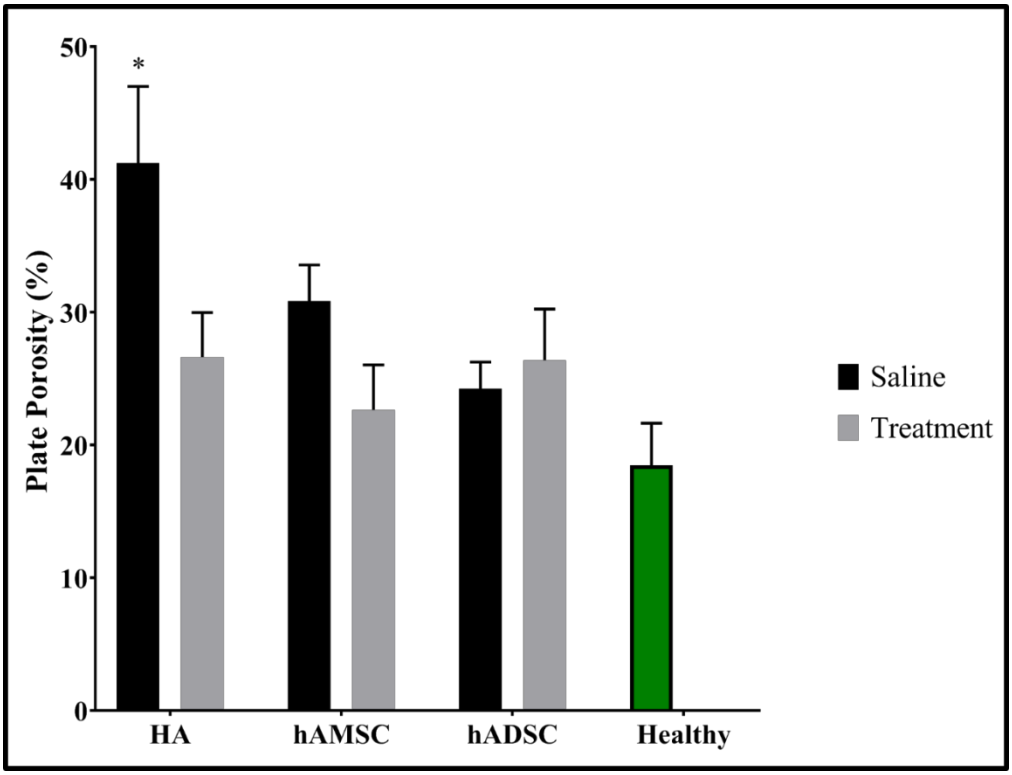

Figure A.5: Average subchondral bone plate porosity in the medial compartment of the tibia. The star represents statistical significance in which ($p<0.05$).

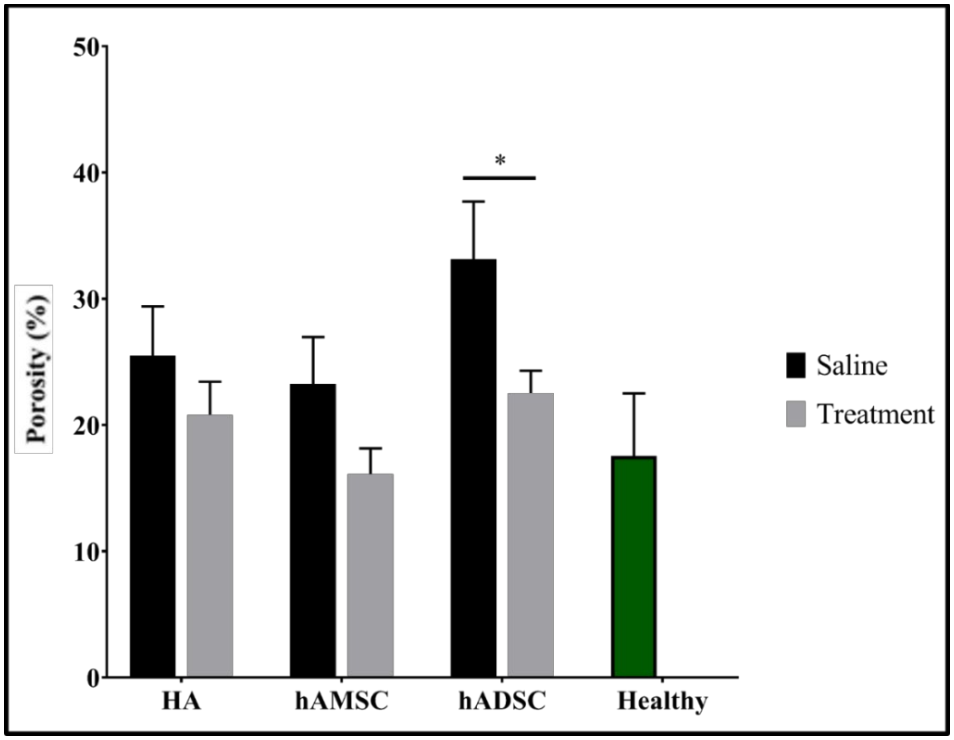

Figure A.6: Average subchondral bone plate porosity in the lateral compartment of the tibia. The star represents statistical significance in which ($p<0.05$).

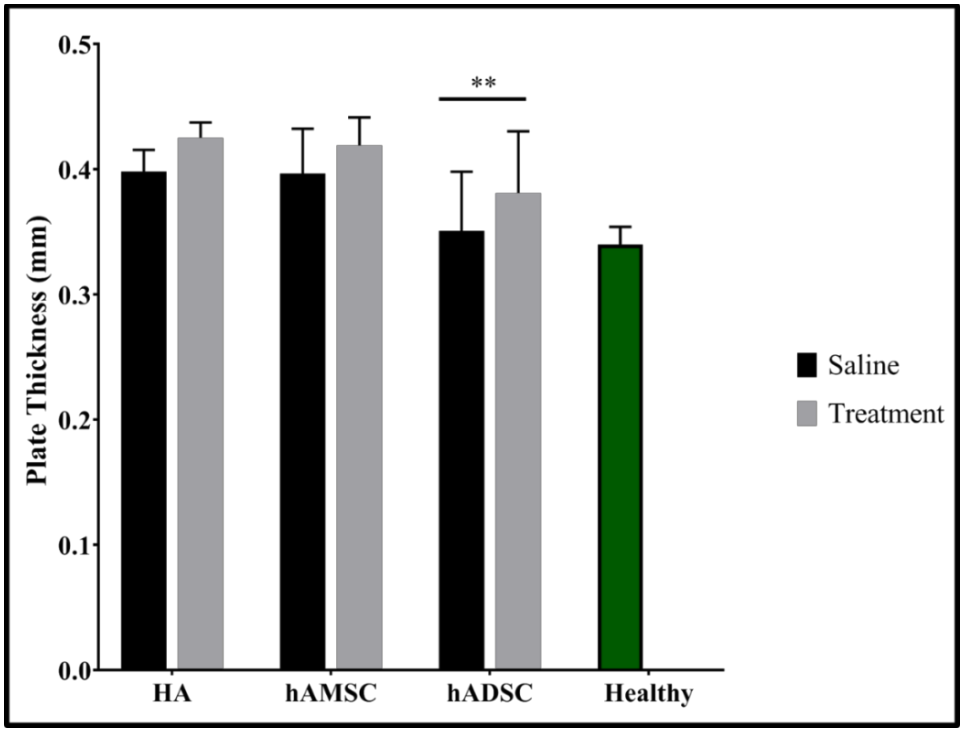

Figure A.7: Average subchondral bone plate thickness in the lateral compartment of the tibia. Two star represents statistical significance in which ($p<0.01$).

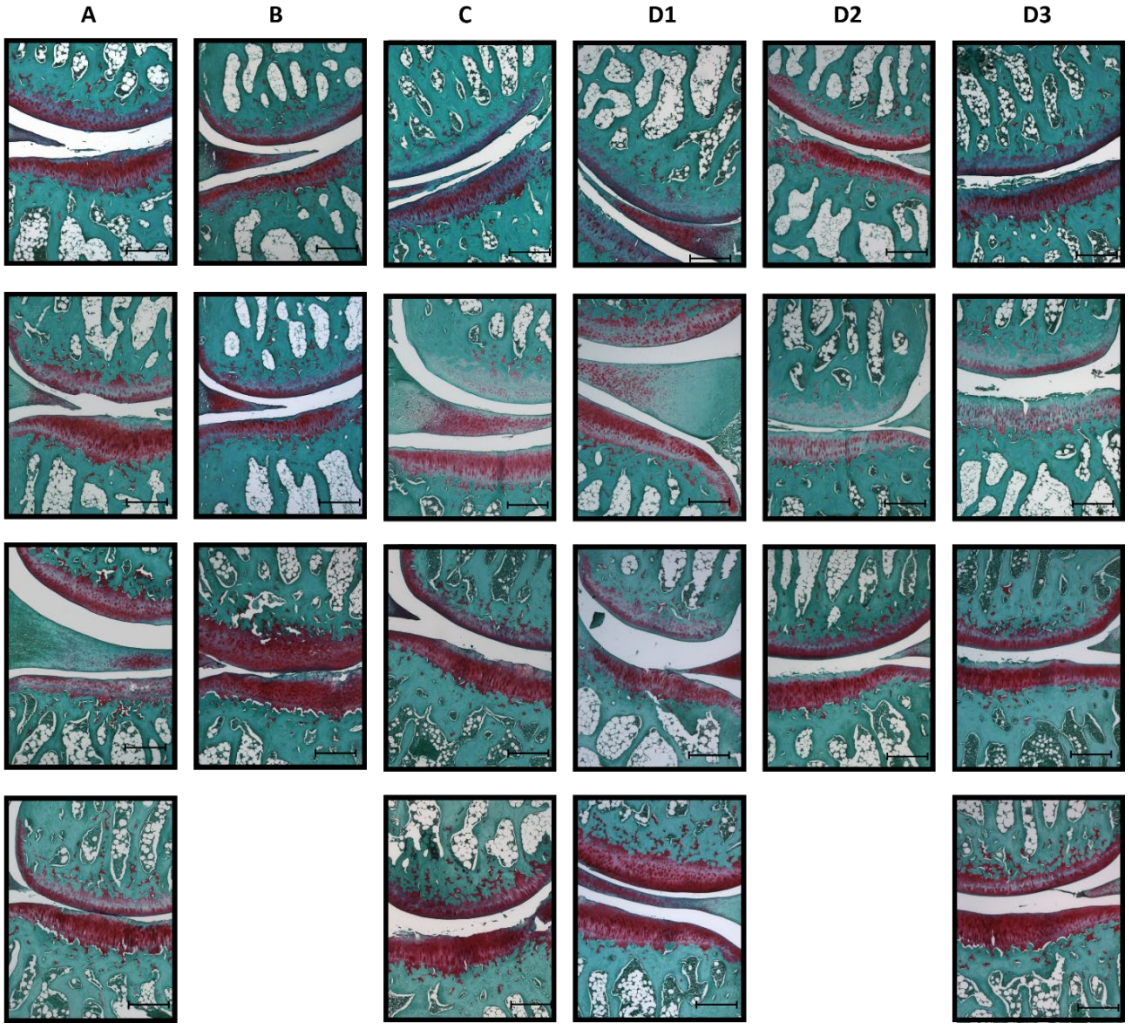

Figure A.8: All Safranin-O stained 9-month old DHGP knees for semi-quantitative histological evaluation. Column A represents HA treatment, column B represents hADSC treatment, column C represents hAMSC treatment, and columns D1, D2, and D3 represent the paired and corresponding saline controls.

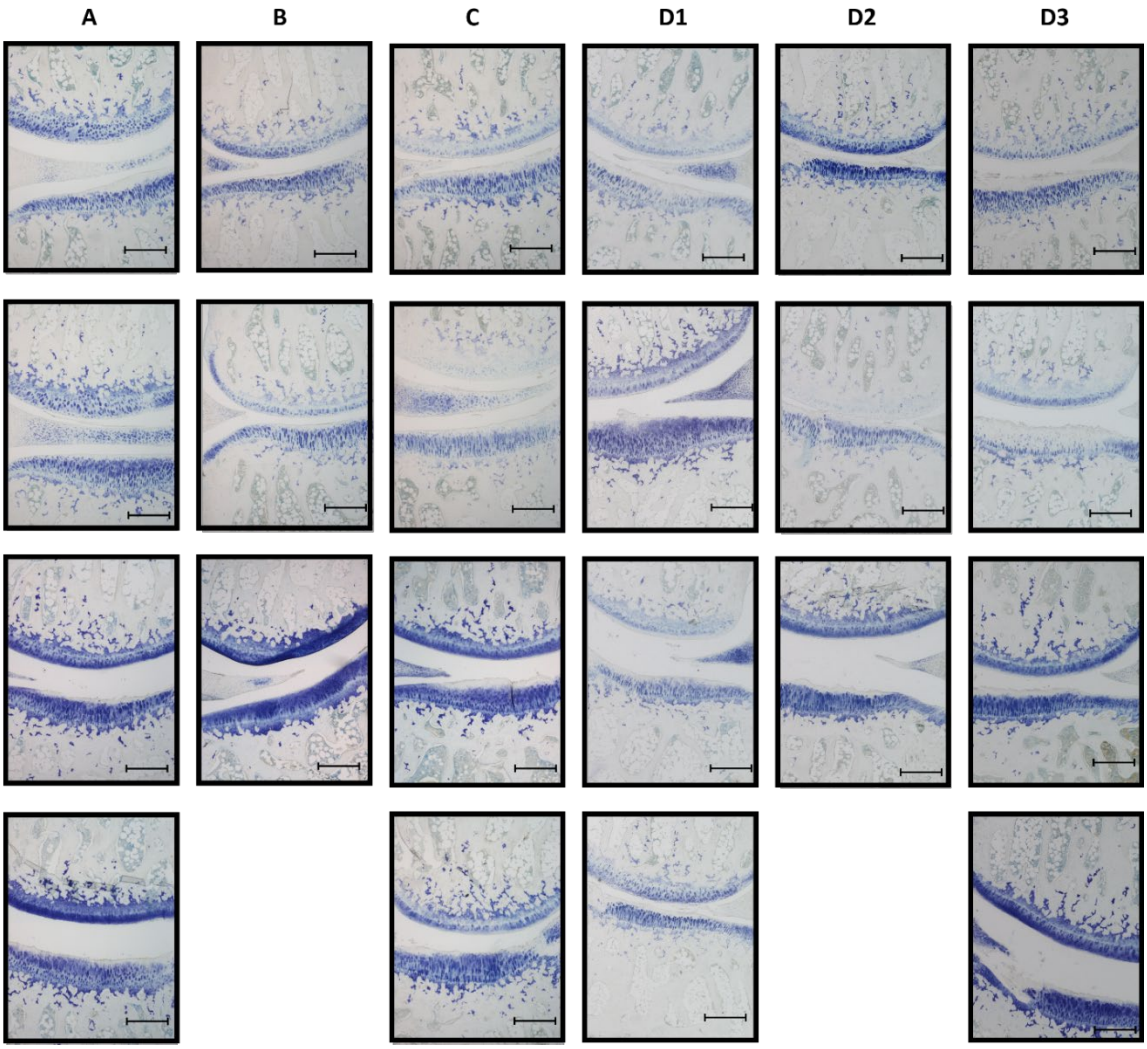

Figure A.9: All Toluidine Blue stained 9-month old DHGP knees for semi-quantitative histological evaluation. Column A represents HA treatment, column B represents hADSC treatment, column C represents hAMSC treatment, and columns D1, D2, and D3 represent the paired and corresponding saline controls.

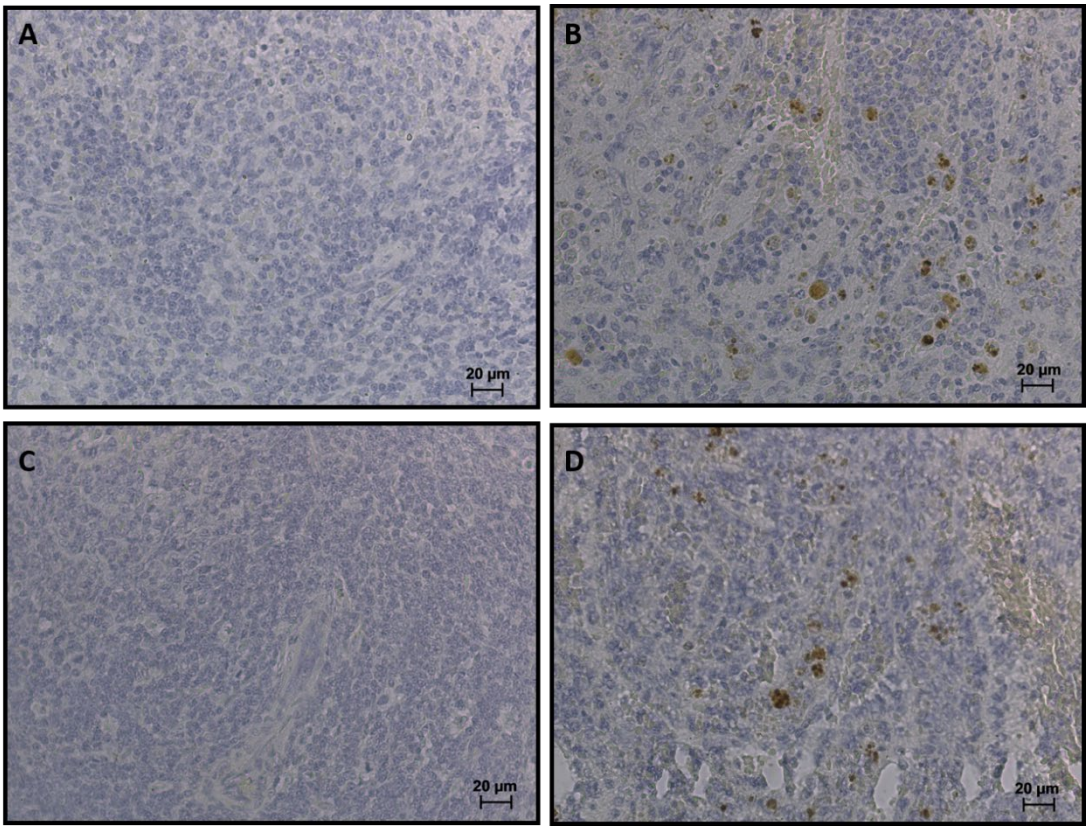

Figure A.10: Harvested DHGP spleen as a positive control for detection of DHGP macrophages via IHC. Panels A and C represent the negative control, while panels B and D represent the positive control containing Mouse Anti-Guinea Macrophage primary antibody, in which positive staining is evident in both positive samples.

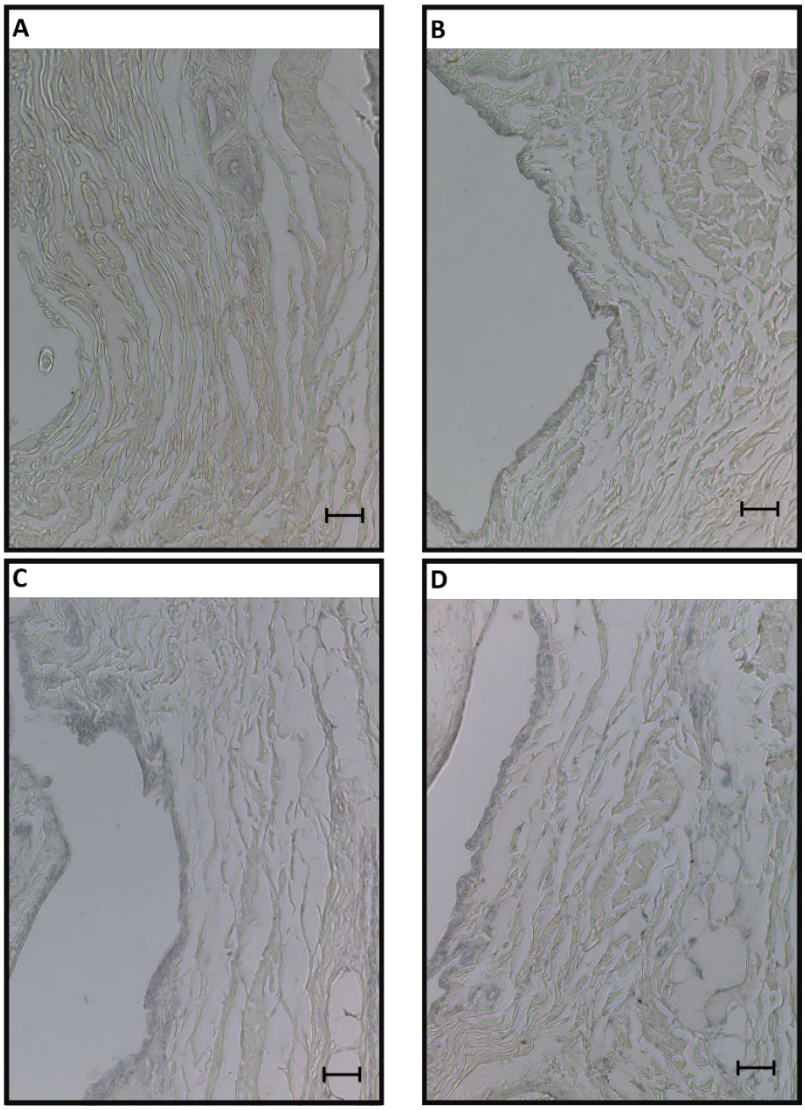

Figure A.11: Representative synovium samples of 9-month old DHGPs that were targeted for detection of DHGP macrophages. Panel A represents the negative control of and HA treated DHGP, while panel B represents the positive control. Similarly, panel C represents the negative control of a saline injected DHGP knee, while panel D represents the positive control. No positive staining is observed in all images.

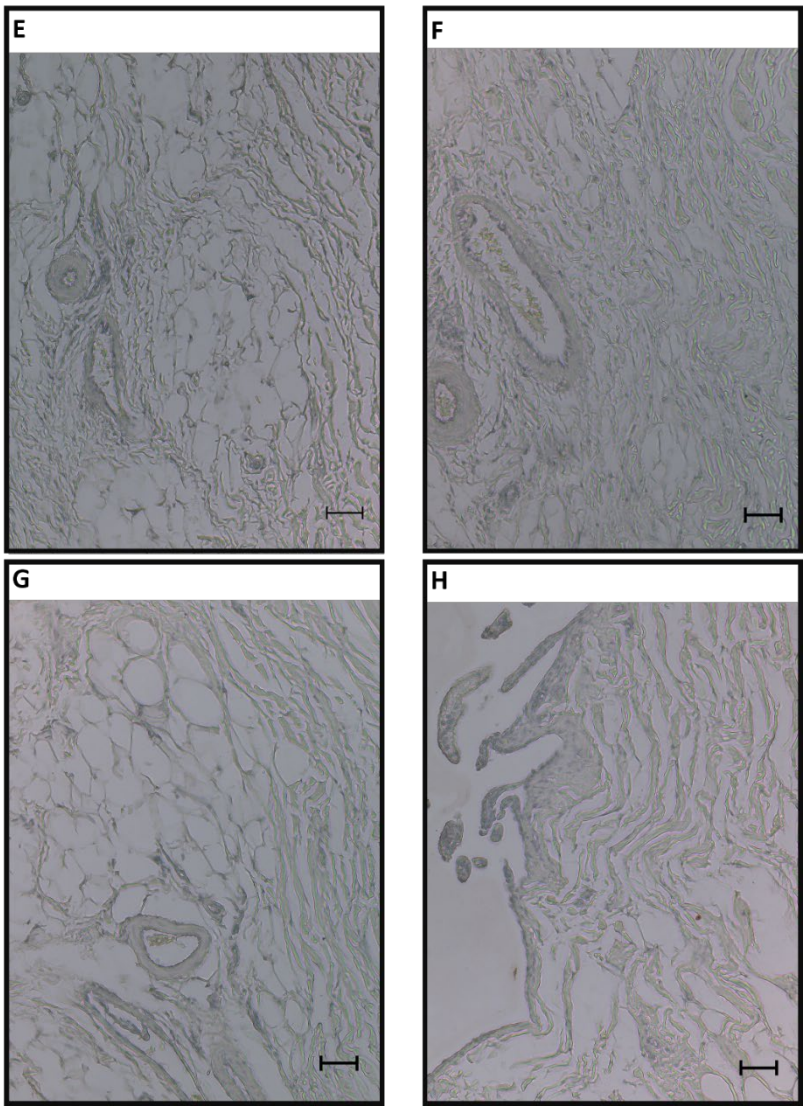

Figure A.12: Representative synovium samples of 9-month old DHGPs that were targeted for detection of DHGP macrophages. Panel A represents the negative control of an hAMSC treated DHGP, while panel B represents the positive control. Similarly, panel C represents the negative control of an hADSC injected DHGP knee, while panel D represents the positive control. No positive staining is observed in all images.

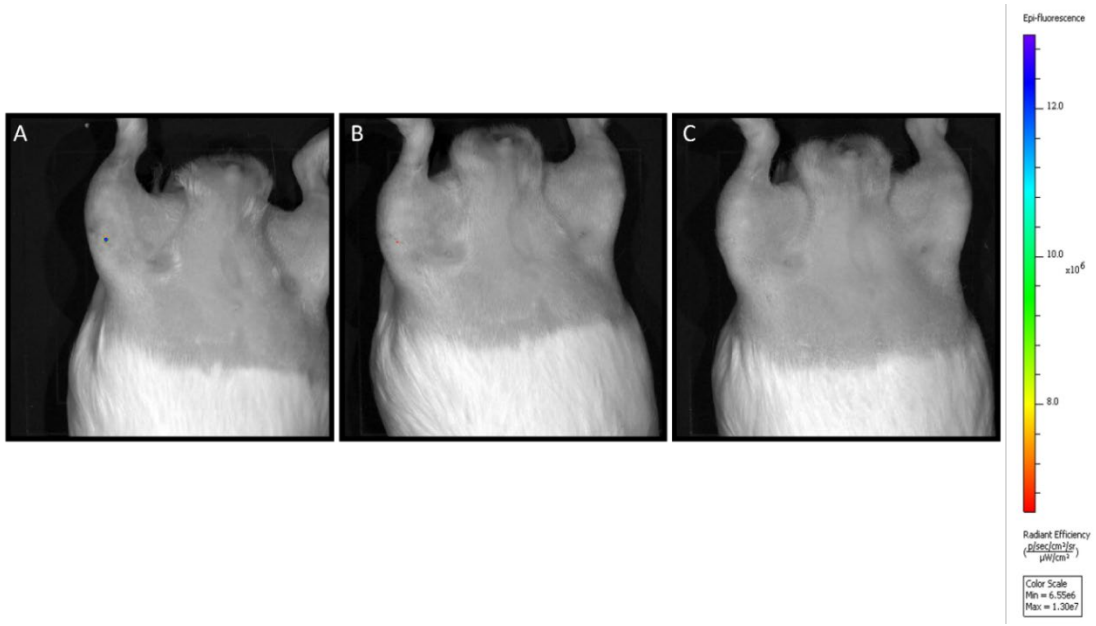

Figure A.13: Longitudinal IVIS Spectrum imaging of a DHGP (animal 3) injected with tagged hAMSCs. Panel A represents Day 0, panel B represents Day 3, and Panel C represents Day 6 in which fluorescence immediately declines.

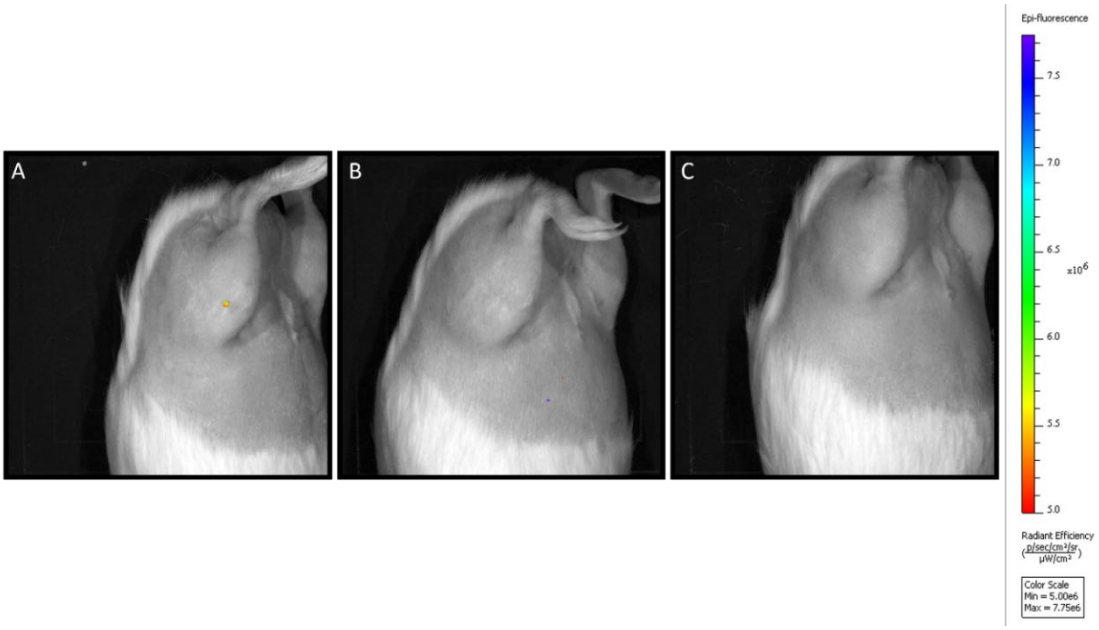

Figure A.14: Longitudinal IVIS Spectrum imaging of a DHGP (animal 4) injected with tagged hAMDCs. Panel A represents Day 0, panel B represents Day 3, and Panel C represents Day 6 in which fluorescence immediately declines.

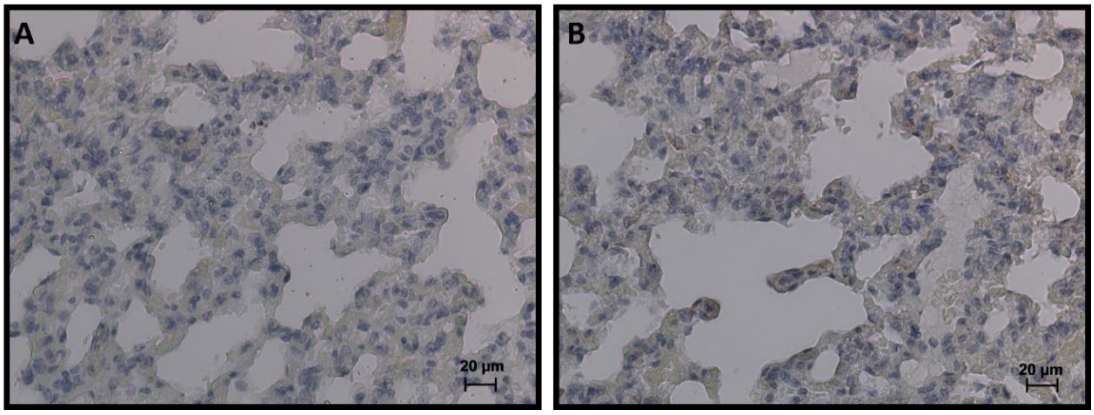

Figure A.15: Representative lung samples of DHGPs injected with tagged hAMSCs that were targeted for detection of human mitochondria. Panel A represents the negative control of the DHGP lung (animal 3), while panel B represents the positive control. Both samples exhibit no human mitochondria detection in the lungs.

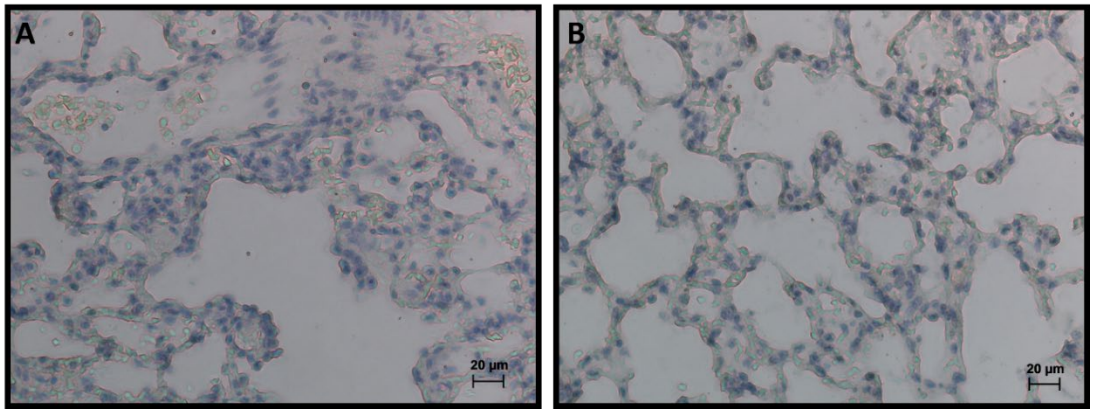

Figure A.16: Representative lung samples of DHGPs injected with tagged hADSCs that were targeted for detection of human mitochondria. Panel A represents the negative control of the DHGP lung (animal 4), while panel B represents the positive control. Both samples exhibit no human mitochondria detection in the lungs.

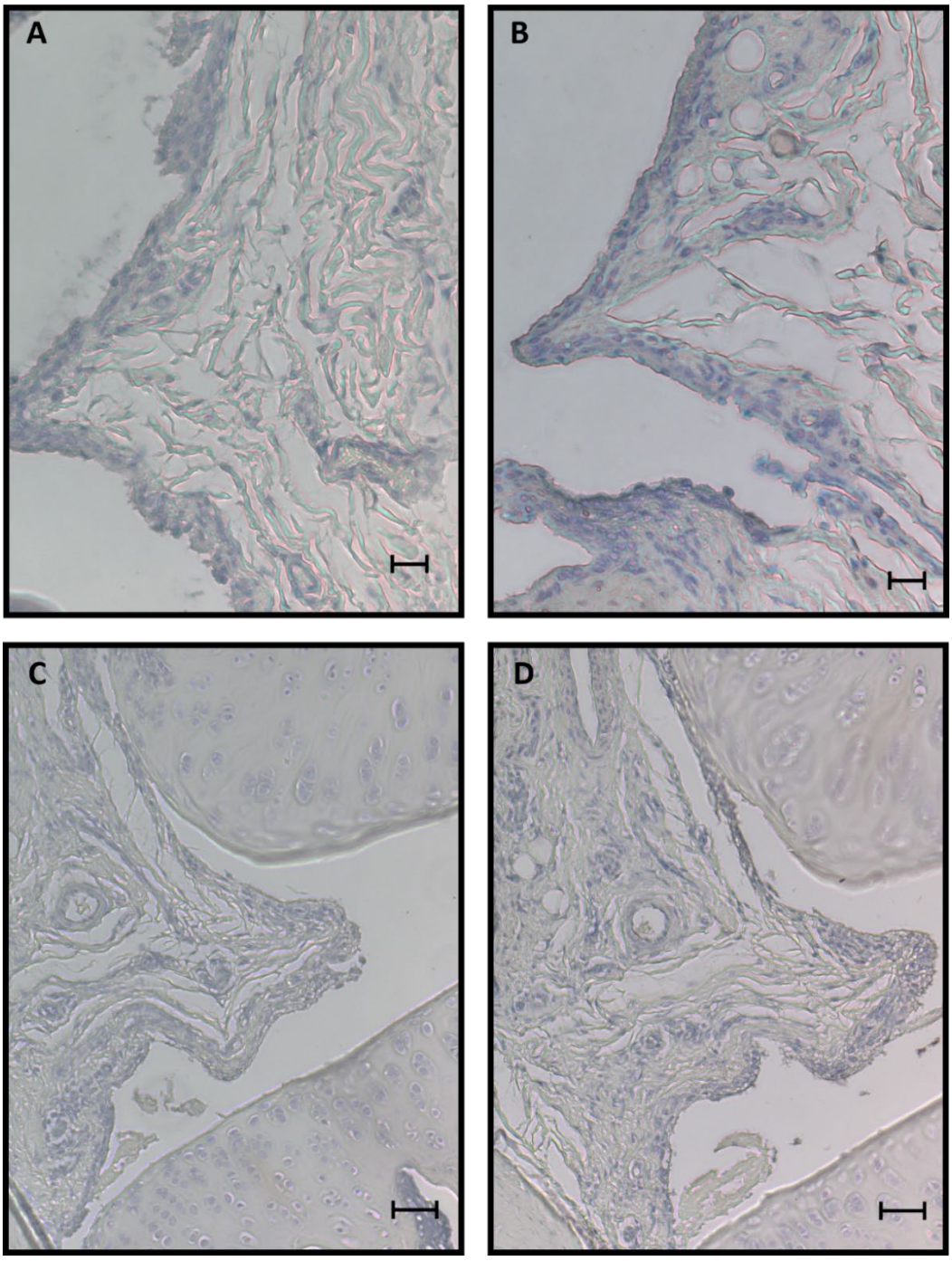

Figure A.17: Representative images of IHC stained synovium and ACL from a DHGP (animal 3) injected with tagged hAMSCs for detection of human mitochondria. Panel A signifies the negative control of the synovium, while panel B represents the positive. Panel C represents the negative control for the ACL, while panel D denotes the positive. All scale bars represent 50 µm.

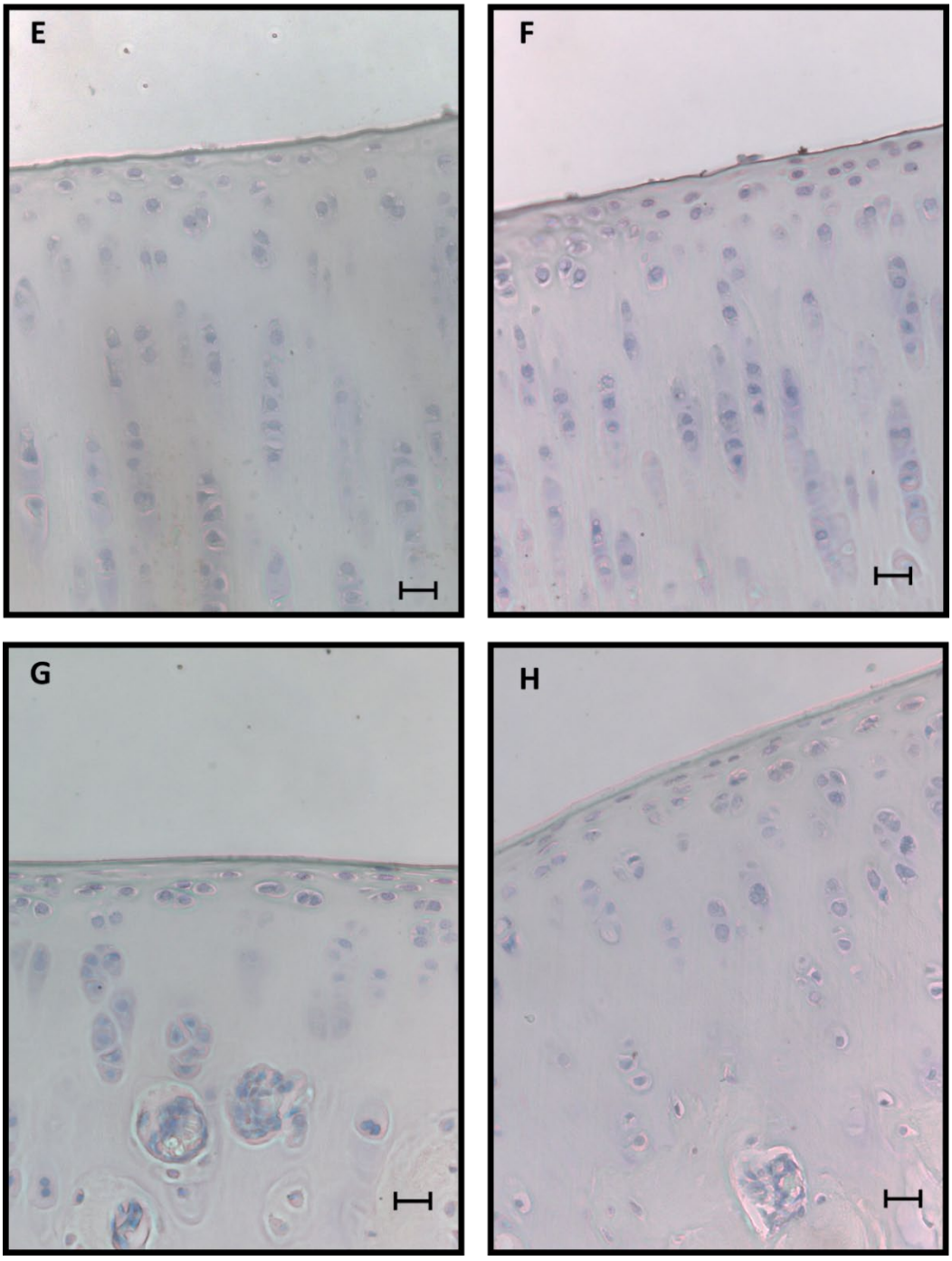

Figure A.18: Representative images of IHC stained tibia and femur articular cartilage from a DHGP (animal 3) injected with tagged hAMSCs for detection of human mitochondria. Panel A signifies the negative control of the synovium, while panel B represents the positive. Panel C represents the negative control for the ACL, while panel D denotes the positive. All scale bars represent 20 µm.

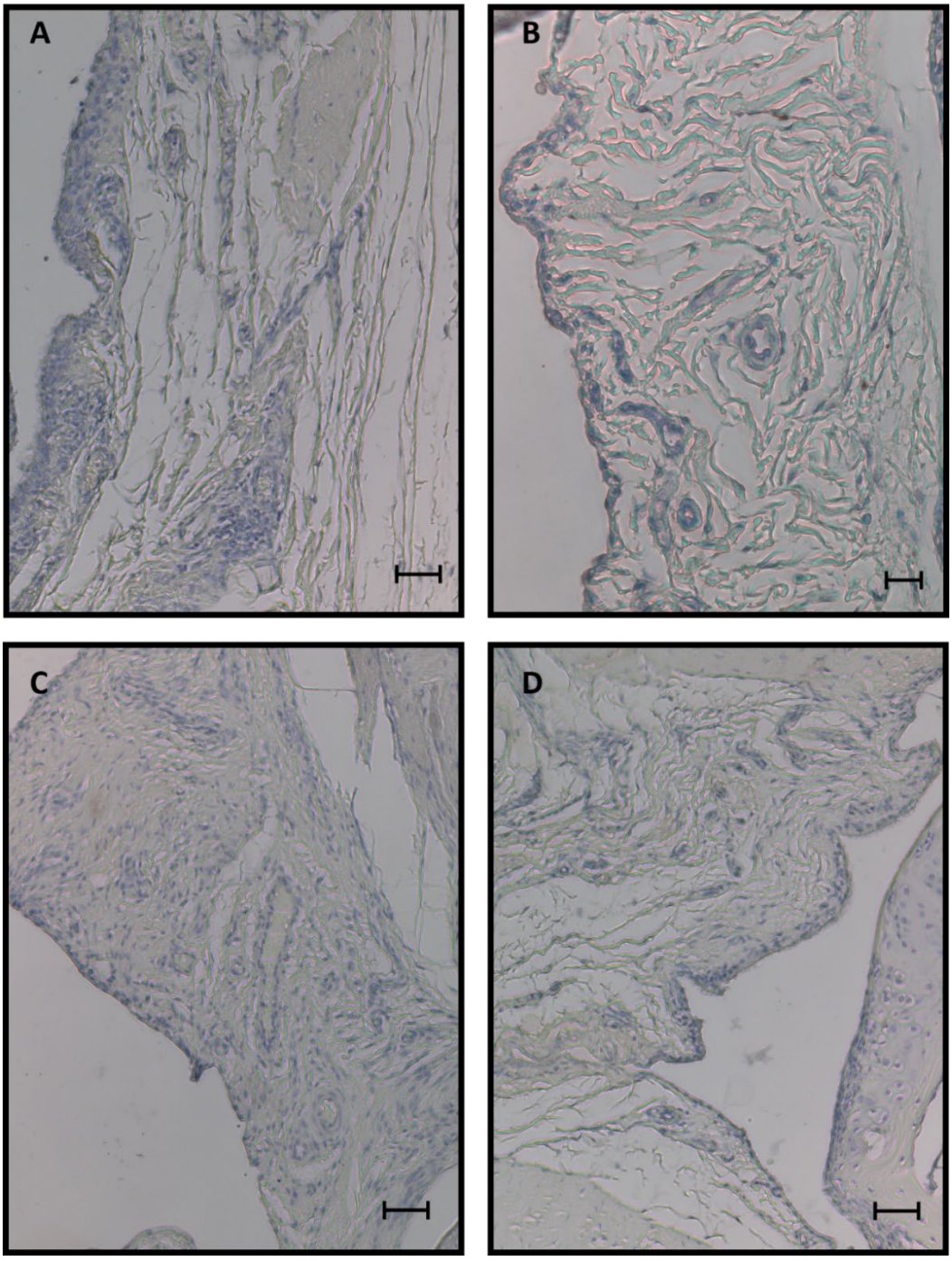

Figure A.19: Representative images of IHC stained synovium and ACL from a DHGP (animal 4) injected with tagged hADSCs for detection of human mitochondria. Panel A signifies the negative control of the synovium, while panel B represents the positive. Panel C represents the negative control for the ACL, while panel D denotes the positive. All scale bars represent 50 µm.

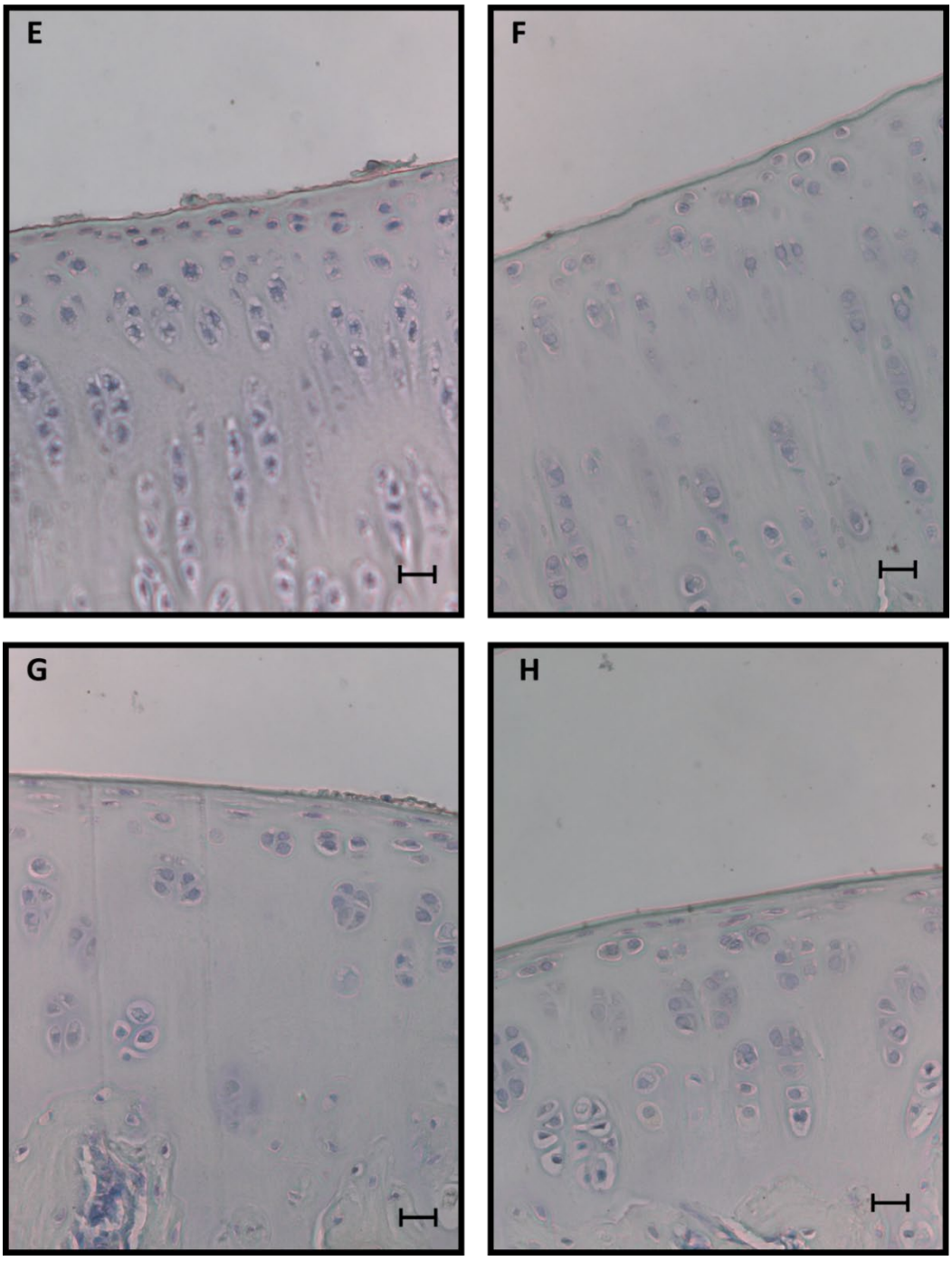

Figure A.20: Representative images of IHC stained tibia and femur articular cartilage from a DHGP (animal 4) injected with tagged hADSCs for detection of human mitochondria. Panel A signifies the negative control of the synovium, while panel B represents the positive. Panel C represents the negative control for the ACL, while panel D denotes the positive. All scale bars represent 20 µm.

REFERENCES

1. Arthritis Research UK Primary Care Centre, Keele University. *Musculoskeletal Matters*. 2010.
2. Lawrence RC, Felson DT, Helmick CG, et al. Estimates of the prevalence of arthritis and other rheumatic conditions in the United States. Part II. *Arthritis Rheum*. 2008;58(1):26-35. doi:10.1002/art.23176
3. No WV, Cheng Y, Hootman J, Murphy L. Morbidity and Mortality Weekly Report. Prevalence of doctor-diagnosed arthritis and arthritis-attributable activity limitation: United States, 2007-2009. *MMWR Morb Mortal Wkly Rep*. 2010;59(39):2007-2009. doi:10.1001/jama.296.22.2671
4. Wallace IJ, Worthington S, Felson DT, et al. Knee osteoarthritis has doubled in prevalence since the mid-20th century. *Proc Natl Acad Sci U S A*. 2017;114(35):9332-9336. doi:10.1073/pnas.1703856114
5. Li G, Yin J, Gao J, et al. Subchondral bone in osteoarthritis: Insight into risk factors and microstructural changes. *Arthritis Res Ther*. 2013. doi:10.1186/ar4405
6. Loeser RF, Goldring SR, Scanzello CR, Goldring MB. Osteoarthritis: A disease of the joint as an organ. *Arthritis Rheum*. 2012. doi:10.1002/art.34453
7. Scanzello CR, Goldring SR. The role of synovitis in osteoarthritis pathogenesis. 2012. doi:10.1016/j.bone.2012.02.012
8. Zhang W, Moskowitz RW, Nuki G, et al. OARSI recommendations for the management of hip and knee osteoarthritis, Part I: Critical appraisal of existing treatment guidelines and systematic review of current research evidence.

Osteoarthr Cartil. 2007;15(9):981-1000. doi:10.1016/J.JOCA.2007.06.014

9. Wojdasiewicz P, Poniatowski ŁA, Szukiewicz D. The role of inflammatory and anti-inflammatory cytokines in the pathogenesis of osteoarthritis. *Mediators Inflamm*. 2014. doi:10.1155/2014/561459
10. Scanzello CR. Chemokines and inflammation in osteoarthritis: Insights from patients and animal models. *J Orthop Res*. 2017. doi:10.1002/jor.23471
11. Monfort J, Rotés-Sala D, Segalés N, et al. Comparative efficacy of intra-articular hyaluronic acid and corticoid injections in osteoarthritis of the first carpometacarpal joint: Results of a 6-month single-masked randomized study. *Jt Bone Spine*. 2015;82(2):116-121. doi:10.1016/J.JBSPIN.2014.08.008
12. Bannuru RR, Vaysbrot EE, Sullivan MC, McAlindon TE. Relative efficacy of hyaluronic acid in comparison with NSAIDs for knee osteoarthritis: A systematic review and meta-analysis. *Semin Arthritis Rheum*. 2014;43(5):593-599. doi:10.1016/J.SEMARTHRIT.2013.10.002
13. Moreland LW. Intra-articular hyaluronan (hyaluronic acid) and hylans for the treatment of osteoarthritis: mechanisms of action. *Arthritis Res Ther*. 2003;5(2):54-67. http://www.ncbi.nlm.nih.gov/pubmed/12718745. Accessed June 29, 2018.
14. Leighton R, Fitzpatrick J, Smith H, Crandall D, Flannery CR, Conrozier T. Systematic clinical evidence review of NASHA (Durolane hyaluronic acid) for the treatment of knee osteoarthritis. *Open Access Rheumatol Res Rev*. 2018;Volume 10:43-54. doi:10.2147/OARRR.S162127

15. Ikeuchi M, Izumi M, Aso K, Sugimura N, Kato T, Tani T. Effects of intra-articular hyaluronic acid injection on immunohistochemical characterization of joint afferents in a rat model of knee osteoarthritis. *Eur J Pain*. 2015;19(3):334-340. doi:10.1002/ejp.551

16. Vannabouathong C, Del Fabbro G, Sales B, et al. Intra-articular Injections in the Treatment of Symptoms from Ankle Arthritis: A Systematic Review. *Foot Ankle Int*. June 2018:107110071877937. doi:10.1177/1071100718779375

17. Zhang L, Hu J, Athanasiou KA. The role of tissue engineering in articular cartilage repair and regeneration. *Crit Rev Biomed Eng*. 2009;37(1-2):1-57. http://www.ncbi.nlm.nih.gov/pubmed/20201770. Accessed June 29, 2018.

18. Rubash H. Hip and Knee Replacements in Canada: Canadian Joint Replacement Registry 2015 Annual Report. 2015;603(September):1-20.

19. Tapp H, Hanley EN, Patt JC, Gruber HE. Adipose-Derived Stem Cells: Characterization and Current Application in Orthopaedic Tissue Repair. *Exp Biol Med*. 2008;234(1):1-9. doi:10.3181/0805/MR-170

20. Lee EH. The potential of stem cells in orthopaedic surgery. *J Bone Jt Surg - Br Vol*. 2006;88-B(7):841-851. doi:10.1302/0301-620X.88B7.17305

21. Otto WR, Wright NA. Mesenchymal stem cells: from experiment to clinic. *Fibrogenesis Tissue Repair*. 2011;4:20. doi:10.1186/1755-1536-4-20

22. Flandry F, Hommel G. Normal Anatomy and Biomechanics of the KneFlandry, F., & Hommel, G. (2011). Normal Anatomy and Biomechanics of the Knee. Sports Medicine and Arthroscopy Review, 19(2), 82–92.

https://doi.org/10.1097/JSA.0b013e318210c0aae. *Sports Med Arthrosc*. 2011;19(2):82-92. doi:10.1097/JSA.0b013e318210c0aa

23. Chatra PS. Bursae around the knee joints. *Indian J Radiol Imaging*. 2012;22(1):27-30. doi:10.4103/0971-3026.95400

24. Human Knee Joint Anatomy Revisited Human Anatomy Knee - Human Anatomy Lesson - Anatomy Sciences. http://anatomysciences.com/human-knee-joint-anatomy-revisited/human-knee-joint-anatomy-revisited-human-anatomy-knee-human-anatomy-lesson-3/. Accessed September 15, 2018.

25. Houard X, Goldring MB, Berenbaum F. Homeostatic Mechanisms in Articular Cartilage and Role of Inflammation in Osteoarthritis. *Curr Rheumatol Rep*. 2013;15(11):375. doi:10.1007/s11926-013-0375-6

26. Sophia Fox AJ, Bedi A, Rodeo SA. The basic science of articular cartilage: structure, composition, and function. *Sports Health*. 2009;1(6):461-468. doi:10.1177/1941738109350438

27. Schmidt TA, Gastelum NS, Nguyen QT, Schumacher BL, Sah RL. Boundary lubrication of articular cartilage: Role of synovial fluid constituents. *Arthritis Rheum*. 2007;56(3):882-891. doi:10.1002/art.22446

28. Smith MD. The normal synovium. *Open Rheumatol J*. 2011;5:100-106. doi:10.2174/1874312901105010100

29. Antonacci JM, Schmidt TA, Serventi LA, et al. Effects of equine joint injury on boundary lubrication of articular cartilage by synovial fluid: role of hyaluronan. *Arthritis Rheum*. 2012;64(9):2917-2926. doi:10.1002/art.34520

30. Das S, Banquy X, Zappone B, Greene GW, Jay GD, Israelachvili JN. Synergistic Interactions between Grafted Hyaluronic Acid and Lubricin Provide Enhanced Wear Protection and Lubrication. *Biomacromolecules*. 2013;14(5):1669-1677. doi:10.1021/bm400327a

31. Blewis ME, Lao BJ, Schumacher BL, Bugbee WD, Sah RL, Firestein GS. Interactive cytokine regulation of synoviocyte lubricant secretion. *Tissue Eng Part A*. 2010;16(4):1329-1337. doi:10.1089/ten.TEA.2009.0210

32. Buckwalter JA, Mankin HJ. Articular cartilage: tissue design and chondrocyte-matrix interactions. *Instr Course Lect*. 1998;47:477-486. http://www.ncbi.nlm.nih.gov/pubmed/9571449. Accessed July 6, 2018.

33. Mow VC, Kuei SC, Lai WM, Armstrong CG. Biphasic Creep and Stress Relaxation of Articular Cartilage in Compression: Theory and Experiments. *J Biomech Eng*. 1980;102(1):73. doi:10.1115/1.3138202

34. Mow VC, Ratcliffe A, Robin Poole A. Cartilage and diarthrodial joints as paradigms for hierarchical materials and structures. *Biomaterials*. 1992;13(2):67-97. doi:10.1016/0142-9612(92)90001-5

35. Responte DJ, Natoli RM, Athanasiou KA. Collagens of articular cartilage: structure, function, and importance in tissue engineering. *Crit Rev Biomed Eng*. 2007;35(5):363-411. http://www.ncbi.nlm.nih.gov/pubmed/19392643. Accessed July 6, 2018.

36. Eyre D. Collagen of articular cartilage. *Arthritis Res*. 2002;4(1):30. doi:10.1186/ar380

37. Yanagishita M. Function of proteoglycans in the extracellular matrix. *Acta Pathol Jpn*. 1993;43(6):283-293. http://www.ncbi.nlm.nih.gov/pubmed/8346704. Accessed July 6, 2018.

38. Vynios DH. Metabolism of cartilage proteoglycans in health and disease. *Biomed Res Int*. 2014;2014:452315. doi:10.1155/2014/452315

39. Bakkum BW. Microscopic Anatomy of the Zygapophysial Joints, Intervertebral Discs, and Other Major Tissues of the Back. *Clin Anat Spine, Spinal Cord, Ans*. January 2014:586-637. doi:10.1016/B978-0-323-07954-9.00014-1

40. Roughley PJ, Lee ER. Cartilage proteoglycans: Structure and potential functions. *Microsc Res Tech*. 1994;28(5):385-397. doi:10.1002/jemt.1070280505

41. KIANI C, CHEN L, WU YJ, YEE AJ, YANG BB. Structure and function of aggrecan. *Cell Res*. 2002;12(1):19-32. doi:10.1038/sj.cr.7290106

42. Knudson CB, Knudson W. Cartilage proteoglycans. *Semin Cell Dev Biol*. 2001;12(2):69-78. doi:10.1006/scdb.2000.0243

43. Zaucke F. Cartilage Glycoproteins. In: *Cartilage*. Cham: Springer International Publishing; 2016:55-81. doi:10.1007/978-3-319-29568-8_3

44. Akkiraju H, Nohe A. Role of Chondrocytes in Cartilage Formation, Progression of Osteoarthritis and Cartilage Regeneration. *J Dev Biol*. 2015;3(4):177-192. doi:10.3390/jdb3040177

45. Bhosale AM, Richardson JB. Articular cartilage: structure, injuries and review of management. *Br Med Bull*. 2008;87(1):77-95. doi:10.1093/bmb/ldn025

46. Science H, Zealand N, Poole C a, Science H, Zealand N. Articular cartilage

chondrons: form, function and failure. *J Anat*. 1997;191:1-13. doi:10.1046/j.1469-7580.1997.19110001.x

47. Loeser RF, Goldring SR, Scanzello CR, Goldring MB. Osteoarthritis: a disease of the joint as an organ. *Arthritis Rheum*. 2012;64(6):1697-1707. doi:10.1002/art.34453

48. Schulze-Tanzil G. Activation and dedifferentiation of chondrocytes: Implications in cartilage injury and repair. *Ann Anat - Anat Anzeiger*. 2009;191(4):325-338. doi:10.1016/J.AANAT.2009.05.003

49. Sakata R, Iwakura T, Reddi AH. Regeneration of Articular Cartilage Surface: Morphogens, Cells, and Extracellular Matrix Scaffolds. *Tissue Eng Part B Rev*. 2015;21(5):461-473. doi:10.1089/ten.TEB.2014.0661

50. Kalamegam G, Memic A, Budd E, Abbas M, Mobasheri A. A Comprehensive Review of Stem Cells for Cartilage Regeneration in Osteoarthritis. In: *Advances in Experimental Medicine and Biology*. ; 2018. doi:10.1007/5584_2018_205

51. Havelka S, Horn V, Spohrová D, Valouch P. The calcified-noncalcified cartilage interface: the tidemark. *Acta Biol Hung*. 1984;35(2-4):271-279. http://www.ncbi.nlm.nih.gov/pubmed/6242456. Accessed July 6, 2018.

52. Suri S, Walsh DA. Osteochondral alterations in osteoarthritis. *Bone*. 2012;51(2):204-211. doi:10.1016/J.BONE.2011.10.010

53. Madry H, van Dijk CN, Mueller-Gerbl M. The basic science of the subchondral bone. *Knee Surgery, Sport Traumatol Arthrosc*. 2010;18(4):419-433. doi:10.1007/s00167-010-1054-z

54. Radin EL, Rose RM. Role of subchondral bone in the initiation and progression of cartilage damage. *Clin Orthop Relat Res*. 1986;(213):34-40. http://www.ncbi.nlm.nih.gov/pubmed/3780104. Accessed July 5, 2018.

55. Milz S, Putz R. Quantitative morphology of the subchondral plate of the tibial plateau. *J Anat*. 1994;185 (Pt 1)(Pt 1):103-110. http://www.ncbi.nlm.nih.gov/pubmed/7559105. Accessed July 5, 2018.

56. Goldring SR. Alterations in periarticular bone and cross talk between subchondral bone and articular cartilage in osteoarthritis. *Ther Adv Musculoskelet Dis*. 2012;4(4):249-258. doi:10.1177/1759720X12437353

57. Tessier JJ, Bowyer J, Brownrigg NJ, et al. Characterisation of the guinea pig model of osteoarthritis by in vivo three-dimensional magnetic resonance imaging. *Osteoarthr Cartil*. 2003;11(12):845-853. http://www.ncbi.nlm.nih.gov/pubmed/14629960. Accessed July 14, 2018.

58. Mobasheri A, Kalamegam G, Musumeci G, Batt ME. Chondrocyte and mesenchymal stem cell-based therapies for cartilage repair in osteoarthritis and related orthopaedic conditions. *Maturitas*. 2014;78(3):188-198. doi:10.1016/J.MATURITAS.2014.04.017

59. Uth K, Trifonov D. Stem cell application for osteoarthritis in the knee joint: A minireview. *World J Stem Cells*. 2014;6(5):629-636. doi:10.4252/wjsc.v6.i5.629

60. Larsson S, Englund M, Struglics A, Lohmander LS. Interleukin-6 and tumor necrosis factor alpha in synovial fluid are associated with progression of radiographic knee osteoarthritis in subjects with previous meniscectomy.

Osteoarthr Cartil. 2015;23(11):1906-1914. doi:10.1016/j.joca.2015.05.035

61. Mathiessen A, Conaghan PG. Synovitis in osteoarthritis: current understanding with therapeutic implications. *Arthritis Res Ther*. 2017;19(1):18. doi:10.1186/s13075-017-1229-9

62. Knee Osteoarthritis - An Overview - Robert Howells. http://www.roberthowells.com.au/conditions-and-treatment/knee-osteoarthritis-overview/. Accessed September 15, 2018.

63. Goldring MB. Chondrogenesis, chondrocyte differentiation, and articular cartilage metabolism in health and osteoarthritis. *Ther Adv Musculoskelet Dis*. 2012;4(4):269-285. doi:10.1177/1759720X12448454

64. van der Kraan PM, van den Berg WB. Chondrocyte hypertrophy and osteoarthritis: role in initiation and progression of cartilage degeneration? *Osteoarthr Cartil*. 2012;20(3):223-232. doi:10.1016/J.JOCA.2011.12.003

65. Goldring MB, Otero M. Inflammation in osteoarthritis. *Curr Opin Rheumatol*. 2011;23(5):471-478. doi:10.1097/BOR.0b013e328349c2b1

66. Huebner JL, Otterness IG, Freund EM, Caterson B, Kraus VB. Collagenase 1 and collagenase 3 expression in a guinea pig model of osteoarthritis. *Arthritis Rheum*. 1998;41(5):877-890. doi:10.1002/1529-0131(199805)41:5<877::AID-ART16>3.0.CO;2-#

67. Rose BJ, Kooyman DL. A Tale of Two Joints: The Role of Matrix Metalloproteases in Cartilage Biology. *Dis Markers*. 2016;2016:4895050. doi:10.1155/2016/4895050

68. Goldring MB, Otero M, Tsuchimochi K, Ijiri K, Li Y. Defining the roles of inflammatory and anabolic cytokines in cartilage metabolism. *Ann Rheum Dis*. 2008;67 Suppl 3(0 3):iii75-82. doi:10.1136/ard.2008.098764

69. Kraus VB, Huebner JL, DeGroot J, Bendele A. The OARSI histopathology initiative - recommendations for histological assessments of osteoarthritis in the guinea pig. *Osteoarthr Cartil*. 2010. doi:10.1016/j.joca.2010.04.015

70. Saklatvala J. Tumour necrosis factor α stimulates resorption and inhibits synthesis of proteoglycan in cartilage. *Nature*. 1986;322(6079):547-549. doi:10.1038/322547a0

71. Borzì RM, Mazzetti I, Cattini L, Uguccioni M, Baggiolini M, Facchini A. Human chondrocytes express functional chemokine receptors and release matrix-degrading enzymes in response to C-X-C and C-C chemokines. *Arthritis Rheum*. 2000;43(8):1734-1741. doi:10.1002/1529-0131(200008)43:8<1734::AID-ANR9>3.0.CO;2-B

72. Sellam J, Berenbaum F. The role of synovitis in pathophysiology and clinical symptoms of osteoarthritis. *Nat Rev Rheumatol*. 2010;6(11):625-635. doi:10.1038/nrrheum.2010.159

73. Rigoglou S, Papavassiliou AG. The NF-κB signalling pathway in osteoarthritis. *Int J Biochem Cell Biol*. 2013;45(11):2580-2584. doi:10.1016/j.biocel.2013.08.018

74. Pan J, Zhou X, Li W, Novotny JE, Doty SB, Wang L. In situ measurement of transport between subchondral bone and articular cartilage. *J Orthop Res*. 2009;27(10):1347-1352. doi:10.1002/jor.20883

75. Lajeunesse D, Massicotte F, Pelletier J-P, Martel-Pelletier J. Subchondral bone sclerosis in osteoarthritis: not just an innocent bystander. *Mod Rheumatol*. 2003;13(1):0007-0014. doi:10.3109/s101650300001

76. Intema F, Hazewinkel HAW, Gouwens D, et al. In early OA, thinning of the subchondral plate is directly related to cartilage damage: results from a canine ACLT-meniscectomy model. *Osteoarthr Cartil*. 2010;18(5):691-698. doi:10.1016/j.joca.2010.01.004

77. Batiste DL, Kirkley A, Laverty S, Thain LMF, Spouge AR, Holdsworth DW. Ex vivo characterization of articular cartilage and bone lesions in a rabbit ACL transection model of osteoarthritis using MRI and micro-CT. *Osteoarthr Cartil*. 2004;12(12):986-996. doi:10.1016/j.joca.2004.08.010

78. Radakovich LB, Marolf AJ, Shannon JP, Pannone SC, Sherk VD, Santangelo KS. Development of a microcomputed tomography scoring system to characterize disease progression in the Hartley guinea pig model of spontaneous osteoarthritis. *Connect Tissue Res*. December 2017:1-11. doi:10.1080/03008207.2017.1409218

79. Teeple E, Jay GD, Elsaid KA, Fleming BC. Animal Models of Osteoarthritis: Challenges of Model Selection and Analysis. *AAPS J*. 2013;15(2):438-446. doi:10.1208/s12248-013-9454-x

80. Oegema TR, Visco D. Animal models of osteoarthritis. 1999;1(4):349-367.

81. Lampropoulou-Adamidou K, Lelovas P, Karadimas E V., et al. Useful animal models for the research of osteoarthritis. *Eur J Orthop Surg Traumatol*. 2014;24(3):263-271. doi:10.1007/s00590-013-1205-2

82. Kuyinu EL, Narayanan G, Nair LS, Laurencin CT. Animal models of osteoarthritis: classification, update, and measurement of outcomes. *J Orthop Surg Res*. 2016;11:19. doi:10.1186/s13018-016-0346-5

83. Gregory MH, Capito N, Kuroki K, Stoker AM, Cook JL, Sherman SL. A review of translational animal models for knee osteoarthritis. *Arthritis*. 2012;2012:764621. doi:10.1155/2012/764621

84. Kim JE, Song D, Kim SH, Jung Y, Kim SJ. Development and characterization of various osteoarthritis models for tissue engineering. Lammi MJ, ed. *PLoS One*. 2018;13(3):e0194288. doi:10.1371/journal.pone.0194288

85. Fenty MC, Dodge GR, Kassey VB, Witschey WRT, Borthakur A, Reddy R. Quantitative cartilage degeneration associated with spontaneous osteoarthritis in a guinea pig model. *J Magn Reson Imaging*. 2012;35(4):891-898. doi:10.1002/jmri.22867

86. Jimenez PA, Glasson SS, Trubetskoy O V, Haimes HB. Spontaneous osteoarthritis in Dunkin Hartley guinea pigs: histologic, radiologic, and biochemical changes. *Lab Anim Sci*. 1997;47(6):598-601. http://www.ncbi.nlm.nih.gov/pubmed/9433695. Accessed July 15, 2018.

87. Huebner JL, Kraus VB. Assessment of the utility of biomarkers of osteoarthritis in the guinea pig. *Osteoarthr Cartil*. 2006. doi:10.1016/j.joca.2006.03.007

88. Yan J-Y, Tian F-M, Wang W-Y, et al. Age Dependent Changes in Cartilage Matrix, Subchondral Bone Mass, and Estradiol Levels in Blood Serum, in Naturally Occurring Osteoarthritis in Guinea Pigs. *Int J Mol Sci*.

2014;15(8):13578-13595. doi:10.3390/ijms150813578

89. Holan V, Hermankova B, Kossl J. Perspectives of Stem Cell–Based Therapy for Age-Related Retinal Degenerative Diseases. *Cell Transplant*. 2017;26(9):1538-1541. doi:10.1177/0963689717721227

90. Ma C-J, Liu X, Che L, Liu Z-H, Samartzis D, Wang H-Q. Stem Cell Therapies for Intervertebral Disc Degeneration: Immune Privilege Reinforcement by Fas/FasL Regulating Machinery. *Curr Stem Cell Res Ther*. 2015;10(4):285-295. http://www.ncbi.nlm.nih.gov/pubmed/25381758. Accessed July 22, 2018.

91. Lunn JS, Sakowski SA, Hur J, Feldman EL. Stem cell technology for neurodegenerative diseases. *Ann Neurol*. 2011;70(3):353-361. doi:10.1002/ana.22487

92. Mundra V, Gerling IC, Mahato RI. Mesenchymal Stem Cell-Based Therapy. *Mol Pharm*. 2013;10(1):77-89. doi:10.1021/mp3005148

93. Zhang J, Huang X, Wang H, et al. The challenges and promises of allogeneic mesenchymal stem cells for use as a cell-based therapy. *Stem Cell Res Ther*. 2015;6(1):234. doi:10.1186/s13287-015-0240-9

94. Pittenger MF, Mackay AM, Beck SC, et al. Multilineage potential of adult human mesenchymal stem cells. *Science*. 1999;284(5411):143-147. http://www.ncbi.nlm.nih.gov/pubmed/10102814. Accessed July 23, 2018.

95. Kocan B, Maziarz A, Tabarkiewicz J, Ochiya T, Banaś-Ząbczyk A. Trophic Activity and Phenotype of Adipose Tissue-Derived Mesenchymal Stem Cells as a Background of Their Regenerative Potential. *Stem Cells Int*. 2017;2017:1-13.

doi:10.1155/2017/1653254

96. van Buul GM, Villafuertes E, Bos PK, et al. Mesenchymal stem cells secrete factors that inhibit inflammatory processes in short-term osteoarthritic synovium and cartilage explant culture. *Osteoarthr Cartil*. 2012;20(10):1186-1196. doi:10.1016/j.joca.2012.06.003

97. Nae S, Bordeianu I, Stăncioiu AT, Antohi N. Human adipose-derived stem cells: definition, isolation, tissue-engineering applications. *Rom J Morphol Embryol*. 2013;54(4):919-924. http://www.ncbi.nlm.nih.gov/pubmed/24398986. Accessed July 24, 2018.

98. Baer PC, Geiger H. Adipose-Derived Mesenchymal Stromal/Stem Cells: Tissue Localization, Characterization, and Heterogeneity. *Stem Cells Int*. 2012;2012:1-11. doi:10.1155/2012/812693

99. Strem BM, Hicok KC, Zhu M, et al. Multipotential differentiation of adipose tissue-derived stem cells. *Keio J Med*. 2005;54(3):132-141. http://www.ncbi.nlm.nih.gov/pubmed/16237275. Accessed July 24, 2018.

100. Burrow KL, Hoyland JA, Richardson SM. Human Adipose-Derived Stem Cells Exhibit Enhanced Proliferative Capacity and Retain Multipotency Longer than Donor-Matched Bone Marrow Mesenchymal Stem Cells during Expansion In Vitro. *Stem Cells Int*. 2017;2017:2541275. doi:10.1155/2017/2541275

101. Zaminy A, Ragerdi Kashani I, Barbarestani M, Hedayatpour A, Mahmoudi R, Farzaneh Nejad A. Osteogenic differentiation of rat mesenchymal stem cells from adipose tissue in comparison with bone marrow mesenchymal stem cells:

melatonin as a differentiation factor. *Iran Biomed J*. 2008;12(3):133-141. http://www.ncbi.nlm.nih.gov/pubmed/18762816. Accessed July 26, 2018.

102. Cheng K-H, Kuo T-L, Kuo K-K, Hsiao C-C. Human adipose-derived stem cells: Isolation, characterization and current application in regeneration medicine. *Genomic Med Biomarkers, Heal Sci*. 2011;3(2):53-62. doi:10.1016/J.GMBHS.2011.08.003

103. Song Y, Du H, Dai C, et al. Human adipose-derived mesenchymal stem cells for osteoarthritis: a pilot study with long-term follow-up and repeated injections. *Regen Med*. 2018;13(3):295-307. doi:10.2217/rme-2017-0152

104. Leong DT, Nah WK, Gupta A, Hutmacher DW, Woodruff MA. The osteogenic differentiation of adipose tissue-derived precursor cells in a 3D scaffold/matrix environment. *Curr Drug Discov Technol*. 2008;5(4):319-327. http://www.ncbi.nlm.nih.gov/pubmed/19075612. Accessed July 26, 2018.

105. Ilic D, Polak JM. Stem cells in regenerative medicine: introduction. *Br Med Bull*. 2011;98(1):117-126. doi:10.1093/bmb/ldr012

106. Si J-W, Wang X-D, Shen SG. Perinatal stem cells: A promising cell resource for tissue engineering of craniofacial bone. *World J Stem Cells*. 2015;7(1):149-159. doi:10.4252/wjsc.v7.i1.149

107. Evangelista M, Soncini M, Parolini O. Placenta-derived stem cells: new hope for cell therapy? *Cytotechnology*. 2008;58(1):33-42. doi:10.1007/s10616-008-9162-z

108. Bailo M, Soncini M, Vertua E, et al. Engraftment potential of human amnion and chorion cells derived from term placenta. *Transplantation*. 2004;78(10):1439-

1448. http://www.ncbi.nlm.nih.gov/pubmed/15599307. Accessed July 26, 2018.

109. Wolbank S, Peterbauer A, Fahrner M, et al. Dose-Dependent Immunomodulatory Effect of Human Stem Cells from Amniotic Membrane: A Comparison with Human Mesenchymal Stem Cells from Adipose Tissue. *Tissue Eng*. 2007;13(6):1173-1183. doi:10.1089/ten.2006.0313

110. Li H, Niederkorn JY, Neelam S, et al. Immunosuppressive Factors Secreted by Human Amniotic Epithelial Cells. *Investig Opthalmology Vis Sci*. 2005;46(3):900. doi:10.1167/iovs.04-0495

111. Topoluk N, Steckbeck K, Siatkowski S, Burnikel B, Tokish J, Mercuri J. Amniotic mesenchymal stem cells mitigate osteoarthritis progression in a synovial macrophage-mediated in vitro explant coculture model. *J Tissue Eng Regen Med*. 2018. doi:10.1002/term.2610

112. Topoluk N, Hawkins R, Tokish J, Mercuri J. Amniotic Mesenchymal Stromal Cells Exhibit Preferential Osteogenic and Chondrogenic Differentiation and Enhanced Matrix Production Compared With Adipose Mesenchymal Stromal Cells. *Am J Sports Med*. 2017;45(11):2637-2646. doi:10.1177/0363546517706138

113. Man GS, Mologhianu G. Osteoarthritis pathogenesis - a complex process that involves the entire joint. *J Med Life*. 2014;7(1):37-41. http://www.ncbi.nlm.nih.gov/pubmed/24653755. Accessed September 10, 2018.

114. Orozco L, Munar A, Soler R, et al. Treatment of Knee Osteoarthritis With Autologous Mesenchymal Stem Cells. *Transplant J*. 2013;95(12):1535-1541. doi:10.1097/TP.0b013e318291a2da

115. Wang W, Cao W. Treatment of osteoarthritis with mesenchymal stem cells. *Sci China Life Sci*. 2014;57(6):586-595. doi:10.1007/s11427-014-4673-7

116. Fujiwara N, Kobayashi K. Macrophages in inflammation. *Curr Drug Targets Inflamm Allergy*. 2005;4(3):281-286. http://www.ncbi.nlm.nih.gov/pubmed/16101534. Accessed September 10, 2018.

117. Wang T, Wen CY, Yan CH, Lu WW, Chiu KY. Spatial and temporal changes of subchondral bone proceed to microscopic articular cartilage degeneration in guinea pigs with spontaneous osteoarthritis. *Osteoarthr Cartil*. 2013. doi:10.1016/j.joca.2013.01.002

118. Vincent KR, Conrad BP, Fregly BJ, Vincent HK. The pathophysiology of osteoarthritis: a mechanical perspective on the knee joint. *PM R*. 2012;4(5 Suppl):S3-9. doi:10.1016/j.pmrj.2012.01.020

119. Vidarsson G, Dekkers G, Rispens T. IgG subclasses and allotypes: from structure to effector functions. *Front Immunol*. 2014;5:520. doi:10.3389/fimmu.2014.00520

120. Kurtz A. Mesenchymal stem cell delivery routes and fate. *Int J Stem Cells*. 2008;1(1):1-7. doi:10.15283/ijsc.2008.1.1.1

121. Becker A De, Riet I Van. Homing and migration of mesenchymal stromal cells: How to improve the efficacy of cell therapy? *World J Stem Cells*. 2016;8(3):73. doi:10.4252/wjsc.v8.i3.73

122. Tögel F, Yang Y, Zhang P, Hu Z, Westenfelder C. Bioluminescence imaging to monitor the in vivo distribution of administered mesenchymal stem cells in acute kidney injury. *Am J Physiol Renal Physiol*. 2008;295(1):F315-21.

doi:10.1152/ajprenal.00098.2008

123. Eggenhofer E, Benseler V, Kroemer A, et al. Mesenchymal stem cells are short-lived and do not migrate beyond the lungs after intravenous infusion. *Front Immunol*. 2012;3:297. doi:10.3389/fimmu.2012.00297

124. Eggenhofer E, Luk F, Dahlke MH, Hoogduijn MJ. The life and fate of mesenchymal stem cells. *Front Immunol*. 2014;5:148. doi:10.3389/fimmu.2014.00148

125. Sato M, Uchida K, Nakajima H, et al. Direct transplantation of mesenchymal stem cells into the knee joints of Hartley strain guinea pigs with spontaneous osteoarthritis. *Arthritis Res Ther*. 2012. doi:10.1186/ar3735

126. Fischer UM, Harting MT, Jimenez F, et al. Pulmonary Passage is a Major Obstacle for Intravenous Stem Cell Delivery: The Pulmonary First-Pass Effect. *Stem Cells Dev*. 2009;18(5):683-692. doi:10.1089/scd.2008.0253

127. Barbash IM, Chouraqui P, Baron J, et al. Systemic Delivery of Bone Marrow–Derived Mesenchymal Stem Cells to the Infarcted Myocardium. *Circulation*. 2003;108(7):863-868. doi:10.1161/01.CIR.0000084828.50310.6A

128. Heng BC, Haider HK, Sim EKW, Cao T, Ng SC. Strategies for directing the differentiation of stem cells into the cardiomyogenic lineage in vitro. *Cardiovasc Res*. 2004;62(1):34-42. doi:10.1016/j.cardiores.2003.12.022

129. Choudhary P, Booth H, Gutteridge A, et al. Directing Differentiation of Pluripotent Stem Cells Toward Retinal Pigment Epithelium Lineage. *Stem Cells Transl Med*. 2017;6(2):490-501. doi:10.5966/sctm.2016-0088

130. Roelandt P, Vanhove J, Verfaillie C. Directed Differentiation of Pluripotent Stem Cells to Functional Hepatocytes. In: *Methods in Molecular Biology (Clifton, N.J.)*. Vol 997. ; 2013:141-147. doi:10.1007/978-1-62703-348-0_11

131. Diekman BO, Guilak F. Stem cell-based therapies for osteoarthritis: challenges and opportunities. *Curr Opin Rheumatol*. 2013;25(1):119-126. doi:10.1097/BOR.0b013e32835aa28d

132. Vinardell T, Sheehy EJ, Buckley CT, Kelly DJ. A comparison of the functionality and in vivo phenotypic stability of cartilaginous tissues engineered from different stem cell sources. *Tissue Eng Part A*. 2012;18(11-12):1161-1170. doi:10.1089/ten.TEA.2011.0544

133. Amer MH, White LJ, Shakesheff KM. The effect of injection using narrow-bore needles on mammalian cells: administration and formulation considerations for cell therapies. *J Pharm Pharmacol*. 2015;67(5):640-650. doi:10.1111/jphp.12362

134. Foster AA, Marquardt LM, Heilshorn SC. The diverse roles of hydrogel mechanics in injectable stem cell transplantation. *Curr Opin Chem Eng*. 2017;15:15-23. doi:10.1016/j.coche.2016.11.003

135. Aguado BA, Mulyasasmita W, Su J, Lampe KJ, Heilshorn SC. Improving Viability of Stem Cells During Syringe Needle Flow Through the Design of Hydrogel Cell Carriers. *Tissue Eng Part A*. 2012;18(7-8):806-815. doi:10.1089/ten.tea.2011.0391

136. Lee KY, Mooney DJ. Alginate: properties and biomedical applications. *Prog Polym Sci*. 2012;37(1):106-126. doi:10.1016/j.progpolymsci.2011.06.003

137. Abbina S, Siren EMJ, Moon H, Kizhakkedathu JN. Surface Engineering for Cell-Based Therapies: Techniques for Manipulating Mammalian Cell Surfaces. *ACS Biomater Sci Eng*. October 2017:acsbiomaterials.7b00514. doi:10.1021/acsbiomaterials.7b00514

138. Cheng H, Byrska-Bishop M, Zhang CT, et al. Stem cell membrane engineering for cell rolling using peptide conjugation and tuning of cell–selectin interaction kinetics. *Biomaterials*. 2012;33(20):5004-5012. doi:10.1016/j.biomaterials.2012.03.065

139. Woodsworth DJ, Holt RA. Cell-Based Therapeutics: Making a Faustian Pact with Biology. *Trends Mol Med*. 2017;23(2):104-115. doi:10.1016/j.molmed.2016.12.004

140. Saeui CT, Mathew MP, Liu L, Urias E, Yarema KJ. Cell Surface and Membrane Engineering: Emerging Technologies and Applications. *J Funct Biomater*. 2015;6(2):454-485. doi:10.3390/jfb6020454

141. Escobar Ivirico JL, Bhattacharjee M, Kuyinu E, Nair LS, Laurencin CT. Regenerative Engineering for Knee Osteoarthritis Treatment: Biomaterials and Cell-Based Technologies. *Engineering*. 2017;3(1):16-27. doi:10.1016/J.ENG.2017.01.003

142. Lim KS, Lee DY, Valencia GM, Won Y-W, Bull DA. Cell surface-engineering to embed targeting ligands or tracking agents on the cell membrane. *Biochem Biophys Res Commun*. 2017;482(4):1042-1047. doi:10.1016/j.bbrc.2016.11.155

143. Imagawa K, de Andrés M, Hashimoto K, et al. The epigenetic effect of

glucosamine and a nuclear factor-kappa B (NF-kB) inhibitor on primary human chondrocytes – Implications for osteoarthritis. *Biochem Biophys Res Commun*. 2011;405(3):362-367. doi:10.1016/j.bbrc.2011.01.007

144. Niederberger E, Geisslinger G. The IKK-NF-κB pathway: a source for novel molecular drug targets in pain therapy? *FASEB J*. 2008;22(10):3432-3442. doi:10.1096/fj.08-109355

145. Kapoor M, Martel-Pelletier J, Lajeunesse D, Pelletier J-P, Fahmi H. Role of proinflammatory cytokines in the pathophysiology of osteoarthritis. *Nat Rev Rheumatol*. 2011;7(1):33-42. doi:10.1038/nrrheum.2010.196